

**Cosmological Constraints from a Measurement of the  
Polarization Power Spectra of the Cosmic Microwave  
Background with the SPTpol Experiment**

by

**J. W. Henning**

B.A., University of Chicago, 2007

M.S., University of Colorado, 2010

A thesis submitted to the  
Faculty of the Graduate School of the  
University of Colorado in partial fulfillment  
of the requirements for the degree of  
Doctor of Philosophy  
Department of Astrophysical and Planetary Sciences  
2014

This thesis entitled:  
Cosmological Constraints from a Measurement of the Polarization Power Spectra of the Cosmic  
Microwave Background with the SPTpol Experiment  
written by J. W. Henning  
has been approved for the Department of Astrophysical and Planetary Sciences

---

Assoc. Prof. Nils Halverson

---

Prof. Jason Glenn

---

Prof. Jack Burns

---

Assoc. Prof. Jeremy Darling

---

Assoc. Prof. Oliver DeWolf

Date \_\_\_\_\_

The final copy of this thesis has been examined by the signatories, and we find that both the content and the form meet acceptable presentation standards of scholarly work in the above mentioned discipline.

Henning, J. W. (Ph.D., Astrophysical and Planetary Science)

Cosmological Constraints from a Measurement of the Polarization Power Spectra of the Cosmic  
Microwave Background with the SPTpol Experiment

Thesis directed by Assoc. Prof. Nils Halverson

SPTpol is a polarization-sensitive receiver installed on the South Pole Telescope in its third season of mapping Cosmic Microwave Background (CMB) temperature and polarization anisotropies. The receiver contains 588 (180) dual polarization pixels at 150 (95) GHz comprising a total of 1536 transition edge sensor bolometers. In its first year, SPTpol mapped  $100 \text{ deg}^2$  to a depth of  $\sim 8$  and  $10 \mu\text{K-arcmin}$  at 150 GHz in temperature and polarization, respectively. With this deep field map, the SPTpol collaboration produced the first statistically significant detection ( $7.7 \sigma$ ) of gravitational lensing *B*-mode polarization. Additionally, the SPTpol experiment just completed its first of three years mapping  $500 \text{ deg}^2$  to a depth of  $\sim 12$  and  $15 \mu\text{K-arcmin}$  in temperature and polarization at 150 GHz. High signal-to-noise measurements of the polarization power spectra from the survey will further constrain cosmological parameters and extensions to the  $\Lambda$ CDM cosmological model. Measurements of large-scale polarization anisotropies will also place tighter constraints on the existence of primordial *B*-mode polarization generated by gravitational waves from the epoch of inflation.

In this work we discuss the development of the SPTpol receiver and, in particular, the seven 150 GHz detector modules at the heart of the focal plane. We describe the observational strategies used during the first two seasons of SPTpol measurements as well as the reduction of detector timestreams into maps and CMB polarization power spectra. To extract constraints on cosmological parameters from the SPTpol power spectra we have written a new Bayesian likelihood module for the CosmoMC Markov Chain Monte Carlo package, which we also describe. Finally, we present cosmological constraints from the first year of SPTpol observations. Pre-existing constraints on  $\Lambda$ CDM parameters improve by a few percent with the inclusion of these data. While this is a

modest step forward in our understanding of the early universe, the completed SPTpol dataset will have the power to tightly constrain the sum of neutrino masses and help determine the source of recently detected large-scale  $B$ -mode polarization.

## **Dedication**

To my great-grandmother Anna Payne. She always wanted to go to college and further her education. Unfortunately, the realities of life in the mid-1930s forced her to stay home, help raise her siblings, and work the family farm. I hope I've been able to take advantage of all the opportunities you couldn't and then some.

## Acknowledgements

There's no way I could thank everyone who helped me along the way, but I'll try to highlight some of them. First of all, my parents are the best anyone could ever hope for, and I'm only here because of their endless love, encouragement, and patience. I couldn't hope to be even a tenth as good a parent one day as they were and still are to me. Second, I have to thank my brother Nick for his support and helping to keep me sane. You gave me great advice in college and I try to keep it in mind every day. Third, I'm quite... quirky... and I was lucky enough to find a partner who not only loves me for my quirks but who also shares most of them with me. Callan, I can't wait for our turtle, Strider. And I would be remiss if I forgot to thank her parents, who are incredibly welcoming and supportive. Thanks for being my second family. Fourth, I've met a lot of great people in graduate school, especially my fellow Armer House roommates. Devin, Sam, Adam, Anthony, Jordan, Grant (and Greg because, hey, the flood weeks count)... you've all been fantastic and have really made my time in Boulder special. I couldn't have asked for a better set of colleagues and friends. Fifth, I absolutely have to thank my advisor Nils Halverson and lab mentor Jay Austermann for their guidance and always being willing to talk a problem over with me. And that is rarely easy to do because I'm *terrible* at providing context; I just launch into whatever it is that's giving me problems. It takes a lot of patience to put up with that - and my occasional clumsiness in lab - and they both have it in spades. Finally, it has been a pleasure and a sincere honor to count myself as a member of the SPT collaboration. I've never met a more talented and dedicated group of researchers and I am incredibly privileged to have been given the chance to be a part of it.

## Contents

### Chapter

<b>1</b>	<b>Introduction</b>	<b>1</b>
1.1	Cosmology . . . . .	4
1.1.1	Expansion and the Friedmann Equations . . . . .	5
1.1.2	Initial Conditions with Inflation . . . . .	9
1.1.3	$\Lambda$ CDM Cosmological Model . . . . .	12
1.2	CMB Temperature Anisotropies . . . . .	15
1.2.1	The Photon-Baryon Plasma . . . . .	15
1.2.2	The Temperature Angular Power Spectrum . . . . .	18
1.2.3	Sensitivity to Cosmology . . . . .	20
1.3	CMB Polarization . . . . .	23
1.3.1	Linear Polarization and the Stokes Parameters . . . . .	23
1.3.2	Polarizing the CMB . . . . .	25
1.4	Outline . . . . .	31
<b>2</b>	<b>The South Pole Telescope and the SPTpol Receiver</b>	<b>32</b>
2.1	The South Pole Telescope . . . . .	32
2.2	The SPTpol Receiver . . . . .	35
2.3	Detector Technology . . . . .	38
2.3.1	95 GHz Pixels . . . . .	41

2.3.2	150 GHz Pixels . . . . .	43
2.4	Frequency-Domain Multiplexing . . . . .	44
<b>3</b>	<b>SPTpol 150 GHz Module Design</b>	<b>46</b>
3.1	Introduction . . . . .	46
3.2	Module Design . . . . .	46
3.2.1	Corrugated Silicon Platelet Feed Horn Array . . . . .	47
3.2.2	Detector Arrays . . . . .	50
3.2.3	Mounting Hardware . . . . .	54
3.2.4	RF Shielding . . . . .	58
3.2.5	Passive Readout Electronics . . . . .	60
3.3	Dark Properties . . . . .	62
3.4	Optical Properties . . . . .	64
<b>4</b>	<b>Observations and Data Products</b>	<b>68</b>
4.1	CMB Field Observations . . . . .	68
4.2	2012 Observations . . . . .	71
4.3	2013 Observations . . . . .	72
4.4	Datasets . . . . .	72
<b>5</b>	<b>Data Reduction: From Timestreams to Power Spectra</b>	<b>74</b>
5.1	Timestream Processing . . . . .	74
5.1.1	Timestream Filtering . . . . .	76
5.1.2	Absolute Telescope Boresight Pointing . . . . .	77
5.2	Maps . . . . .	82
5.2.1	Absolute Calibration . . . . .	88
5.2.2	Polarization Angle Calibration . . . . .	89
5.2.3	$T \rightarrow P$ Deprojection . . . . .	90

5.2.4	Data Quality Cuts . . . . .	91
5.3	Pseudo-Spectra . . . . .	92
5.4	Estimation of Unbiased Power Spectra: the MASTER Algorithm . . . . .	94
5.4.1	Mode-Coupling . . . . .	95
5.4.2	Beam Function . . . . .	97
5.4.3	Transfer Function . . . . .	99
5.4.4	Bandpower Window Functions . . . . .	101
5.4.5	Bandpower Covariance Matrix . . . . .	103
5.5	Jackknives . . . . .	109
<b>6</b>	<b>Cosmological Parameter Fitting</b>	<b>111</b>
6.1	Bayesian Likelihood . . . . .	111
6.2	Fisher Forecasting . . . . .	113
6.2.1	Fisher Formalism . . . . .	113
6.2.2	Generalized Fisher Formalism . . . . .	115
6.2.3	Estimating the Bandpower Covariance Matrix . . . . .	117
6.2.4	SPTpol Forecasts . . . . .	118
6.3	Parameter Fitting Through MCMC . . . . .	121
6.3.1	Markov Chain Monte Carlo . . . . .	121
6.3.2	Chain Convergence . . . . .	124
6.3.3	The SPTpol Likelihood . . . . .	124
6.3.4	Likelihood Validation . . . . .	127
6.3.5	Adding WIMP Annihilation . . . . .	130
<b>7</b>	<b>Results</b>	<b>133</b>
7.1	Bandpowers . . . . .	133
7.1.1	SPTpol Bandpower Validation . . . . .	137
7.2	Cosmological Constraints from SPTpol . . . . .	143

7.2.1	$\Lambda$ CDM constraints . . . . .	143
7.2.2	Extensions to $\Lambda$ CDM . . . . .	151
7.3	Discussion . . . . .	154
<b>8</b>	<b>Future Work</b>	160
	<b>Bibliography</b>	165
	<b>Appendix</b>	
<b>A</b>	Determination of Science Band Frequencies in Detector Timestreams	170

## Tables

### **Table**

1.1	$\Lambda$ CDM Parameter Definitions . . . . .	13
2.1	SPTpol Optical Loading . . . . .	34
2.2	SPTpol Bandpass Summary . . . . .	37
2.3	SPTpol Detector Properties . . . . .	41
3.1	Detector Dark Properties . . . . .	63
4.1	SPTpol Observing Breakdown: January 27, 2012 - April 15, 2014 . . . . .	73
5.1	PTEs for SPTpol 2012 Deep Field Jackknife Tests . . . . .	110
6.1	SPTpol Fisher Forecasts for $\Lambda$ CDM Parameters . . . . .	119
6.2	CosmoMC minimizer results for 204 sets of simulated SPTpol bandpowers. . . . .	128
7.1	SPTpol 150 GHz <i>TE</i> Power Spectrum . . . . .	134
7.2	SPTpol 150 GHz <i>EE</i> Power Spectrum . . . . .	134
7.3	$\Lambda$ CDM constraints - SPTpol Only . . . . .	147
7.4	$\Lambda$ CDM constraints . . . . .	147
7.5	$\Lambda$ CDM Extensions . . . . .	155

## Figures

### Figure

1.1	Recent high signal-to-noise CMB polarization power spectra measurements plotted in units of $\mu\text{K}^2$ as a function of spherical harmonic multipole $l$ . In 2013 the SPTpol collaboration recently published a lensing correlation detection of $B$ modes consistent with the best-fit $\Lambda\text{CDM}$ model (rising dashed line at $l \gtrsim 100$ ) (21). The POLARBEAR collaboration has also published lensing $B$ -mode measurements (22). In early 2014 the BICEP2 experiment submitted a first detection of large-scale $B$ modes consistent with a tensor-to-scalar ratio $r = 0.2$ (dashed line at $l \lesssim 100$ ) (23). Also plotted are data from ACTPol (24), QUIET (14), QUaD (10), and WMAP (25). . . . .	3
1.2	Samples from a Markov Chain Monte Carlo (MCMC) calculation of parameter constraints using Planck CMB temperature anisotropy measurements (15). The color map corresponds to values of $\Omega_\Lambda$ at a given point in $\ln(10^{10} A_s) - \sigma_8$ space. . . . .	13
1.3	CMB $TT$ power spectrum from a Planck best-fit $\Lambda\text{CDM}$ model (31) (black). The shaded region shows the smallest possible uncertainties for single multipoles set by cosmic variance. . . . .	19
1.4	Effects of increasing $\Omega_b h^2$ (top) and $\Omega_c h^2$ (bottom) on the CMB $TT$ power spectrum while keeping $H_0$ and $\Omega_k$ fixed. Parameter values increase according to dashed, solid, and thick lines. . . . .	22
1.5	Graphic depicting the directional relations between Stokes $Q$ , $U$ , and $V$ . . . . .	24

1.6 Directions of polarization patterns for positive and negative $E$ - and $B$ -mode anisotropies.	28
1.7 Effects of increasing $\Omega_b h^2$ (top) and $\Omega_c h^2$ (bottom) on the CMB $EE$ polarization power spectrum while keeping $H_0$ and $\Omega_k$ fixed. Parameter values increase according to dashed, solid, and thick lines. . . . .	30
2.1 The SPT with newly installed primary mirror guard ring, side shields, and snout to mitigate polarized ground pickup for SPTpol observations. . . . .	33
2.2 Cut-away view of the SPT secondary mirror cryostat (50). Light rays enter the system after bouncing off the primary mirror located off-image to the upper left. They terminate on the SPTpol focal plane housed in a separate cryostat. Both cryostats, however, share the same vacuum. . . . .	33
2.3 The SPTpol focal plane. (Left) Feedhorns before band-defining filters are installed. (Right) Back side of focal plane with cryogenic readout electronics boards, thermal sinking points, and additional structures to increase the rigidity of the readout boards. . . . .	36
2.4 Metal mesh filters define the high-edge of the bandpasses. (Left) 95 GHz filter installed. (Right) 150 GHz filter plus harmonic blocker. . . . .	37
2.5 SPTpol bandpass transmission. Black is the South Pole atmospheric transmission with 0.26 mm PWV, the median value during winter months (52). The 150 GHz bandpass is plotted in red while the 90 GHz bandpass is in blue. Bandpasses for the 2012 (2013) observing season are in solid (dashed) lines. SPTpol bandpass transmissions have been normalized to a maximum value of one. . . . .	37
2.6 Internal view of SPTpol 95 GHz pixel. (Top) Cutaway of single feed plus pixel package. (Bottom) Magnified view of 95 GHz pixel and TES structure. Inside the choke the waveguide is 2.35 mm in diameter, which defines the low-frequency edge of the detector bandpass. Figure from (59). . . . .	42

2.7 A prototype SPTpol 150 GHz pixel. The device is 5 mm across with a 1.6 mm OMT. Bandpass-defining stub filters shown here were not included in the final pixels. Figure appears in (60). . . . .	43
2.8 (Top) Circuit schematic of a DfMUX readout system, adapted from (61). © 2008 IEEE. (Bottom) One of 144 frequency combs measuring detector resonant frequencies in the SPTpol experiment. . . . .	45
3.1 The SPTpol focal plane. Seven 84-pixel modules of 150 GHz detectors sit at the center of the camera, while 180 individually packaged 95 GHz pixels surround the modules, for a total of 768 polarization-sensitive pixels (1536 detectors). The focal plane is $\sim$ 225 mm in diameter. . . . .	48
3.2 (Top) One of seven 150 GHz corrugated silicon platelet feed horn arrays in the SPTpol focal plane. The array is 2.3 inches wide and contains 84 feed horns with 4.26 mm apertures. (Bottom) Cross-sectional view of the feed horn profiles showing the corrugations and waveguides. . . . .	49
3.3 (Top) Schematic of one SPTpol 150 GHz pixel. Areas with white hashing are regions where the silicon substrate has been etched away leaving released silicon nitride. (Bottom) One of the seven SPTpol 150 GHz detector arrays during module assembly, before installing the BS wafer. The array is 2.3 inches across. . . . .	51
3.4 Expanded cross-sectional view of the detector wafer sandwich. Boss features in the WIP slip into the back-etched cavities of each pixel OMT, extending the horn waveguide to the OMT and providing pixel-waveguide registration. The BS wafer terminates the waveguides with $\lambda/4$ backshorts. . . . .	52

3.5 (Top) BS wafer with filled moats. The moats alternately rotate by 45° to match the alternating rotations of the pixels. (Bottom) A schematic of the BS moat and OMT fence layout with respect to pixel features. The moats are aligned to be above each TES island, and the OMT fence closes the gap between the detector array and BS array except where microstrip lines are present. . . . .	53
3.6 (Top) Flexible invar tabs used to connect the silicon feed horn arrays to the metal mounting structures in the 150 GHz modules. Each tab is 0.5 mm thick, while the flexing portion is 0.4 mm thick to reduce stress near the epoxy joint. The flexible portion of the tab, between the registration features, is 7.4 mm long. (Bottom) The tabs installed on a feed horn array prior to module assembly. . . . .	56
3.7 (Top) Mounting ring with beryllium copper clamps installed in a module. The invar tabs screw into the six feet in the ring, while four flexible cables are clamped down to the outer walls of the ring. The beryllium copper clamps supply vertical pressure to the detector wafer stack. (Bottom) The interface plate installed on top of the mounting ring with its many mounting holes. The flexible readout cables snake underneath the plate and come out the center of the module. . . . .	57
3.8 (Top) Image of RF skirts, showing flexure portion. (Bottom) Skirts installed with final RF tape applied as the module is prepared for shipment to the South Pole. . .	59
3.9 (Top) Populated LC board. (Bottom) Two LC boards with protective shielding in place and mounted to a module. . . . .	61
3.10 (Top) Return loss for six horns in one SPTpol feed horn array. Dashed line is the expectation for the feed horn profile only. (Middle) 300 K insertion loss measurements of the same horns. (Bottom) Beam profile at 150 GHz for one representative horn. Dots are measurements while solid lines are expectations from simulations. . .	65

3.11 (Top) Measurements of the electrothermal time constant of one representative detector at several points in its superconducting transition. Devices exhibit time constants $< 1$ ms at nominal operation points. (Bottom) Power spectral densities (PSDs) for three devices in the same 150 GHz pixel. “X” and “Y” are optically loaded while the “Dark” device is not coupled to the sky. All three device PSDs have white noise levels consistent with expectations. The PSD of the differenced timestreams of the optically loaded devices shows a much reduced $1/f$ knee. . . . .	66
4.1 Azimuth and elevation coordinates for a single CMB field observation. The telescope starts at low elevation and scans right and left before taking an elevation step and repeating. The field is split into “lead” and “trail” halves, which are forced to match in azimuth for removal of ground contamination. Lead and trail coordinates have been offset by $0.05^\circ$ in azimuth and elevation for clarity. . . . .	69
5.1 Example bolometer timestream as a detector scans across the center of RCW38. Additional optical power from the source reduces the requisite electrical power to keep the detector biased at the same point in its transition, causing the source to manifest as a drop in readout current. . . . .	75
5.2 (Top) Representative azimuth bearing axis tilt measurement with corresponding fit to determine pointing parameters $a_2$ and $a_3$ . (Bottom) $a_2$ (blue) and $a_3$ (red) as a function of time since SPTpol deployment in January 2012. The azimuth axis tilt grows by several arcminutes per year. . . . .	79
5.3 Flowchart for how offline pointing model corrections are calculated and applied to the data. “Tilt” and “HII region” parameters are determined ahead of time and saved in auxiliary config files. Corrections for thermometry, metrology, and atmospheric refraction are handled in real-time. Corrections to az/el are added to the raw telescope az/el, coordinates are converted to RA/Dec, and final pointing is passed to the mapper routine for binning timestreams into pixels. . . . .	81



5.7 CMB $E$ -mode polarization map from the SPTpol 500 deg $^2$ survey field 2013 observations. Here, colorscale indicates local polarization direction ( $\pm E$ ) expressed as differential intensity. Resolution is 1 arcmin/pixel. The Oblique Lambert azimuthal equal-area projection is applied (80). (Top) Signal or “sum” map, coadding all observations of the 2013 season into a single map. (Bottom) Noise or “difference” map, generated by subtracting coadds of the first and second half of the observing season.	87
5.8 (Top) Two-dimensional biased $E$ -mode pseudo-spectrum from SPTpol 2013 full survey observations with $C_l$ normalization and Fourier resolution $\Delta l = 6.25$ . The spectrum is converted to $D_l$ and azimuthally averaged in multipole bins of $\Delta l = 50$ to generate the more familiar one-dimensional power spectrum. The $E$ -mode acoustic peaks are clearly visible as harmonic rings with high signal-to-noise even before azimuthal averaging. The vertical stripe of much lower power at low $l_x$ is due to timestream polynomial subtraction along the scan direction, which is mostly parallel to $l_x$ . (Bottom) $E$ -mode noise power spectrum with the same color scale. Sample variance is not included. A small rise in noise is visible below $l \sim 150$ but otherwise the noise is white. . . . .	93
5.9 (Top left) The SPTpol 2012 150 GHz deep field apodization window. The edges of the region transition to zero using a 15' cosine taper. Point sources with $> 50$ mJ flux at 150 GHz are masked with 5' disks and a 5' cosine taper. (Top right) The $TT$ mode-coupling matrix, log scale. (Bottom left) The $EE$ mode-coupling matrix, log scale. (Bottom right) The $TE$ mode-coupling matrix, log scale. White elements are negative. When binned to $\Delta l=50$ bandpowers, mode-coupling due to the apodization window between Fourier modes is $< 10\%$ . . . . .	96
5.10 The SPTpol 2012 deep field 150 GHz beam function $B_l$ and its fractional errors $\delta B_l/B_l$ . $B_l$ is arbitrarily normalized to unity at $l = 0$ . . . . .	98

5.11 The SPTpol 2012 deep field 150 GHz transfer functions $F_l$ , binned to $\Delta l = 50$ . The $TE$ transfer function, not plotted for clarity, is the geometric mean of the $TT$ and $EE$ transfer functions. The initial iterations exhibit oscillations from mode-coupling induced by the map apodization window, but by the fifth and final iteration only the effects of timestream filtering on the power spectra remain. . . . .	100
5.12 The lowest three bandpower window functions for the SPTpol 2012 150 GHz deep field $EE$ power spectrum. Window functions are calculated with a resolution of $\Delta l = 5$ . . . . .	102
5.13 (Top) $TE \times EE$ cross-covariance matrix measured from $10^5$ cross-spectra simulations. (Bottom) Cross-covariance matrix constructed using auto-covariance block diagonals.	107
6.1 Partial derivatives of CMB power spectra with respect to $\Lambda$ CDM cosmological parameters used to obtain parameter Fisher forecasts. Derivatives are calculated numerically using CAMB and the step sizes printed in the figure legend. (Top Left) $D_l^{TT}$ derivatives. (Top Right) $D_l^{EE}$ derivatives. (Bottom Left) $D_l^{TE}$ derivatives. Dashed lines are negative values. . . . .	117
6.2 The SPTpol 150 GHz 2012 deep field $TE$ (Top) and $EE$ (Bottom) power spectra (black) plotted with averaged Fisher forecasted bandpowers for the 2012 deep field and completed full survey (red/blue). Forecasted bandpowers are offset by $\Delta l \pm 15$ for clarity. The average of 100 random bandpower realizations agrees with the input cosmological theory (solid line). Forecasted error bars for the deep field are everywhere comparable to but better than the measured uncertainties, as expected. . .	120
6.3 Representative 2-D slice in the $\Omega_c h^2 - \Omega_b h^2$ plane of a Markov chain. The color bar designates at what fractional point in the chain each step takes place. The initial steps of the chain in dark blue are “burn-in.” When the first half of the chain is thrown out, however, the remaining steps are draws from the desired probability distribution function $P(\vec{\theta})$ . . . . .	123

6.4	2-D marginalized parameter likelihood contour grid resulting from a test chain using a realization of simulated SPTpol bandpowers. Contours show the 68 and 95% confidence regions. In red are constraints from Planck that define the input cosmology for the sims. In black (blue) are constraints from $\Delta l = 50$ ( $\Delta l = 100$ ) simulated bandpowers. We also used the actual SPTpol deep field bandpower covariance matrix and window functions for this test. The cosmological constraints all match within a fraction of the $1-\sigma$ uncertainties on the parameters. This simultaneously validates the likelihood module, bandpower covariance matrix, and the bandpower window functions. . . . .	129
6.5	Perturbations to the CMB power spectra $\delta D_l$ from WIMP annihilation scaled to $e_{\text{WIMP}} = 1$ ( $p_{\text{ann}}(z) = 2 \times 10^{-27} \text{ cm}^3/\text{s}/\text{GeV}$ ). (Top) Corrections to the <i>TE</i> spectrum. (Bottom) Corrections to the <i>EE</i> spectrum. . . . .	131
7.1	The SPTpol 150 GHz 2012 deep field <i>TE</i> (Top) and <i>EE</i> (Bottom) power spectra on a linear scale. We measure six acoustic peaks in the <i>EE</i> spectrum with high significance and achieve the highest signal-to-noise measurements of the <i>EE</i> damping tail to date. The solid black lines in both plots are the $\Lambda\text{CDM}$ expectation from Planck (31) <i>TT</i> measurements and have not been fitted to the SPTpol data. . . . .	135
7.2	The SPTpol 150 GHz 2012 deep field <i>TE</i> (Top) and <i>EE</i> (Bottom, log scale) power spectra, plotted with data from BICEP2 (23), WMAP (25), QUIET W-band (14), and QUaD (94). The solid black lines in both plots are the $\Lambda\text{CDM}$ expectation from Planck (31) <i>TT</i> measurements and have not been fitted to the SPTpol data. . . . .	136
7.3	<i>Pseudo-spectra</i> SPTpol 150 GHz deep field bandpowers (blue) overplotted with 95 GHz bandpowers (red). Error bars include noise variance only. The two sets of bandpowers agree within errors. Since the bandpowers are biased by filtering and analysis systematics, the black theory line is meant only to guide the eye. . . . .	139

7.4 SPTpol 2012 deep field bandpowers (black) overplotted with bandpowers calculated with an alternate pipeline (red). The solid black line is the Planck $\Lambda$ CDM expectation. The two sets of bandpowers agree well indicating no obvious bias introduced by either analysis pipeline. . . . .	140
7.5 SPTpol 2012 deep field bandpowers (black dots) overplotted with bandpowers from four 100 deg <sup>2</sup> sub-fields from 2013 full survey observations. The solid black line is the Planck $\Lambda$ CDM expectation. 2013 bandpowers have been offset horizontally for clarity. Differences between the four fields are consistent with sample variance. . . .	142
7.6 1-D marginalized $\Lambda$ CDM constraints from 2012 SPTpol data (red). Constraints from the separate 2013 sub-fields are also included. $H_0$ is a derived quantity, while $P_{\text{cal}}$ , $D_{3000}^{\text{PS}_{\text{EE}}}$ , and $D_{3000}^{\text{PS}_{\text{TE}}}$ are nuisance parameters in the SPTpol likelihood. The fourth nuisance parameter $T_{\text{cal}}$ is not shown as it is tightly constrained by its Gaussian prior. . . .	144
7.7 SPTpol 2012 deep field bandpowers with two $\Lambda$ CDM model curves. The solid blue line is the Planck $\Lambda$ CDM expectation while the solid red line is the SPTpol best-fit model. Dashed lines are residuals for the respective models. . . . .	145
7.8 2-D marginalized constraints on the scalar amplitude $\ln 10^{10}(A_s)$ and $P_{\text{cal}}$ for the SPTpol 2012 deep field bandpowers. A strong degeneracy between the two parameters is evident. . . . .	148
7.9 1-D marginalized $\Lambda$ CDM parameter constraints. . . . .	149
7.10 2-D marginalized $\Lambda$ CDM parameter likelihoods. . . . .	150
7.11 2-D marginalized $\Lambda$ CDM + $\alpha_{-1}$ parameter likelihoods. <i>As of printing these chains had not fully converged.</i> . . . . .	156
7.12 2-D marginalized $\Lambda$ CDM + ewIMP parameter likelihoods. . . . .	157
7.13 2-D marginalized $\Lambda$ CDM + $r$ parameter likelihoods. <i>As of printing these chains had not fully converged.</i> . . . . .	158
8.1 SPTpol 2013 survey field 2-D $EE$ pseudo-power spectrum in $C_l$ normalization. . . .	161

- 8.2 Preliminary SPTpol 2013 survey field  $TE$  and  $EE$  power spectra with noise variance error bars. Bandpower resolution is  $\Delta l = 6.25$ . The Planck  $\Lambda$ CDM model is in black. In red we plot the raw pseudo-spectra while in blue we partially unbias the bandpowers by taking into account the instrument beam and a by-eye calibration factor of 0.85. Mode-coupling and the filter transfer function have been ignored. . . 162

## Chapter 1

### Introduction

Cosmologists have made remarkable progress over the past two decades in understanding the contents, structure, and evolution of the universe. Detailed observations of temperature and polarization anisotropies in the Cosmic Microwave Background (CMB) provide a straightforward means to study a young and relatively simple universe before the formation of large-scale structure. The CMB also carries information about the low-redshift universe since cosmic structure alters primordial anisotropies. For example, gravitational lensing of the CMB caused by large-scale structure can be used to make a census of and map the distribution of matter (1; 2; 3; 4). Localized spectral distortions of the CMB from inverse-Compton scattering known as the thermal Sunyaev-Zel'dovich effect (SZE) (5; 6) mark locations of galaxy clusters, which can be used to study dark energy and its effects on the expansion of the universe (7). The optical depth of the CMB informs our understanding of the epoch of reionization. Finally, measurements of the kinetic SZE offer a path toward constraining the timing and duration of reionization (8).

First measured by the COBE satellite (9) and more recently by many other experiments (e.g., 10; 11; 12; 13; 14; 15), CMB anisotropies have motivated a new era of precision cosmology. Coupled with independent measurements of the Hubble constant (16), Type Ia supernovae (17), baryon acoustic oscillations (BAO) (18), and general properties of galaxy clusters (e.g., 19; 20), CMB anisotropy measurements have led to the standard  $\Lambda$ CDM cosmological model, which describes a spatially flat universe composed predominantly of dark energy ( $\sim 69\%$  of total energy content of the universe) and cold dark matter ( $\sim 26\%$ ) with structure sourced by nearly scale-invariant

Gaussian fluctuations during its earliest moments.

Through a combination of satellite, balloon-borne, and ground-based observations over the past decade, the power spectrum of CMB temperature anisotropies has been measured with high signal-to-noise over angular scales ranging from the full sky down to  $\sim 1'$ . Current CMB experiments are now focusing efforts on taking high-fidelity observations of the even-parity *E*-mode and far fainter odd-parity *B*-mode polarization angular power spectra to further probe fundamental physics and the initial conditions of the universe. Knowledge of these polarization anisotropies can break parameter degeneracies in the temperature power spectrum and point to deviations from the standard  $\Lambda$ CDM cosmological model. Figure 1.1 provides a compilation of recent CMB polarization measurements.

In this work, we describe the development, deployment, data analysis, and first cosmological constraints from a new CMB polarization experiment, SPTpol. To acknowledge the contributions of many people the use of the first-person plural is used throughout, however the content highlights the particular contributions of the author, who had a significant hand in all stages of the experiment. These contributions include detector development and receiver design, instrument deployment and characterization, software generation and validation for several key components of the data reduction pipeline, and the creation of the likelihood analysis used to obtain cosmological parameter constraints, which are the main result of this work.

This introductory chapter aims to orient the reader and motivate the cosmological model with which we interpret the cosmological significance of the CMB observations presented here. It begins with a discussion of an expanding universe with a Friedmann-Lemaître-Robertson-Walker (FLRW) spacetime metric, its initial conditions under the framework of inflation, and the current leading cosmological model ( $\Lambda$ CDM). We then discuss the CMB, its temperature anisotropies and their power spectrum, and what we might learn about the early universe from studying it. Next, we describe the generation of CMB polarization and the *E*- and *B*-mode power spectra. The introduction finally concludes with an outline of the remaining chapters.

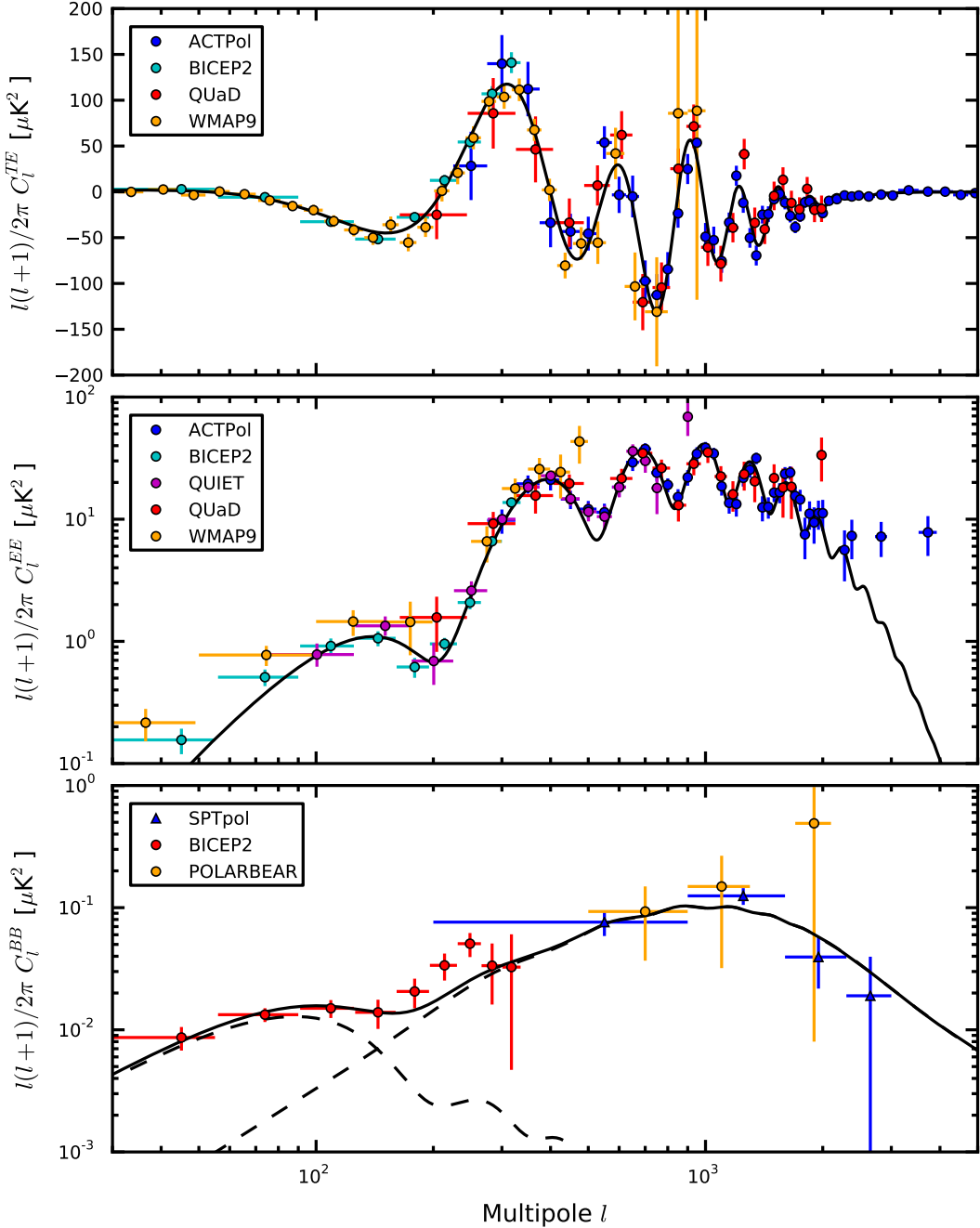


Figure 1.1: Recent high signal-to-noise CMB polarization power spectra measurements plotted in units of  $\mu\text{K}^2$  as a function of spherical harmonic multipole  $l$ . In 2013 the SPTpol collaboration recently published a lensing correlation detection of  $B$  modes consistent with the best-fit  $\Lambda\text{CDM}$  model (rising dashed line at  $l \gtrsim 100$ ) (21). The POLARBEAR collaboration has also published lensing  $B$ -mode measurements (22). In early 2014 the BICEP2 experiment submitted a first detection of large-scale  $B$  modes consistent with a tensor-to-scalar ratio  $r = 0.2$  (dashed line at  $l \lesssim 100$ ) (23). Also plotted are data from ACTPol (24), QUIET (14), QUaD (10), and WMAP (25).

## 1.1 Cosmology

Modern cosmology began with the formulation of General Relativity (26) and the discovery that the universe is expanding (27). This paradigm-shifting discovery immediately implied a period of extreme density and temperature in the early universe labeled the “Big Bang.” While the idea of a big bang and an expanding universe led to strong theoretical expectations for such things as the Cosmic Microwave Background and the formation of the light elements during big bang nucleosynthesis, the Big Bang theory had several troubling problems. How could the observed CMB be so uniform in temperature across distances that could never have been in causal contact (the Horizon Problem)? Why is the observed curvature of the universe so close to flat when the equations of General Relativity require the curvature to increase in amplitude over time? Furthermore, Grand Unification Theories predict the creation of heavy magnetic monopole particles in the early universe yet none have been observed. Finally, while incredibly uniform, there are nevertheless small anisotropies in the CMB corresponding to density fluctuations in the early universe. What generated these fluctuations?

It was only with the development of the theory of inflation in the 1980s that these questions had theoretically motivated answers. Together with present-day observations of the expansion of the universe, temperature and polarization anisotropies in the CMB, the BAO feature in galaxy-galaxy distance correlations, and the physics of galaxy clusters, the Big Bang theory and the concept of inflation have culminated in the  $\Lambda$ CDM cosmological model. So far inflation has little verified observational evidence, however, and we know that  $\Lambda$ CDM cannot be the final answer since it ignores known physics that have measurable effects on the universe. Through new observations of these and other cosmological probes we seek to more accurately measure parameters in the  $\Lambda$ CDM model in search of new physics and a better understanding of the initial conditions of the universe.

This section is inspired and adapted from discussions in (28; 29; 30) and begins with a review of the Friedmann equations and the properties of an expanding universe. We then briefly discuss the concept of inflation and how early quantum fluctuations in the spacetime metric lead to the

large-scale structure observed today. The section concludes with a description of the  $\Lambda$ CDM model and its parameters, which is the theoretical framework with which the observations and analyses discussed in this work are interpreted.

### 1.1.1 Expansion and the Friedmann Equations

We begin by considering an expanding universe that obeys the *cosmological principle*: on large scales the universe is homogeneous and isotropic. Following this principle, we assume that observations made of the universe on Earth would look statistically identical to observations made, say, half an observable universe away. In this case all three spatial dimensions are expanding as a function of time following the diagonal Friedmann-Lemaître-Robertson-Walker (FLRW) spacetime metric in cartesian coordinates for a flat universe,

$$g_{\mu\nu} = \begin{pmatrix} -c^2 & 0 & 0 & 0 \\ 0 & a(t)^2 & 0 & 0 \\ 0 & 0 & a(t)^2 & 0 \\ 0 & 0 & 0 & a(t)^2 \end{pmatrix}. \quad (1.1)$$

Here  $c$  is the speed of light and  $a(t)$  is the expansion scale factor at time  $t$ . The scale factor parameterizes the relative size of the universe and is defined to be unity today and approaches zero as  $t \rightarrow 0$ . It is often advantageous to consider distances in a coordinate system where the expansion of the universe is factored out like what we have done here; the scale factor just resizes the “grid” one works on. These are called *comoving* coordinates. For example, the comoving horizon at time  $t$ , which is the comoving distance light has traveled since time  $t = 0$ , is simply

$$\eta(a) \equiv \int_0^t \frac{cdt'}{a(t')}. \quad (1.2)$$

The comoving horizon is often used as a time variable called the *conformal time* since it is monotonically increasing with time  $t$  and properly accounts for the expansion of the universe.

Under the FLRW metric we can also express distances in (comoving) spherical  $(r, \theta, \phi)$  coor-

dinates by taking advantage of the isotropy of the universe

$$\begin{aligned} ds^2 &= -c^2 dt^2 + a(t)^2 d\sigma^2 \\ d\sigma^2 &= \frac{dr^2}{1 - \kappa r^2} + r^2 d\Omega^2 \\ d\Omega^2 &= d\theta^2 + \sin^2 \theta d\phi^2. \end{aligned} \tag{1.3}$$

Following the nomenclature of (28) we parameterize the general curvature of the universe with  $\kappa$ , which takes on values continuously from  $-1 \leq \kappa \leq 1$ . In the limiting cases of  $\kappa = \{-1, 0, 1\}$  the spatial part of the FLRW metric  $d\sigma^2$  becomes

$$d\sigma^2 = \begin{cases} d\chi^2 + \sin \chi d\Omega^2, & \kappa = 1 \\ d\chi^2 + \chi d\Omega^2, & \kappa = 0 \\ d\chi^2 + \sinh \chi d\Omega^2, & \kappa = -1 \end{cases}, \tag{1.4}$$

corresponding to closed, flat, and open spatial geometries, respectively. We have also introduced a curvature-corrected comoving radial distance  $\chi$ ,

$$d\chi = \frac{dr}{\sqrt{1 - \kappa r^2}}. \tag{1.5}$$

The scale factor  $a(t)$  can also be expressed as a function of the observable redshift parameter  $z$ . Redshift is a measure of how much a photon's observed wavelength  $\lambda_{\text{obs}}$  has stretched due to cosmic expansion since it was emitted when it had wavelength  $\lambda_{\text{emit}}$ . Quantitatively, redshift and the scale factor are related via

$$\begin{aligned} z &\equiv \frac{\lambda_{\text{obs}} - \lambda_{\text{emit}}}{\lambda_{\text{emit}}} \\ (1+z) &= \frac{\lambda_{\text{obs}}}{\lambda_{\text{emit}}} = \frac{1}{a}. \end{aligned} \tag{1.6}$$

From this definition we see that  $z = 0$  today and  $z \rightarrow \infty$  as  $a$  or  $t \rightarrow 0$ .

We are not just interested in the expansion of the universe but also its rate of expansion, which is parameterized by the Hubble parameter  $H$ . It is defined to be the logarithmic time derivative of the scale factor:

$$H(a) \equiv \frac{1}{a} \frac{da}{dt}. \tag{1.7}$$

$H = H_0$  today and is currently measured to be  $67.8 \pm 0.77 \text{ km s}^{-1} \text{ Mpc}^{-1}$ (31), which has overall units of 1/time. It is often re-expressed as a function of  $h$  (called the reduced Hubble constant),

$$H_0 = 100h \text{ km s}^{-1} \text{Mpc}^{-1}. \quad (1.8)$$

Inverting  $H_0$  gives the Hubble time,  $t_H$ , a rough estimate of the age of the universe neglecting any changes to the rate of expansion as a function of time. This estimate turns out to be 14.5 Gyr, which is reasonably close to the current number of  $13.798 \pm 0.037$  Gyr (31). Multiplying the Hubble time by the speed of light gives the Hubble distance,  $d_H$ , and a Hubble volume is defined to be a sphere with radius  $d_H$ .

The rate of expansion is sensitive to time (or scale factor, or redshift), however. This dependence is expressed with the first Friedmann equation

$$H(a)^2 = \left(\frac{\dot{a}}{a}\right)^2 = \frac{8\pi G}{3c^2}\rho(a) - \frac{\kappa}{a^2 c^2}, \quad (1.9)$$

where  $G$  is the gravitational constant,  $\rho(a)$  is the energy density of the universe with scale factor  $a$ , and overdots denote derivatives with respect to time  $t$ . We also define the critical density  $\rho_{\text{cr}}$ ,

$$\rho_{\text{cr}}(a) = \frac{3H(a)c^2}{8\pi G}, \quad (1.10)$$

and the ratio of density to the critical density is the density parameter  $\Omega(a) = \rho(a)/\rho_{\text{cr}}(a)$ .  $\Omega$  is the sum of densities from each component of the universe,

$$\Omega = \sum_i \Omega_i = \sum_i \frac{\rho_i}{\rho_{\text{cr}}}, \quad (1.11)$$

where  $i \in \{\gamma, b, c, \Lambda\}$  corresponding to radiation, baryons, cold (pressureless) dark matter, and vacuum or dark energy, respectively. For this treatment we lump neutrinos in with the radiation term as they are highly relativistic but one could keep track of their density separately and in practice this is done (32). We will take  $\Omega_0$  to mean  $\Omega(a = 1)$ . As elucidated in (28), the critical density relates the density of the universe to its curvature via

$$\Omega - 1 = \frac{\kappa}{H^2 a^2 c^2} = -\Omega_k. \quad (1.12)$$

We have used a short-hand notation of expressing curvature as having an effective energy density ratio  $\Omega_k$  for simplicity. Note that  $\Omega_k$  is not included in Equation 1.11 since curvature is generated only by what populates the stress-energy tensor  $T^{\mu}_{\nu}$ , namely physical sources of energy density.

The total density  $\Omega$  will depend on with what the universe is filled and how the density of each of these constituents changes with the scale factor. These density relationships are governed by the conservation of energy as expressed in General Relativity,

$$\frac{\dot{\rho}}{\rho} = -3(1+w)\frac{\dot{a}}{a}, \quad (1.13)$$

where  $w$  is the constant equation of state of a (relativistic) perfect fluid with pressure  $p$  and density  $\rho$ ,

$$p = w\rho c^2. \quad (1.14)$$

If we assume that each constituent of the universe can be approximated as a perfect fluid then we find

$$\rho_i(a) = \begin{cases} \rho_{\gamma,0} a^{-4}, & w = 1/3 \text{ (radiation)} \\ \rho_{b,c,0} a^{-3}, & w = 0 \text{ (baryonic and cold dark matter)} \\ \rho_{\kappa,0} a^{-2}, & w = -1/3 \text{ (curvature)} \\ \rho_{\Lambda,0} a^0, & w = -1 \text{ (vacuum energy)} \end{cases}, \quad (1.15)$$

where  $i \in \{\gamma, b, c, \kappa, \Lambda\}$  again corresponding to radiation, baryons, cold dark matter, curvature, and dark energy, respectively, and  $\rho_{i,0}$  are the measured densities today. We will hereafter drop the use of subscript zeros. It is worth noting that the dark energy (or cosmological constant) density is constant; while the other components of the universe dilute over time, the relative contribution of  $\Omega_\Lambda$  grows and eventually dominates the energy density of the universe. This has profound consequences for the acceleration of the scale factor  $a$ , which can be calculated from the second Friedmann equation,

$$\frac{\ddot{a}}{a} = -\frac{4\pi G}{3c^2}\rho(1+3w). \quad (1.16)$$

We see that when the universe is dominated by a component with  $w < -1/3$  the acceleration  $\ddot{a} > 0$  and the expansion of the universe accelerates.

Using these density functions we can expand the first Friedmann equation to reveal how the relative contribution to  $\Omega$  from each component changes as a function of scale factor or equivalently of redshift:

$$\begin{aligned}\Omega(a) &= \sum_i \Omega_i(a) = \Omega_\gamma a^{-4} + \Omega_m a^{-3} + \Omega_k a^{-2} + \Omega_\Lambda \\ \Omega(z) &= \sum_i \Omega_i(z) = \Omega_\gamma(1+z)^4 + \Omega_m(1+z)^3 + \Omega_k(1+z)^2 + \Omega_\Lambda.\end{aligned}\tag{1.17}$$

Here  $\Omega_m = \Omega_b + \Omega_c$ . If we can measure the density parameters  $\Omega_i$  then we can reconstruct the expansion history of the universe and predict its future by evaluating the Friedmann equations. Observational methods that are sensitive to the density parameters, preferably in orthogonal ways to avoid degeneracies between parameters, are thus highly interesting and informative.

### 1.1.2 Initial Conditions with Inflation

In the 1980s the inflationary paradigm was introduced to solve the Horizon, Flatness, and Monopole problems (see 33, and references therein). The model of inflation posits an early period of superluminal expansion  $\sim 10^{-35}$  s after the Big Bang. During inflation, the universe expands in size by at least 60 e-foldings, forcing the causal horizon to shrink by the same factor. Regions of space once causally connected and in thermal equilibrium are therefore quickly separated by vast distances much greater than the current Hubble radius. This effectively *freezes in* thermal fluctuations on scales larger than the causal horizon. Only at later times when these scales re-enter the horizon can anisotropies begin to evolve. Inflation thus solves the Horizon problem by providing a means for large scales on the sky to be in rough thermal equilibrium. Additionally, any potentially large initial curvature is greatly diluted by the rapid expansion making the universe immediately after expansion at least 60 e-foldings flatter than measured today. Finally, the volume of an initially causally-connected patch of the universe increases by at least a factor of  $e^{60*3} \simeq 10^{78}$  during inflation. Since magnetic monopoles would be produced right before or perhaps during inflation with a density of about one per Hubble volume (30) the density of monopoles after inflation is fantastically small rendering any chance of observing one today virtually zero. Inflation therefore

neatly solves these three major problems of the Big Bang theory, and we will soon see it also solves the fourth “density fluctuation” problem.

The simplest (slow-roll) models of inflation consider a scalar field  $\phi$  called the inflaton with potential  $V(\phi)$  that permeates space (29). During inflation there is significant vacuum energy and  $V(\phi)$  slowly rolls “downhill” from its roughly constant value. This configuration has negative pressure and causes exponential expansion according to the second Friedmann equation. Furthermore, if the universe contains something other than the inflaton before inflation begins then rapid expansion causes the vacuum energy to quickly dominate the universe (30). Eventually the inflaton decays, however, which slows inflation while the potential settles into a new (but not necessarily global) minimum. The energy associated with  $V(\phi)$  is here converted to radiation and matter in a process known as *reheating*. These new particles then dominate the energy density making  $\ddot{a} < 0$  and a normal FLRW period of expansion begins. This decelerating period of normal expansion continues until the universe is once again dominated by vacuum energy, which appears to be the case today with  $\Omega_\Lambda \sim 0.7$ . Mathematically, today’s period of accelerating expansion is the same as that during the inflationary epoch  $10^{-35}$  s after the Big Bang.

Through the process of inflation the curvature is effectively set to zero, regardless of its initial value, and the universe is populated with radiation and matter. Work in the 1980s, however, revealed that the density of these new particles is not perfectly uniform across space (34; 35; 36; 37), which explained the origin of the density fluctuations in the early universe. Under the assumption that gravity is quantized, quantum fluctuations in the (cartesian) spacetime metric would produce small perturbations in curvature across space (29):

$$g_{\mu\nu} = \begin{pmatrix} -c^2(1 + 2\Psi) & 0 & 0 & 0 \\ 0 & a^2(1 + 2\Phi) + h_+ & h_x & v_{xz} \\ 0 & h_x & a^2(1 + 2\Phi) - h_+ & v_{yz} \\ 0 & v_{xz} & v_{yz} & a^2(1 + 2\Phi) \end{pmatrix}. \quad (1.18)$$

The functions  $\Psi$  and  $\Phi$  represent scalar (density) fluctuations in the Newtonian gravitational potential and spatial curvature, respectively.  $v_{xz}$  and  $v_{yz}$  are vector perturbations, which are set

to zero by inflation like the total curvature so we will not consider them in this work. Finally,  $h_+$  and  $h_\times$  are tensor perturbations related to gravitational waves propagating (arbitrarily) along the  $\hat{z}$ -direction. These waves propagate at the speed of light, causing distortions in the spacetime curvature as they pass.

During inflation these quantum fluctuations are blown up to scales larger than the current causal horizon, which “freezes” them in before they can change further. Fluctuations at increasingly larger scales then re-enter the horizon after inflation as the Hubble radius increases. The result after inflation are power spectra of nearly scale-invariant primordial scalar (s) and tensor (t) perturbations (38):

$$\begin{aligned} P_s &= A_s \left( \frac{k}{k_0} \right)^{n_s - 1} \\ P_t &= A_t \left( \frac{k}{k_0} \right)^{n_t}, \end{aligned} \tag{1.19}$$

where the amplitudes  $A_s$  and  $A_t$  are defined at a pivot scale  $k_0$ . Smaller modes with larger wavenumber  $k$  enter the horizon earlier. By convention  $P_s$  is scale-invariant when the scalar spectral tilt  $n_s = 1$  as is  $P_t$  when the tensor spectral tilt is  $n_t = 0$ . Over cosmic time gravity acts on these primordial fluctuations, which grow and eventually form galaxies and galaxy clusters.

A deviation from true scale-invariance is expected for the power spectra of initial fluctuations since inflation has to end (30). The rate of decay of the inflaton potential is dependent on derivatives of the potential field and is parameterized for slow-roll models in natural units by the dimensionless parameters

$$\begin{aligned} \epsilon &\equiv \frac{m_p^2}{16\pi} \left( \frac{1}{V} \frac{dV}{d\phi} \right)^2 \\ \eta &\equiv \frac{m_p^2}{8\pi} \left( \frac{1}{V} \frac{d^2V}{d\phi^2} \right), \end{aligned} \tag{1.20}$$

which are model dependent but often similar in amplitude and much less than unity. Here  $m_p$  is the planck mass. The scalar and tensor spectral tilts can be expressed in terms of these so-called slow-roll parameters

$$\begin{aligned} n_s &= 1 - 6\epsilon - 2\eta \\ n_t &= -2\epsilon. \end{aligned} \tag{1.21}$$

Since  $\epsilon$  is positive the power spectra of both scalar and tensor fluctuations for many models of inflation are expected to be slightly tilted.

A final parameter of observational significance is the tensor-to-scalar ratio  $r$ , which quantifies the relative contributions of primordial tensor and scalar fluctuations to the spacetime metric,

$$r \equiv \frac{A_t}{A_s}. \quad (1.22)$$

Since tensor perturbations are an expected result of inflation, a detection of non-zero  $r$  would be strong evidence that inflation took place and that it is the source of the initial curvature fluctuations in the universe. Finally, since gravitational waves are only generated by quantum fluctuations in the spacetime metric, a non-zero  $r$  would also be evidence that gravity is indeed truly quantized, and the values of  $r$  and  $n_t$  could give theorists new information and clues about the unification of gravity with the other forces of nature (30).

### 1.1.3 $\Lambda$ CDM Cosmological Model

Given current measurements of large-scale structure (18), the Hubble parameter (16), and anisotropies in the temperature of the CMB (e.g. 39; 13; 25; 31; 40) among other cosmological probes, we seek a physically motivated cosmological model that fits the data with as few parameters as possible. In the past 15 years  $\Lambda$ CDM has emerged as a leading candidate. In the process it has made several a priori predictions that have since been observationally verified, including the location of the BAO feature (41) and the presence of CMB polarization anisotropies with similar acoustic structures to those observed in the temperature fluctuations (42; 10).

In  $\Lambda$ CDM, the universe is assumed flat ( $\kappa = 0$ ) and is dominated at present times by a cosmological constant or dark energy with equation of state  $w = -1$ , which is causing the expansion of the universe to accelerate as discussed in Section 1.1.1. The CDM refers to cold (pressureless) dark matter, which is the next largest constituent of the universe in late times. Current measurements show that there is  $\sim$  six times more dark matter than baryonic matter. Dark matter does not interact with matter or radiation except gravitationally. While difficult to detect directly, it therefore

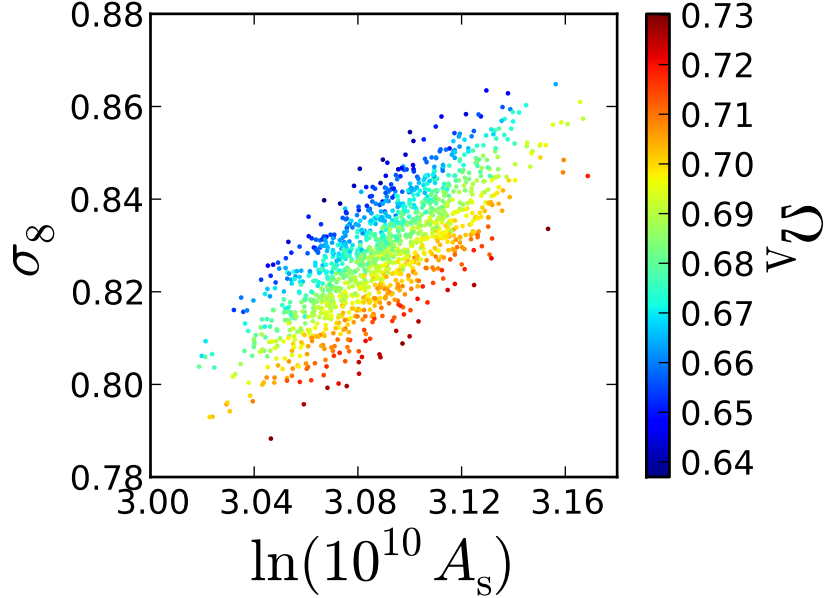


Figure 1.2: Samples from a Markov Chain Monte Carlo (MCMC) calculation of parameter constraints using Planck CMB temperature anisotropy measurements (15). The color map corresponds to values of  $\Omega_\Lambda$  at a given point in  $\ln(10^{10} A_s) - \sigma_8$  space.

Table 1.1:  $\Lambda$ CDM Parameter Definitions

Parameter	Value <sup>(a)</sup>	Description
<b>Free</b>		
$\Omega_b h^2$	$0.02214 \pm 0.00024$	Baryon density ratio
$\Omega_c h^2$	$0.1187 \pm 0.0017$	CDM density ratio
$100\theta_s$	$1.04147 \pm 0.00056$	$100 \times$ angular size of the sound horizon at decoupling
$n_s$	$0.9608 \pm 0.0054$	Primordial scalar fluctuation spectral tilt
$\ln(10^{10} A_s)$	$3.091 \pm 0.025$	Amplitude of primordial scalar perturbations
$\tau^{(b)}$	$0.092 \pm 0.013$	Optical depth due to reionization
<b>Derived</b>		
$\Omega_\Lambda$	$0.692 \pm 0.01$	Dark energy density ratio
$H_0$	$67.80 \pm 0.77$	Expansion rate today in $\text{km s}^{-1} \text{ Mpc}^{-1}$
$\sigma_8$	$0.826 \pm 0.012$	Amplitude of linear matter fluctuations at $8 h^{-1}$ Mpc scales.
<b>Fixed</b>		
$k_0$	$0.05 \text{ Mpc}^{-1}$	Pivot scale for scalar and tensor perturbations
$\Omega_k$	0	Curvature density ratio
$w$	-1	Equation of state of dark energy
$\Omega_\gamma h^2$ <sup>(c)</sup>	$2.47 \times 10^{-5}$	Radiation density ratio
$\sum m_\nu$	0.06 eV	(Minimum) sum of neutrino masses
$T_0$	$2.7255 \text{ K}$	CMB temperature today
$r$	0	Tensor-to-scalar ratio
$n_t$	0	Primordial tensor fluctuation spectral tilt

**Notes:**

(a) Current parameter values taken from PLANCK+WP+HIGHL+BAO constraints in Table 5 of (31).

(b) The optical depth  $\tau$  suppresses all scales smaller than the horizon at reionization. See section 1.2.

(c)  $\Omega_\gamma h^2$  is defined entirely by natural constants and the CMB temperature.

has several indirect gravitational effects, for example on the dynamics of galaxies (43) and galaxy clusters (44), the strength of gravitational lensing (45), and the amplitude of CMB temperature anisotropies. The large amount of dark matter compared to baryonic matter is required to bring observations of all of these effects into agreement.

The value of  $\Omega_\Lambda$ , and hence the time when dark energy starts dominating the energy density of the universe, effects the rate of structure formation. If  $\Omega_\Lambda$  “turns on” early in the history of the universe, then gravity does not have much time to generate large overdensities before expansion dilutes pre-existing potential wells. In this case few structures like galaxy clusters will form. On the other hand, if  $\Omega_\Lambda$  turns on much later then gravity has more time to create large overdensities and therefore more galaxy clusters. This effect on structure formation can be measured in part through the parameter  $\sigma_8$ , the RMS amplitude of linear matter density fluctuations measured today on  $8 h^{-1}$  Mpc scales. By its definition  $\sigma_8$  is highly-correlated with  $A_s$  (the amplitude of *primordial* density fluctuations), but it is also anti-correlated with  $\Omega_\Lambda$  as can be seen in Figure 1.2, which is the expected behavior.

$\Lambda$ CDM is characterized by six free cosmological parameters and several fixed parameters. Several more parameters can be derived under the assumption of zero curvature and a cosmological constant with equation of state  $w = -1$ . We summarize these parameters in Table 1.1. Many more common cosmological parameters are derived, such as the age of the universe today  $t_0$  and the redshift at the epoch of recombination  $z_*$ , but we do not report their values here for brevity. There is some choice in parameterization, for example whether to use  $H_0$ ,  $\Omega_\Lambda$ , or  $100\theta_s$  (the sound horizon when the CMB was emitted — see Section 1.2.1) as a free parameter and derive the others.  $\Lambda$ CDM assumes zero curvature so by construction we derive the dark energy density to be  $\Omega_\Lambda = 1 - \Omega_m - \Omega_\gamma$ . Furthermore, the sound horizon  $100\theta_s$  is less degenerate with other parameters than  $H_0$  so we make  $H_0$  a derived quantity, however we apply external constraints or *priors* on  $H_0$  limiting its allowed values. The cosmological constraints presented in this work are in the form of means and 68% confidence levels for the free and derived parameters of the  $\Lambda$ CDM model.

## 1.2 CMB Temperature Anisotropies

The temperature fluctuations of the CMB are particularly sensitive to the physics of the early universe. As such, measuring their power spectrum can yield a bounty of cosmological information. We again adapt arguments made in (28; 29; 30) to explore how to tie theory to observations. The section begins with a description of the photon-baryon plasma before the epoch of recombination, which is important for understanding the structure and origin of CMB temperature and polarization anisotropies. With the anisotropies sufficiently motivated, we then provide the framework for quantifying the level of temperature anisotropies at various scales in the form of an angular power spectrum. Finally, we point out salient features of the temperature power spectrum and explore how these features are affected by  $\Lambda$ CDM model parameters.

### 1.2.1 The Photon-Baryon Plasma

After inflation the universe expands and cools according to the Friedmann equations, with temperature falling linearly with redshift.<sup>1</sup> For the first  $\sim 380,000$  years after the Big Bang high temperatures keep protons ionized and free electrons result in a small photon mean free path rendering the universe opaque to radiation. Frequent scatterings between photons and electrons (Thomson interactions) and electrons and baryons (Coulomb interactions) produce a tightly coupled fluid known as the photon-baryon plasma.

The photon-baryon plasma exhibits some interesting properties resulting from this tight coupling. Baryons fall into dark matter gravitational potential wells causing overdensities. The photons are pulled in with them, however, and the resulting radiation pressure provides a restoring force to the original increase in density. This is the configuration of a simple harmonic oscillator and thus density oscillations are induced in the photon-baryon fluid, the so-called *acoustic* oscillations. Baryons are not massless particles, however, so their additional gravity supplies an extra forcing term to the harmonic oscillator causing them to sink further into the potential wells. As described

---

<sup>1</sup> So long as matter stays in thermal equilibrium with the background radiation the temperature of the universe is  $T(z) = T_0(1 + z)$  with  $T_0 = 2.7255$  K, the average temperature of the CMB today.

in (29) the resulting toy configuration is that of a forced harmonic oscillator,

$$\ddot{\delta} + \frac{k}{m}\delta = \frac{F_0}{m}, \quad (1.23)$$

where  $\delta$  is the amplitude of a density fluctuation,  $k$  is the spring constant for the restoring force from radiation pressure, and  $F_0$  is the external driving force from the baryons. The solution as a function of time is that of a cosine oscillating about a point above zero,

$$\delta = A \cos \omega t + \frac{F_0}{m\omega^2}, \quad (1.24)$$

where  $m$  is the mass of a particle and  $\omega$  is the frequency of oscillation. We note that because the baryon forcing term offsets the zero-point of oscillations the density maxima (odd or compression peaks) have higher absolute amplitudes than the density minima (even or rarefaction peaks). Measurements of asymmetric amplitudes between the compression and rarefaction acoustic peaks are therefore very sensitive to the baryon content of the universe.

Another interesting consequence of tight coupling in the photon-baryon fluid is that the acoustic fluctuations in photon temperature, which just track the baryon overdensities, travel at the sound speed

$$c_s = \sqrt{\frac{1}{3(1+R)}} c \quad ; \quad R \equiv \frac{3\Omega_b}{4\Omega_\gamma}, \quad (1.25)$$

where it is clear that adding baryons decreases the sound speed. With this information we define the comoving sound horizon

$$r_s(z) = \int_0^{\eta(z)} c_s d\eta', \quad (1.26)$$

which is the comoving distance traveled by a sound wave at conformal time  $\eta(z)$  (29).

These acoustic oscillations persist until the universe cools to  $\sim 3000$  K. The distribution of free electrons is then no longer energetic enough to keep hydrogen ionized and the protons and electrons recombine during what is known as the *epoch of recombination*. Without free electrons photons decouple from baryons and begin free streaming as the universe becomes transparent for the first time. The radiation field, which will eventually redshift to microwave wavelengths over cosmic time, thus maintains the acoustic thermal fluctuations imprinted on it by baryons immediately

before its “last scattering.” This is the origin of both the CMB and its temperature anisotropies. Since the optical depth of the universe  $\tau \gg 1$  before the epoch of recombination the CMB is the oldest electromagnetic radiation we can study to learn about the early universe.

A detailed calculation of CMB temperature fluctuations resulting from sound waves in the photon-baryon plasma assuming initial conditions set by inflation (see, e.g., 29) reveals that the acoustic oscillations should have extrema at scales corresponding to harmonics of  $r_s(z_*)$ , the sound horizon evaluated at the redshift of matter-radiation decoupling. This is often expressed as the angular size of the sound horizon today

$$\theta_s = \frac{r_s(z_*)}{D_A(z_*)}, \quad (1.27)$$

where  $D_A(z_*) = \chi/(1 + z_*)$  is the angular diameter distance to the epoch of recombination. Recall that the curvature-corrected comoving radial distance  $\chi = r$  for a flat universe, but  $\chi > r$  when the curvature  $\kappa > 0$  and  $\chi < r$  when  $\kappa < 0$ . The acoustic peaks therefore encode information about  $\kappa$ .

The scale of the first acoustic peak corresponds to the sound horizon at matter-radiation decoupling. Density fluctuations at this scale had only just performed one compression since entering the horizon. These acoustic peaks would persist to arbitrarily small scales if it were not for the finite mean free path of photons. Any anisotropies at scales smaller than the photon mean free path are suppressed by photon diffusion in a process known as diffusion or Silk damping (46).

From briefly studying the physics of the photon-baryon plasma, we have found a set of expectations for features in the CMB temperature anisotropy power spectrum. We should observe a series of acoustic peaks at scales corresponding to harmonics of the sound horizon  $\theta_s$  at the epoch of recombination. Furthermore, the scale of the first peak constrains the curvature of the universe. Due to the presence of baryons, odd peaks will also be enhanced over even peaks. Finally, at small scales the acoustic peaks should be suppressed by photon scattering in what is known as the CMB *damping tail*.

### 1.2.2 The Temperature Angular Power Spectrum

During the epoch of recombination the radiation field decouples from baryons and starts free streaming carrying with it the imprint of the baryon density fluctuations, which are observable today as temperature anisotropies in the CMB. If we make a full-sky map of these fluctuations  $\delta T$  we can express them in terms of a spherical harmonic expansion on the sky

$$\frac{\delta T}{T}(\theta, \phi) = \sum_{l=0}^{\infty} \sum_{m=-l}^l a_{lm}^T Y_m^l(\theta, \phi), \quad (1.28)$$

where  $\theta$  and  $\phi$  are the polar and azimuthal coordinates on a sphere and  $l$  is the multipole moment. We have made explicit that the amplitude coefficients for the spherical harmonics are for the *temperature* anisotropy field. We also note as an aside that for small scales it is reasonable to approximate multipoles as flat-sky Fourier modes,  $l \simeq k$ .

A power spectrum is defined by measuring the variance of the  $a_{lm}^T$  coefficients (29),

$$\begin{aligned} \langle a_{lm}^T a_{l'm'}^{*,T} \rangle &= \delta_{ll'} \delta_{mm'} C_l^{TT} \\ C_l^{TT} &= \frac{1}{2l+1} \sum_{m=-l}^l |a_{lm}^T|^2, \end{aligned} \quad (1.29)$$

where  $\delta_{xx'}$  is the kronecker delta. Temperature anisotropies at any given scale or multipole  $l$  will have zero mean across the sky,  $\langle a_{lm}^T \rangle = 0$ , but there is non-zero variance in the  $a_{lm}^T$  coefficients and this is what the CMB temperature power spectrum quantifies as a function of angular scale. Note also that the number of independent  $a_{lm}^T$  coefficients at a given multipole is finite, namely  $2l+1$ . There is therefore a fundamental statistical limit to the knowledge we have of anisotropies at any given scale. This uncertainty is called *cosmic variance*,

$$\delta C_{l,\text{CV}}^{TT} = \sqrt{\frac{2}{2l+1}} C_l^{TT}. \quad (1.30)$$

If an experiment measures less than the full sky then  $2l+1$  modes per multipole is an overestimate of the available modes. *Sample variance* is an approximation that factors in the fraction of observed sky  $f_{\text{sky}}$ ,

$$\delta C_{l,\text{SV}}^{TT} = \sqrt{\frac{2}{(2l+1)f_{\text{sky}}}} C_l^{TT}. \quad (1.31)$$

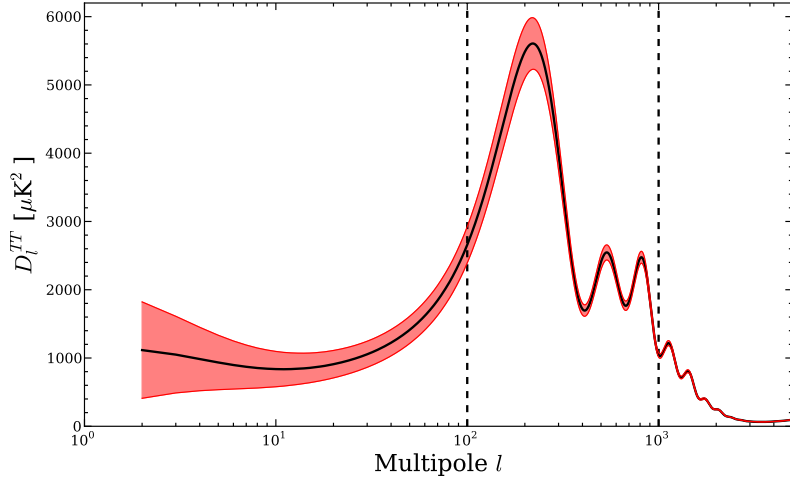


Figure 1.3: CMB  $TT$  power spectrum from a Planck best-fit  $\Lambda$ CDM model (31) (black). The shaded region shows the smallest possible uncertainties for single multipoles set by cosmic variance.

$f_{\text{sky}}$  is always less than one since even satellite experiments must mask out portions of the sky contaminated by galactic foreground signals. A theoretical  $C_l^{TT}$  spectrum is plotted in Figure 1.3 in units of  $\mu\text{K}^2$ . Historically, the spectrum is multiplied by  $l(l+1)/2\pi$  to make an  $n_s = 1$  scale-invariant spectrum constant in multipole  $l$  (29), which is the power spectrum scaling used in this figure as well as the rest of this work,

$$D_l \equiv \frac{l(l+1)}{2\pi} C_l. \quad (1.32)$$

The shaded region defines the cosmic variance uncertainty limit for individual multipoles  $l$ . This represents the most accurate measurement one could make of the temperature anisotropies, i.e. observations over the full sky with zero noise. We can decrease our uncertainties by binning single multipoles into *bandpowers* at the expense of losing information about the shape of the spectrum. We can also measure other spectra, such as the power spectra of polarization anisotropies. Beyond those two caveats, however, by measuring the CMB power spectra with uncertainties limited by cosmic variance up to some multipole  $l_{\text{max}}$  we will have extracted all available information at those scales.

Figure 1.3 also delineates three important regions of the  $TT$  spectrum. Large angular scales or

multipoles  $l \lesssim 100$  represent super-horizon fluctuations at the epoch of recombination. These scales were larger than the sound horizon at  $z_*$  and therefore never experienced acoustic oscillations. They are therefore measurements of the primordial anisotropies laid down by inflation modulo effects experienced as the photons free streamed to us today. One important phenomenon known as the Integrated Sachs-Wolfe (ISW) effect most strongly effects this region of the spectrum. Anisotropies are enhanced by photons blueshifting while falling into gravitational wells. However, the potential wells are diluted by the expansion of the universe as the photon climbs out. The net result is an increase in photon energy observed as a higher CMB temperature at relevant scales. The opposite is true for photons that pass through potential “hills.” This enhancement in anisotropy variance at large scales is partially responsible for the first acoustic peak being significantly higher than the rest.

Between multipoles of  $100 \lesssim l \lesssim 1000$  the acoustic peaks set up by oscillations in the photon-baryon plasma are clearly visible. The first and third peaks correspond to scales compressing once and twice, respectively, before matter-radiation decoupling. The second peak is at scales that underwent one compression and one rarefaction. At multipoles  $l \gtrsim 1000$  the damping tail is observed, where photon diffusion suppresses the acoustic oscillations. Several physically interesting extensions to the  $\Lambda$ CDM model affect the power of the damping tail, so high-resolution measurements of the CMB will be crucial for probing new physics (47).

### 1.2.3 Sensitivity to Cosmology

The CMB temperature angular power spectrum  $C_l^{TT}$  is a fundamental observable whose features depend on the underlying cosmology. The location of its acoustic peaks as quantified by  $\theta_s$  helps set the curvature of the universe and is the reason for assuming the curvature is flat in  $\Lambda$ CDM. The relative heights of the even and odd peaks is controlled by the level of baryons  $\Omega_b h^2$ , and the ratio of the first and second peaks to the third is sensitive to the amount of dark matter  $\Omega_c h^2$  through its indirect effect on the expansion rate at early times.

Figure 1.4 demonstrates some of these effects. Increasing  $\Omega_b h^2$  increases the disparity between

even and odd peaks, driving the odd (compression) peaks to higher amplitudes. More baryons also reduces the sound speed, which pushes the sound horizon and the first acoustic peak to smaller scales. The spacing of the harmonic peaks necessarily increases as the frequency of oscillations in the photon-baryon plasma decreases with  $c_s$ . Changing  $\Omega_c h^2$  affects the redshift  $z_{\text{eq}}$  at which matter and radiation equally contribute to  $\Omega$ . For example, decreasing  $\Omega_c h^2$  causes  $z_{\text{eq}}$  to also decrease (matter-radiation equality happens later and therefore closer to recombination) (47). This means that radiation contributes more to gravitational potential wells at smaller scales or equivalently earlier in time. Because the density of radiation is  $\propto (1+z)^4$ , this also means that potential wells will partially dilute while baryons compress in them. The increase in local radiation pressure compared to the reduced gravity drives the amplitude of the acoustic oscillations up in what is called *radiation driving*. The relative heights of the first and second peaks to the third offer a measure of which scales feel this additional radiation driving and therefore the amount of dark matter through its effect on  $z_{\text{eq}}$ .

The effect of the amplitude of primordial scalar fluctuations  $A_s$  as well as the scalar spectral tilt  $n_s$  are to simply scale the overall amplitude of the  $TT$  spectrum and relative power of large to small scales, respectively. A lower  $n_s$  corresponds to a redder  $TT$  spectrum with more power at large scales (low multipoles) relative to small scales (high multipoles). Unfortunately for the  $TT$  spectrum there is a final parameter, the optical depth  $\tau$  due to reionization, that is completely degenerate with the scalar amplitude. Once the universe becomes reionized at late times scatterings of CMB photons off of free electrons partially erases anisotropy information at scales smaller than the current horizon. Thus the amplitude of fluctuations measured on the sky are reduced by  $e^{-\tau}$  at nearly all scales. Since the amplitude of the  $TT$  spectrum actually measures  $A_s e^{-2\tau}$ , the relative importance of  $A_s$  and  $\tau$  are impossible to determine. Measurements of CMB polarization at large scales corresponding to times after reionization can break this degeneracy, however.

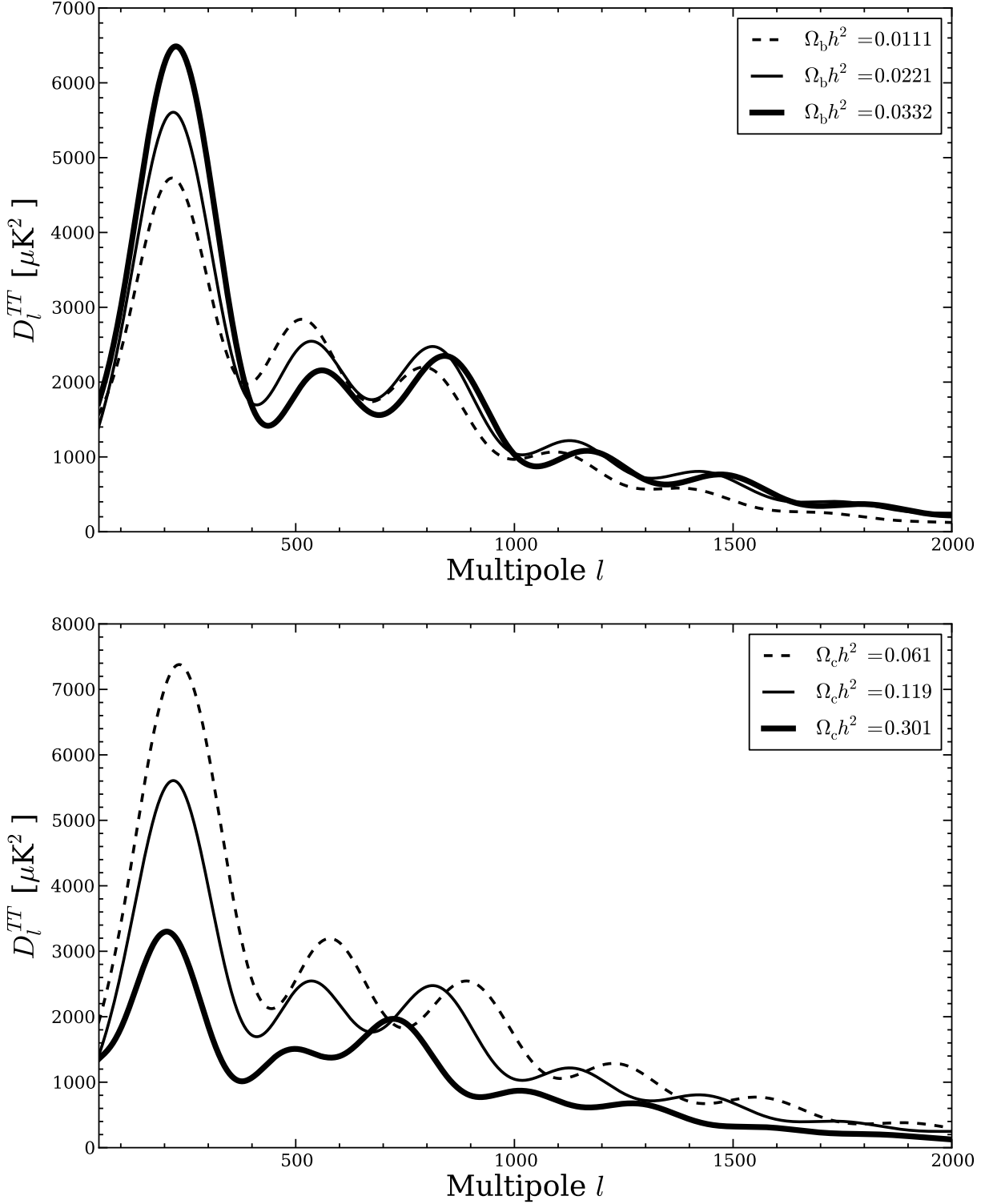


Figure 1.4: Effects of increasing  $\Omega_b h^2$  (top) and  $\Omega_c h^2$  (bottom) on the CMB  $TT$  power spectrum while keeping  $H_0$  and  $\Omega_k$  fixed. Parameter values increase according to dashed, solid, and thick lines.

## 1.3 CMB Polarization

In addition to having temperature anisotropies, the CMB is also weakly polarized at the  $\sim 10\%$  level. These polarization anisotropies are sensitive to the same physics that generate the CMB  $TT$  power spectrum and thus provide a way around the cosmic variance limit. However, as we will explore, additional physical phenomena beside primordial density fluctuations can generate polarization. Precise measurements of CMB polarization can thus improve our knowledge of the photon-baryon fluid and  $\Lambda$ CDM parameters as well as offer new windows on the very early universe and structure formation. We begin this section with a discussion of how polarization is generated and parameterized by the Stokes parameters. We then explore more specifically the mechanisms for generating polarization in the CMB itself. Finally, we discuss the power spectra of CMB polarization and what cosmological information can be gleaned from them. Arguments in this section are adapted and compiled from discussions in (48; 29; 49).

### 1.3.1 Linear Polarization and the Stokes Parameters

The polarization of a photon is defined as the direction parallel to its **E**-field. It is possible to decompose polarization into two orthogonal directions, say, in the  $\hat{\epsilon}_1$  and  $\hat{\epsilon}_2$  directions. In this way, the **E**-field of any propagating photon can be expressed as

$$\mathbf{E}(\mathbf{x}, t) = (\hat{\epsilon}_1 E_1 + \hat{\epsilon}_2 E_2) e^{i\mathbf{k}\cdot\mathbf{x} - i\omega t}. \quad (1.33)$$

Note that in general  $E_1$  and  $E_2$  are complex coefficients so that phase information of the two basis **E** waves may be kept. In the case of linearly polarized light the phase difference between  $E_1$  and  $E_2$  is zero. By placing  $E_1$  and  $E_2$  out of phase by  $90^\circ$  one makes a basis set out of two “circularly” polarized waves such that the direction of the first **E**-field, call it  $\hat{\epsilon}_+$ , is constantly changing with positive rotation while the second,  $\hat{\epsilon}_-$ , is changing with negative rotation. These circular basis vectors are related to the linear ones via (48)

$$\hat{\epsilon}_\pm = \frac{1}{\sqrt{2}}(\hat{\epsilon}_1 \pm i\hat{\epsilon}_2). \quad (1.34)$$

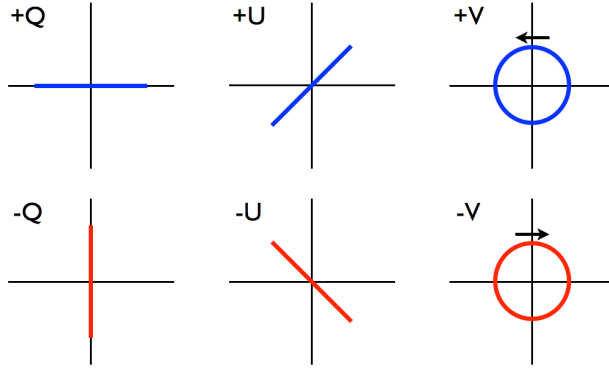


Figure 1.5: Graphic depicting the directional relations between Stokes  $Q$ ,  $U$ , and  $V$ .

If one is capable of measuring  $E_1$  and  $E_2$ ,  $E_+$  and  $E_-$ , or a combination thereof then one can fully define the polarization of the incident radiation.

These basis vectors are only physically useful if one can measure incoming radiation with respect to them. For this we can utilize the Stokes polarization parameters. These parameters are combinations of **E**-field magnitudes that distinguish between different types of polarization, i.e., linear or circular. There are four Stokes parameters,  $I$ ,  $Q$ ,  $U$ , and  $V$ , where

$$\begin{aligned}
 I &= |E_x|^2 + |E_y|^2 = |E_a|^2 + |E_b|^2 = |E_+|^2 + |E_-|^2 \\
 Q &= |E_x|^2 - |E_y|^2 = -2\text{Re}(E_a^* E_b) \\
 U &= 2\text{Re}(E_x E_y^*) = |E_a|^2 - |E_b|^2 \\
 V &= 2\text{Im}(E_x E_y^*) = |E_+|^2 - |E_-|^2,
 \end{aligned} \tag{1.35}$$

and where  $E_a$  and  $E_b$  are the **E**-fields in orthogonal directions  $\hat{\epsilon}_a$  and  $\hat{\epsilon}_b$  that are rotated with respect to  $\hat{\epsilon}_x$  and  $\hat{\epsilon}_y$  by  $45^\circ$ .

Figure 1.5 demonstrates the relationships between the Stokes parameters.  $Q$  and  $U$  are both measures of linear polarization while  $V$  is a measure of circular polarization.  $I$  is simply the total intensity of the light. The Stokes parameters are related such that

$$I^2 \geq Q^2 + U^2 + V^2. \tag{1.36}$$

The equality is for coherent light. If light is partially coherent then the phases between the two constituent **E**-fields in each Stokes parameter will vary with time “mixing”  $E_x$  into  $E_y$ , for example. The mixing results in destructive interference and reduces the total intensity of the light (48). Since in general light is not perfectly coherent, in practice time-averaged magnitudes ( $\langle |E_x|^2 \rangle$ ,  $\langle |E_y|^2 \rangle$ , etc.) are measured. By measuring  $Q$ ,  $U$ , and  $V$ , one can fully characterize the polarization state of the incident radiation.

### 1.3.2 Polarizing the CMB

In this section we describe some of the underlying physics producing polarization in the CMB. This is followed with a discussion of the decomposition of polarization into  $E$  modes and  $B$  modes. The section concludes with a discussion of the theoretical  $EE$  and  $BB$  power spectra and what we stand to learn from them.

#### 1.3.2.1 Sources of Polarization

We now turn to physical processes that produce polarization in the CMB. Let us begin with a review of Thomson scattering between a photon and an electron. A single photon with polarization vector  $\hat{\epsilon}_0$  travels toward an electron. The electron senses the **E**-field of the photon and begins oscillating up and down in the  $\hat{\epsilon}_0$  direction. Since the particle is oscillating at the frequency of the incoming photon, and hence constantly accelerating, it radiates a photon at the same frequency in some new direction with polarization vector  $\hat{\epsilon}_1$ . The process appears as if the original photon, which was absorbed by the electron, has simply scattered off the electron in a new direction. The direction of polarization  $\hat{\epsilon}_1$  is not known before the scattering, but certain directions are favored by others as one can see by looking at the differential Thomson scattering cross-section (48)

$$\frac{d\sigma_T}{d\Omega} = \left( \frac{e^2}{m_e c^2} \right)^2 |\hat{\epsilon}_1^* \cdot \hat{\epsilon}_0|^2, \quad (1.37)$$

which shows that the cross-section for scattering is greatest when the polarization vectors of the incoming and outgoing photons are parallel. Thomson scattering thus tends to preserve the direction

of linear polarization of a single photon.

Let us now consider Thomson scattering of an electron in an isotropic bath of photons corresponding to the CMB spectrum monopole moment or equivalently the spherical harmonic  $Y_0^0$ . Here the intensity of radiation is the same in every direction. Note that since the CMB is a blackbody to high accuracy, and since the blackbody intensity curve is monotonic in temperature, higher intensity is associated with higher temperature. In this configuration, it is clear from symmetry that the total polarization from Thomson scattering will be zero even though a single scattering event gives polarized light (29); for every linearly polarized scattered photon there is another scattered photon with polarization in an orthogonal direction resulting in no net polarization.

A similar situation arises for a dipole anisotropy in the radiation field corresponding to the spherical harmonics  $Y_1^{0,\pm 1}$ . For concreteness, we assume there is a dipole moment in temperature only in the  $\hat{\epsilon}_x$  direction, with an electron at the origin. Radiation coming from the  $\pm\hat{\epsilon}_{y,z}$  directions has the same temperature and so produces no net polarization in the scattered directions. Radiation from the  $\pm\hat{\epsilon}_x$  directions have different temperatures because of the dipole anisotropy but these differences cancel at the origin where the light is incident on the electron. Therefore the light scatters off the electron in such a way as to produce no net polarization.

We must turn to a quadrupole anisotropy, spherical harmonics  $Y_2^{0,\pm 1,\pm 2}$ , to successfully output polarized light. Indeed, thanks to the orthogonality of the spherical harmonics, the quadrupole moment is the only local anisotropy that can produce polarization via Thomson scattering. Consider now the case where an electron sees a local quadrupole with hotter radiation above and below it and cooler radiation to its sides. Even though the incident radiation is in general unpolarized the scattered radiation is influenced more by the hotter (more intense) radiation than the cooler. This favors the hotter radiation's scattered direction in the quadrupole over the cooler radiation's scattered direction resulting in overall linearly polarized light. Note that in all three quadrupole cases, Thomson scattering results in *linearly* polarized light and therefore we do not expect to see circular polarization in the CMB. We thus anticipate, and generally assume, that Stokes parameter  $V = 0$  in the CMB and so measuring  $Q$  and  $U$  will fully define the polarization.

What mechanisms, then, produce quadrupole anisotropies in the photon-baryon fluid before the epoch of recombination? We see there are three sets of spherical harmonics associated with the quadrupole moment and there are three physical perturbations that produce them: scalar, vector, and tensor perturbations corresponding to  $m = 0, \pm 1, \pm 2$ , respectively (49). Scalar perturbations are simply density perturbations resulting from gravity. Consider a plane wave perturbation throughout the photon-baryon fluid with peaks and troughs of hotter and cooler radiation. Movements of the baryons will be in the same direction as the plane wave, away from the hotter regions and towards the cooler. If you are an electron sitting at a crest or trough then locally you see a temperature quadrupole and Thomson scattering from that point will result in linearly polarized light. Vector perturbations come from vortical motions in the fluid, which we argued above should be erased by inflation. Finally, tensor perturbations result from gravitational waves. This is an oscillating stretching of photon wavelengths in the plane of a wave's peaks and troughs, which is orthogonal to its direction. The stretching of wavelengths preferentially in one direction also results in a local quadrupole anisotropy.

### 1.3.2.2 *E Modes and B Modes*

It would be informative if by mapping  $Q$  and  $U$  we could recover information about the state and distribution of matter at the epoch of recombination. Since the absolute directions of  $Q$  and  $U$  are arbitrarily defined, usually by the configuration of an experiment measuring them, they provide little direct physical implications. However, if they are re-expressed in a different basis set then one gains power to say more about the underlying physics. This new basis set contains the *E* modes (even-parity or “curl-less”) and *B* modes (odd-parity or “divergence-less”). In Fourier space they are related to  $Q$  and  $U$  at a particular multipole moment  $l$  via the relations

$$\begin{aligned} E_l &= +Q_l \cos 2\phi_l + U_l \sin 2\phi_l \\ B_l &= -Q_l \sin 2\phi_l + U_l \cos 2\phi_l, \end{aligned} \tag{1.38}$$

where  $Q_l$  and  $U_l$  are the Fourier transforms of  $Q$  and  $U$  and  $\phi_l = \arctan l_y/l_x$  is the phase angle between  $l_x$  and  $l_y$ . *E*-mode anisotropies are such that their intensities change in directions per-

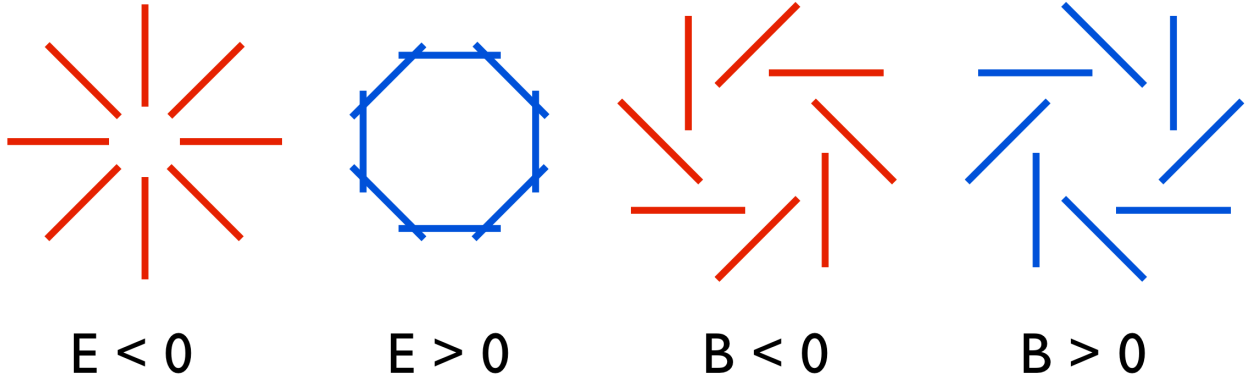


Figure 1.6: Directions of polarization patterns for positive and negative  $E$ - and  $B$ -mode anisotropies.

pendicular or parallel to the direction of local polarization, which exhibits even parity.  $B$ -mode anisotropies, on the other hand, change in directions  $45^\circ$  rotated from the polarization direction, which is odd-parity behavior. See Figure 1.6. The orthogonal characteristics of  $E$ - and  $B$ -modes give us knowledge about the physics during recombination as well as the growth of structure after matter-radiation decoupling.

The “curl-less” and “divergence-less” analogies of  $E$  and  $B$  modes are useful in determining which types of perturbations generate them. Scalar perturbations appear like a local divergence, with fluid streaming from hot to cold. There is no “curl” in this situation and so one expects only an  $E$ -mode contribution from scalar density fluctuations (49). Tensor perturbations decompose into “curl” and “divergence” components and so generate both  $E$  and  $B$  modes. It is worth emphasizing that while both scalar and tensor perturbations generate  $E$  modes, only tensor perturbations can source primordial  $B$ -mode polarization.

A couple caveats should be addressed. First, Thomson scattering only produces  $E$ -mode polarization. The direction of polarization is a result of one direction of scattered light being more intense than the orthogonal direction and in this scenario there is no way to scatter light  $45^\circ$  off the quadrupole axis. The question then arises from where do the  $B$  modes actually originate? The answer lies in the difference between local anisotropies sensed by an electron and larger-scale

anisotropies. Larger-scale perturbations modulate the local quadrupole signal changing the sign and/or amplitude of the local polarization (49). This can mix  $E$  modes into  $B$  modes. Even though Thomson scattering cannot produce  $B$  modes from local scatterings,  $B$  modes are nevertheless produced by more global perturbations modulating the local quadrupole fluctuations. Second, the presence of intervening structure at small angular scales means that  $E$ -mode polarization can be gravitationally lensed. As Figure 1.6 illustrates, this introduces a curl component by slightly twisting the polarization vectors, which mixes part of the  $E$ -mode signal into *lensing*  $B$  modes at high  $l$ .

### 1.3.2.3 $EE$ , $TE$ , and $BB$ Power Spectra

We can define power spectra  $C_l^{EE}$  and  $C_l^{BB}$  for  $E$ -mode and  $B$ -mode polarization anisotropies just as we defined the temperature power spectrum. Since the scalar density fluctuations in the photon-baryon plasma generate local quadrupole moments that electrons sense, we expect the  $EE$  spectrum to exhibit acoustic peak features. Acoustic peaks are out of phase by  $90^\circ$  between the  $TT$  and  $EE$  spectra since the resulting polarization amplitude scales with the velocity of the fluid in local quadrupole anisotropies and the fluid velocity is maximum between fluid oscillation extrema. Given the shared physical source of the temperature and  $E$ -mode polarization anisotropies, we expect the fluctuations to be correlated and so we also define the  $TE$  power spectrum,

$$C_l^{TE} = \frac{1}{2l+1} \sum_{m=-l}^l \left( a_{lm}^T a_{lm}^{*,E} + a_{lm}^E a_{lm}^{*,T} \right). \quad (1.39)$$

The  $TT$ ,  $EE$ , and  $TE$  spectra all constrain parameters in similar ways given their shared dependence on the physics of the early universe. Figure 1.7 demonstrates how the  $EE$  spectrum changes with baryonic and dark matter density, which cause similar effects to those seen on the  $TT$  spectrum. Current measurements of the polarization power spectra from several experiments are plotted in Figure 1.1. The acoustic peaks are clear in the  $EE$  and  $TE$  spectra in modern measurements, and the  $BB$  spectrum has only just been detected.

As discussed above the  $BB$  spectrum has two sources: lensing  $B$  modes at small angular

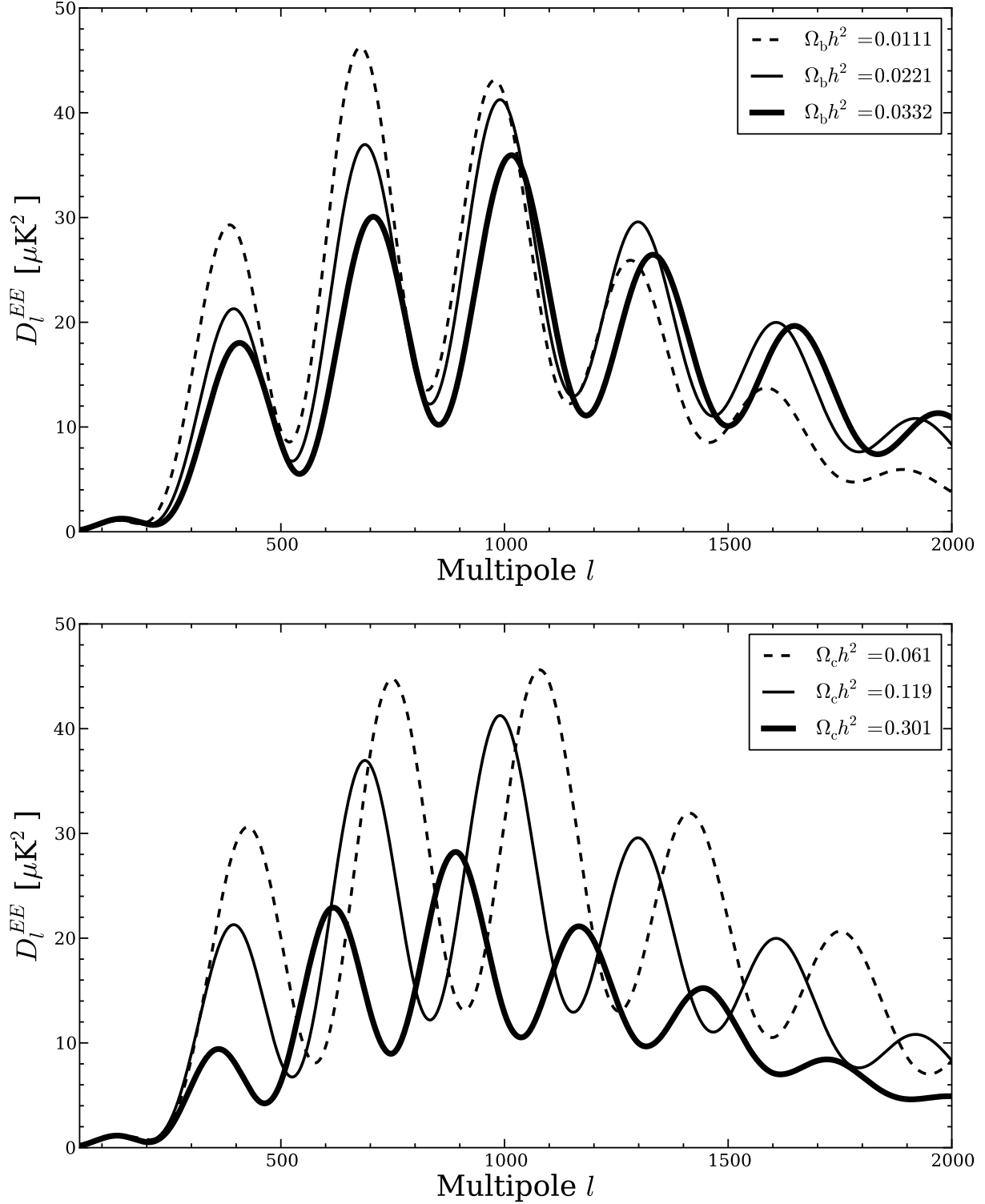


Figure 1.7: Effects of increasing  $\Omega_b h^2$  (top) and  $\Omega_c h^2$  (bottom) on the CMB  $EE$  polarization power spectrum while keeping  $H_0$  and  $\Omega_k$  fixed. Parameter values increase according to dashed, solid, and thick lines.

scales and inflationary gravitational-wave (IGW)  $B$ -modes generated by gravitational waves from the epoch of inflation at large angular scales. The amplitude of IGW  $B$  modes therefore constrains the energy scale of inflation. We again point out that a non-zero detection of the tensor-to-scalar ratio  $r$  not only strongly hints at the existence of gravitational waves but also implies that gravity is quantized. The scientific knowledge to be gained from IGW  $B$ -mode polarization as well as its importance is evident. The lensing  $B$  modes are a significant foreground, however. To measure gravitational-wave  $B$  modes over a wider range of multipoles to better constrain the tensor spectral index  $n_t$  and learn more about inflation the lensing  $B$  modes will need to be accurately measured and removed.

## 1.4 Outline

This chapter has reviewed the concepts necessary to motivate and interpret the cosmological constraints presented in this work. Chapter 2 discusses the design of the SPTpol receiver as well as the detector technologies it employs. Relevant information about the South Pole Telescope (SPT), in which SPTpol is installed, will also be addressed. Chapter 3, largely a copy of a SPIE proceedings article written by the author, describes in detail the design and development of the seven 150 GHz detector modules at the center of the SPTpol focal plane, which the author led. In Chapter 4 we describe observational strategies and relevant nomenclature necessary to understand the analysis methods discussed below. We also define the datasets used in this analysis. Chapter 5 details the analysis pipeline written to generate maps and CMB temperature and polarization power spectra from SPTpol observations. The chapter highlights major contributions from the author, including telescope pointing corrections, unbiasing of measured power spectra, and the calculation of the bandpower covariance matrix. In Chapter 6 we explain the methodologies used to obtain cosmological parameter fits from SPTpol data products, which were also led by the author. We present the main results of this analysis in the form of polarization power spectra and new cosmological parameter constraints in Chapter 7. This work concludes in Chapter 8 with some remarks on near-term projects extending the analysis presented here.

## Chapter 2

### The South Pole Telescope and the SPTpol Receiver

As we discussed in Chapter 1 there is much to gain from observations of CMB polarization anisotropies. Measurements of the polarization power spectra can side-step the cosmic variance limit in information obtained from the temperature anisotropy power spectrum and help to constrain new physics beyond the  $\Lambda$ CDM model. With this in mind, we designed and built a new polarization-sensitive receiver for the South Pole Telescope (SPT) called SPTpol. This chapter summarizes the salient features of the SPTpol receiver as well as the telescope. We also describe the detector and readout technologies that make detecting sub- $\mu$ K temperature and polarization anisotropies possible.

#### 2.1 The South Pole Telescope

The SPTpol receiver is installed in the SPT, which is located 1 km from the geographic South Pole and the Amundsen-Scott South Pole Station. At a physical elevation of 9,301 ft above sea level and in the center of the Antarctic Plateau, the median precipitable water vapor (PWV) at the South Pole is less than 0.5 mm (52) making the site an ideal location to observe microwave frequencies. The telescope is a 10-meter off-axis Gregorian with a primary mirror surface accuracy better than 25  $\mu$ m, which provides diffracted-limited resolution of 1.6, 1.2, and 1.0 mm at 95, 150, and 220 GHz, respectively across a 1.2° diameter field-of-view (53). To mitigate polarized ground pickup a 1-m guard ring was installed around the primary in the 2011-2012 austral summer maintenance season. New side shields that span the length of the telescope boom to the new guard

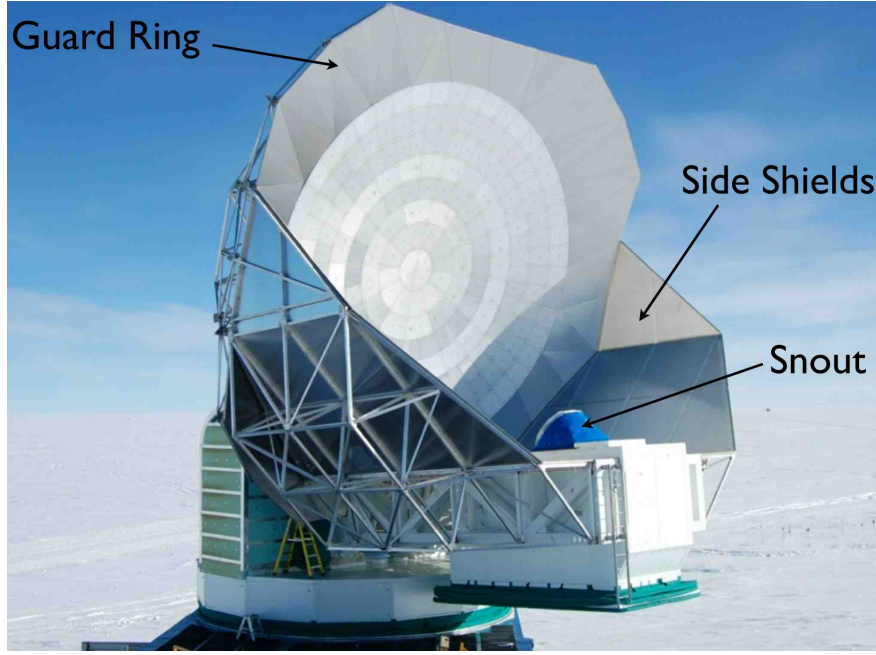


Figure 2.1: The SPT with newly installed primary mirror guard ring, side shields, and snout to mitigate polarized ground pickup for SPTpol observations.

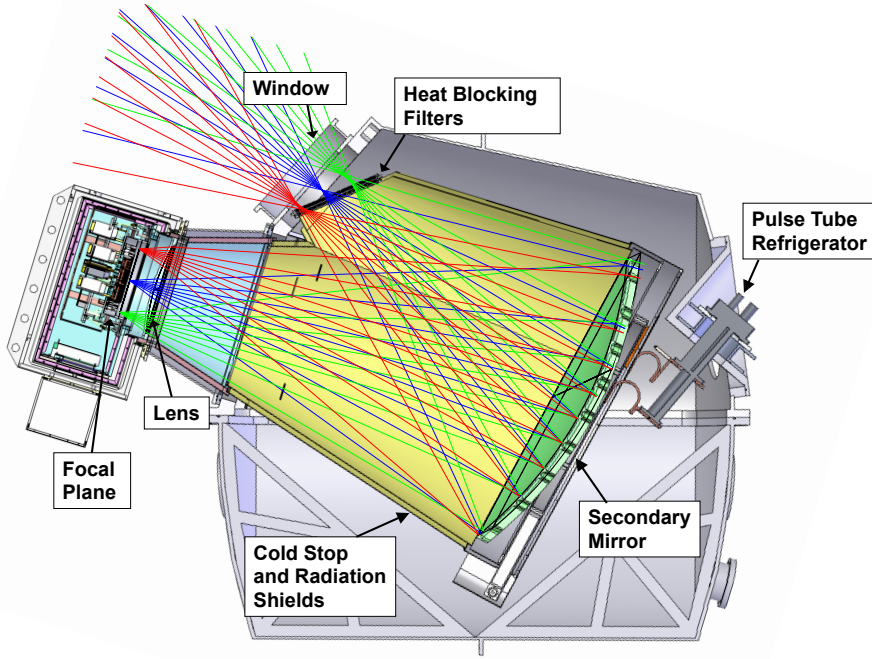


Figure 2.2: Cut-away view of the SPT secondary mirror cryostat (50). Light rays enter the system after bouncing off the primary mirror located off-image to the upper left. They terminate on the SPTpol focal plane housed in a separate cryostat. Both cryostats, however, share the same vacuum.

Table 2.1: SPTpol Optical Loading

Element	$T_e$ [K]	$\eta$	$L_s$	$T_s$ [K]	$\eta_e$	$\eta_{\text{cum}}$	$P_{\text{opt}}$ [pW]
Bolometer	0.25	0 (0)	0.55 (0.55)	0.25	0.45 (0.45)	1.0 (1.0)	$\sim 0$ ( $\sim 0$ )
Cavity	0.25	0 (0)	0 (0)	0.25	1.0 (1.0)	0.450 (0.450)	$\sim 0$ ( $\sim 0$ )
Feed horn	0.25	0 (0)	0 (0)	0.25	1.0 (1.0)	0.450 (0.450)	$\sim 0$ ( $\sim 0$ )
Band-def filters	0.25	0.05 (0.05)	0 (0)	0.25	0.95 (0.95)	0.450 (0.450)	$\sim 0$ ( $\sim 0$ )
Harmonic Blocker	0.25	0.05 (0.05)	0 (0)	0.25	0.95 (0.95)	0.427 (0.427)	$\sim 0$ ( $\sim 0$ )
IC Blocker	0.50	0.05 (0.05)	0 (0)	0.50	0.95 (0.95)	0.406 (0.406)	$\sim 0$ ( $\sim 0$ )
Lens	6.00	0.02 (0.02)	0.02 (0.02)	10.0	0.96 (0.96)	0.385 (0.385)	0.08 (0.09)
Lens filter	6.00	0.05 (0.05)	0 (0)	10.0	0.95 (0.95)	0.370 (0.370)	0.06 (0.07)
Secondary	10.0	0.09 (0.33)	0.02 (0.05)	10.0	0.88 (0.63)	0.352 (0.352)	0.26 (1.1)
10 K filter	10.0	0.05 (0.05)	0 (0)	10.0	0.95 (0.95)	0.313 (0.211)	0.10 (0.09)
IR Shader	100.0	0.01 (0.01)	0 (0)	100.0	0.99 (0.99)	0.297 (0.211)	0.24 (0.25)
70 K filter	100.0	0.05 (0.05)	0 (0)	100.0	0.95 (0.95)	0.294 (0.209)	1.18 (1.23)
IR shader	100.0	0.01 (0.01)	0 (0)	100.0	0.99 (0.99)	0.279 (0.198)	0.23 (0.23)
IR shader	100.0	0.01 (0.01)	0 (0)	100.0	0.99 (0.99)	0.277 (0.196)	0.22 (0.23)
Window	300.0	0.01 (0.01)	0 (0)	300.0	0.99 (0.99)	0.274 (0.194)	0.67 (0.67)
Primary	220.0	0.02 (0.02)	0 (0)	10.0	0.98 (0.98)	0.271 (0.192)	1.09 (1.21)
Atmosphere	230.0	0.12 (0.07)	0 (0)	230.0	0.88 (0.92)	0.266 (0.189)	5.96 (3.87)
CMB (band avg.)	2.73	1.0 (1.0)	0 (0)	2.73	0 (0)	0.201 (0.143)	0.22 (0.13)
<b>Total</b>							<b>10.3 (9.2)</b>

**Notes:** See text for definitions. Values for 95 (150) GHz are quoted assuming a feed horn plus detector efficiency of 90%. Data from (51).

ring were installed the following year for the second season of SPTpol observations. Finally, an absorbing “snout” was installed on top of the telescope boom where the beam enters the telescope structure to further control polarization systematics. Figure 2.1 shows the primary mirror, the guard ring, the new side shields, and the snout in early 2012.

During observations light reflects off the primary and passes through an environmental window at the base of the snout where it enters the telescope structure. It then passes through a zotefoam<sup>1</sup> vacuum window where it enters a cryostat that fully encompasses the 1-m secondary mirror of the telescope. Figure 2.2 demonstrates the light path through the rest of the (cold) optics chain. Several IR-reducing metal mesh capacitive filters<sup>2</sup> reduce the heat load on the system. The rays then strike the secondary mirror, which acts as a cold stop cooled to  $\sim 10$  K. The secondary mirror is surround by eccosorb HR-10,<sup>3</sup> a high-emissivity material in millimeter wavelengths. The secondary cryostat also has several thermally isolated radiation shields at 300, 50, and 4 K to reduce

<sup>1</sup> <http://www.zotefoams.com/>

<sup>2</sup> <http://www.astro.cardiff.ac.uk>

<sup>3</sup> <http://www.eccosorb.com/products-eccosorb-hr.htm>

ambient temperature radiation heating the mirror. The cryostat is cooled with a Cryomech PT410 pulse tube cooler<sup>4</sup> and is cryogen-free. After striking the secondary mirror, light rays enter the SPTpol receiver cryostat. Another series of metal mesh filters further reduce the incident power, and a weak lens focuses the rays on the SPTpol focal plane. The receiver cryostat is cooled to  $\sim 270$  mK in operation by a Cryomech PT415 pulse tube cooler and a custom Simon Chase  $^3\text{He}$ - $^4\text{He}$ - $^3\text{He}$  sorption refrigerator<sup>5</sup>.

Table 2.1 summarizes the optical loading power on the 95 and 150 GHz detectors from the telescope optics chain (51). For each element in the system we list emission temperature  $T_e$ , emissivity  $\eta$ , scattering fraction  $L_s$ , scattering temperature  $T_s$ , transmission (or reflection) efficiency  $\eta_e$ , cumulative transmission efficiency  $\eta_{\text{cum}}$  up to that element in the optics chain, and the resulting optical power  $P_{\text{opt}}$  incident on a single-polarization detector. Values for 150 GHz detectors are given in parentheses. We assume a feed horn plus detector efficiency of 90%, which agrees with detector and receiver characterization tests (54). The total optical power incident on the focal plane is  $\sim 10$  pW with less than 0.25 pW from in-band CMB power. The optical loading budget must be well-understood when designing detectors to maximize sensitivity while minimizing detector noise. We describe the detector technology in more detail in Section 2.3.

## 2.2 The SPTpol Receiver

The SPTpol receiver is a dichroic polarization-sensitive instrument. At the center of the focal plane 588 dual-polarization pixels are divided into seven independent 84-pixel modules sensitive to 150 GHz. Around the focal plane perimeter 180 dual-polarization pixels sensitive to 95 GHz are individually installed. The pixel count is 768 for a total of 1536 optically sensitive detectors. Each 150 GHz module also has four “dark” detectors uncoupled to incident radiation for diagnostic purposes. Light is coupled to the detectors by feed horns, which in turn couple to the incident radiation on the focal plane. The front of the focal plane is shown in the left of Figure 2.3, where

---

<sup>4</sup> <http://www.cryomech.com/products/cryorefrigerators/pulse-tube>

<sup>5</sup> <http://www.chasecryogenics.com/3h-coolers.html>

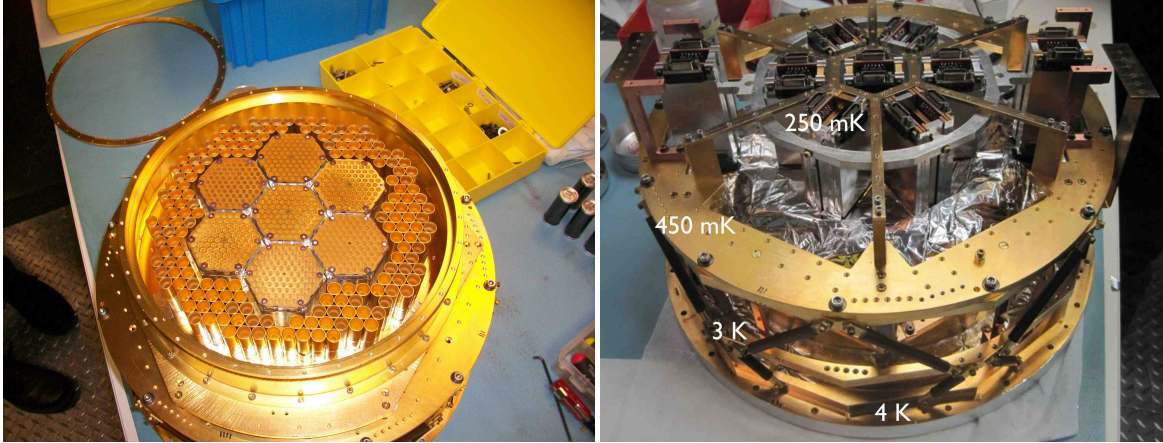


Figure 2.3: The SPTpol focal plane. (Left) Feedhorns before band-defining filters are installed. (Right) Back side of focal plane with cryogenic readout electronics boards, thermal sinking points, and additional structures to increase the rigidity of the readout boards.

the feed horns are clearly visible. The back of the focal plane (right) exhibits cold readout electronics boards and thermal sinking structures.

The receiver has four temperature stages to shield the focal plane from its environment. Each stage is thermally isolated by thin Vespe<sup>6</sup> legs, which have low thermal conductivity while providing rigidity to the receiver. The detectors and cold mK readout electronics are attached to the 250 mK ultra-cold (UC) head of the Chase fridge. Readout cables are thermally shorted to the inter-cold (IC) stage at 450 mK and heat-exchanger (HEX) at  $\sim 3$  K before reaching the 4 K cold electronics. The receiver's thermal stages are labeled in the right of Figure 2.3.

Bandpasses that define to what frequencies of light detectors will be sensitive are created with a combination of feed horn waveguides and metal mesh filters. A waveguide acts as a high-pass filter only allowing modes with wavelengths smaller than the size of the waveguide through. The feed horn waveguides thus define the low frequency (high-pass) side of the bandpasses. The high frequency (low-pass) edges of the bands are defined by additional metal mesh filters. Both 95 and 150 GHz low-pass filters also have a harmonic blocker to reduce high-frequency or “blue” leaks in the filter transmission, however the 150 GHz low-pass filter doubles as the 95 GHz harmonic

---

<sup>6</sup> <http://www.dupont.com>

Table 2.2: SPTpol Bandpass Summary

Band	$\nu_0$	$\Delta\nu$	$\nu_1$	$\nu_2$
2012 Observations				
150	$145.8 \pm 0.3$	$44.5 \pm 1.1$	119.4	172.4
95	$91.4 \pm 0.6$	$30.8 \pm 2.7$	73.0	109.7
2013 Observations				
150	$146.6 \pm 0.7$	$45.0 \pm 2.5$	119.4	174.5
95	$93.4 \pm 1.0$	$34.6 \pm 2.5$	73.0	114.8

**Notes:** All values are in GHz.  $\nu_0$  is the band center while  $\Delta\nu$  is the effective bandwidth.  $\nu_1$  and  $\nu_2$  are the low and high 25% transmission points, respectively.

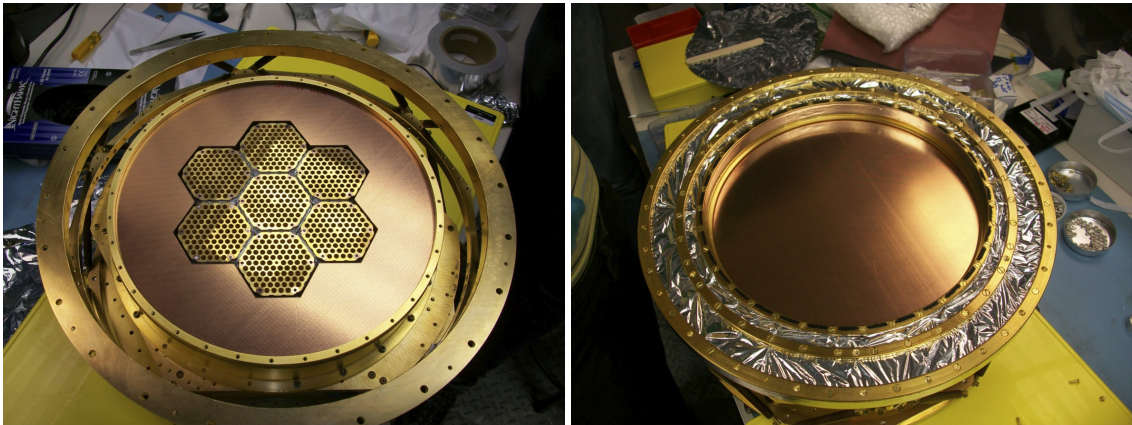


Figure 2.4: Metal mesh filters define the high-edge of the bandpasses. (Left) 95 GHz filter installed. (Right) 150 GHz filter plus harmonic blocker.

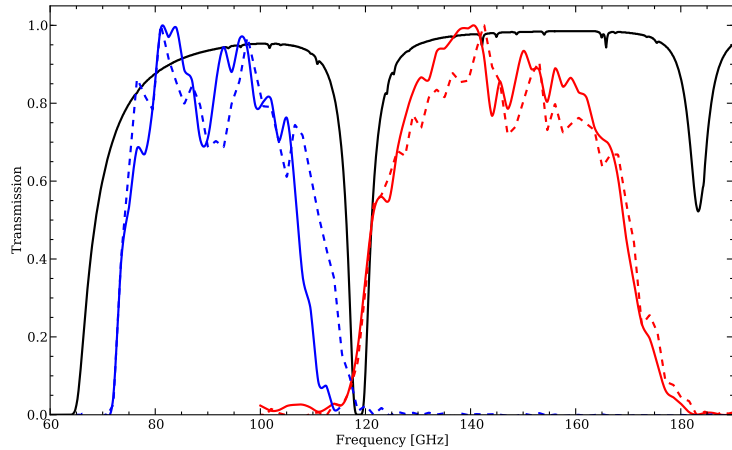


Figure 2.5: SPTpol bandpass transmission. Black is the South Pole atmospheric transmission with 0.26 mm PWV, the median value during winter months (52). The 150 GHz bandpass is plotted in red while the 90 GHz bandpass is in blue. Bandpasses for the 2012 (2013) observing season are in solid (dashed) lines. SPTpol bandpass transmissions have been normalized to a maximum value of one.

blocker. We show the three band-defining filters being installed in Figure 2.4 while the resulting bandpasses at 95 and 150 GHz are plotted in Figure 2.5 for the 2012 and 2013 observing seasons. For comparison the atmospheric transmission with 0.26 mm PWV at the South Pole is also plotted. The bands are designed to fit in windows of high atmospheric transmission between water and oxygen lines that cause both heavy absorption and additional detector loading if the band has significant transmission inside the lines. Central frequencies, effective bandwidths, and the 25% transmission low and high edges of the bandpasses are summarized in Table 2.2 for the 2012 and 2013 observing seasons. New low-pass filters were installed between seasons to increase sensitivity to higher frequencies.

### 2.3 Detector Technology

Both the 95 and 150 GHz detectors in the SPTpol focal plane are transition edge sensor (TES) bolometers. Bolometers are simply heat detectors, where incident radiation is absorbed by a detector, raising its temperature. By monitoring changes in detector temperature one infers changes in incident radiation. These devices have three basic components: a temperature-dependent resistor, or thermistor, with temperature  $T_d$ , an absorber with heat capacity  $C$ , and a weak thermal link with thermal conductance  $G$  between the thermistor/absorber and a thermally stable bath of temperature  $T_b$ . The heat capacity  $C$  and thermal conductance  $G$  set the characteristic time constant for the detector,  $\tau_0 = C/G$ . The detector requires roughly time  $\tau_0$  after absorbing radiation before being able to make a new independent measurement of the incident light.

The SPTpol TES thermistors are superconductors, the resistance of which are strongly dependent on temperature. Above a critical temperature  $T_c$  the superconducting material has “normal” resistance  $R_N$  that obeys Ohm’s law  $V = IR$ . Below  $T_c$  the resistance rapidly drops to zero, at which point the material is superconducting. This *superconducting transition* is an ideal state in which to operate a device, as here the resistance varies most strongly with temperature. TESs are therefore detectors operated in their superconducting transitions. A slight increase in temperature from the absorption of a photon results in a relatively large increase in resistance.

To maintain stability we operate the detectors in voltage biased mode, which creates negative electrothermal feedback. In the presence of zero incident radiation at bath temperature  $T_b$ , we apply a constant electrical bias voltage  $V_b$  to the device. Power is dissipated in the detector since

$$P_e = \frac{V_b^2}{R(T)}, \quad (2.1)$$

where  $R$  is the resistance of the thermistor.  $V_b$  is chosen so that Joule heating raises the detector temperature to  $T_d \sim T_c$ , the center of the thermistor's superconducting transition. Some of this power is conducted away by the weak link to the thermal bath, but the detector finds an equilibrium resistance/temperature exponentially with time constant  $\tau_0$ , ignoring any power that may itself radiate away (55). In the presence of incident radiation, the detector absorbs optical power  $P_{\text{opt}}$  as well as electrical bias power  $P_e$ , which increases  $T_d$  above  $T_c$ . This in turn raises the device's resistance and thus *drops* the dissipated electrical bias power according to Equation 2.1. The detector temperature decreases and a new equilibrium is reached. Negative electrothermal feedback forces the total power dissipated in a device  $P_{\text{tot}}$  to be constant,

$$P_{\text{tot}} = P_e + P_{\text{opt}} = \text{constant}, \quad (2.2)$$

and it greatly increases the dynamic range of the device since it stays near the same superconducting transition point.

The narrower the superconducting transition of a device the more sensitive it will be to small thermal fluctuations from CMB power. We quantify the width of the superconducting transition with the dimensionless quantity

$$\alpha = \frac{d \ln R}{d \ln T}. \quad (2.3)$$

TES bolometers can achieve an  $\alpha$  of up to 500 (55). Since a larger  $\alpha$  means the detector responds more quickly to temperature deviations,  $\alpha$  also acts as a large additional effective thermal conductance, greatly reducing the effective time constant of a device (56; 57). Our TES bolometers have time constants of  $< 1$  ms (58).  $\alpha$  is also related to the strength of the negative electrothermal

feedback quantified by the loop gain  $\mathcal{L}$  (55),

$$\mathcal{L}(\omega) = \frac{-\delta P_e}{\delta P_{\text{tot}}} = \frac{P_e \alpha}{G T_b (1 + i\omega\tau_0)} = \frac{\mathcal{L}}{1 + i\omega\tau_0}. \quad (2.4)$$

Here  $\omega$  is the frequency of an optical signal. The loop gain decreases at high frequencies due to the detector time constant  $\tau_0$ . The larger  $\mathcal{L}$  the closer  $T_d$  stays at the desired transition bias point when there is a change in incident optical power. With finite loop gain, if  $P_{\text{opt}}$  is great enough to increase  $T_d$  above  $T_c$  then the detector will return to its normal resistance state and lose most of its sensitivity in a process called *saturation*. The total expected experiment loading, from both electrical bias and incident optical power, must be well-modeled when designing a device to avoid detector saturation while in operation. Given the loading model shown in Table 2.1, SPTpol detectors were designed with saturation powers  $P_{\text{sat}} \sim 25$  pW to account for electrical biasing power  $P_e$  to operate each device.

The sensitivity of a detector in operation can be parameterized by its responsivity  $S$  (55),

$$S = \frac{\delta I}{\delta P_{\text{opt}}} = \frac{-1}{V_b} \frac{\mathcal{L}}{\mathcal{L} + 1} \frac{1}{1 + i\omega\tau_0}. \quad (2.5)$$

The responsivity measures the ratio of the change in electrical current through the device  $\delta I$  with the change in incident optical power  $\delta P_{\text{opt}}$ . This is also referred to as detector gain. At frequencies below the time constant cutoff and in the limit of high loop gain, the responsivity is just the negative inverse of the voltage bias  $V_b$ . The responsivity or gain is an important detector property that must be well characterized over time to correctly convert to and interpret the absolute amplitude of sky power observed by a detector.

Both the 95 and 150 GHz detectors in SPTpol are TES devices. Though the basic functionality of the devices is the same, the detectors were designed and fabricated by different groups and with different facilities. The following subsections will summarize the main differences between the 95 and 150 GHz pixels while Table 2.3 lists general detector properties.

Table 2.3: SPTpol Detector Properties

	95 GHz	150 GHz
$R_N$	$1.0 \pm 0.1 \Omega$	$1.2 \pm 0.2 \Omega$
$T_c$	$535 \pm 35 \text{ mK}$	$478 \pm 29 \text{ mK}$
$P_{\text{sat}}$	$44 \pm 11 \text{ pW}$	$22.4 \pm 5.7 \text{ pW}$
$\tau_0$	$0.5 - 1 \text{ ms}$	$0.5 - 1 \text{ ms}$

**Notes:** See text for definitions. Data from (51).

### 2.3.1 95 GHz Pixels

A 95 GHz pixel is installed in its own separate profiled feed plus waveguide module. Using HFSS<sup>7</sup> simulations we designed the profiling to emulate the polarization properties of more traditional corrugated circular feeds, which are more difficult and expensive to fabricate than profiled feeds. The circular waveguide in each 95 GHz pixel module defines the low-frequency end of the detector bandpass. Finally, the detectors are mounted above a quarter-wavelength backshort to optimize coupling to the electric field of the TE<sub>11</sub> mode launched by the circular waveguide. A 95 GHz pixel module is shown in cross-section in Figure 2.6.

Each detector is fabricated on an individual silicon chip at Argonne National Laboratory. A thin palladium-gold (PdAu) absorbing stripe is deposited on a relieved thermally isolated silicon-nitride (SiN) membrane. The geometry of the so-called SiN “island” legs attaching it to the rest of the pixel controls the thermal conductance  $G$  between the device and the pixel bath temperature. The orientation of the membrane in the waveguide defines its polarization angle with respect to the electric field of the TE<sub>11</sub> mode. A second detector chip is rotated by 90° and mounted on top of the first chip making a polarization-sensitive pixel. The distance between detectors is controlled by laying 25  $\mu\text{m}$  Al bonding wire between the chips (59).

Incident power is dissipated by the lossy PdAu, which heats up a TES on the edge of the membrane (Figure 2.6). The resulting change in current through the device is read through a pair of superconducting niobium (Nb) electrical leads. Since a high detector  $\alpha$  can cause instability deep in the superconducting transition during operation, Nb dots are deposited on the TES membrane

<sup>7</sup> <http://www.ansys.com/Products/Simulation+Technology/Electronics/Signal+Integrity/ANSYS+HFSS>

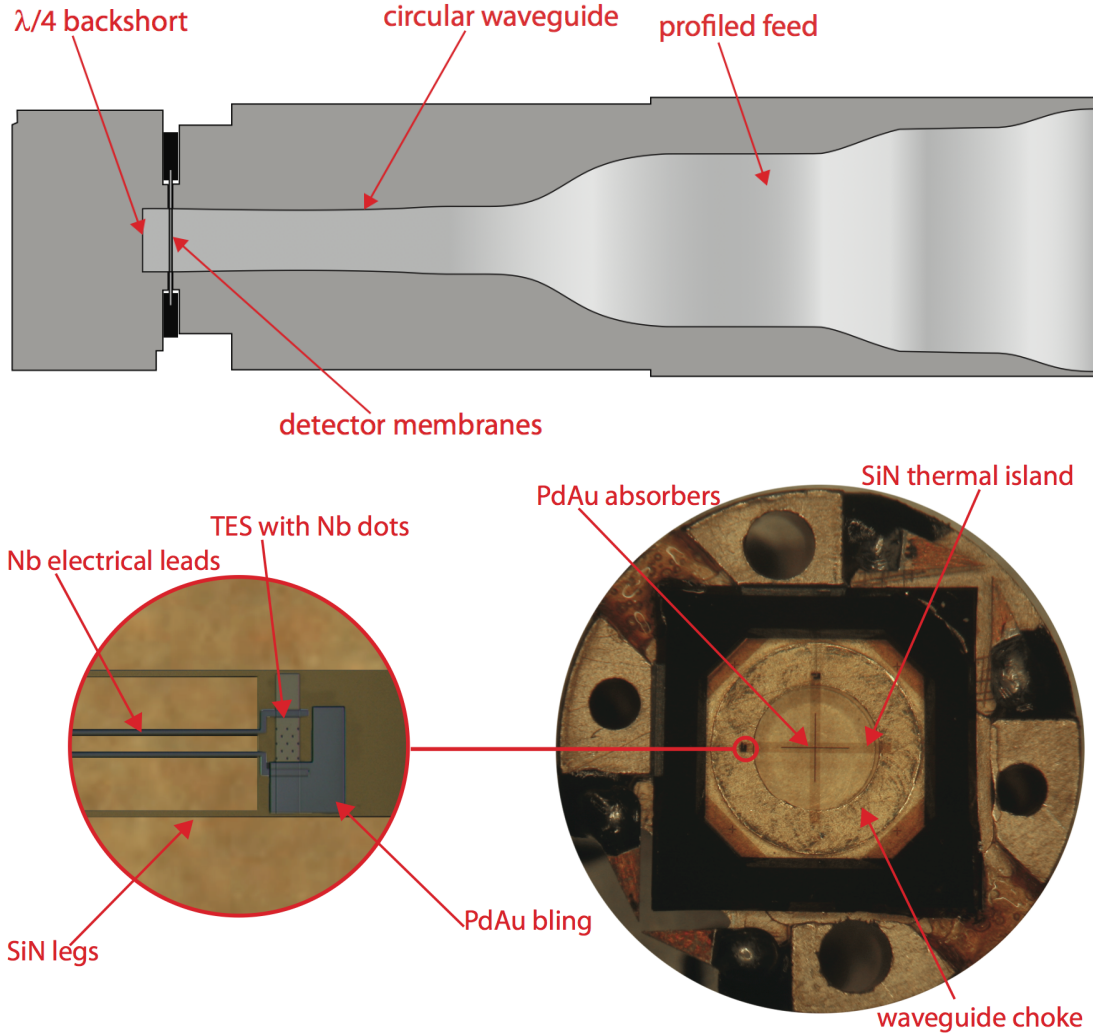


Figure 2.6: Internal view of SPTpol 95 GHz pixel. (Top) Cutaway of single feed plus pixel package. (Bottom) Magnified view of 95 GHz pixel and TES structure. Inside the choke the waveguide is 2.35 mm in diameter, which defines the low-frequency edge of the detector bandpass. Figure from (59).

to decrease  $\alpha$  in the 95 GHz pixels (59). Finally, additional PdAu overlaps the TES to increase its heat capacity and slow down the intrinsic electrothermal time constant of the device. A summary of 95 GHz detector properties appears in Table 2.3.

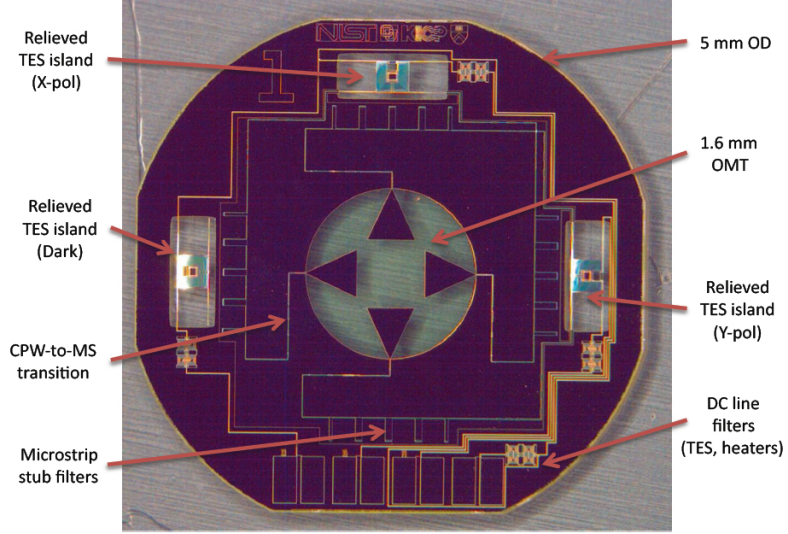


Figure 2.7: A prototype SPTpol 150 GHz pixel. The device is 5 mm across with a 1.6 mm OMT. Bandpass-defining stub filters shown here were not included in the final pixels. Figure appears in (60).

### 2.3.2 150 GHz Pixels

A prototype SPTpol 150 GHz pixel fabricated at NIST-Boulder is shown in Figure 2.7. Incident light is feed horn-coupled to a 1.6 mm orthomode transducer (OMT) that splits the signal into two orthogonal polarization states. The light is then propagated through coplanar waveguide (CPW) and finally lossless Nb microstrip to two TESs. As in the 95 GHz pixels a single TES is sensitive to a single polarization state, though in this case both devices are fabricated on the same chip. A third “dark” TES is sometimes included for characterizing electrothermal properties, calibration tests, and controlling systematics. Each TES is thermally isolated by floating on a relieved SiN island supported by SiN legs, the dimensions of which determine the thermal conductance  $G$  of the device. An Au meander surrounding the TES converts the signal to heat via ohmic dissipation, which is finally sensed by the TES. Basic detector properties for the fielded 150 GHz pixels are summarized in Table 2.3. We give more details about the detector wafers and mechanical packaging in Chapter 3 but we note here that detector property uniformity is increased dramatically by fabricating devices on the same silicon wafer as was done for the 150 GHz arrays.

## 2.4 Frequency-Domain Multiplexing

The detectors operate at temperatures below  $\sim 500$  mK so stringent control of the receiver's power budget is critical for maintaining base temperatures for extended periods. Besides dissipation of optical power, power conducted by readout wires for thousands of detectors could easily saturate the cooling power of the Chase fridge. In order to limit thermal loading on the receiver's mK temperature stages from readout wiring we use a digital frequency-domain multiplexing (DfMUX) readout scheme (61).

With DfMUX readout, each detector is placed in a distinct *LCR* resonance circuit. See Figure 2.8 for a schematic. A comb of different biasing frequencies is sent as a single *carrier* signal to multiple detectors simultaneously. Each detector is biased by a different carrier frequency, for which its *LCR* circuit uniquely has low impedance. The number of detectors biased by a single carrier signal, and therefore a single pair of wires, is the system's multiplexing factor. In SPTpol the multiplexing factor is 12 and there are 144 such frequency combs to read out the entire focal plane. Resonances for a single comb are plotted in Figure 2.8. The height and width of each resonance while in operation are inversely proportional to the detector resistance, which changes with optical loading.

For a given comb, changes in current through each device is summed through a single inductor, which relays the information as a change in magnetic flux through a series array of superconducting quantum interference devices (SQUIDs). To maintain a large dynamic range in the SQUIDs a *nulling* signal is also injected through the inductor. The nullder is  $180^\circ$  out-of-phase with the carrier signal, which cancels the relatively large carrier amplitude leaving only small changes in current through the TESs. Finally, the SQUID array output signal is demodulated to retrieve changes in readout current for each device separately. This demodulated readout current is the raw detector measurement with which to start an analysis.

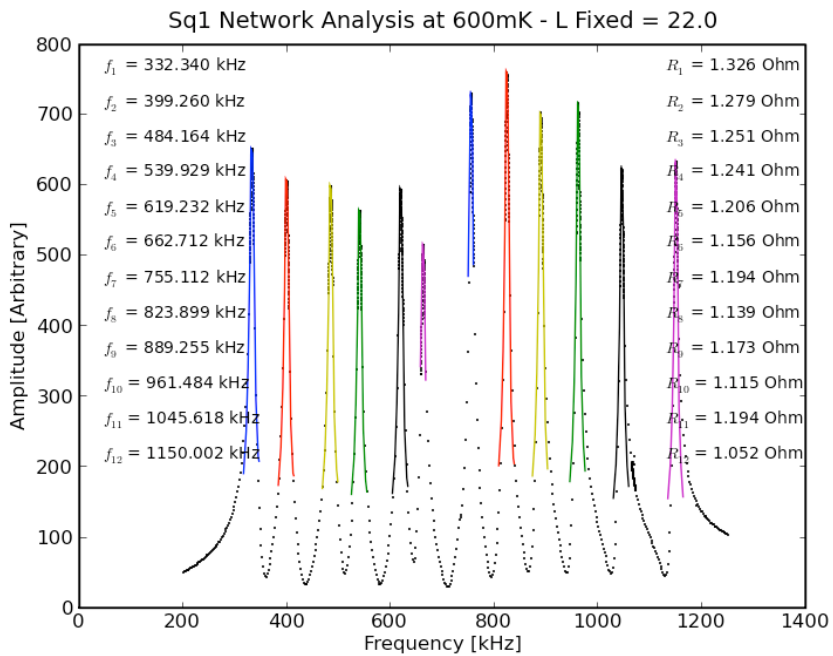
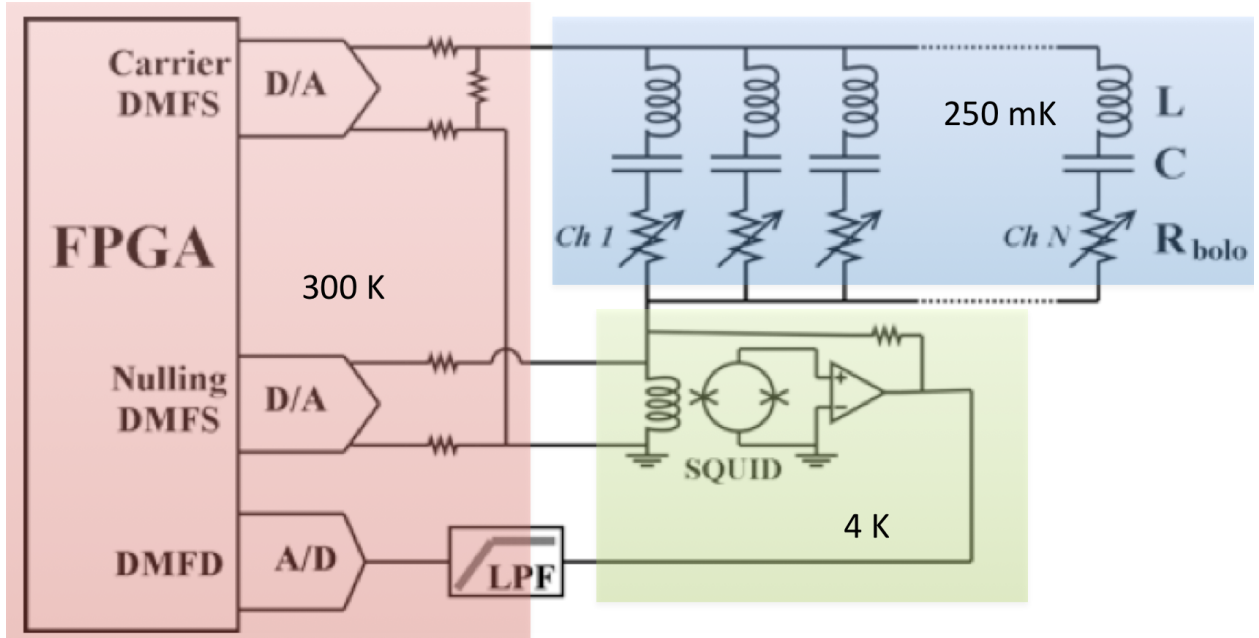


Figure 2.8: (Top) Circuit schematic of a DfMUX readout system, adapted from (61). © 2008 IEEE. (Bottom) One of 144 frequency combs measuring detector resonant frequencies in the SPTpol experiment.

## Chapter 3

### SPTpol 150 GHz Module Design

#### 3.1 Introduction

In this chapter we discuss the design and detector properties of the 150 GHz portion of the SPTpol focal plane, which has been split into seven 84-pixel modules. Each module is an independent camera including coupling feed horns, radio frequency (RF) shielding, and passive readout electronics. The chapter is organized as follows: Section 3.2 describes the module design in detail. Notable features of both individual hardware elements and the modules as a whole are discussed. Section 3.3 provides a summary of detector dark properties, including critical temperatures, normal resistances, and saturation powers. Finally, Section 3.4 reviews the lab-measured optical properties of the modules, namely detector optical efficiencies and electrothermal time constants, as well as early optical results for silicon platelet corrugated feed horn arrays developed at NIST-Boulder.

#### 3.2 Module Design

A large focal plane poses significant challenges for fabrication, assembly, and testing. To mitigate these issues, portions of SPTpol were designed with a modular format. While the 95 GHz band of SPTpol is comprised of 180 polarization-sensitive pixels (360 detectors fabricated at Argonne National Laboratory) individually packaged with corresponding light-coupling feed horns (59), the 150 GHz portion of the focal plane is split into seven identical modules, each containing 2.3 inch wide monolithic feed horn and detector arrays fabricated at NIST in Boulder, CO. Figure 3.1 shows a front-side view of the SPTpol focal plane where the 150 GHz modules

and 95 GHz pixel assemblies are clearly distinguishable. Modularity has several benefits. First, maintaining detector uniformity is easier when fabricating across smaller wafers. Second, a modular design makes possible testing whole units of the focal plane without requiring the full experiment apparatus. This greatly increases testing throughput and accelerates feedback into the design process. Finally, the modular units are simple to install into and remove from the SPTpol focal plane, which makes in-field modifications more tractable and timely. In the following subsections we describe in detail distinguishing characteristics of the module components.

### 3.2.1 Corrugated Silicon Platelet Feed Horn Array

When coupling free space to detectors, corrugated feed horns exhibit several appealing characteristics, namely high transmission efficiency, low cross-polarization and sidelobes, highly symmetric beam shapes, and wide bandwidths (62). Since measuring CMB polarization anisotropies requires tight control of systematics, many past experiments with relatively few pixels used individual corrugated feed horns (63; 64; 65; 66; 67; 68; 69; 70). Modern experiments contain many hundreds of tightly packed pixels, however, and the production of a corresponding monolithic feed horn array with standard electroforming techniques would be prohibitively difficult and expensive. Instead, the SPTpol 150 GHz modules contain monolithic arrays of corrugated feed horns built up from 33 silicon platelets, each 500  $\mu\text{m}$  thick, which have been stacked and gold-plated. The arrays were developed and fabricated at NIST-Boulder (71; 72). In addition to the attractive properties that corrugated feed horns exhibit, these silicon platelet arrays are coefficient of thermal expansion (CTE) matched to the detector arrays (also fabricated on silicon wafers), have lower thermal mass compared to conventional aluminum feed horns, and maintain high thermal conductivity despite being silicon in bulk due to the gold-plating.

Each of the seven SPTpol feed horn arrays are 2.3 inches wide and 16.5 mm tall, contain 84 single-moded corrugated feed horns with 4.26 mm apertures, and are optimized for a bandpass centered at 145 GHz. The feed horns taper off to a section of 1.22 mm wide square waveguide, which is used to define the lower edge of the bandpass, and ends with a single 1.6 mm diameter

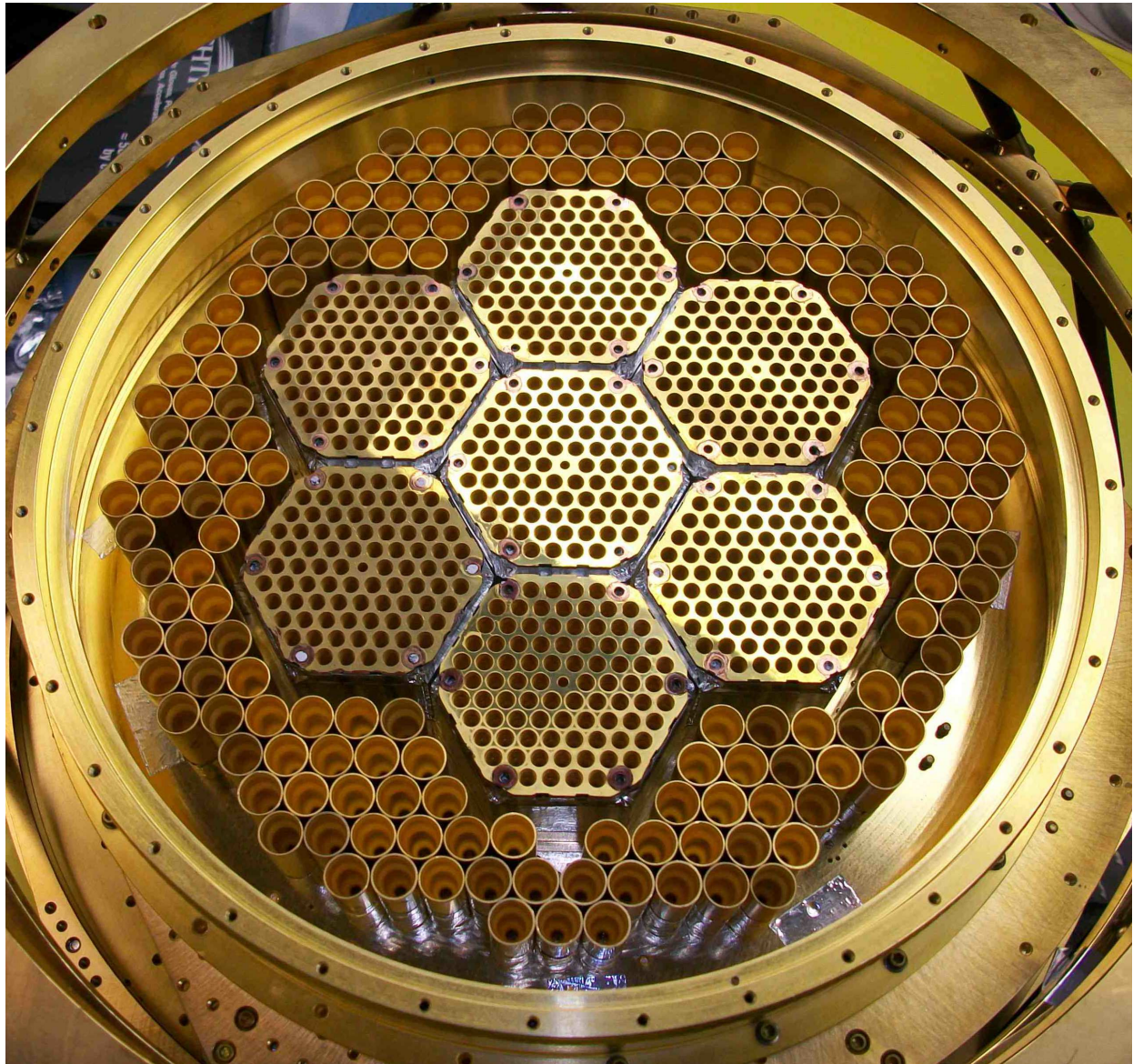


Figure 3.1: The SPTpol focal plane. Seven 84-pixel modules of 150 GHz detectors sit at the center of the camera, while 180 individually packaged 95 GHz pixels surround the modules, for a total of 768 polarization-sensitive pixels (1536 detectors). The focal plane is  $\sim 225$  mm in diameter.

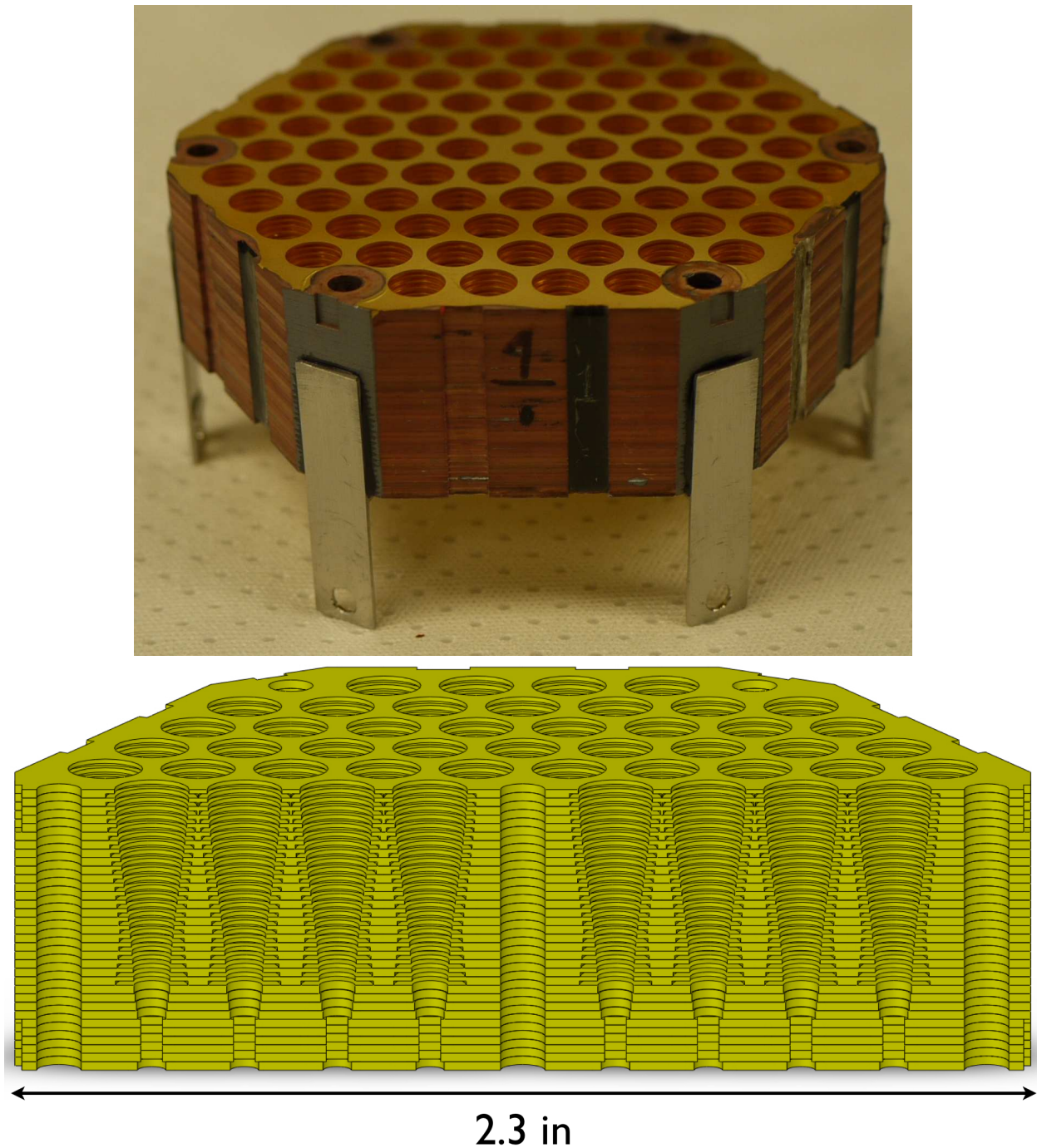


Figure 3.2: (Top) One of seven 150 GHz corrugated silicon platelet feed horn arrays in the SPTpol focal plane. The array is 2.3 inches wide and contains 84 feed horns with 4.26 mm apertures. (Bottom) Cross-sectional view of the feed horn profiles showing the corrugations and waveguides.

circular waveguide platelet. The left of Figure 3.2 is a picture of one SPTpol feed horn array, while the right shows a cross-section of a feed horn array to highlight the feed horn profile. 300 K vector network analyzer (VNA) measurements reveal that the feed horns have excellent uniformity in transmission properties, both across a single array and between the seven arrays. See Section 3.4 below for details.

### 3.2.2 Detector Arrays

Each module contains a detector array containing 84 dual-polarization pixels operated at  $\sim 270$  mK. The arrays are monolithically fabricated by photolithography techniques on silicon wafers at NIST-Boulder. The pixels are the result of development by the TRUCE collaboration (58; 73; 60; 74; 72). Figure 3.3 shows a schematic of a single pixel as well as one SPTpol detector array. Power is coupled to a released orthomode transducer (OMT), which splits the light into two orthogonal polarization states. The coupled power then travels down a coplanar waveguide (CPW) to microstrip transition, then through microstrip, and is eventually deposited on two transition edge sensor (TES) islands by a length of lossy gold meander. The TES devices themselves are made of an aluminum manganese alloy. TES devices operating in the middle of their superconducting transitions are extremely sensitive to small changes in incoming optical power. We use a digital frequency-domain multiplexing readout system developed at McGill University (75) to measure the change in detector temperature and therefore optical signal from the sky. Superconducting microstrip carries the signal from the TES out from each pixel and to the array edges where four banks of 90 wire bonding pads exist.

So that each detector array is sensitive to both Stokes  $Q$  and  $U$  polarization parameters, the orientation of an OMT is rotated by  $45^\circ$  with respect to its neighbors in an alternating pattern. By installing the 150 GHz modules into the SPTpol focal plane rotated by  $30^\circ$  with respect to one another, we simultaneously measure Stokes  $Q$  and  $U$  with three sets of independent measurements. These independent measurements allow for more tests to search for systematics in the data.

In addition to two optically-coupled TES devices per pixel, five pixels on each array also

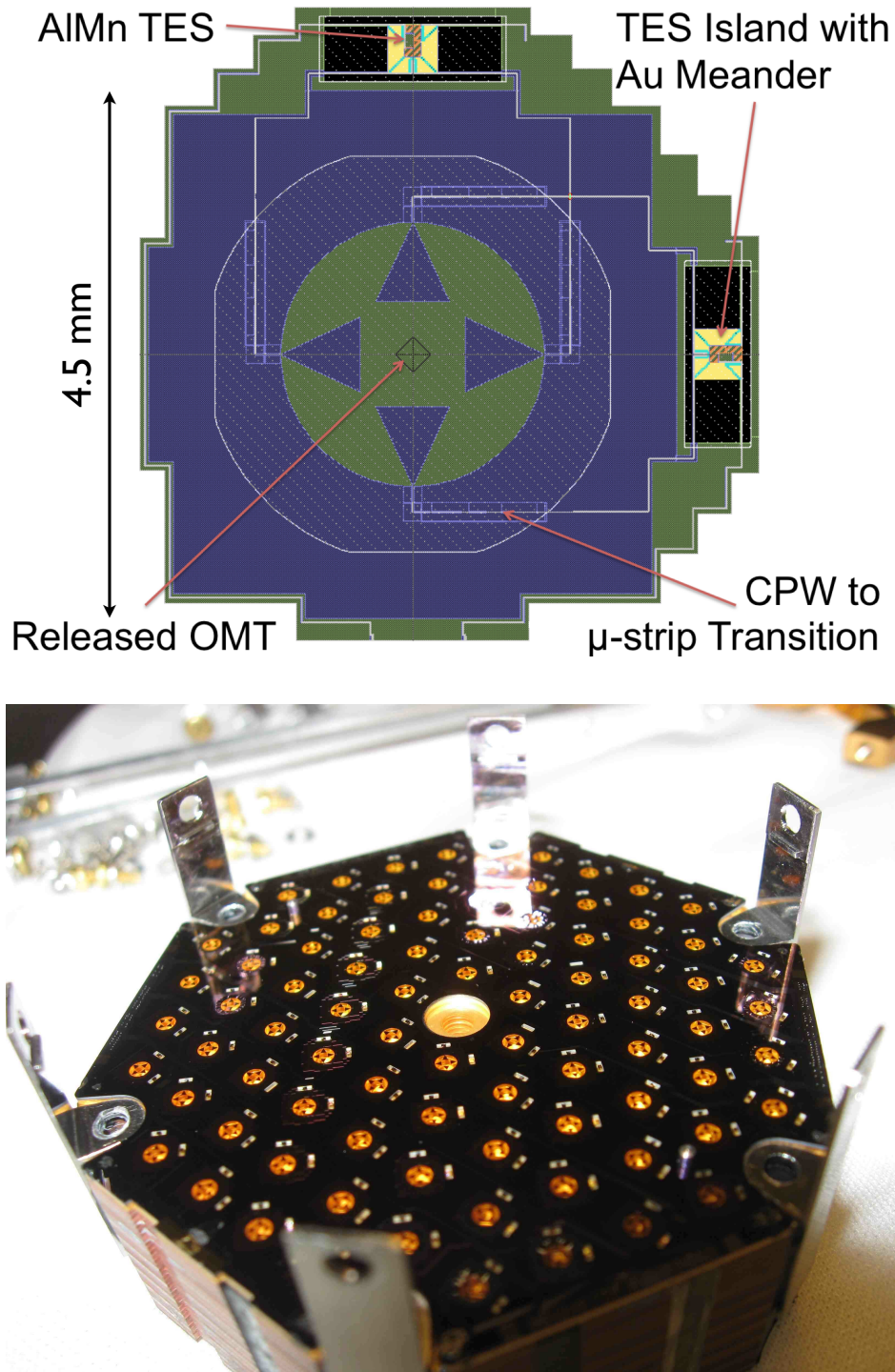


Figure 3.3: (Top) Schematic of one SPTpol 150 GHz pixel. Areas with white hashing are regions where the silicon substrate has been etched away leaving released silicon nitride. (Bottom) One of the seven SPTpol 150 GHz detector arrays during module assembly, before installing the BS wafer. The array is 2.3 inches across.

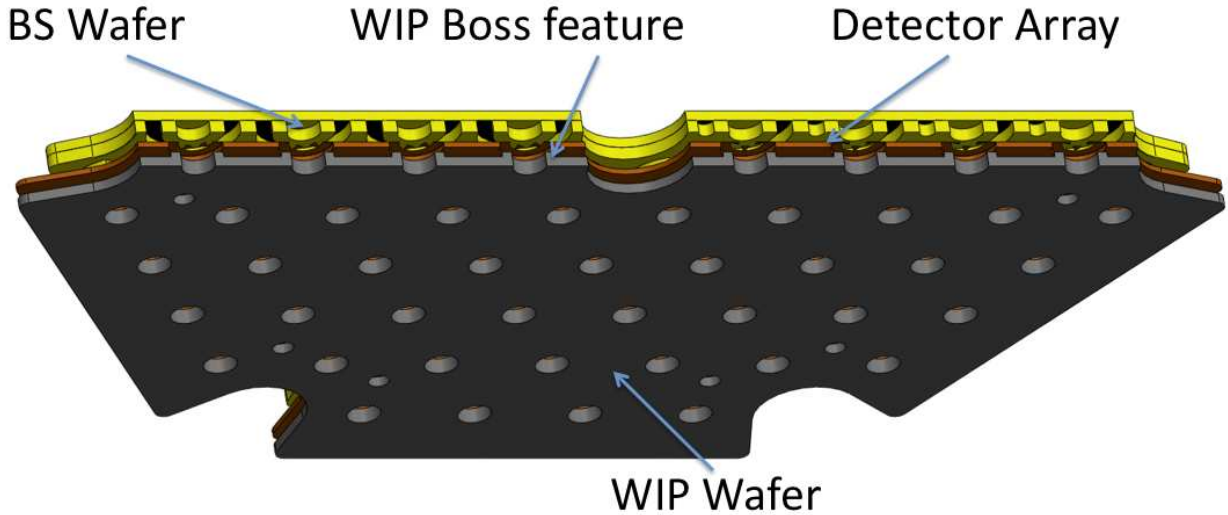


Figure 3.4: Expanded cross-sectional view of the detector wafer sandwich. Boss features in the WIP slip into the back-etched cavities of each pixel OMT, extending the horn waveguide to the OMT and providing pixel-waveguide registration. The BS wafer terminates the waveguides with  $\lambda/4$  backshorts.

have a third TES, which is not connected to the OMT and is therefore a “dark” device. These dark TESs provide diagnostic checks for each array and can be used to test for non-OMT coupling power. Including the dark devices, each array has a total of 173 detectors. There are also two normal resistors on each array, which can be used to determine the array temperature.

Each detector wafer is sandwiched between two ancillary silicon wafers that not only physically protect the detectors, but also help maximize in-band coupling, reduce out-of-band coupling, and minimize optical crosstalk. Figure 3.4 shows an expanded cross-sectional view of the complete detector array sandwich. The first ancillary wafer is a waveguide interface plate (WIP) located between the feed horns and a detector array. The WIP contains  $250 \mu\text{m}$  tall boss features that continue the circular waveguide from the end of the feed horn to within  $25 \mu\text{m}$  of the lower surface of the released pixel OMTs. The boss features neatly register within the back-etched cavities behind the OMTs and along with  $1 \text{ mm}$  wide slip fit alignment pins in the feed horn array provide OMT-waveguide alignment to  $\sim 25 \mu\text{m}$ .

The second ancillary silicon wafer is a  $\lambda/4$  backshort (BS) wafer, shown in Figure 3.5. Not

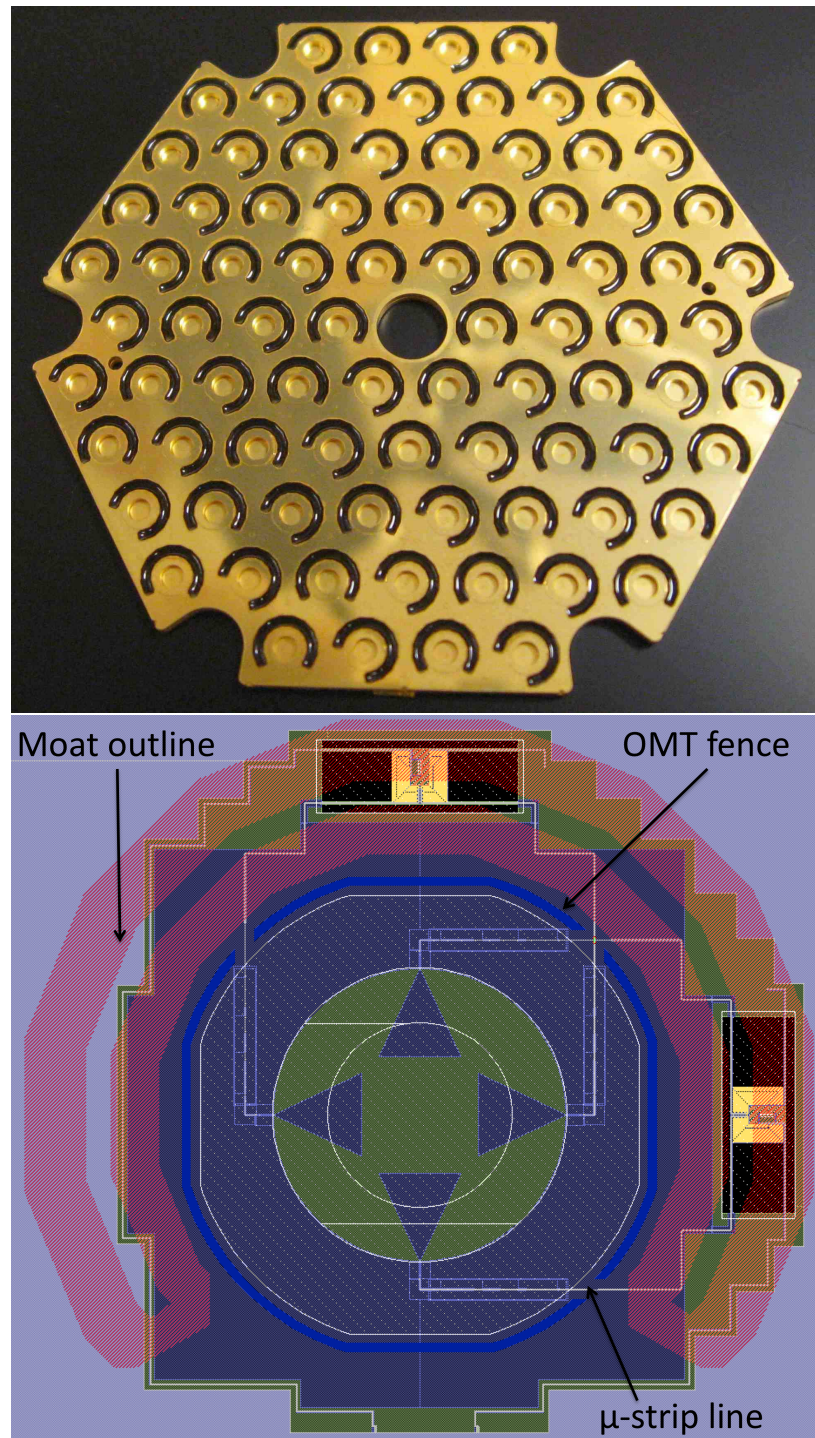


Figure 3.5: (Top) BS wafer with filled moats. The moats alternately rotate by  $45^\circ$  to match the alternating rotations of the pixels. (Bottom) A schematic of the BS moat and OMT fence layout with respect to pixel features. The moats are aligned to be above each TES island, and the OMT fence closes the gap between the detector array and BS array except where microstrip lines are present.

only does the backshort wafer terminate the waveguides, but it also contains eccosorb (76) filled moats positioned above each TES island. During detector development we found that prototype devices had a tendency to absorb high frequency out-of-band power coupling directly to the TES silicon nitride islands (74). This was exacerbated by using on-chip  $\lambda/4$  stub filters to define the bandpass so that no filtering was applied before light coupled through the feed horns. By placing black material above or below the TES islands, however, the amount of out-of-band power picked up by the devices reduced by factors of 2-3. SPTpol pixels use low-pass filters in front of the feed horns to define the band, which removes high frequency out-of-band light. We nevertheless installed the eccosorb moats to absorb any stray non-OMT-coupled light that may regardless find its way to our detectors.

Additionally, the BS wafer rests on top of the detector wafer in the sandwich. To not crush the detectors, it is stood off from the detector array by 25  $\mu\text{m}$  tall silicon dots scattered across the BS wafer. This creates a 25  $\mu\text{m}$  gap between the pixel OMTs and the backshort cavities, which allows light to leak out of the waveguide and couple to the TES's directly instead of through the OMT and microstrip. To reduce this potential source of optical crosstalk, the backshort cavities are surrounded by 25  $\mu\text{m}$  tall silicon fences to close as much of the gaps as possible. The only remaining gaps allow the microstrip underneath to leave the cavity and continue to the devices themselves. Figure 3.5 contains an illustration of the moat geometry and OMT fencing with respect to the pixel layout.

### **3.2.3 Mounting Hardware**

While the feed horn and detector sandwich arrays are both made of silicon, the rest of the focal plane and modules are comprised of copper and aluminum. Since these metals contract  $\sim 20$  times more than silicon when cooling from 300 to 4 K, we need a mounting scenario that prevents fracturing the detector arrays, the feed horns, or both. We use six flexible T-shaped tabs made of invar mounted to the six corners of the feed horn array, shown in Figure 3.6. As the copper mounting components in the module shrink with respect to the silicon upon cooling, the tabs flex to

absorb the size difference. Invar has a linear coefficient of thermal expansion that is only twice that of silicon, a negligible difference over the size scales in question resulting in differential contraction between the invar and silicon of  $< 4 \mu\text{m}$ .

The tabs are permanently adhered to a silicon feed horn array using a thin layer of stycast 2850 (77) on the corner walls of the array. Alignment features in both the feed horn array and the tabs ensure the tabs are installed in the proper position. Prototype tests using copper tabs revealed that differential contraction between copper and silicon produced enough stress in the stycast epoxy to weaken the glue joint, which caused the tabs to fall off upon multiple thermal cycles. We optimized the shape of the invar tabs to reduce stress on the epoxy joint, making the flexible portion 7.4 mm long. While the tab is 0.5 mm thick, the flexible portion of each tab is thinned to 0.4 mm to direct the point of highest stress in the tab away from the epoxy joint. Additionally, the mounting hardware to which the tabs attach is oversized at 300 K. Upon cooling to 4 K, the distance between two opposite tab mounting points equals the width of the feed horn array, so that at operating temperatures where the epoxy is most brittle there is zero flexing in the tabs and negligible stress to the epoxy joints.

While this invar/epoxy configuration proved robust to multiple thermal cycles, the invar-silicon joint must remain intact to ensure pointing and beam properties are consistent throughout an observing season. For additional security, #2-56 threaded invar posts were epoxied into through-holes in each of the six corners of the feed horn arrays, again using stycast as the epoxy. A mounting tab protruding from the invar tabs slips over these threaded mounting posts, is epoxied into place, and a nut screwed onto the post provides vertical pressure. With the added nut-and-bolt mounting, we ensure that even in the unlikely event that one of the lateral epoxy joints fail, the tab is still securely in place. The tabs can be seen installed on a feed horn array in Figure 3.6.

The invar tabs attach to a star-shaped copper mounting ring, shown in Figure 3.7. The ring serves multiple functions in the module. First, it acts as the point to which the invar tabs, and therefore the feed horn array, can mount. The mounting ring shape is designed to provide tool access, both for assembling various components of the module as well as for wire bonding the

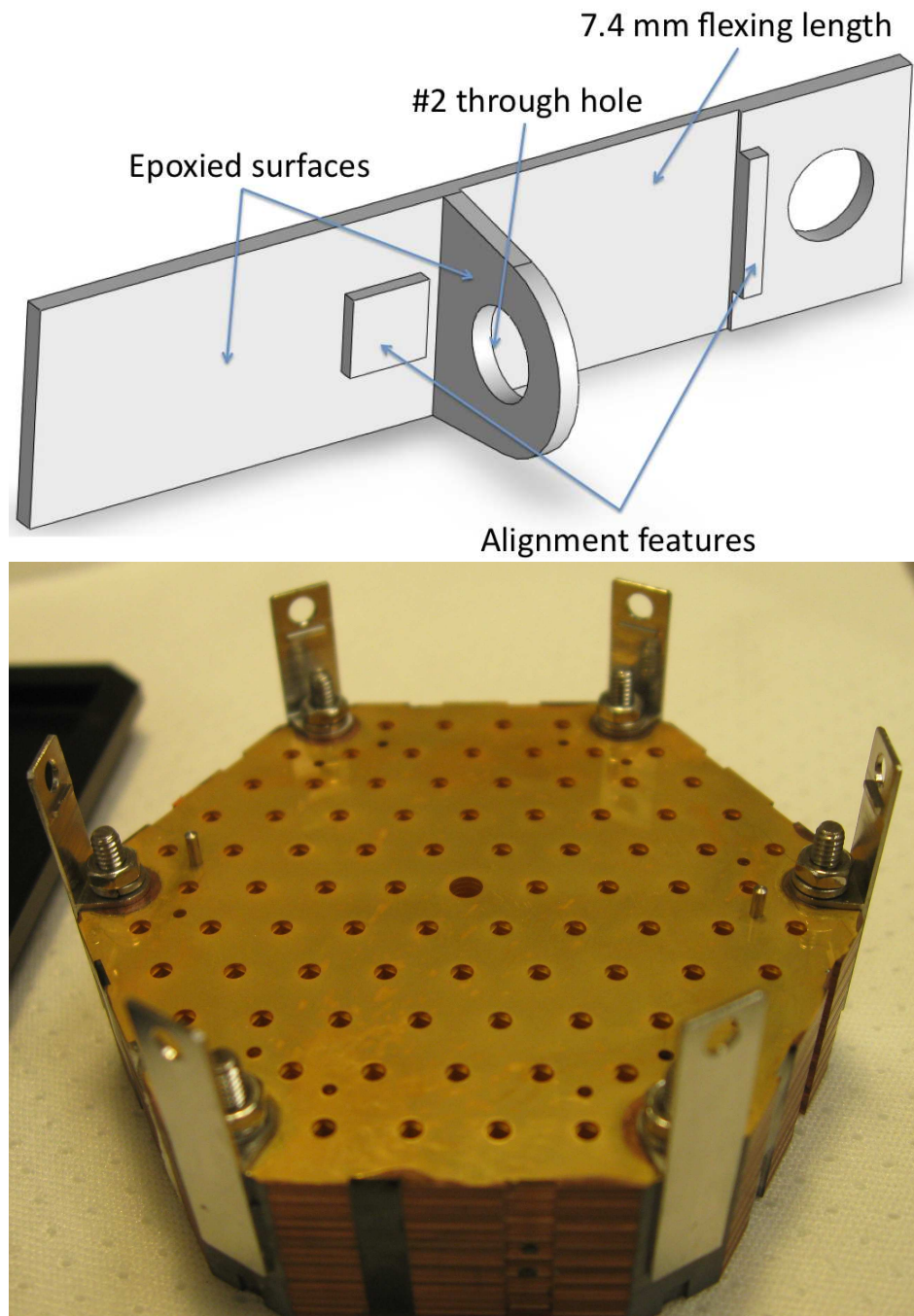


Figure 3.6: (Top) Flexible invar tabs used to connect the silicon feed horn arrays to the metal mounting structures in the 150 GHz modules. Each tab is 0.5 mm thick, while the flexing portion is 0.4 mm thick to reduce stress near the epoxy joint. The flexible portion of the tab, between the registration features, is 7.4 mm long. (Bottom) The tabs installed on a feed horn array prior to module assembly.

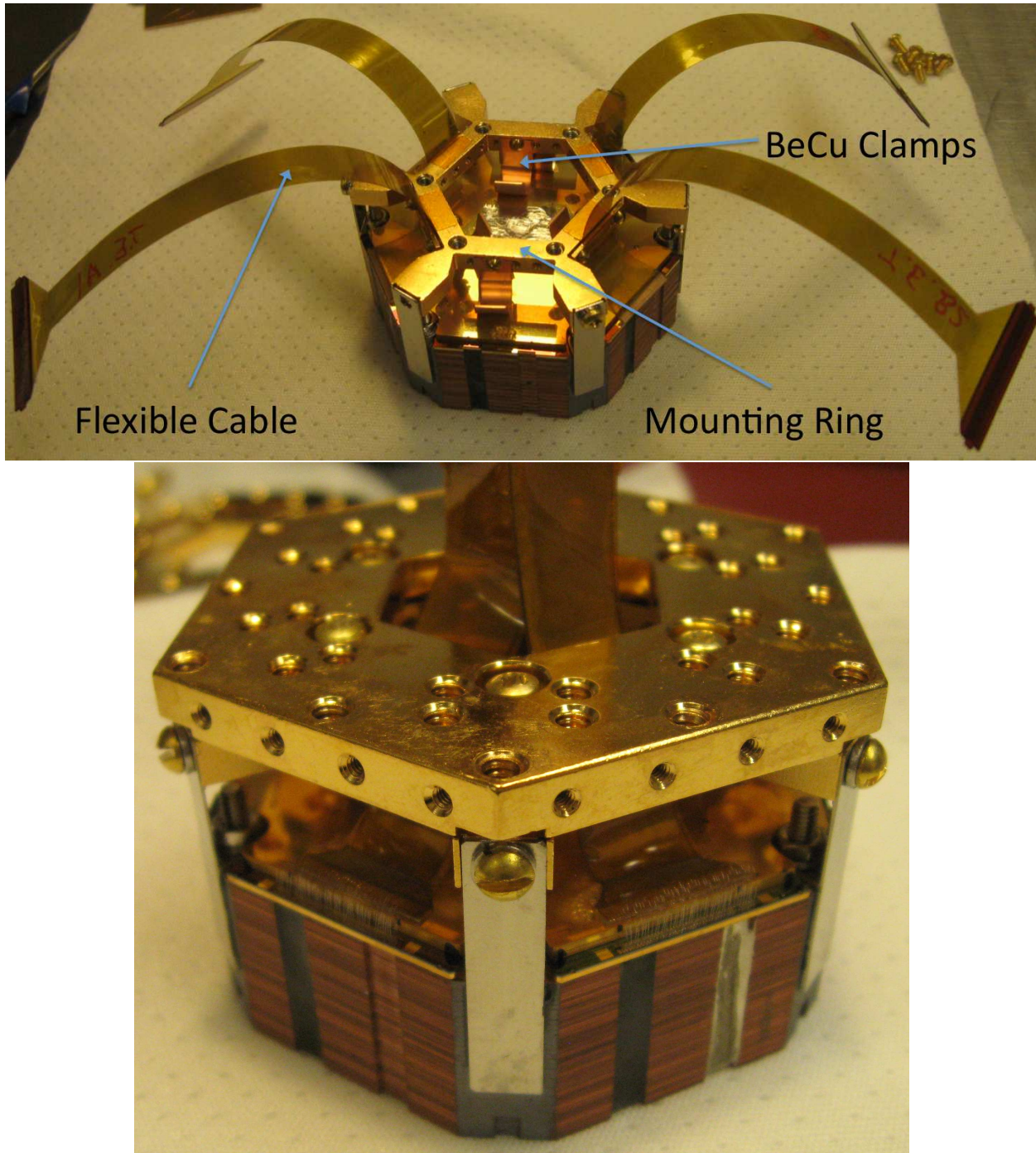


Figure 3.7: (Top) Mounting ring with beryllium copper clamps installed in a module. The invar tabs screw into the six feet in the ring, while four flexible cables are clamped down to the outer walls of the ring. The beryllium copper clamps supply vertical pressure to the detector wafer stack. (Bottom) The interface plate installed on top of the mounting ring with its many mounting holes. The flexible readout cables snake underneath the plate and come out the center of the module.

detector arrays to flexible readout cables (see Section 3.2.5). Each of the six sides of the mounting ring has #0-80 tapped mounting holes, which are used to screw down strain relief bars for the readout cables as well as to hold beryllium copper clips that vertically constrain the detector wafer sandwich. Second, the mounting ring functions as a heat strap between the silicon feed horns and detectors and the focal plane millikelvin plate. The thermal conductivity of invar is three orders of magnitude lower than copper below 1 K, so the invar tabs play an insignificant role in cooling the silicon. Instead, cooling is achieved through the beryllium copper vertical clamps, as well as the RF skirts (see Section 3.2.4) that mount to a copper interface plate which itself attaches to the mounting ring. This interface plate, also shown in Figure 3.7, provides a location for more structure mounting. In addition to the RF shields, the readout board sub-assembly attaches here. The interface plate is also the surface that bolts directly to the focal plane millikelvin plate.

### 3.2.4 RF Shielding

RF light can couple directly to our readout electronics, acting as a source of extra noise in our system. As an independent camera, each module must be RF-tight when installed in the focal plane, only allowing light to enter the module through the feed horns, before which capacitive metal mesh low-pass filters define the upper edge of our observing band and the high-pass filter of the feed horn waveguide defines the lower edge of the band. Having long flexible tabs between the silicon feed horns and metal mounting hardware leaves the sides of the module completely open. To close these large gaps, thin copper skirts shown in Figure 3.8 attach to the sides of the interface plate and come down the length of the module, to roughly a half inch from the top of the silicon feed horn array.

These RF skirts also act as a mechanical shield for the delicate wire bonds on the detector wafers, only a few millimeters away from the edge of the feed horn array. Aluminum tape seals the small gaps left between the skirts, adhering to the sides of the feed horn array. Figure 3.8 shows a complete module assembly, with RF skirts installed and aluminum tape applied. Since the feed horns are metal-plated, there is a contiguous conducting surface all the way from the feed horn

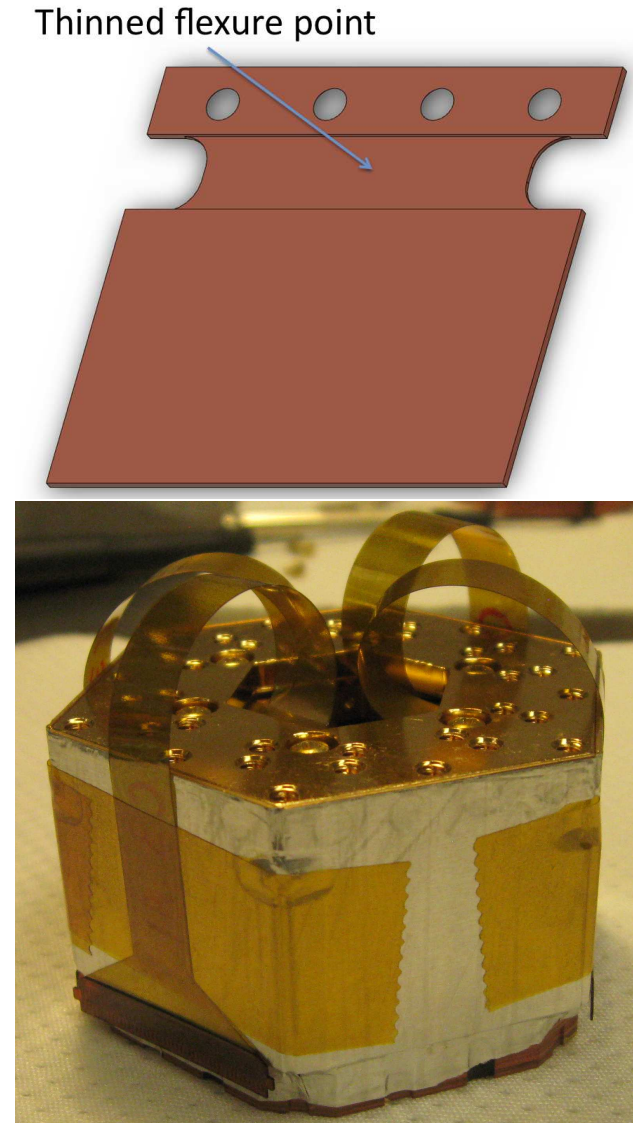


Figure 3.8: (Top) Image of RF skirts, showing flexure portion. (Bottom) Skirts installed with final RF tape applied as the module is prepared for shipment to the South Pole.

apertures to the focal plane millikelvin plate when the module is installed ensuring light can only enter the system through the feed horns.

As mentioned previously, the RF skirts also cool the silicon feed horn and detector arrays. The interface plate to which the skirts attach is the same width as the silicon arrays at 300 K. As the module cools, the interface plate shrinks with respect to the silicon array. The differential

contraction squeezes the RF skirts tighter against the walls of the feed horn array, which provides pressure points through which to cool the silicon. Too much pressure on the silicon from the skirts could chip or crack it, however. To avoid this outcome, the RF skirts have a horizontal band across them that has been thinned to act as a flexure point, reducing the total pressure on the feed horn array while allowing the skirts to supply enough pressure to effectively cool the silicon.

### 3.2.5 Passive Readout Electronics

To reduce loading on the millikelvin stage, the detectors are read out with a digital frequency-domain multiplexing (DfMUX) readout system (75). In a frequency-domain system, each detector is placed in series with an inductor  $L$  and capacitor  $C$  making an  $RLC$  resonance circuit. We AC bias many detectors simultaneously with a “comb” of bias frequencies sent along a single pair of wires. Given the  $L$  and  $C$  in series with a detector, each detector only sees the bias tone to which its resonance circuit is tuned. The signals are then sent to a series array of 100 superconducting quantum interference devices (SQUIDs) followed by a low-noise amplifier cooled to 4 K, which together amplify the detector signals. The SPTpol DfMUX system uses a multiplexing factor of  $12\times$ , so 12 detectors (6 pixels) are biased with one set of wires and one SQUID series array.

While the SQUID arrays are cooled to 4 K, the passive  $LC$  resonance circuits reside with the detector arrays and are therefore cooled to  $\sim 270$  mK. Printed circuit boards containing inductors and capacitors that define the resonance frequency of each detector ( $LC$  boards) are connected via aluminum supports to the 150 GHz modules. Each board has 12 photolithographed chips of eight  $22\ \mu\text{H}$  inductors fabricated at NIST-Boulder, as well as capacitors stacked to achieve the requisite capacitance. Therefore, each board can define the resonance frequencies for up to 96 different detectors. In practice, only 90 channels on each of two  $LC$  boards are needed to define the resonance channels for all the detectors in a single 150 GHz module.

To protect the delicate inductor chips and wire bonds connecting them to the circuit boards, thin aluminum shields are placed over the  $LC$  boards. Since the fiberglass body of the circuit board is black at infrared wavelengths, the aluminum shields also reduce the surface area of the boards

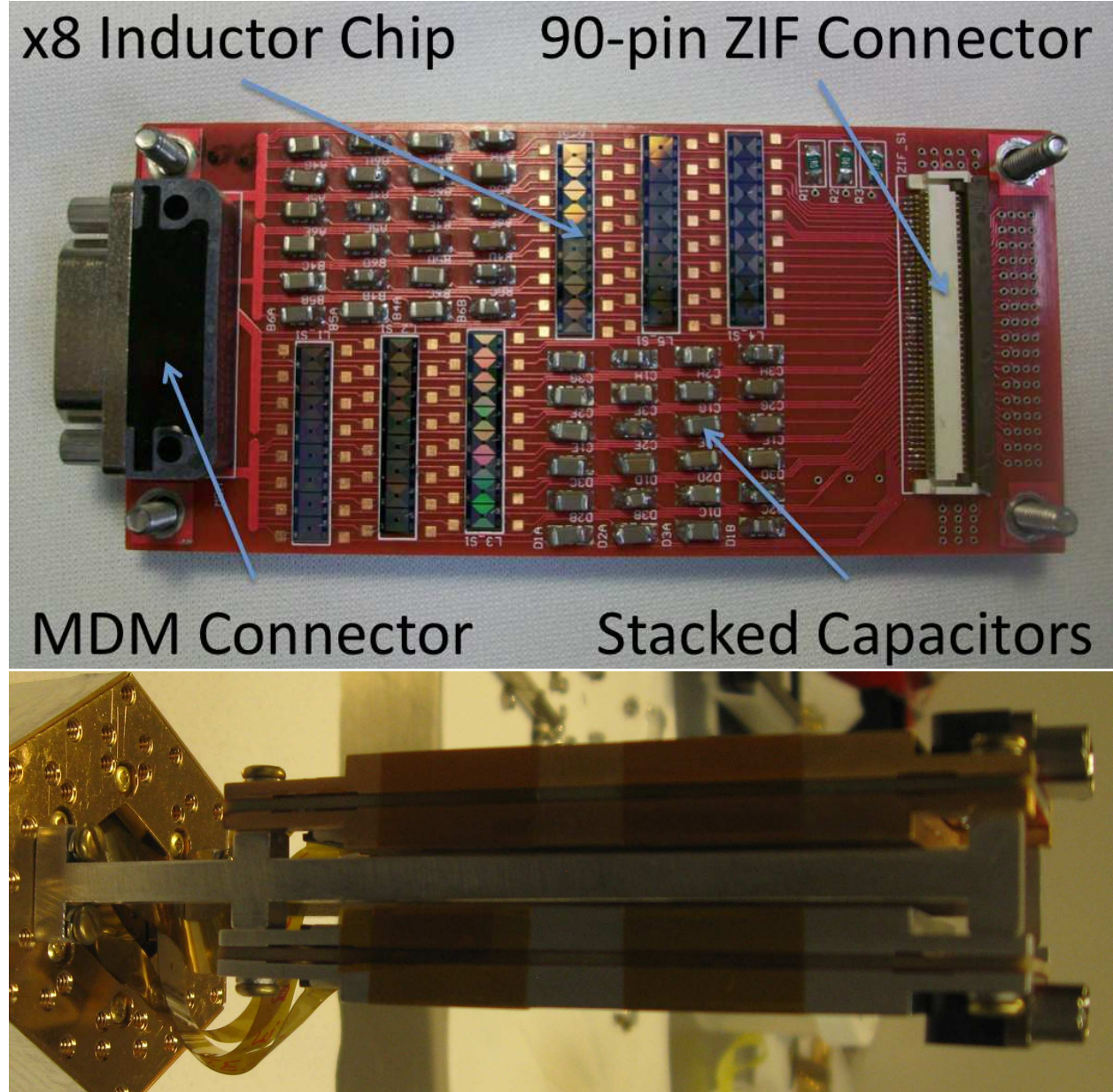


Figure 3.9: (Top) Populated LC board. (Bottom) Two LC boards with protective shielding in place and mounted to a module.

that could otherwise terminate warm stray light in the experiment cryostat, reducing the parasitic heat load on the millikelvin refrigerator.

The *LC* boards are physically displaced from the detector arrays by several inches in each module. To bridge the gap, we use the flexible circuit cables mentioned previously. The cables contain 90 copper traces printed on a polyimide substrate, which are 47  $\mu\text{m}$  wide and have 94  $\mu\text{m}$  center-center pitch. The traces are tinned to be superconducting to reduce parasitic resistance in the *RLC* circuits. A final polyimide overlay layer protects the traces and reduces the chance of electrical shorts between the cables and module hardware. The cables are rubber cemented into position and strain-relieved with clamping bars. One end of the cable has a series of bare copper bond pads. We wire bond from the detector array bond pads to the flexible cable pads using 25  $\mu\text{m}$  thick aluminum bonding wire. The other end of the flexible cable has 90 zero-insertion-force (ZIF) contacts. This end of the cable is then easily attached to an *LC* board by plugging into a ZIF connector on the board. Two cables plug into each *LC* board, which are populated on both the front and back sides.

### 3.3 Dark Properties

Several detector properties can be obtained by measuring the current through a device as a function of applied voltage bias (an *IV* curve)(58; 74). Please refer to the cited references for examples of this measurement technique. Lab observations of device IV curves provided measurements of dark properties for five of the seven deployed detector arrays. We also fitted the width and height of detector *RLC* resonance peaks above and below device superconducting transitions to obtain normal resistances  $R_N$  and parasitic resistances in series with detectors, respectively. There are systematics at the level of 10-20% for these resonance fits due to calibration uncertainties in the lab, however devices observing the sky can be well calibrated to a celestial source. Table 3.1 contains a summary of the results for each wafer. Means and standard deviations are provided, as well as the number of detectors measured. Normal resistances and measured saturation powers are corrected for in-series parasitic resistance, and only devices with both *RLC* resonance fits and

Table 3.1: Detector Dark Properties

Wafer	$T_c$ (mK)		$R_N$ ( $\Omega$ )		$P_{\text{sat}}$ (pW)	
C1	$476.8 \pm 2.0$	87	$1.1 \pm 0.1$	76	$20.9 \pm 3.8$	74
C3	$463.3 \pm 7.1$	132	$1.2 \pm 0.2$	134	$19.6 \pm 2.4$	134
C4	$467.1 \pm 3.2$	114	$1.2 \pm 0.2$	123	$21.4 \pm 2.5$	122
C5	$467.6 \pm 2.2$	131	$1.2 \pm 0.2$	131	$21.0 \pm 3.0$	131
D4 Low	$478.2 \pm 34.0$	48	$1.3 \pm 0.3$	48	$19.9 \pm 2.4$	48
D4 High	$538.9 \pm 32.3$	76	$1.0 \pm 0.1$	76	$34.9 \pm 4.3$	76
Avg (No D4 High)	$468.9 \pm 12.4$	512	$1.2 \pm 0.2$	512	$20.6 \pm 2.9$	509
Avg (With D4 High)	$478.0 \pm 28.6$	588	$1.2 \pm 0.2$	588	$22.5 \pm 5.7$	585

**Notes:** Summary of in-lab detector dark tests for five of the seven deployed detector wafers. Wafer D4 has a clear bimodal distribution in device properties and has been split into “D4 Low” and “D4 High.” Means and standard deviations are given as well as the number of devices tested for each wafer and property.

*IV* curve measurements are included. Four of the wafers show good uniformity in superconducting critical temperature  $T_c$ , normal resistance, and saturation power  $P_{\text{sat}}$ . Wafer D4, however, does have a clear bimodal distribution of devices, split into “Low” and “High” columns based on whether devices have saturation powers above or below 25 pW. Disregarding the “High” outlier distribution in wafer D4, the average dark properties across the five lab-tested arrays are  $T_c = 468.9 \pm 12.4$  mK,  $R_N = 1.2 \pm 0.2 \Omega$ , and  $P_{\text{sat}} = 20.6 \pm 2.9$  pW. Including all measured devices on the five arrays the averages are  $T_c = 478.0 \pm 28.6$  mK,  $R_N = 1.2 \pm 0.2 \Omega$ , and  $P_{\text{sat}} = 22.5 \pm 5.7$  pW.

During detector development, early device designs exhibited high values for  $\alpha = d \log R / d \log T$ , a dimensionless ratio that quantifies the sharpness of a device’s superconducting transition. Higher values for  $\alpha$  means a device is more sensitive to changes in temperature, (the loop gain of the device is proportional to  $\alpha$  in the device transition), but also means the device can become unstable when biased too deep in the transition. Indeed, our early devices were unstable at operating bias points of  $\sim 0.8 R_N$ , near typical operating points for our 150 GHz detectors (51). We tested several TES geometries to find an appropriate transition shape and deposited a non-superconducting metal, palladium gold (“bling”), around each TES to increase the detectors’ time constants. We found that having a solid bar for the TES and extending the bling over the edge of the microstrip leads

heading to the TES and into the TES region itself lowered  $\alpha$  sufficiently while keeping 150 GHz detector loop gains in transition at an acceptable level. A companion paper (59) discusses SPTpol 95 GHz pixel development and provides further detail about how the TES geometry affects  $\alpha$ .

### 3.4 Optical Properties

Before integration into 150 GHz modules, we measured the return loss and insertion loss for each silicon feed horn array at 300 K. Representative results for one feed horn array are provided in Figure 3.10, where measurements for six separate horns are overplotted. All horn arrays show return loss of  $< -20$  dB at 300 K except for the frequency range 133-138 GHz. The dashed line in the return loss plot represents the expectation for the feed horn profile only, not including the square to circular waveguide section, which is known to have a return loss of  $\sim -20$  dB. The insertion loss at 300 K is in the middle plot of Figure 3.10 and is  $\sim -0.2$  dB  $\simeq 5\%$  on average.

Figure 3.10 (Right) shows pre-deployment 150 GHz VNA measurements of one representative feed horn. Dots are measurements of the H-plane, E-plane, and cross-polarization, while solid lines are expectations from simulations. The beam power drops below -20 dB at  $\sim \pm 40^\circ$  from the beam center, and cross-polarization power is below -25 dB. Measured beams of the detectors as deployed on the telescope also appear nominal, with an average full width half maximum (FWHM) of 1.06 arcminutes and beam eccentricity of  $e = 0.04$  for the 150 GHz pixels (51).

Optical efficiency measurements were taken for a small subset of detectors prior to SPTpol deployment. Using a set of metal mesh capacitive low-pass filters to define the upper edge of our bandpass, we illuminated the detectors with radiation from a cold load set to several temperatures between 4 and 30 K. The measured difference in power compared to the expected in-band power gives the detector plus feed horn optical efficiency (74). These measurements indicated detector optical efficiencies of  $\sim 90\%$ .

We measured the electrothermal time constants of many devices in the lab at various points in their superconducting transitions. We apply an AC voltage bias of frequency  $\omega$  to a detector just as we would in standard operation, but also apply additional voltage bias at a second bias

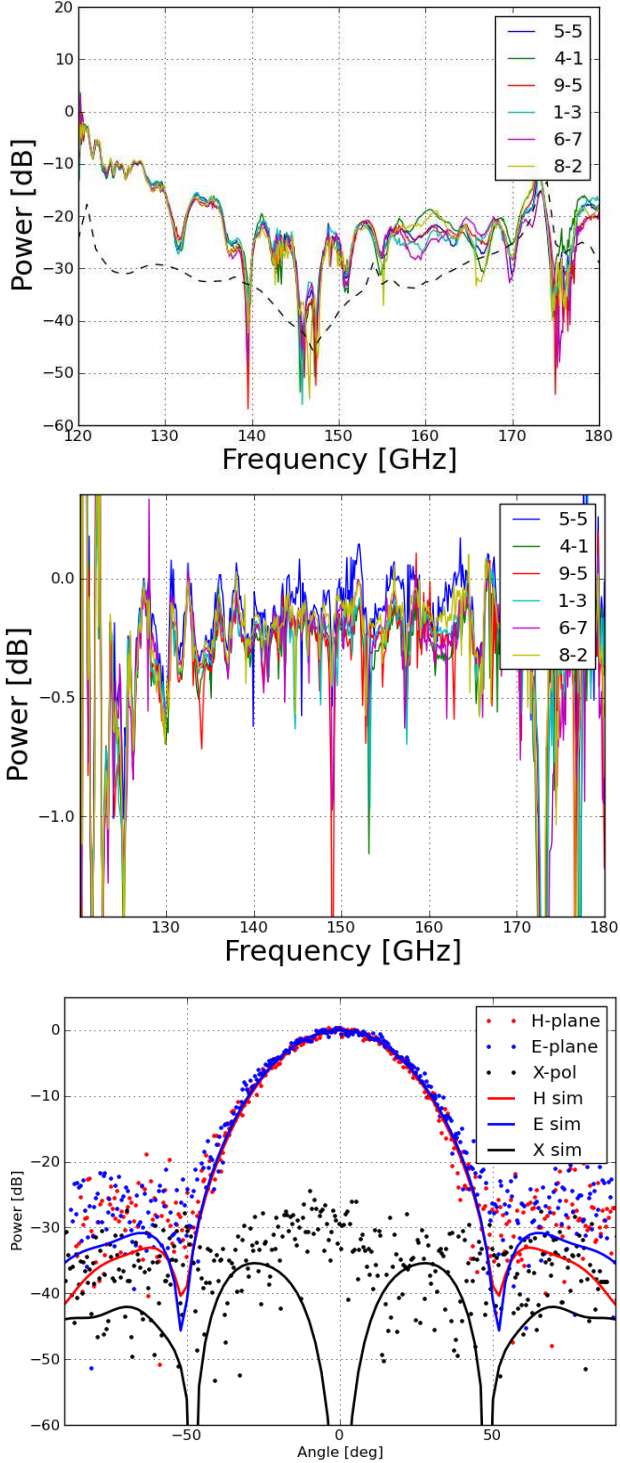


Figure 3.10: (Top) Return loss for six horns in one SPTpol feed horn array. Dashed line is the expectation for the feed horn profile only. (Middle) 300 K insertion loss measurements of the same horns. (Bottom) Beam profile at 150 GHz for one representative horn. Dots are measurements while solid lines are expectations from simulations.

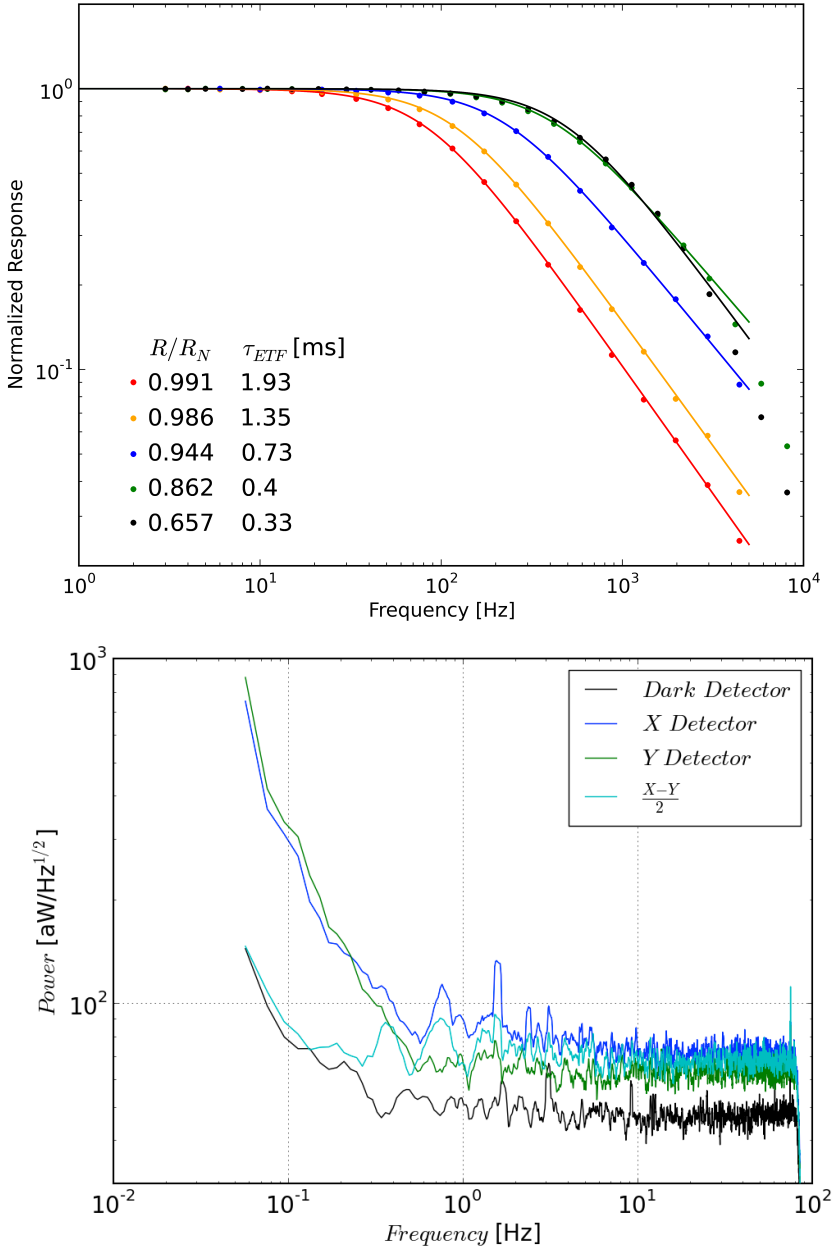


Figure 3.11: (Top) Measurements of the electrothermal time constant of one representative detector at several points in its superconducting transition. Devices exhibit time constants  $< 1$  ms at nominal operation points. (Bottom) Power spectral densities (PSDs) for three devices in the same 150 GHz pixel. “X” and “Y” are optically loaded while the “Dark” device is not coupled to the sky. All three device PSDs have white noise levels consistent with expectations. The PSD of the differenced timestreams of the optically loaded devices shows a much reduced  $1/f$  knee.

tone  $\omega + \delta\omega$ , which amplitude-modulates the detector response. The output current amplitude at the negative sideband  $\omega - \delta\omega$  (where no external voltage is applied) is a pure measurement of the electrothermal response of the device (78). We plot the response as a function of  $\delta\omega$  and fit a single pole to the data, which gives us the time constant of the device. A representative plot of electrothermal time constant measurements is shown in Figure 3.11. These measurements are taken several times when the device is biased at different points in its transition. Across the arrays the electrothermal time constants are generally  $< 1$  ms while in the superconducting transition.

We have also measured detector noise between field observations while on the telescope. Figure 3.11 shows the noise for three detectors in a single representative 150 GHz pixel. Detectors “X” and “Y” are optically coupled and looking at the sky, while the “Dark” detector is not optically active. Given in-lab calibration factors with systematics at the 10 - 20% level, the white noise levels of all the devices are consistent with expectations,  $47 \text{ aW}/\sqrt{\text{Hz}}$  with no optical loading and  $76 \text{ aW}/\sqrt{\text{Hz}}$  with nominal optical load. Additionally, differencing optically loaded detector timestreams removes correlated long timescale atmospheric fluctuations. As a result, the power spectral density of the differenced timestreams shows a significant reduction in the  $1/f$  knee, increasing the frequency range that can be used for extracting relevant science.

## Chapter 4

### Observations and Data Products

The SPTpol receiver was installed in January 2012 and with the exception of two brief maintenance periods has been observing continuously ever sense. In this short chapter we describe the observational strategies used during the 2012 and 2013 seasons and define related nomenclature to orient the reader for a detailed discussion of data analysis in the following chapters. We begin by discussing the structure of a single CMB field observation and required ancillary calibration measurements. We then describe 2012 observations in particular, followed by a similar explanation for 2013 measurements. The chapter concludes with a short note on the average observing efficiency so far obtained by SPTpol and which datasets will be used in the following cosmological analysis.

#### 4.1 CMB Field Observations

The CMB polarization anisotropies of interest are at an amplitude of a few  $\mu\text{K}$  and lower. Since current detectors are background noise-limited (their intrinsic noise is less than the Poisson noise of the background sky signal) the only options at our disposal to increase signal-to-noise are to measure the sky with more pixels and for longer periods of time. While the signal-to-noise of a single observation is low, by stacking or *coadding* thousands of observations of a single patch over several years the noise averages down and the small-amplitude sky signal of interest becomes evident.

The primary unit of this coadding process is a single CMB field observation. Since bolometers are sensitive to *changes* in incident power, during one such observation the SPT maps a patch of

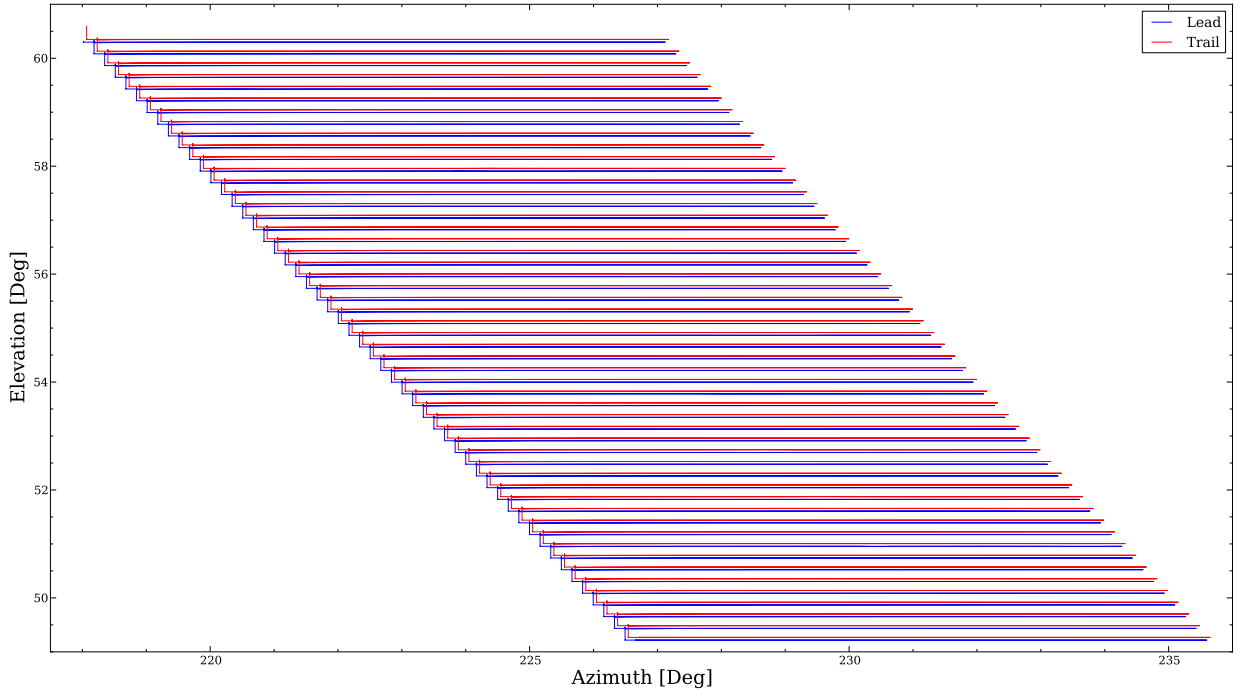


Figure 4.1: Azimuth and elevation coordinates for a single CMB field observation. The telescope starts at low elevation and scans right and left before taking an elevation step and repeating. The field is split into “lead” and “trail” halves, which are forced to match in azimuth for removal of ground contamination. Lead and trail coordinates have been offset by  $0.05^\circ$  in azimuth and elevation for clarity.

sky by continuously raster scanning. At constant elevation the SPT scans right and then left. We refer to these as *right-going* and *left-going* scans. After a right/left scan set, the telescope makes a small step in elevation and observations continue. When the telescope reaches the top of the defined CMB field it returns to a lower elevation to start a new observation. Given pixel spacing on the focal plane and the size of each elevation step, a single CMB field observation does not obtain uniform elevation coverage. To fill in the resulting coverage gaps, observations begin at a number of slightly different elevations or *dither steps*. By combining observations at each dither step, a single uniform-coverage observation or *bundle* can be defined. The azimuth and elevation coordinates for a single CMB field observation are plotted in Figure 4.1.

There are potentially large polarized systematic signals related to features on the static

ground surrounding the telescope. Since these systematics can potentially dwarf the small CMB polarization signal, our scan strategy includes methods to mitigate such ground pick-up. The CMB field is divided into two patches, a “lead” patch and a “trail” patch. We observe the lead patch for 35 minutes, during which the sky rotates by 35 minutes of Right Ascension (5 degrees on the sky in the center of the patch). By this point the trail patch has caught up in azimuth and we begin observations again. With this lead-trail strategy, both halves of the CMB field are observed over exactly the same patch of ground. By subtracting the lead map from the trail map we remove any systematic signal from the ground. While this analysis method impedes our ability to *image* particular features in CMB temperature and polarization anisotropies, the *statistical* properties in both patches should remain the same. A power spectrum analysis such as that described in the following chapter would therefore yield the same statistical information without the ground signal contaminant.

This observation and analysis strategy is attractive from the standpoint of controlling systematics, but it has significant downsides. The resulting power spectra have higher sample variance since the effective area on the sky being analyzed is reduced by a factor of two. Furthermore, the final map depth is  $\sqrt{2}$  shallower since the same observing duration is spent on twice the area. The option to perform a lead-trail analysis is therefore reserved for situations when ground pick-up is expected or indeed measured when cleaning CMB field maps. Please refer to Section 5.5 for more details about map cleaning and validation. We *do not* perform a lead-trail analysis in this work, however field observations were nevertheless observed in the lead-trail fashion described above.

Besides the CMB field observations themselves, several ancillary observations are also periodically made for calibration purposes. Approximately once every fridge cycle ( $\sim 36$  hours), the magnitude and direction of tilt of the telescope azimuth bearing axis is measured with tilt meters. This is needed for telescope pointing corrections discussed in the following chapter. Also once per fridge cycle the entire focal plane is scanned across RCW38 and MAT5A, two HII regions in the Milky Way. The temperature of RCW38 at millimeter wavelengths is well known and we use these

observations to calibrate and convert our detector measurements from current to units of K<sub>CMB</sub>.<sup>1</sup> MAT5A observations are also part of our pointing corrections. Between CMB field observations we take short RCW38 measurements, where only a fraction of the focal plane passes over the source. These “very fast” scans are used for tracking short-term changes in telescope pointing. Periodic measurements of a chopped thermal source behind the secondary mirror (known as the calibrator) as well as “elevation nods” are used to interpolate detector calibrations between RCW38 observations and to measure the change in detector sensitivity as a function of elevation, respectively. Finally, observations with the telescope not moving, called noise stares, are also periodically taken to determine the noise properties of each detector while in operation.

## 4.2 2012 Observations

During the 2012 observation season, from roughly February to late November, we focused efforts on obtaining a deep map of a relatively small patch of sky. This field, centered at RA23h30DEC-55, is referred to in this work as the SPTpol *deep field* or sometimes the “2012 deep field.” The patch was designed to be only 100 deg<sup>2</sup> on the sky. While a small area such as this results in significant sample variance in a power spectrum analysis, the focus of these observations was a statistically significant detection of lensing *B* modes. Lensing *B* modes peak at multipoles  $l \sim 1000$  and so a potential detection benefits from a deeper map more than a wider map. Indeed, the SPTpol collaboration published the first detection of lensing *B* modes using data from the 2012 deep field observations (21). Cross-correlating with HERSCHEL-SPIRE measurements, which trace large-scale structure that gravitationally lenses passing CMB *E*-mode polarization into lensing *B* modes, we found evidence for *B* modes in our deep field map inconsistent with zero amplitude at 7.7  $\sigma$ .

---

<sup>1</sup> All temperatures reported or plotted in this work are implicitly in K<sub>CMB</sub>. We measure changes in CMB intensity *B* and we report these changes as temperature fluctuations K<sub>CMB</sub> of a 2.73 K blackbody. The conversion factor between intensity and temperature is just the derivative of the blackbody function  $\frac{dB}{dT}$  evaluated at 2.73 K.

### 4.3 2013 Observations

After our positive detection of lensing  $B$  modes, observations changed focus to placing tighter constraints on the tensor-to-scalar ratio  $r$ . Since IGW  $B$  modes peak at low multipoles, we now wanted to map a larger area of sky to beat down sample variance errors. In 2013 we switched to observing the SPTpol *survey field*, centered at RA0H30DEC-57.5. The survey field is 500 deg<sup>2</sup> and completely overlaps the deep field. We continued to observe in lead-trail mode. Since the lead and trail halves are wider in the survey field, we increased the azimuth scan speed of the telescope in order to ensure the lead and trail halves completely overlapped in azimuth. The faster scan speed was also meant to force interesting science signals to appear in our data at higher frequencies and therefore further away from intrinsic low-frequency noise in our system and detectors. This allows us to study lower multipole modes otherwise buried in instrument noise. A short discussion of choosing this so-called “science band” and how it related to scan speed is given in Appendix A.

### 4.4 Datasets

We cannot observe the deep and survey fields with 100% efficiency. Downtime occurs for regular telescope maintenance during the austral winter as well as for significant periods during the summer season when telescope and receiver repairs and upgrades take place. Additionally, after the reserves of liquid helium have boiled off in the mK fridge during normal operation, the fridge must be cycled to re-condense liquid helium and re-cool the receiver to base temperatures. This takes several hours every roughly 36 hours. Finally, periodic calibration measurements discussed above must take place to correctly interpret CMB field data.

A total of 809 days elapsed between SPTpol first-light on January 27, 2012 and April 15, 2014. In that period, 45.4% of the total available time was spent observing CMB fields. During austral summer months when the Sun is in the SPTpol deep and survey fields, secondary CMB fields are measured to look for new galaxy clusters. Of the 367.4 days of integration time on CMB fields, 39.1% (37.3%) of it has been spent on the deep (survey) field. A further 148.8 days of integration

Table 4.1: SPTpol Observing Breakdown: January 27, 2012 - April 15, 2014

Target	Integration Time [Days]
<b>CMB Fields</b>	
RA23H30DEC-55 (Deep Field)	143.8
RA0HDEC-57.5 (Survey Field)	137.0
RA5H30DEC-55	31.4
RA23HDEC-35	16.6
RA1HDEC-35	10.8
RA3HDEC-35	6.9
RA5HDEC-35	9.8
RA3HDEC-25	11.1
<b>Astronomical Sources</b>	
RCW38	41.0
MAT5A	21.6
CEN A	15.4
OTHER <sup>(a)</sup>	4.6
<b>Auxiliary Sources</b>	
CALIBRATOR	36.0
EL NODS	10.1
NOISE STARES	9.7
POLCAL	10.3

**Notes:** 809 days elapsed between SPTpol first-light and April 15, 2014. 516.2 days of integration time has been spent on observations, which is broken down by target above.

<sup>(a)</sup> Other includes Venus, Mars, and the Moon used for beam measurements.

time have been spent observing calibration sources. Table 4.1 summarizes how observation time has been spent since first-light.

As Table 4.1 demonstrates, a wealth of data, both cosmological and astrophysical, has been obtained with the SPTpol receiver. The cosmological analysis presented in this work focuses entirely on the 150 GHz 2012 deep field observations. While intermediate analysis products for 2013 data are often used as examples in the following chapters, *they are not included in the final cosmological constraints presented in Chapter 7*. A future cosmological analysis is underway that considers the first year of survey field observations, however, which we briefly discuss in Chapter 8.

## Chapter 5

### Data Reduction: From Timestreams to Power Spectra

In this chapter we discuss data reduction and analysis techniques used to process SPTpol observations into maps and power spectra. Enormous information compression takes place, transforming  $\sim 10^{12}$  detector time samples over the course of one observing season into  $\sim 10^2$  numbers encoding the CMB temperature and polarization power spectra. We begin the chapter by describing detector timestream filtering and cleaning. The chapter proceeds with a discussion of map-making and additional filtering steps made at the map-level. We next describe the generation of biased power spectrum estimates from the processed maps, which is followed by a discussion of unbiased power spectrum estimation via the MASTER algorithm. The chapter concludes with a description of map and power spectrum validation through jackknife null tests.

#### 5.1 Timestream Processing

Over the course of an observing season, we record  $\sim 10^{12}$  bolometer samples from the 1536 optically sensitive detectors in the SPTpol receiver in the form of time-ordered-data (TOD). TOD, otherwise known as timestreams, record the electrical current supplied to a bolometer to maintain a specified bias point in its superconducting transition as a function of time. As a bolometer scans over a bright point source, for example, additional optical power from the sky is incident on the detector, requiring less electrical power to maintain the detector bias point. Therefore, additional optical power presents itself as a negative dip in bolometer timestreams. We provide an example timestream of a bolometer observing the HII region RCW38 in Figure 5.1.

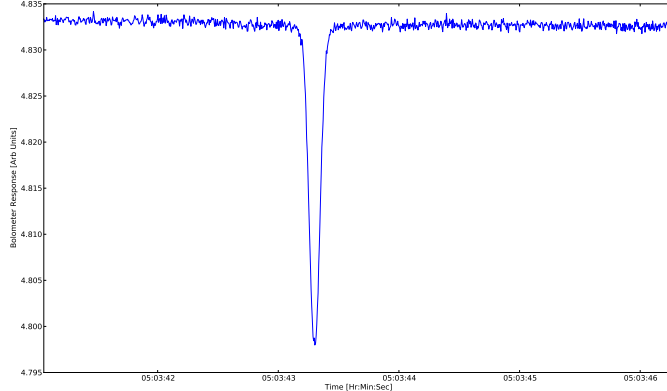


Figure 5.1: Example bolometer timestream as a detector scans across the center of RCW38. Additional optical power from the source reduces the requisite electrical power to keep the detector biased at the same point in its transition, causing the source to manifest as a drop in readout current.

The raw timestreams are calibrated to be in units of  $K_{CMB}$  by calculating bolometer gain or responsivity (response per degree Kelvin) using a combination of regular observations of RCW38 and calibrator stares. At the beginning of each fridge cycle (roughly every 36 hours), each bolometer scans across RCW38 to obtain current bolometer gains. Bolometer responsivity is a function of detector bias point and therefore of optical loading levels and thus changes with weather and elevation. During a fridge cycle, we make regular calibrator stares: the bolometers observe a hot thermal source behind the secondary mirror of the telescope. Light from the calibrator is fed via light pipe through a hole in the mirror. By monitoring changing responses to the calibrator we can interpolate bolometer gains between RCW38 observations. Additionally, periodic elevation nods are taken where the telescope makes small dips in elevation. These dips change the airmass we look through and therefore the atmospheric loading on the bolometers, which provides a measure of bolometer gain versus elevation.

Since polarization is a differential measurement between two detectors, *relative* gain mismatch between two detectors in a polarization-sensitive pixel can leak temperature into polarization. For example, if the gains between two bolometers are changing too rapidly to be accurately interpolated

over given the cadence of calibrator observations, a significant  $1/f$  noise component will remain in the differenced timestream reducing sensitivity to low-multipole modes in resulting maps. For the work presented here, where the signal-to-noise in the  $TE$  and  $EE$  spectra at relatively low multipoles  $l \sim 500$  is high, map noise is sub-dominant to sample variance and therefore the effects of relative gain mismatch are neglected. It will become a focus of attention in future  $BB$  spectra analyses, however, when placing constraints on primordial  $B$  modes from inflation where the sample variance is more than an order of magnitude smaller.

### 5.1.1 Timestream Filtering

Before mapmaking, timestreams are lightly filtered to reduce computational needs and remove several contaminating signals. Bolometer TOD are recorded at  $\sim 191$  Hz, which represents modes on the sky far smaller than our beam. We down-sample the timestreams by a factor of four to reduce memory and computational requirements. To avoid high-frequency noise aliasing into the SPTpol science band ( $\sim 1 - 3$  Hz) we low-pass filter the timestreams at a frequency corresponding to a multipole moment of  $l = 10,000$ . The low-pass frequency is different for each bolometer timestream as it depends on the angular velocity on the sky and therefore telescope elevation. See Appendix A for details.

To remove low-frequency noise from the atmosphere and the instrument itself, each timestream is effectively high-pass filtered by removing a fourth-order Legendre polynomial fit on a per-scan basis (one left- or right-going scan at a single elevation step). If a bolometer scans over a point source brighter than 50 mJ (at 150 GHz) during the scan then TOD taken within  $5'$  of the point source is masked from the fit. For the angular extent of a single scan during 2012 observations, a fourth order polynomial subtraction equates to  $1.3^\circ$  on the sky per degree of freedom in the fit.

Finally, we Fourier transform the timestreams and obtain their power spectral densities (PSDs). Spectral lines corresponding to harmonics of the pulse tube cooler frequency of 1.53 Hz are notched and the timestreams are inverse Fourier transformed. We also save the integrated PSD power in several bands to be used during mapmaking for inverse variance weighting the

timestreams.

### 5.1.2 Absolute Telescope Boresight Pointing

During observations the antenna control unit uses an “online” pointing model to roughly track a source or a field of interest to within a few arcminutes RMS from observation to observation. For full-season coadds, however, we require sub-arcminute RMS pointing to maintain sensitivity to small-scale features and/or point sources at multipoles out to  $l \sim 10,000$ . Thus, during data analysis we re-calculate the absolute telescope pointing using an “offline” pointing model. Offline pointing corrects for a series of effects on the raw telescope boresight azimuth and elevation achieving RMS pointing of  $12''$  averaged over a full observing season.

The offline pointing model contains ten parameters that define corrections to the telescope’s azimuth and elevation during an observation:

$$\begin{aligned}\delta az &= (a_2 \cos az + a_3 \sin az) \tan el + (a_4 - det) \tan el + \frac{a_5}{\cos el} \\ \delta el &= a_0 \sin el + a_1 \cos el - (a_2 \sin az - a_3 \cos az) - a_6 - del - \theta_{\text{refr}}.\end{aligned}\quad (5.1)$$

Below we describe what each parameter is, the size of the correction it makes, and how we determine the parameter.

- **$a_0, a_1$ :** Amplitude of telescope boom flexure due to gravity. Boom flexure varies with the elevation of the telescope and changes by  $\sim 20''$  for  $40^\circ < el < 65^\circ$ . Being partially degenerate with  $a_6$ ,  $a_0$  and  $a_1$  are iteratively solved for by alternately freezing them for fits of  $a_6$  and vice versa until they converge. These parameters are static so long as the telescope structure remains constant but must be recalculated whenever the telescope boom is modified. For example between the 2011 and 2012 observing seasons side shields attached to the boom and primary mirror were removed to install a new guard ring around the primary mirror, which changed the values of  $a_0$  and  $a_1$ . Similarly, between the 2012 and 2013 seasons new larger side shields were installed, again changing the boom flexure parameters.
- **$a_2, a_3$ :** Amplitude of azimuth bearing axis tilt. The azimuth axis is not perfectly perpen-

dicular to the ground, with a tilt magnitude of  $\sim 3'$ . The tilt actually increases by several arcminutes per year as the telescope settles on its snow/ice foundation. This necessitates the occasional re-leveling of the telescope to “zero” the azimuth axis. Due to the az tilt a scan commanded to be at constant elevation instead slightly varies in elevation as a function of azimuth, generating sinusoidal shifts in the apparent position of an object as it moves across the sky. In RA/Dec coordinates, a point source thus shows up as a large circle when many observations taken at different times (azimuths) are coadded. This is the dominant correction made by the offline pointing model.

Approximately once per fridge cycle, a series of “az tilt” measurements of the telescope are taken. The telescope stops at a series of azimuths during which we record tilt meter readings. A sinusoidal model is fit to the measurements to determine the current values of  $a_2$  and  $a_3$ . We interpolate between tilt measurements to obtain values of the tilt parameters for every time sample during an observation. Figure 5.2 shows a representative tilt measurement with fit parameters, as well as the values of  $a_2$  and  $a_3$  since the deployment of SPTpol in January of 2012. The gap in measurements is during the telescope servicing period between the 2012 and 2013 observing seasons.

- **$a_4$ ,  $a_5$ ,  $a_6$ :** These parameters are the elevation axis tilt, the cross-elevation collimation (horizontal zero-point), and the elevation collimation (vertical zero-point), respectively.  $a_4$  fluctuates with a daily RMS of  $12''$  and is partially degenerate with  $a_5$ , which is  $\sim 11'$  and dependent on telescope focus bench position. The vertical zero-point  $a_6$  is  $\sim 14'$  with a  $20''$  daily RMS. We take regular observations of two HII regions, RCW38 ( $\text{Dec} = -47.51^\circ$ ) and MAT5A ( $\text{Dec} = -61.362^\circ$ ). For each observation we correlate a bolometer’s timestream with a template timestream of the observed source. The time at which the correlation is greatest signifies when the bolometer was pointed directly at the source. We record the pointing coordinates of the telescope at this time. After subtracting known bolometer pointing offsets from telescope boresight we obtain a cloud of data points measuring the position

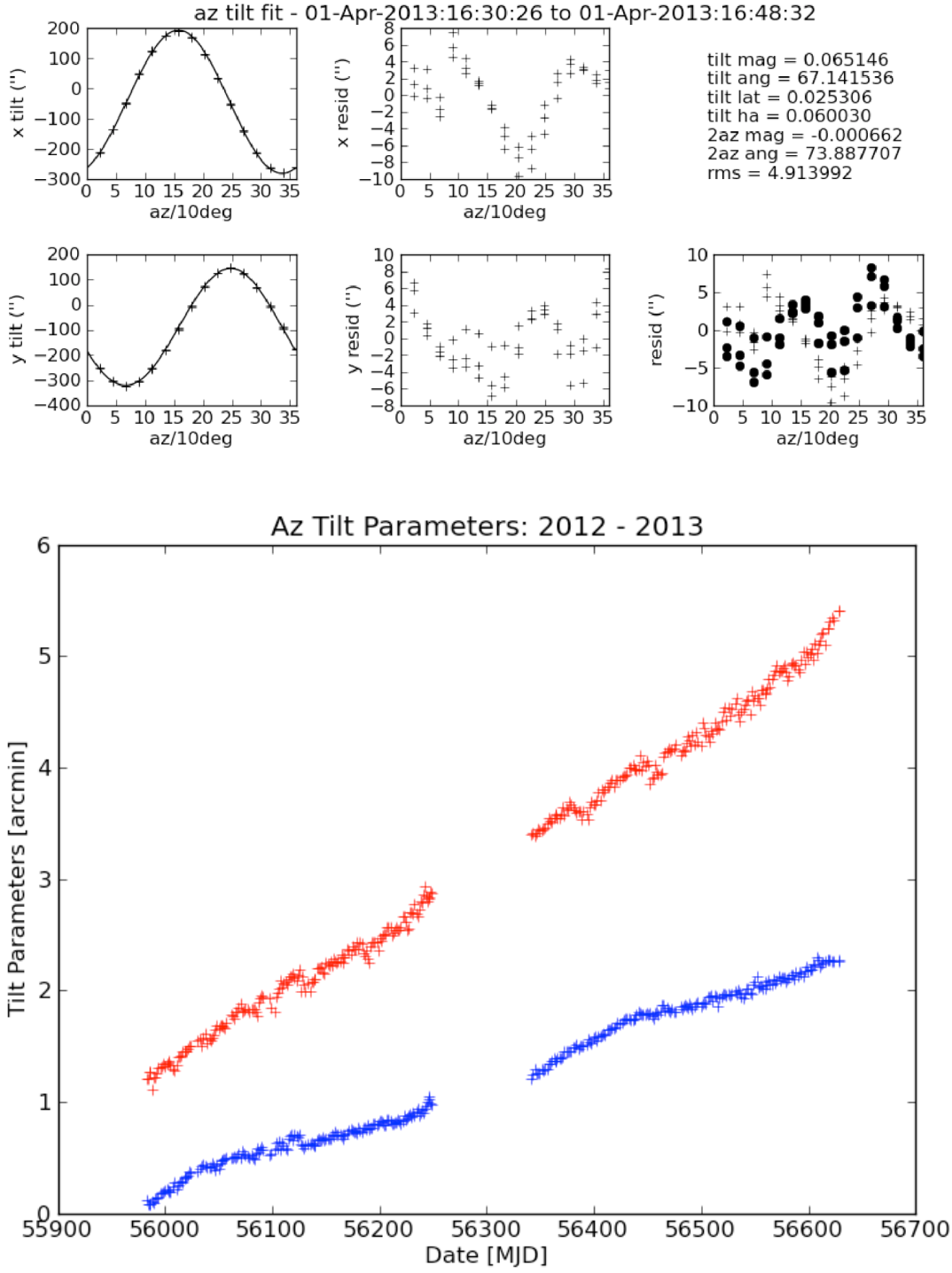


Figure 5.2: (Top) Representative azimuth bearing axis tilt measurement with corresponding fit to determine pointing parameters  $a_2$  and  $a_3$ . (Bottom)  $a_2$  (blue) and  $a_3$  (red) as a function of time since SPTpol deployment in January 2012. The azimuth axis tilt grows by several arcminutes per year.

of the telescope boresight when centered over the source relative to the absolute position of the source. With  $a_5$  fixed, we fit this residual az/el offset to obtain measurements of  $a_4$  and  $a_6$ . This also provides an absolute az/el pointing calibration. To obtain pointing corrections for CMB field observations we linearly interpolate between recorded values of  $a_4$ ,  $a_5$ , and  $a_6$ .

The horizontal zero-point  $a_5$  must be fixed in order to determine  $a_4$ . At a given focus position  $a_4$  will vary with  $a_5$  differently between two sources at different elevations due to the  $\cos el$  term in the model. By fixing  $a_5$  at several different values and fitting for the median  $a_4$  over all the observations taken at that focus position, we can find the value of  $a_5$  that gives the same median  $a_4$  fit for both RCW38 and MAT5A. We then fix  $a_5$  to this value for all other observations taken at the same telescope focus position.

- ***det, del***: Corrections for telescope metrology and thermometry, which both have  $\sim 20''$  daily RMS. The telescope structure can warp due to differential ambient temperature variations from the wind and the Sun, for example. Tens of sensors continuously record the temperature of the telescope structure. These are combined to form a measurement of warping in the telescope boom, both up/down and left/right, at each time sample,
- $\theta_{\text{refr}}$ : Correction for atmospheric refraction. We follow (79) to calculate  $\theta_{\text{refr}}$  as a simple function of ambient temperature and pressure while assuming atmospheric partial pressure due to water vapor is negligible,

$$\theta_{\text{refr}} \cong 77.6 \times 10^{-6} \left[ \frac{P}{1 \text{ mb}} \right] \left[ \frac{1 \text{ K}}{T} \right] \cot el, \quad (5.2)$$

where  $P$  and  $T$  are the ambient atmospheric pressure and temperature. The refraction correction is  $\sim 30''$  for typical elevations.

The offline pointing calculation is separated into several blocks and procedures based on the prior knowledge necessary to determine each model parameter. A flowchart of the entire procedure is plotted in Figure 5.3. Determining so-called “tilt” and “HII Region” parameters requires ancillary

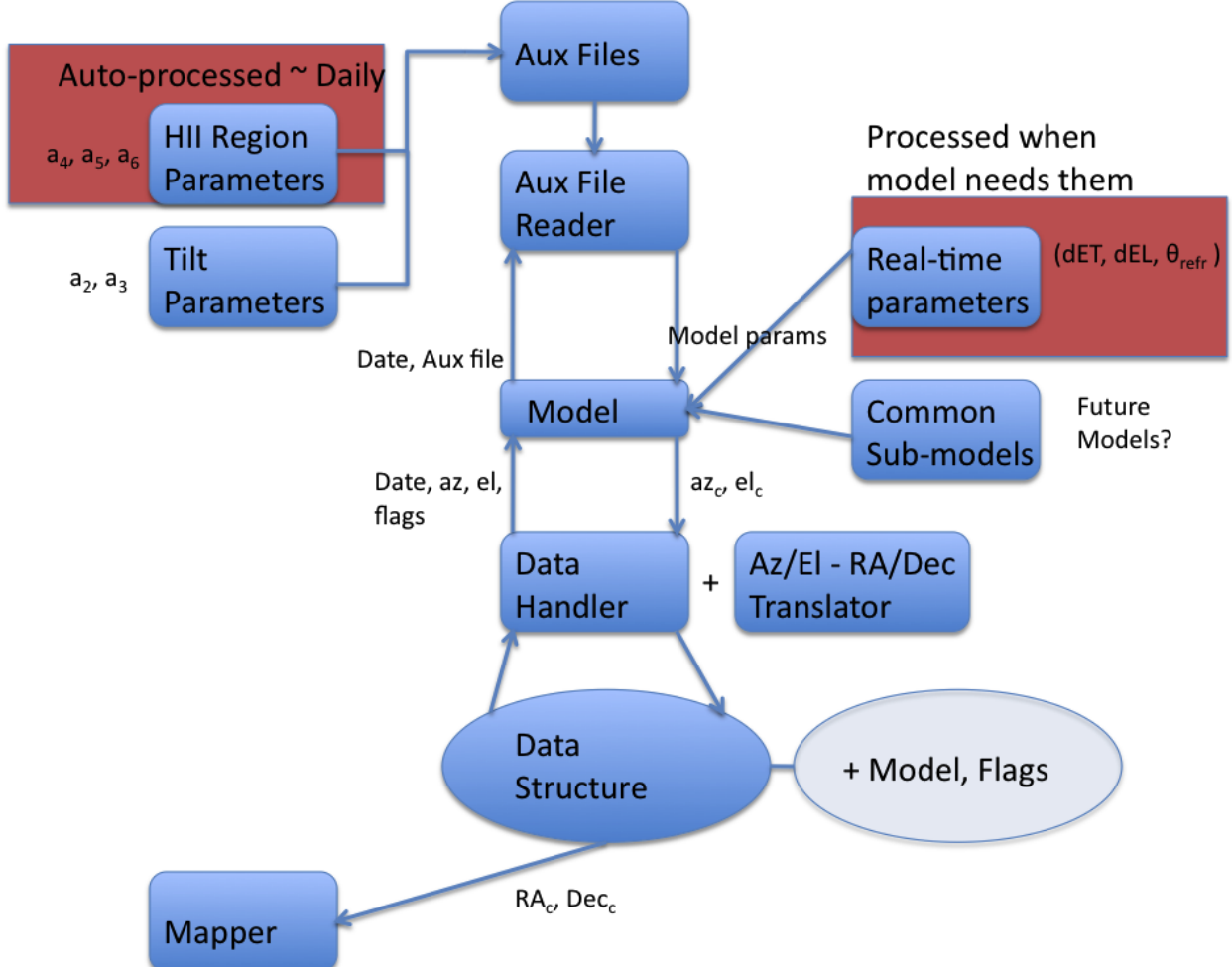


Figure 5.3: Flowchart for how offline pointing model corrections are calculated and applied to the data. “Tilt” and “HII region” parameters are determined ahead of time and saved in auxiliary config files. Corrections for thermometry, metrology, and atmospheric refraction are handled in real-time. Corrections to az/el are added to the raw telescope az/el, coordinates are converted to RA/Dec, and final pointing is passed to the mapper routine for binning timestreams into pixels.

telescope observations and is relatively slow. These parameters, therefore, are calculated in advance and stored in auxiliary config files to be called as necessary when maps are being generated. When a user wants to create an offline pointing-corrected map, the raw pointing data is passed to the pointing data handler, which requests modifications be made according to an input pointing model and relevant software flags. Based on the timestamps of the raw pointing, the model then pulls the relevant pointing parameters from the pre-processed auxiliary files and interpolates to match

the input data timestamps. Thermometry, metrology, and atmospheric refraction corrections are calculated on-the-fly. Once the model has generated az/el corrections, they are passed back to the pointing handler, converted to RA/Dec coordinates, and finally passed to mapmaking routines.

## 5.2 Maps

With knowledge of corrected telescope boresight pointing as well as detector offsets from boresight, bolometer timestreams can be mapped to positions on the sky. We choose a map projection and resolution to define a grid of pixels. Each pixel is simply a “pointing bin” with a specified range of Right Ascension and Declination. The bolometer timestreams are then parsed into each map pixel according to its pointing information and inverse variance weighted according to the bolometer’s polarization efficiency and PSDs in the SPTpol science band ( $\sim 1 - 3$  Hz) over the course of an observation. See Appendix A for a discussion of how the science band is determined. Weight maps, recording the number of times bolometers “hit” a map pixel weighted by inverse bolometer noise variance, are also computed. Maps are multiplied by their weight maps before summing.

Individual maps for temperature  $T$  (Stokes total intensity  $I$ ) as well as Stokes  $Q$  and  $U$  are generated using knowledge of each detector’s polarization angle.  $Q$  and  $U$  are defined relative to a specified direction on the sky. We choose horizontal/vertical lines to be  $\pm Q$  in our maps. One caveat is that projecting the curved sky onto a flat map will rotate polarization angles relative to this definition. Since we know the functional form of the projection, however, we can account for this rotation. We therefore “flatten” the polarization angles to maintain a consistent  $Q/U$  definition across the map. After polarization flattening,  $+Q$  is horizontal and  $-Q$  is vertical in the maps. Finally, with knowledge of polarization angle,  $Q$  and  $U$  maps can be combined into an  $E$ -mode map (10). Starting with the Fourier transforms of the  $Q$  and  $U$  maps,  $\tilde{m}_Q$  and  $\tilde{m}_U$ ,

$$\tilde{m}_E = \tilde{m}_Q \cos 2\phi + \tilde{m}_U \sin 2\phi, \quad (5.3)$$

where  $\phi = \arctan l_y/l_x$  is the phase angle between  $l_x$  and  $l_y$ . Inverse Fourier transforming back to

real space results in an  $E$ -mode map, though in practice we never work with real-space  $E$  modes. The (Fourier transforms of)  $T$  and  $E$  maps are the basic inputs for the CMB power spectrum analysis. Figures 5.4, 5.5, 5.6, and 5.7 show the  $T$ ,  $Q$ ,  $U$ , and  $E$ -mode maps for the 2013 500 deg $^2$  full survey observing season. (The SPTpol 100 deg $^2$  deep field used for the cosmological constraints presented here is centered at RA23H30DEC-55 and is part of the full survey centered at RA0H30DEC-57.5).

Map generation is repeated for each individual observation, leaving  $\sim 2500$  lead+trail map pairs for the 2012 deep field and  $\sim 700$  lead+trail pairs for the 2013 full survey field. These single observations are then sorted by dither step, ranked sequentially in time, and in the case of the 2012 deep field observations, combined into 122 “bundles:” map coadds with approximately uniform elevation coverage made from temporally proximate observations with at least one observation at each dither step. Lead and trail bundles are tracked separately, as well as maps made from only left-going or right-going scans. These sub-bundles are used to check for systematics contaminating the maps and are discussed in more detail in Section 5.5.

Coadding all bundles from the 2012 observing season, the deep field reaches a map depth of 7 (10)  $\mu\text{K}\cdot\text{arcmin}$  in temperature  $T$  (Polarization  $P$ ) at 150 GHz. That is, 7 (10)  $\mu\text{K}$  fluctuations in  $T$  ( $P$ ) in a square arcminute pixel have a signal-to-noise ratio of one. Additionally, the full coadd of the 2013 full survey achieved a depth of 12 (17)  $\mu\text{K}\cdot\text{arcmin}$  in  $T$  ( $P$ ). These are the deepest maps ever made of the CMB temperature and polarization anisotropies with this angular resolution ( $\sim 1'$  at 150 GHz). In comparison, the previous record-deep maps were from the SPTsz 2500 deg $^2$  temperature survey with a nominal depth of 18  $\mu\text{K}\cdot\text{arcmin}$  at 150 GHz (13  $\mu\text{K}\cdot\text{arcmin}$  in two 100 deg $^2$  deep fields, one of which is identical to the SPTpol deep field). In other words, with just one year of full survey observations the SPTpol 500 deg $^2$  field is deeper than the deepest 8% of the SPTsz 2500 deg $^2$  survey. Another two years of observing are scheduled for SPTpol after which we project a final map depth of  $\sim 7$  (10)  $\mu\text{K}\cdot\text{arcmin}$  in  $T$  ( $P$ ) in the full 500 deg $^2$  survey and  $\sim 5$  (7)  $\mu\text{K}\cdot\text{arcmin}$  in the deep field.

While survey area increased by a factor of five between the 2012 and 2013 observing seasons

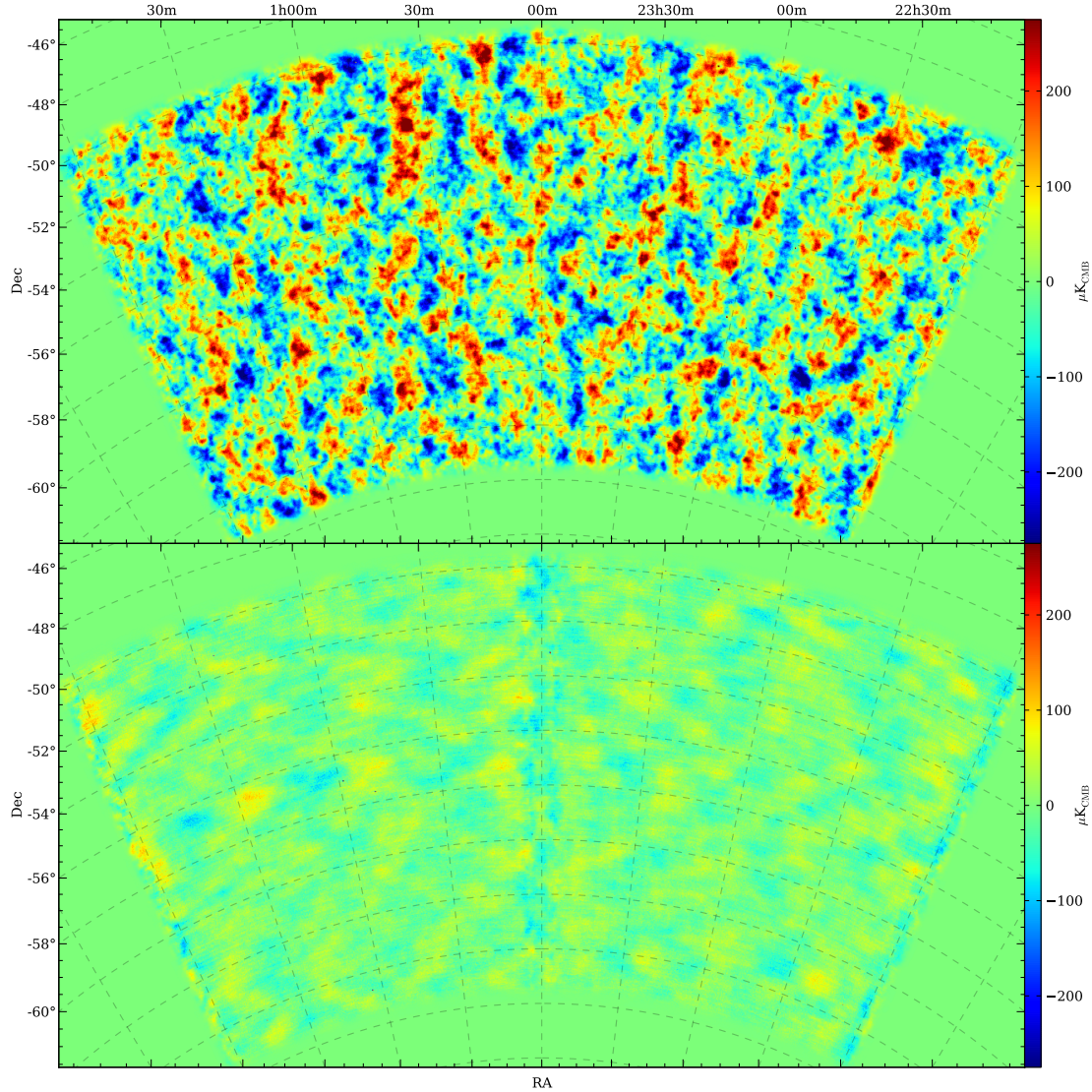


Figure 5.4: CMB  $T$  map from the SPTpol 500  $\text{deg}^2$  survey field 2013 observations. Resolution is 1 arcmin/pixel. The Oblique Lambert azimuthal equal-area projection is applied (80). (Top) Signal or “sum” map, coadding all observations of the 2013 season into a single map. (Bottom) Noise or “difference” map, generated by subtracting coadds of the first and second half of the observing season.  $T$  noise reaches a white floor of  $12.4 \mu\text{K}\cdot\text{arcmin}$  at  $3500 < l < 4500$  when minimal timestamp filtering is applied.

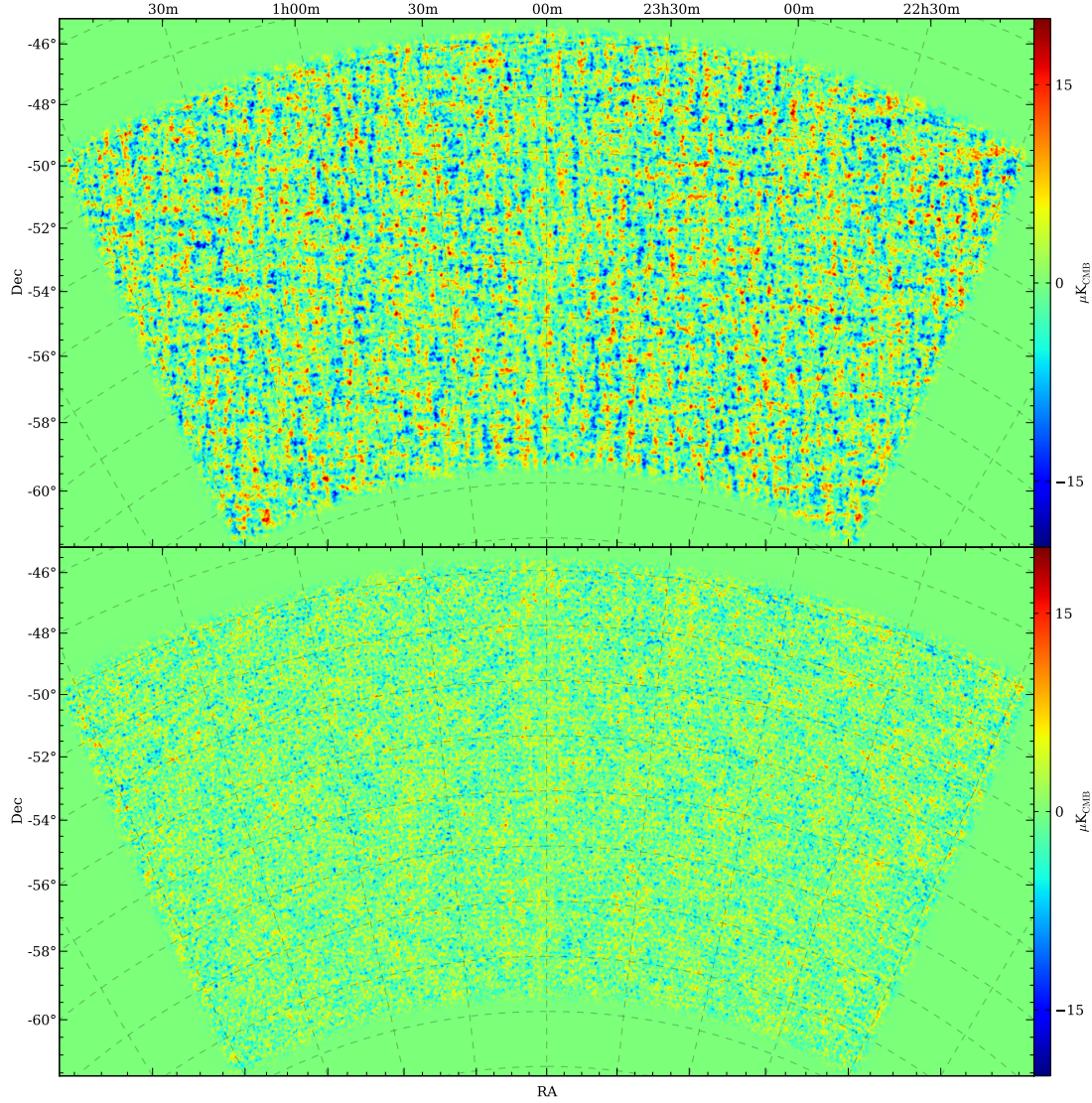


Figure 5.5: CMB Stokes  $Q$  polarization map from the SPTpol 500 deg $^2$  survey field 2013 observations. Here, colorscale indicates local polarization direction ( $\pm Q$ ) expressed as differential intensity. Resolution is 1 arcmin/pixel. The Oblique Lambert azimuthal equal-area projection is applied (80). Polarization angles have been “flattened” to remove curvature induced by the projection. The strong vertical/horizontal features are indicative of  $E$ -mode polarization being imaged with high signal-to-noise. (Top) Signal or “sum” map, coadding all observations of the 2013 season into a single map. (Bottom) Noise or “difference” map, generated by subtracting coadds of the first and second half of the observing season. Stokes  $Q$  noise reaches a white floor of  $16.7 \mu\text{K}\cdot\text{arcmin}$  at  $3500 < l < 4500$  when minimal timestream filtering is applied.

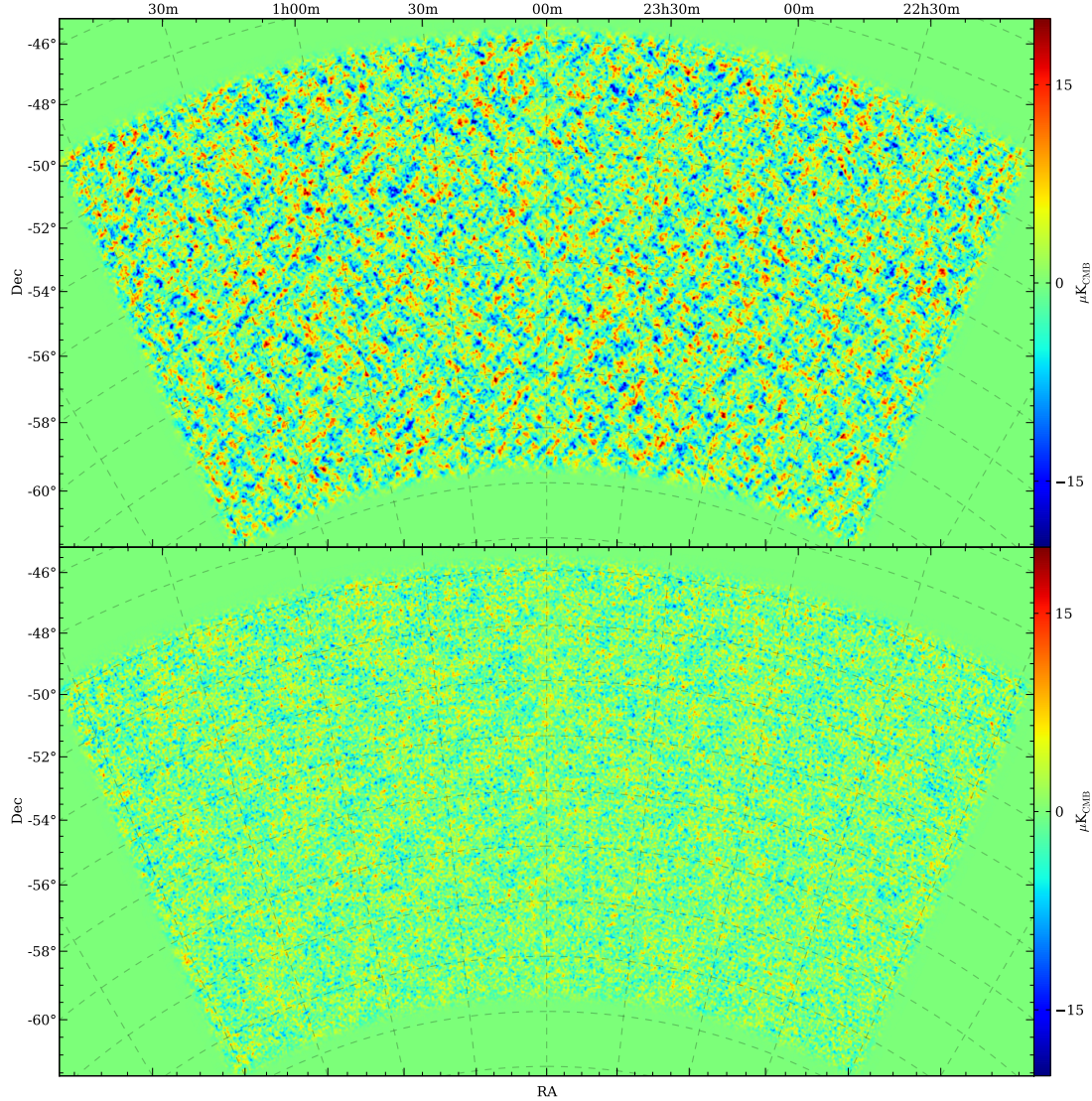


Figure 5.6: CMB Stokes  $U$  polarization map from the SPTpol 500 deg $^2$  survey field 2013 observations. Here, colorscale indicates local polarization direction ( $\pm U$ ) expressed as differential intensity. Resolution is 1 arcmin/pixel. The Oblique Lambert azimuthal equal-area projection is applied (80). Polarization angles have been “flattened” to remove curvature induced by the projection. The strong  $\pm 45^\circ$  features are indicative of  $E$ -mode polarization being imaged with high signal-to-noise. (Top) Signal or “sum” map, coadding all observations of the 2013 season into a single map. (Bottom) Noise or “difference” map, generated by subtracting coadds of the first and second half of the observing season. Stokes  $U$  noise reaches a white floor of  $17.1 \mu\text{K}\cdot\text{arcmin}$  at  $3500 < l < 4500$  when minimal timestream filtering is applied.

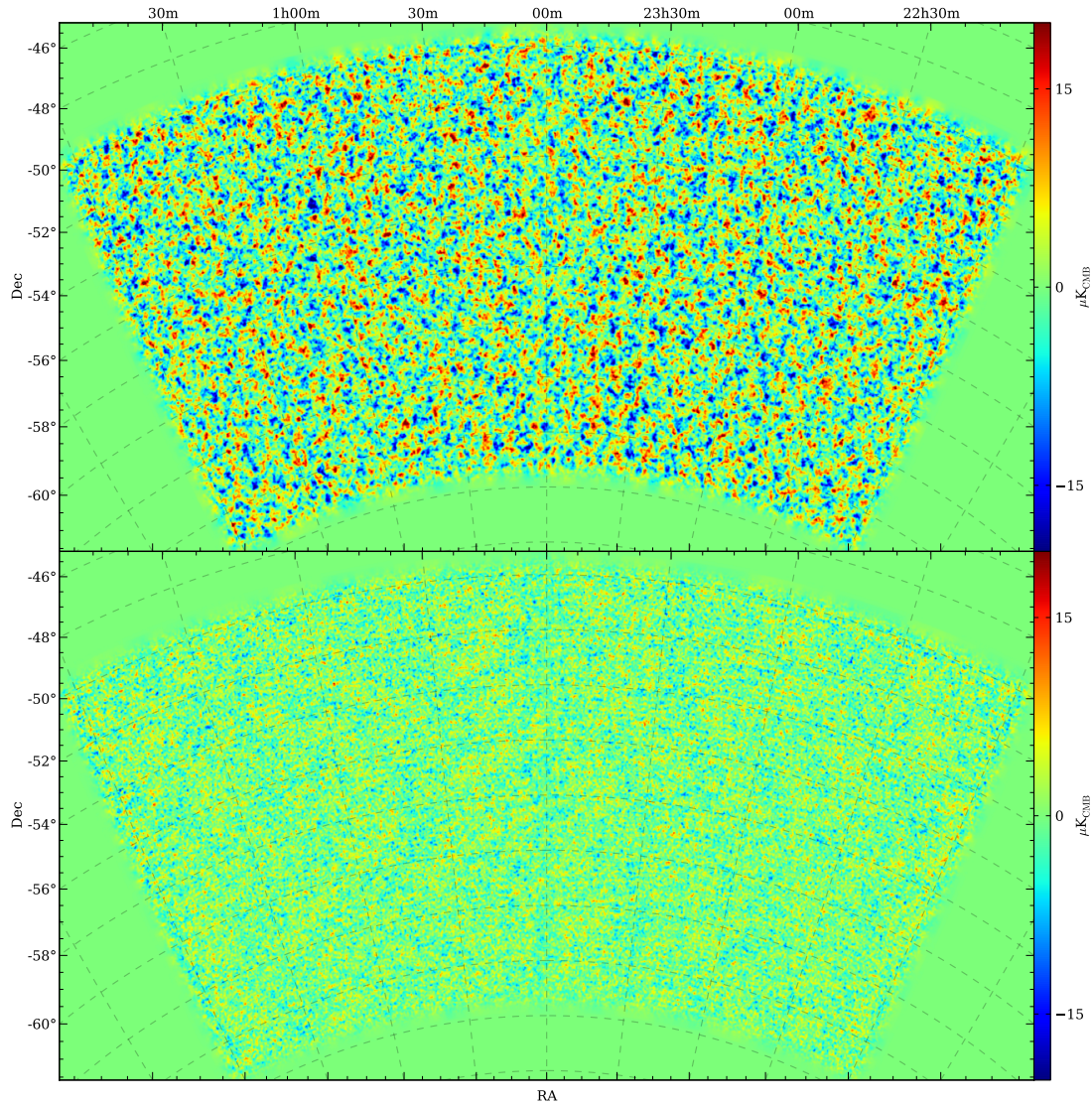


Figure 5.7: CMB  $E$ -mode polarization map from the SPTpol 500 deg $^2$  survey field 2013 observations. Here, colorscale indicates local polarization direction ( $\pm E$ ) expressed as differential intensity. Resolution is 1 arcmin/pixel. The Oblique Lambert azimuthal equal-area projection is applied (80). (Top) Signal or “sum” map, coadding all observations of the 2013 season into a single map. (Bottom) Noise or “difference” map, generated by subtracting coadds of the first and second half of the observing season.

the map depth degraded by *less* than  $\sqrt{5}$ . During the austral summer of 2012-2013 several aspects of the focal plane were upgraded, including the band-defining low-pass filters in the optics chain as well as one of the seven 150 GHz modules. The modifications improved integrated array mapping speed from  $17.9 \mu\text{K}\sqrt{s}$  to  $15.9 \mu\text{K}\sqrt{s}$  at 150 GHz.

### 5.2.1 Absolute Calibration

While individual timestreams are calibrated relative to RCW38, this is only accurate at the  $\sim 10\%$  level. We obtain an absolute calibration based on correlations between SPTpol and absolutely-calibrated SPTsz maps over the deep field. Schematically, we make half-season maps of SPTpol deep field observations and 16 sets of SPTsz maps over the same area of sky using the same filtering choices and accounting for small differences between the beams of the experiments. We then take Fourier transforms of the maps and calculate the cross-spectrum of the SPTpol half-season maps ( $\text{SPTpol} \times \text{SPTpol}$ ). Next, we calculate 16 cross-spectra between the full-season SPTpol map and the 16 SPTsz maps ( $\text{SPTpol} \times \text{SPTsz}_i$ ). We calculate the ratios  $(\text{SPTpol} \times \text{SPTsz}_i) / (\text{SPTpol} \times \text{SPTpol})$  and we find the mean and standard deviation of each multipole bin in the ratios. Finally, we calculate a weighted mean of the ratio by inverse variance weighting each multipole bin. The resulting number is the amount of correlation between uncalibrated SPTpol maps and the calibrated SPTsz maps. By multiplying the SPTpol maps by this correlation number we bootstrap the SPTpol calibration from that of SPTsz. (A similar procedure is used to absolutely calibrate SPTsz to Planck). For the 150 GHz 2012 observations of the deep field, to obtain our final temperature calibration we multiply our maps by

$$A_{150} = 0.8933 \pm 0.0137, \quad (5.4)$$

where the error is the quadrature sum of the  $(\text{SPTpol} \times \text{SPTsz})$  and  $(\text{SPTsz} \times \text{Planck})$  calibration statistical errors.

### 5.2.2 Polarization Angle Calibration

In order to reliably construct maps of Stokes  $Q$  and  $U$  polarization, we require accurate measurements of each detector's polarization angle relative to some pre-defined “zero” angle. The 150 GHz detectors are fabricated on photolithographed monolithic silicon wafers with detector pairs at  $90^\circ$  relative to each other in pixels that alternately rotate by  $45^\circ$ . Additionally, the seven hexagonal wafers are installed in the focal plane with  $60^\circ$  rotations, meaning the 1176 optical 150 GHz bolometers are in polarization angle groups stepped by  $15^\circ$ . Being monolithically fabricated, the nominal polarization orientation of each 150 GHz detector is well known, up to small displacements and rotations introduced during focal plane assembly. However, other potential systematic effects introduced by elements in the optics chain of the telescope, for example polarized reflections off the capacitive metal-mesh band-defining low-pass filters or telescope mirrors, could change the effective polarization angle of a given detector on the sky. Therefore we must rely on measurements of an external polarized calibrator to determine the detector polarization angles.

We constructed a polarized calibrator (polcal) source 3 km from the telescope. A hot thermal source is chopped behind a stationary wire grid polarizer to create a well-defined polarization state to measure. To reduce detector atmospheric loading from observing near the horizon, a large reflector reflects detector beams to  $60^\circ$  elevation. The polcal source is visible through a small hole in the reflector. We focus a single bolometer beam on the polcal and begin rotating a second polarizer to modulate the polarization signal in  $15^\circ$  steps. The response of a detector to the polcal source will be maximum when the rotating wire grid angle is aligned with the detector angle and minimized when the rotating grid is anti-aligned by  $90^\circ$ .<sup>1</sup> A minimum response greater than zero indicates cross-polar pickup (a  $0^\circ$  detector is slightly sensitive to polarization at  $90^\circ$ , for example) and therefore a reduced polarization efficiency. By fitting a sinusoidal model to a detector's response to the polcal source we determine both its polarization angle relative to the polcal fixed grid as well as its polarization efficiency. Since some detectors may be  $\pi/2$  out of phase with the fixed wire

---

<sup>1</sup> In reality, since vertically polarized light excites electrons in a vertical wire grid, which are then reflected, the detector response is maximum when the rotating wire grid is out of phase with its detector angle by  $\pi/2$ .

grid, the measurements are repeated after rotating the fixed grid by  $90^\circ$ .

Each detector is measured several times when possible, achieving a statistical error of less than  $2^\circ$  per detector. For each angle grouping on a given module, we average these measurements to obtain nominal polarization angles and polarization efficiencies for that grouping. Detectors that did not measure the polcal source with sufficient signal-to-noise or were saturated during measurements are assigned the corresponding polarization angle and efficiency for its module angle grouping. With  $< 2^\circ$  statistical error per detector, the focal plane average angle error is  $0.1^\circ$ . A suite of polcal tests were performed modifying the source to maximize potential sources of systematics in the calibration measurement. From these additional tests, we find the systematic error on the average polarization angle of the 150 GHz detectors to be less than  $1^\circ$ .

### 5.2.3 $T \rightarrow P$ Deprojection

A variety of effects can leak total intensity ( $T$ ) measurements into Stokes  $Q$  and  $U$  maps, known as  $T \rightarrow P$  leakage. For example, mis-calibration of gains in a detector pair will produce a scaled “monopole” copy of the  $T$  measurement in the  $Q$  and  $U$  maps. Higher-order effects, such as differential detector pointing or beam ellipticities corresponding to first- and second-derivatives of the  $T$  map, respectively, can also leak  $T$  into  $P$ . Given the low polarization fraction of the CMB,  $T \rightarrow P$  leakage is a serious systematic contaminant that must be addressed.

For this analysis we characterize and *deproject* the monopole leakage term, which generates a false polarization signal  $P' = \epsilon^P T$  for  $P \in \{Q, U\}$ . We measure differential detector pointing to be  $\sim 6''$  and beam ellipticity to be  $< 5\%$ , rendering higher-order  $T \rightarrow P$  leakage terms sub-dominant to the true polarization signal according to simulations for the  $EE$  and  $TE$  power spectra. To estimate the degree of monopole leakage, we take a weighted average of half-season cross-correlated  $T$  and  $P$  maps,

$$\epsilon^P = \frac{\sum_{l=300}^{2500} w_l \frac{C_l^{TP}}{C_l^{TT}}}{\sum_{l=300}^{2500} w_l}. \quad (5.5)$$

Here  $w_l$  is a weighting function designed to minimize the uncertainty of  $\epsilon^P$ . For the 2012 deep field

analysis, we measure  $\epsilon^Q = 0.0105 \pm 0.0010$  and  $\epsilon^U = -0.0137 \pm 0.0010$  while for the 2013 full field analysis we find  $\epsilon^Q = 0.0039 \pm 0.0010$  and  $\epsilon^U = -0.0046 \pm 0.0010$ . Deprojection simply entails subtracting a copy of the measured  $T$  map scaled by  $\epsilon^P$ . To test that the deprojection procedure does not instead *bias* our polarization maps we apply the same procedure to leakage-free simulated maps and find negligible bias in the resulting CMB power spectra.

#### 5.2.4 Data Quality Cuts

Not all bolometer timestreams are included in the final maps. We make a series of data quality cuts to reduce systematics entering our power spectra. At the timestream level, scans are flagged for removal if at least one of several types of “glitches” are detected. For example, an energetic cosmic ray striking a detector will produce a sharp spike in the bolometer timestream, in which case that scan is removed. Occasionally we also observe discrete DC jumps in timestream amplitudes, which are interpreted as changes in SQUID bias due to discrete jumps in magnetic flux quanta. Since a change in SQUID bias point affects the conversion from current to power units during timestream calibration, a bolometer that exhibits DC jumps is flagged and removed for an entire observation. We also cut timestreams based on their noise properties. For each of the seven 150 GHz modules we calculate the median timestream RMS for module bolometers during each observation after masking point sources. If a single timestream exhibits an RMS less than 0.25 times or greater than 3.5 times the median timestream RMS for that module than the timestream is flagged and removed. This step takes place after polynomial subtraction. Timestream cuts remove 5% of the data.

There are also data quality cuts at the bolometer level. If more than five bolometer scans are flagged during an observation then the entire bolometer timestream is removed. If, for example, a SQUID reading out a particular bolometer is turned off during an observation, the bolometer timestream is likewise ignored. During the 2012 observation season, all bolometers from the C4 module were cut due to unexplained excess noise, one seventh of the total 150 GHz array. The entire readout chain, from detector module to room-temperature readout electronics, was replaced for the

2013 season. No evidence of excess noise has since been observed in the new module. Bolometers are also cut if they do not have reliable polarization calibration data. Finally, bolometers that respond poorly to the internal calibrator or to elevation nods cannot be reliably calibrated and are removed from the analysis.

### 5.3 Pseudo-Spectra

Once maps pass all jackknife null tests (see Section 5.5) we combine left-going and right-going bundles into a single set of summed map bundles  $m_i^X$  where  $X$  can be either  $T$  or  $E$  and  $i$  is the bundle index. These bundles contain true sky signal as well as map noise. The noise between bundles should not correlate, however, and we take advantage of this to both generate signal-only power spectra as well as obtain an estimate of our noise power spectra. We take the Fourier transforms of each bundle  $\tilde{m}_{\vec{l},i}^X$  where  $\vec{l} = (l_x, l_y)$  and multiply by  $l(l+1)/2\pi$  to convert to the standard CMB power spectrum normalization:  $D_l^X = l(l+1)C_l^X/2\pi$ . With this normalization convention spectra are flatter over a wide range of multipoles. This is beneficial when binning spectra into bandpowers, where it is ideal if the spectrum is slowly varying over the multipole range being binned. We then multiply  $\tilde{m}_i^X$  by the complex conjugate of a different bundle transform  $\tilde{m}_j^{Y*}$ ,  $i \neq j$ , to generate two-dimensional cross-spectra  $\hat{D}_{ij}^{XY}$  (Figure 5.8). We azimuthally bin this spectrum into bandpowers and take the average over  $i, j$  to obtain an estimate of the binned  $XY$  power spectrum  $\hat{D}_b^{XY}$ . The entire series of steps is neatly encapsulated with the equation

$$\hat{D}_b^{XY} = \left\langle \frac{l(l+1)}{2\pi} \text{Re} \left[ \tilde{m}_{\vec{l},i}^X \tilde{m}_{\vec{l},j}^{Y*} \right] \right\rangle_{l \in b}. \quad (5.6)$$

For  $N$  bundles, there are  $N(N - 1)/2$  unique cross-spectra per  $XY$  spectrum. Thus for 122 bundles, we average 7381 cross-spectra for both the  $TE$  and  $EE$  power spectrum estimates. Since noise doesn't correlate between bundles, the  $\hat{D}_b^{XY}$  are free of noise bias. To estimate the remaining noise variance  $\hat{N}_b^{XY}$  we take the variance of the  $\hat{D}_{b,ij}^{XY}$  bundle cross-spectra (see Section 5.4.5).

The  $\hat{D}_b^{XY}$  are biased estimates of the true  $XY$  spectra and are thus known as “pseudo-spectra.” Several effects during observing and analysis conspire to bias our spectra estimates.

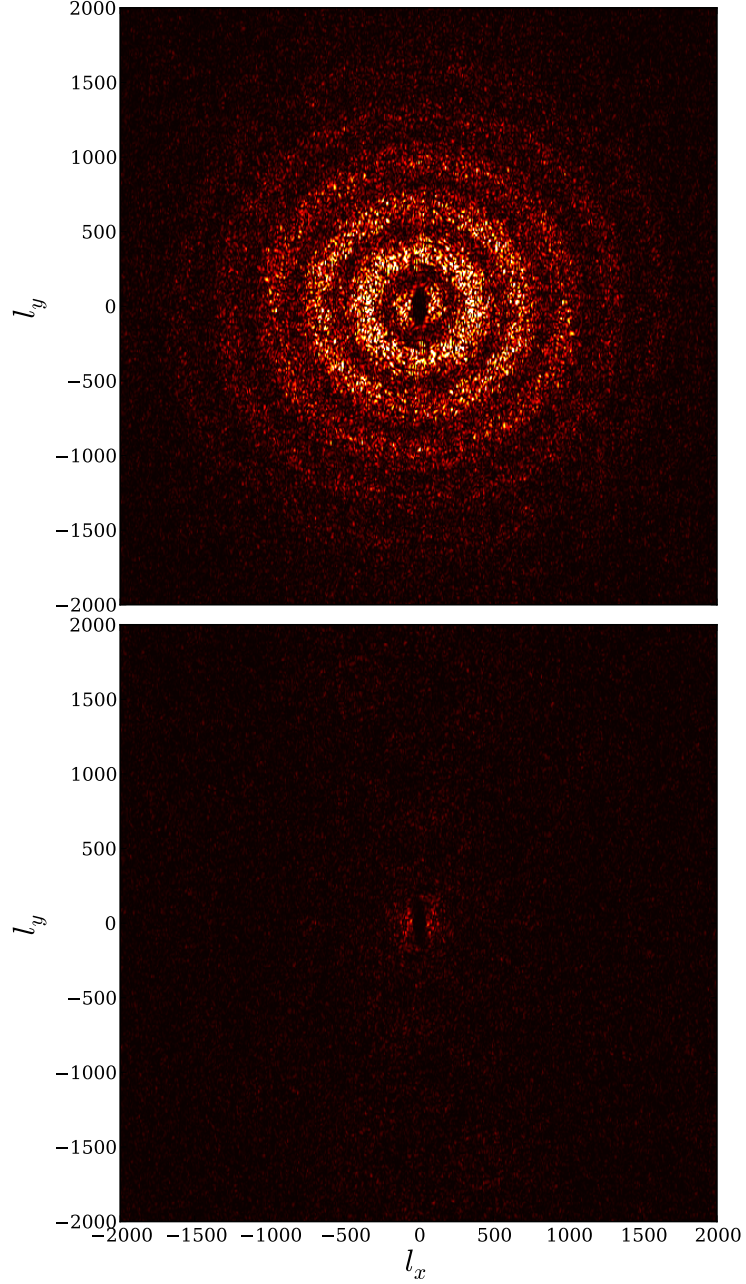


Figure 5.8: (Top) Two-dimensional biased  $E$ -mode pseudo-spectrum from SPTpol 2013 full survey observations with  $C_l$  normalization and Fourier resolution  $\Delta l = 6.25$ . The spectrum is converted to  $D_l$  and azimuthally averaged in multipole bins of  $\Delta l = 50$  to generate the more familiar one-dimensional power spectrum. The  $E$ -mode acoustic peaks are clearly visible as harmonic rings with high signal-to-noise even before azimuthal averaging. The vertical stripe of much lower power at low  $l_x$  is due to timestream polynomial subtraction along the scan direction, which is mostly parallel to  $l_x$ . (Bottom)  $E$ -mode noise power spectrum with the same color scale. Sample variance is not included. A small rise in noise is visible below  $l \sim 150$  but otherwise the noise is white.

Polynomial filtering of timestreams acts as a high-pass filter, reducing the power present in the maps at low multipoles. On the other hand, map pixelization low-pass filters the data reducing power at higher multipoles. Additionally, we observe only a small fraction of sky, and the resulting sky apodization mixes power between Fourier modes and limits the available modes to measure at low multipoles. Finally, the finite resolution of the receiver effectively convolves maps by a roughly Gaussian beam, which likewise multiplies  $\tilde{m}_i^X$  by a Gaussian in Fourier space. To obtain constraints on cosmological parameters, the end goal of this analysis, we must unbias the pseudo-spectra.

#### 5.4 Estimation of Unbiased Power Spectra: the MASTER Algorithm

The maps and their resulting binned power spectra  $\hat{D}_b^{XY}$  are biased measurements of the CMB sky. In order to obtain estimates of the unbiased spectra, we must understand the effects of our observing strategy and analysis pipeline on the intrinsic spectra. We follow the MASTER algorithm (81) to determine what these effects are and remove them from our power spectra estimates. In terms of an unbiased measurement of the binned true sky spectra  $D_{b'}^{XY}$ , the pseudo-spectra are given as

$$\hat{D}_b^{XY} = K_{bb'} D_{b'}^{XY}. \quad (5.7)$$

The “biasing kernel matrix”  $K_{bb'}$  encapsulates a series of linear operations performed on the true spectra. It can be expanded into constituent operations as

$$K_{bb'} = P_{bl} (M_{ll'} [\mathbf{W}] F_{l'} B_{l'}^2) Q_{l'b'}. \quad (5.8)$$

By inverting  $K_{bb'}$  we can obtain an estimate of the unbiased binned true-sky CMB power spectra:

$$D_b^{XY} = K_{bb'}^{-1} \hat{D}_{b'}^{XY}. \quad (5.9)$$

Therefore, we must measure and understand each component of the biasing kernel.

As described in (81),  $P_{bl}$  is the binning operator, which takes independent multipoles  $l$  and

bins them into bandpowers  $b$ ,

$$P_{bl} = \begin{cases} \frac{1}{\Delta l_{(b)}}, & l_{(b-1)} < l < l_{(b)} \\ 0, & \text{otherwise} \end{cases}, \quad (5.10)$$

while  $Q_{lb}$  is its reciprocal operator

$$Q_{lb} = \begin{cases} 1, & l_{(b-1)} < l < l_{(b)} \\ 0, & \text{otherwise} \end{cases}. \quad (5.11)$$

The other components of the kernel matrix, the mode-coupling matrix  $M_{ll'}[\mathbf{W}]$ , the TOD filtering transfer function  $F_{l'}$ , and the beam function  $B_{l'}$  are specific to our experiment and analysis and will be discussed separately in the following sections.

#### 5.4.1 Mode-Coupling

When making full-sky maps each multipole in the resulting spectra are independent of each other due to the orthogonality of the spherical harmonic functions  $Y_l^m$ . When only a portion of the sky is observed, however, the full-sky is multiplied by an effective apodization mask in real space leading to correlations between Fourier modes. The mode-coupling matrix  $M_{ll'}[\mathbf{W}]$  accounts for the mixing induced by the map apodization window  $\mathbf{W}$ . The SPTpol window transitions smoothly from unity in the center of the map region to zero with a cosine apodization over  $15'$  at its boundaries. Point sources with flux  $> 50$  mJ at 150 GHz are also masked with a  $5'$  disk. The disks are tapered to zero with a  $5'$  cosine taper. The SPTpol 2012 deep field sky apodization mask is shown in the top left of Figure 5.9.

The mode-coupling matrix is calculated analytically following the description in Appendix A of (81). Separate matrices are calculated for the  $TT$ ,  $EE$ , and  $TE$  spectra. To conserve power in Fourier space when applying an apodization mask  $\mathbf{W}$  to a real-space map, each coupling matrix is normalized according to

$$\sum_{l'} M_{ll'}[\mathbf{W}] = R^{-2} \int d^2 r \mathbf{W}^2 \equiv w_2, \quad (5.12)$$

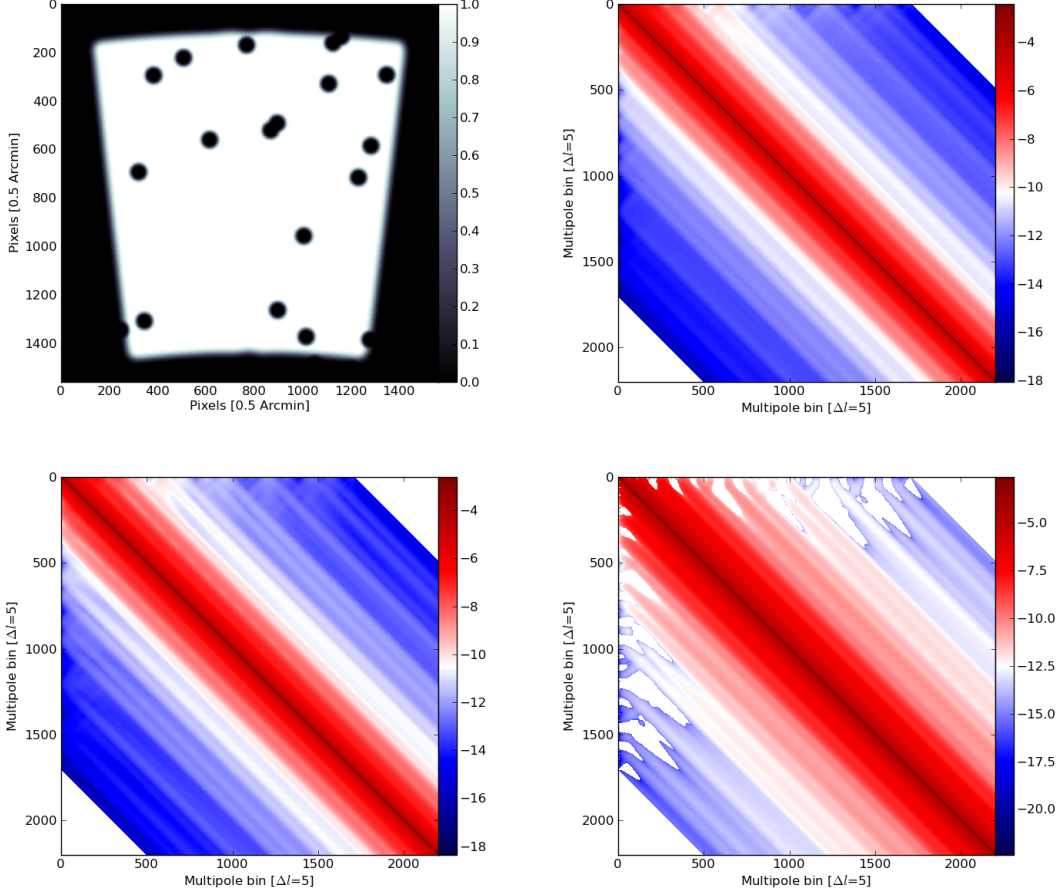


Figure 5.9: (Top left) The SPTpol 2012 150 GHz deep field apodization window. The edges of the region transition to zero using a  $15'$  cosine taper. Point sources with  $> 50$  mJy flux at 150 GHz are masked with  $5'$  disks and a  $5'$  cosine taper. (Top right) The  $TT$  mode-coupling matrix, log scale. (Bottom left) The  $EE$  mode-coupling matrix, log scale. (Bottom right) The  $TE$  mode-coupling matrix, log scale. White elements are negative. When binned to  $\Delta l = 50$  bandpowers, mode-coupling due to the apodization window between Fourier modes is  $< 10\%$ .

where  $R$  is the physical extent of a (projected) map in radians. In theory, the act of apodizing the sky can also couple power between Fourier modes of different spectra. This is automatically taken into account for the  $TT$  and  $EE$  spectra when calculating the  $TE$  mode-coupling matrix and we have ignored coupling between  $BB$ ,  $EE$ , and  $TT$  under the assumption that power in  $EE \gg BB$ . We plot the SPTpol deep field mode-coupling matrices in Figure 5.9. Note that when binned to the final spectrum resolution of  $\Delta l = 50$ , mode-coupling between adjacent spectrum bandpowers is  $< 10\%$ .

### 5.4.2 Beam Function

The telescope optics and pixel feedhorns define a “beam function” or “beam,” which encodes from where on the sky power coupling to the detectors is coming. In other words, it is the instrument’s spatial response to a delta function input (point source). The SPTpol beam is a 1.18’ full-width at half-maximum (FWHM) Gaussian at 150 GHz with a gradually decreasing low-power “shelf” that extends from roughly 5’ to at least a degree beyond the beam center. The true sky is convolved by our beam function during observations, which effectively low-pass filters our data reducing our sensitivity to smaller-scale features in the maps. According to the convolution theorem this is equivalent to multiplying the power spectra of our maps by  $B_l^2$ , the square of the Fourier transform of our beam function (squared since both maps entering the power spectrum have been convolved by the beam function).

We construct our beam function from full-season coadds of point sources and nine observations of the planet Mars. With a maximum angular diameter of 17.9” (82), Mars can be safely treated as a point source in this analysis and therefore a map of Mars is also a measurement of the instrument’s beam. We Fourier transform each observation and azimuthally average to obtain  $B_l$ . We combine many observations of Mars to reduce noise in our measurement of the beam at intermediate angular scales, out to roughly 25’ from the center of Mars. The beam at larger angles primarily affects the low-multipole region of  $B_l$ . Ignoring beam features beyond just 6’ produces a fractional change in  $B_l$  of < 1% at  $l < 300$ . Therefore, for the deep field analysis, where the lowest multipole being considered is  $l = 500$ , we truncate the beam at 45’ and arbitrarily normalize  $B_l$  to unity at  $l = 0$ .

The measurement of the beam must also account for residual telescope pointing jitter, which is not measured with a single observation. The jitter is estimated to be  $\sim 12''$  by measuring the FWHM of full-season coadds of the brightest point sources in the deep field and comparing them to the FWHM of single Mars observations. The Mars observations are convolved with a Gaussian to match the width of the full-season point source coadds. The effective FWHM of the 150 GHz

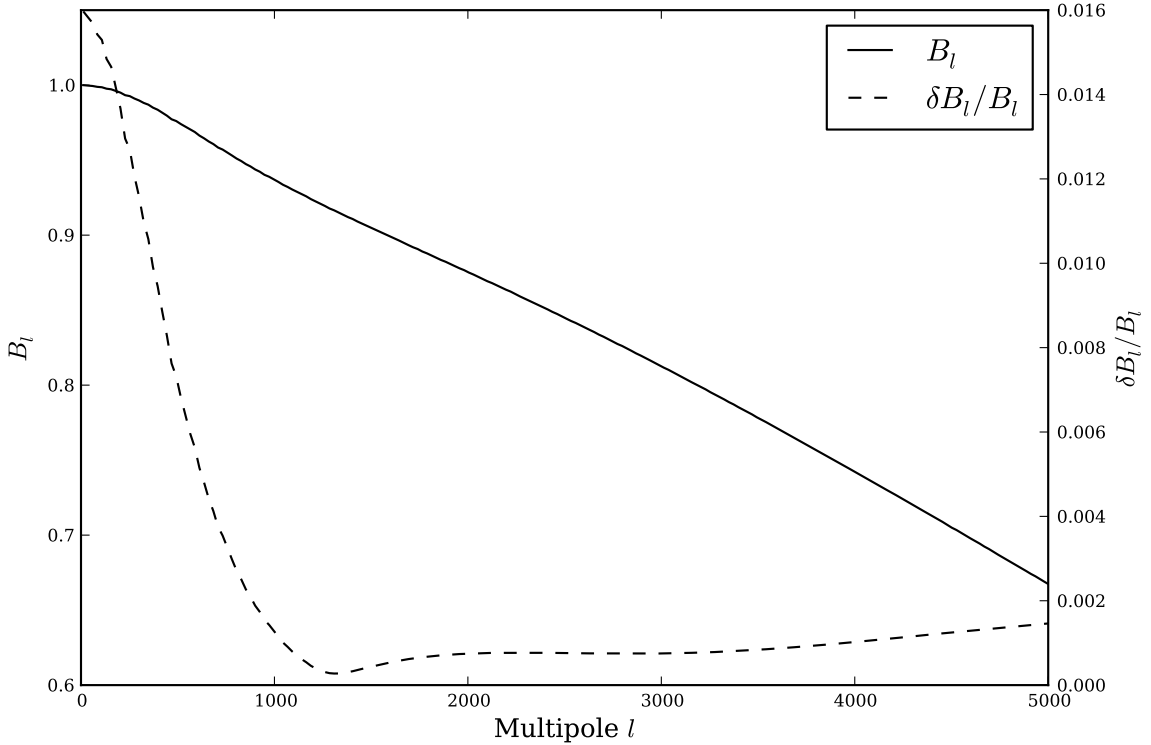


Figure 5.10: The SPTpol 2012 deep field 150 GHz beam function  $B_l$  and its fractional errors  $\delta B_l / B_l$ .  $B_l$  is arbitrarily normalized to unity at  $l = 0$ .

beam including pointing jitter is  $1.18'$ , corresponding to  $l \sim 9000$ , which is more than sufficient for a power spectrum analysis with  $l_{max} = 5000$ . ( $B_l$  drops to 0.67 at  $l = 5000$  when normalized to unity at  $l = 0$ ).

Finally, compared to its maximum value the beam function is down three orders of magnitude where the observed shelf beyond  $\sim 5'$  begins and only decreases farther from the beam center. Measurements of the shelf are therefore noisy compared to the gaussian core of the beam. The shelf is well-fit by an exponential function, however. To reduce noise in the beam function at large angles, azimuthally averaged Mars observations are fit to an exponential between  $5 - 9'$ . We replace the measured beam with the exponential fit for angles  $> 6'$  from the beam center and keep the measured beam inside this cutoff. We take as our beam function  $B_l$  the Fourier transform of this

hybrid beam. Beam errors come from the standard deviation of beam measurements from the nine Mars observations. The SPTpol beam function as well as its fractional errors are plotted in Figure 5.10. Beam errors are less than 1% for the multipole range of interest,  $500 < l < 5000$ .

### 5.4.3 Transfer Function

Before binning into maps detector timestreams are filtered to remove large-scale atmospheric fluctuations and aliased power from scales smaller than the map pixel scale. These effective high- and low-pass filters, respectively, bias our estimates of the true sky power spectra. We quantify the biasing effects of timestream filtering on the true spectra with spectrum transfer functions  $F_l^X$ , where  $X \in \{TT, EE, TE\}$ . From known input theoretical spectra  $C_{l,th}^X$  we generate simulated CMB skies. We “observe” these skies with the actual recorded pointing information from the observations, generating simulated timestreams. These timestreams are then processed identically to the actual data, coadded into bundles, smoothed by the SPTpol beam function, and multiplied by the SPTpol apodization window. The simulated bundles are converted to (biased) power spectra  $\hat{C}_{l,sim}$  following the procedure laid out in Section 5.3. A total of 204 pseudo-spectra realizations are generated. By averaging over many simulations and comparing to the input spectra, we can quantify the collective effects of timestream filtering in our analysis pipeline.

Again following the procedure laid out in (81), we take an iterative approach in calculating  $F_l^X$ . To zeroth order, the transfer functions are simply the ratio of the mean simulated power spectra over the input spectra:

$$F_{l,0}^X = \frac{\langle \hat{C}_{l,sim}^X \rangle}{w_2 C_{l,th}^X B_l^2}. \quad (5.13)$$

Since the beam function is accounted for separately in the kernel  $K_{bb'}$ , we remove its effects on the simulated spectra in the calculation of the transfer function. In this first iteration we approximate the mode-coupling matrix as diagonal and include its normalization factor  $w_2$  to conserve Fourier power in the apodized spectrum. We next iterate the transfer function to remove the effects of

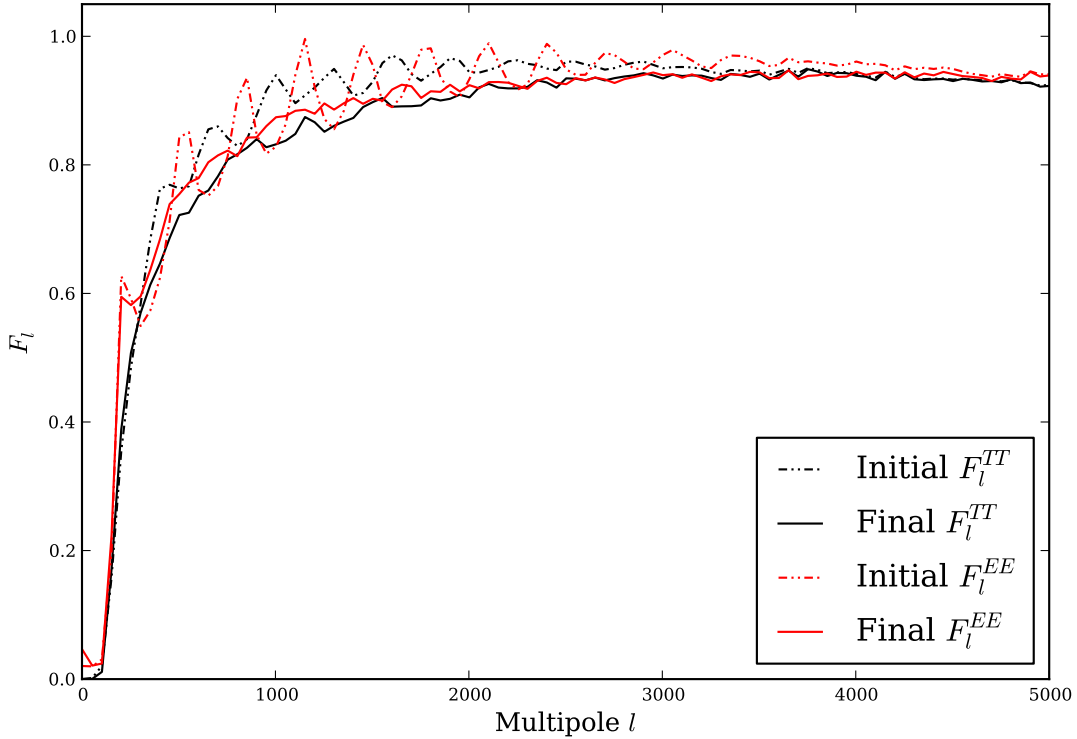


Figure 5.11: The SPTpol 2012 deep field 150 GHz transfer functions  $F_l$ , binned to  $\Delta l = 50$ . The  $TE$  transfer function, not plotted for clarity, is the geometric mean of the  $TT$  and  $EE$  transfer functions. The initial iterations exhibit oscillations from mode-coupling induced by the map apodization window, but by the fifth and final iteration only the effects of timestream filtering on the power spectra remain.

mode-coupling by including  $M_{ll'}[\mathbf{W}]$  in the calculation:

$$F_{l,i+1}^X = F_{l,i}^X + \frac{M_{ll'} F_{l',i}^X C_{l',th} B_{l'}^2}{w_2 C_{l,th} B_l^2}. \quad (5.14)$$

In general  $F_l^X$  converges after the first iteration but we use the fifth iteration for final transfer functions. This iterative approach works well for  $TT$  and  $EE$  spectra, but due to several zero-crossings in the  $TE$  spectrum, the calculation is especially sensitive to Fourier resolution and the specific input theoretical spectrum. Since  $TE$  spectra are generated by taking the cross-spectra of  $T$  and  $E$  maps, we side-step this instability in the  $TE$  transfer function by taking the geometric

mean of the  $TT$  and  $EE$  transfer functions,

$$F_l^{TE} = \sqrt{F_l^{TT} F_l^{EE}}. \quad (5.15)$$

The initial and final iterations of the  $TT$  and  $EE$  SPTpol 2012 deep field transfer functions are plotted in Figure 5.11. The initial iterations exhibit clear oscillations due to mode-coupling from the apodization window, but by the fifth and final iteration they have been completely cleaned.

#### 5.4.4 Bandpower Window Functions

We do not have the sensitivity to make high signal-to-noise measurements of each multipole in a spectrum and therefore bin our spectra into bandpowers of width  $\Delta l \geq 50$  according to

$$D_b = P_{bl} D_l \quad (5.16)$$

for each bandpower  $b$  that covers a specified multipole range, where  $P_{bl}$  is the binning operator. In order to obtain meaningful constraints on cosmological parameters we must compare our binned spectra  $D_b$  to unbinned theoretical spectra  $D_l^{th}$ . We define weighting functions  $W_l^b/l$  indexed by the bandpower  $b$ , known as bandpower window functions, that transform from unbinned to binned power spectrum space:

$$D_b^{th} = \frac{W_l^b}{l} D_l^{th}. \quad (5.17)$$

Once binned, the theoretical spectrum bandpowers can be directly compared to our measured bandpowers.

The window functions specify how much power from each individual multipole contributes to a single bandpower so they are themselves functions of the biasing kernel matrix. Beginning with

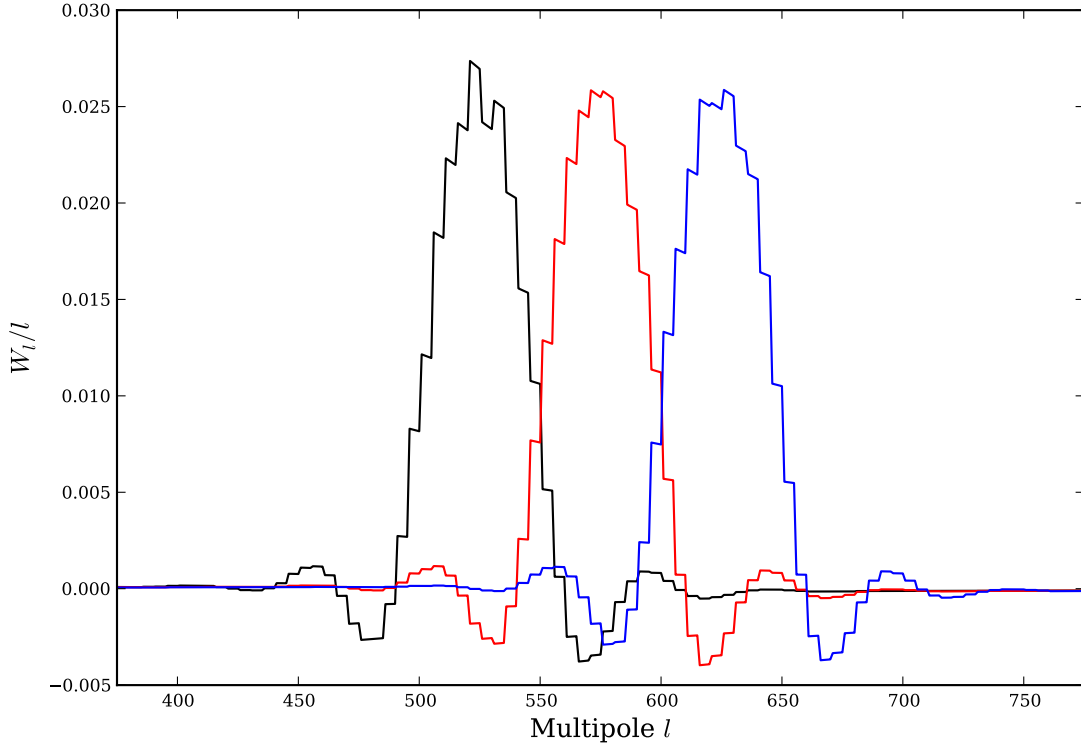


Figure 5.12: The lowest three bandpower window functions for the SPTpol 2012 150 GHz deep field  $EE$  power spectrum. Window functions are calculated with a resolution of  $\Delta l = 5$ .

Equations 5.7 and 5.16,

$$\begin{aligned}
 \frac{W_l^b}{l} D_l^{th} &= D_b^{th} \\
 &= K_{bb'}^{-1} [\hat{D}_{b'}^{th}] \\
 &= K_{bb'}^{-1} [K_{b'b} D_b^{th}] \\
 &= K_{bb'}^{-1} [(P_{b'l'} M_{l'l} F_l B_l^2 Q_{lb}) (P_{bl} D_l^{th})] \\
 &= K_{bb'}^{-1} (P_{b'l'} M_{l'l} F_l B_l^2) D_l^{th}.
 \end{aligned} \tag{5.18}$$

The bandpower window functions are thus

$$\frac{W_l^b}{l} = K_{bb'}^{-1} (P_{b'l'} M_{l'l} F_l B_l^2) \tag{5.19}$$

with normalization

$$\sum_l \frac{W_l^b}{l} = 1. \quad (5.20)$$

We plot the first three SPTpol 150 GHz  $EE$  spectrum bandpower window functions in Figure 5.12 with  $\Delta l = 50$ . The shape of the window functions is largely set by the mode-coupling and therefore the Fourier transform of the map apodization window. It makes intuitive sense that the window functions would resemble sinc functions (the real-space map apodization window is largely a 2-D boxcar) with damped Fourier ringing due to the gradual cosine taper at the edges of the apodization mask. From the window functions it is clear that the mode-coupling induces correlations between adjacent bandpowers.

#### 5.4.5 Bandpower Covariance Matrix

The bandpower covariance matrix  $\mathbf{C}_{bb'}$  quantifies the uncertainties and correlations between bandpowers. This also accounts for correlations between bandpowers from different spectra, giving the covariance matrix a  $2 \times 2$  block structure for  $TE$  and  $EE$  150 GHz spectra included in this analysis. The “on-diagonal” blocks are auto-covariance ( $TE \times TE$  and  $EE \times EE$ ), while the two “off-diagonal” blocks encode correlations between spectra as cross-covariance ( $TE \times EE$ ). The covariance matrix includes contributions from sample variance from limited sky coverage, noise variance from the measured cross-spectra, uncertainties in the instrument beam, and calibration uncertainty.

Sample covariance  $\widehat{\mathbf{C}}_{bb'}^s$  for the auto-covariance blocks is estimated directly from the variance in the set of  $N = 204$  bundle realizations. Each simulated set contains 122 bundles, which match the coverage of the actual data bundles. For each realization, unbiased cross-spectra  $D_{b,i}^{sim}$  are generated exactly as described in Sections 5.3 and 5.4. In general  $D_{b,i}^{sim}$  are vectors including both  $TE$  and  $EE$  bandpowers. We then simply take the variance of these simulated cross-spectra to obtain our estimate of sample covariance:

$$\widehat{\mathbf{C}}_{bb'}^s = \sum_i \frac{\left( D_{b,i}^{sim} - \overline{D_b^{sim}} \right)^T \left( D_{b',i}^{sim} - \overline{D_{b'}^{sim}} \right)}{N - 1}. \quad (5.21)$$

The noise covariance  $\widehat{\mathbf{C}}_{bb'}^n$  is calculated from the variance between the measured cross-spectra  $D_b^{AB}$  and contains two terms. The first term assumes complete independence between cross-spectra and is similar to the sample covariance except that now we are concerned with the variance in our measurement of the sample mean (our measured power spectra):

$$\widehat{\mathbf{C}}_{bb'}^{n1} = \sum_i \frac{\left(D_{b,i}^{AB} - \overline{D_b^{AB}}\right)^T \left(D_{b',i}^{CD} - \overline{D_{b'}^{CD}}\right)}{N(N-1)}, \quad (5.22)$$

where now  $N$  is the number of cross-spectra, and  $AB$  and  $CD$  denote either  $TE$  or  $EE$ . The second term accounts for additional covariance from correlations between cross-spectra since they share a subset of maps between each other. We first calculate an  $N \times N$  map-overlap matrix  $M$ , where rows and columns index a particular cross-spectrum. Its elements are equal to one if two spectra share a map and zero otherwise. The diagonal is left to be zero even though it represents cross-spectra that share two maps, since this is exactly what is calculated in the first noise term above. By taking the outer product of the map-overlap matrix  $M$  with  $\Delta D_{b,i}^{AB} = D_{b,i}^{AB} - \overline{D_b^{AB}}$  we extract the components of each cross-spectrum that correlate with other cross-spectra. Then we find the variance of the sample mean as before:

$$\widehat{\mathbf{C}}_{bb'}^{n2} = \sum_i \frac{\left(\Delta D_{b,i}^{AB}\right)^T \left(M \otimes \Delta D_{b',i}^{CD}\right)}{N(N-1)}. \quad (5.23)$$

The total bandpower covariance matrix from sample and noise covariance is then

$$\widehat{\mathbf{C}}_{bb'} = \widehat{\mathbf{C}}_{bb'}^s + \widehat{\mathbf{C}}_{bb'}^{n1} + \widehat{\mathbf{C}}_{bb'}^{n2}. \quad (5.24)$$

As in previous SPT analyses (e.g. (83), (39), (13)) elements far from the diagonal of the auto-covariance blocks  $\widehat{\mathbf{C}}_{bb'}^{X \times X}$  are noisy due to limited simulated realizations but the general shape is well known given the map apodization window. We therefore “condition” each block in the covariance matrix to conform to the expected shape. Bins are replaced with the average of correlation matrix elements the same distance from the diagonal. Additionally, all elements greater than  $\Delta l = 400$  from the diagonal are set to zero where no correlation is expected. A conditioned covariance matrix

takes the form

$$\mathbf{C}_{bb'} = \frac{\sum_{b_1-b_2=b-b'} \frac{\hat{\mathbf{C}}_{b_1 b_2}}{\sqrt{\hat{\mathbf{C}}_{b_1 b_1} \hat{\mathbf{C}}_{b_2 b_2}}}}{\sum_{b_1-b_2=b-b'} 1}. \quad (5.25)$$

Additional bin-to-bin covariance is generated due to uncertainties in the measurement of the beam function  $B_\ell$ . A “beam correlation matrix” is first constructed,

$$\rho_{ij}^{beam} = \left( \frac{\delta D_i}{D_i} \right) \left( \frac{\delta D_j}{D_j} \right) \quad (5.26)$$

where

$$\frac{\delta D_i}{D_i} = 1 - \left( 1 + \frac{\delta B_i}{B_i} \right)^{-2}, \quad (5.27)$$

and  $\frac{\delta B_i}{B_i}$  comes from the uncertainty in our measurements of Mars (see Section 5.4.2). The beam correlation matrix is then converted to a covariance matrix via the measured bandpowers

$$\mathbf{C}_{ij}^{beam} = \rho_{ij}^{beam} D_i D_j. \quad (5.28)$$

In general,  $D_i$  and  $D_j$  could be either  $TE$  or  $EE$  bandpowers.

Finally, we add covariance from calibration uncertainty  $\sigma_{\text{cal}}$ . There are two sources of calibration uncertainty: imperfect knowledge of our absolute temperature calibration  $A$  and our polarization efficiency  $P$ . Temperature calibration affects the  $TE$  and  $EE$  spectra equally while polarization efficiency enters as the number of polarized input maps in a spectrum. For each block in the covariance matrix we generate a total calibration uncertainty

$$\epsilon_{XY} = \sigma_{\text{cal}}^X \sigma_{\text{cal}}^Y, \quad (5.29)$$

where  $X$  and  $Y$  are either  $TE$  or  $EE$ . Since absolute calibration and polarization efficiency enter at the map level, calibration uncertainty enters as the variance of the map amplitudes squared. For independent random variables  $A$  and  $B$

$$\text{var}(AB) = E[A^2]E[B^2] - E[A^2]^2E[B^2]^2. \quad (5.30)$$

Thus, for maps with uncertainty in amplitude  $A$  and polarization efficiency  $P$ , the calibration error

for each spectrum is

$$\begin{aligned}\sigma_{\text{cal}}^{EE} &= \sqrt{\text{var}(A^2 P^2)} = \sqrt{E[A^4]E[P^4] - E[A^2]^2 E[P^2]^2} \\ \sigma_{\text{cal}}^{TE} &= \sqrt{\text{var}(A^2 P)} = \sqrt{E[A^4]E[P^2] - E[A^2]^2 E[P]^2},\end{aligned}\quad (5.31)$$

which can be further expanded into functions of the mean and variance of  $A$  and  $P$ . The calibration covariance is then defined as

$$\mathbf{C}_{ij}^{\text{cal}} = \epsilon_{XY} D_i D_j, \quad (5.32)$$

where again  $D_i$  and  $D_j$  are  $TE$  or  $EE$  bandpowers corresponding to  $X$  and  $Y$ .

#### 5.4.5.1 $TE \times EE$ Cross-Covariance

The  $TE \times EE$  cross-covariance block is important when simultaneously fitting  $TE$  and  $EE$  bandpowers to account for correlations between the spectra. When applied to this block, the simple conditioning procedure described above results in low signal-to-noise due to the limited number of simulated bundles. Instead of measuring it, we *construct* the  $TE \times EE$  block from the higher signal-to-noise conditioned auto-covariance blocks  $\mathbf{C}_{ll'}^{X \times X}$ . In this section we work with native multipoles  $l$  instead of bins  $b$  but the procedure is the same for both. The diagonal of the  $TE \times EE$  block is defined as an algebraic combination of the auto-covariance diagonals  $\mathbf{C}_{ll}^{X \times X}$  assuming the covariance blocks can be related through theoretical expectations of sample and noise variance.

According to (84)

$$\begin{aligned}\mathbf{C}_{ll}^{TT \times TT} &= \frac{2}{(2l+1)f_{\text{sky}}} (C_l^{TT} + N_l^{TT}) \\ \mathbf{C}_{ll}^{EE \times EE} &= \frac{2}{(2l+1)f_{\text{sky}}} (C_l^{EE} + N_l^{EE}) \\ \mathbf{C}_{ll}^{TE \times TE} &= \frac{1}{(2l+1)f_{\text{sky}}} \left[ (C_l^{TE})^2 + (C_l^{TT} + N_l^{TT}) (C_l^{EE} + N_l^{EE}) \right] \\ \mathbf{C}_{ll}^{TT \times EE} &= \frac{2}{(2l+1)f_{\text{sky}}} (C_l^{TE})^2 \\ \mathbf{C}_{ll}^{TE \times TT} &= \frac{2}{(2l+1)f_{\text{sky}}} C_l^{TE} (C_l^{TT} + N_l^{TT}) \\ \mathbf{C}_{ll}^{TE \times EE} &= \frac{2}{(2l+1)f_{\text{sky}}} C_l^{TE} (C_l^{EE} + N_l^{EE}),\end{aligned}\quad (5.33)$$

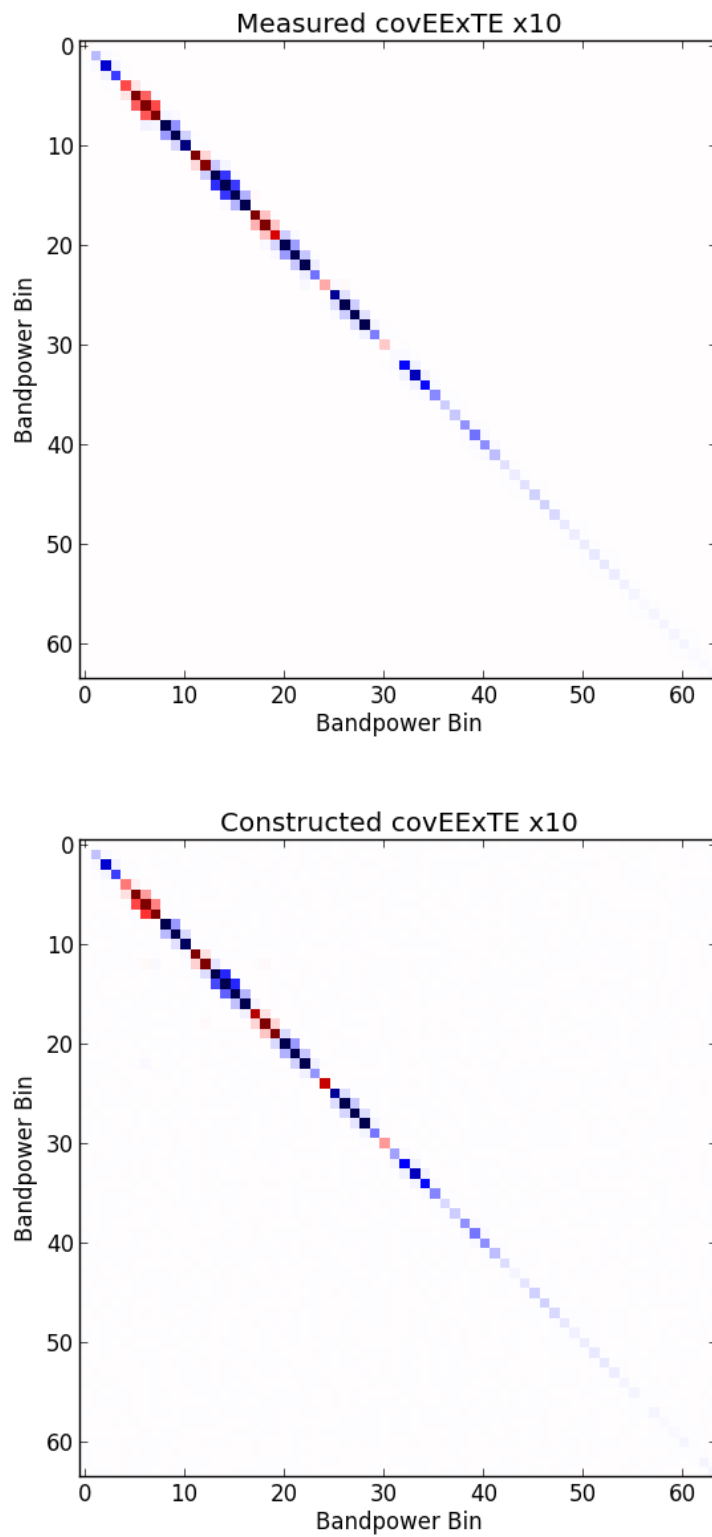


Figure 5.13: (Top)  $TE \times EE$  cross-covariance matrix measured from  $10^5$  cross-spectra simulations. (Bottom) Cross-covariance matrix constructed using auto-covariance block diagonals.

where  $f_{\text{sky}}$  is the fraction of sky observed,  $C_l^X$  is a theoretical power spectrum, and  $N_l^X$  is a noise spectrum. Absorbing  $1/\sqrt{(2l+1)f_{\text{sky}}}$  into each theory and noise spectrum, we can obtain an expression for the diagonal of the  $TE \times EE$  cross-covariance matrix in terms of diagonals of the auto-covariance matrix blocks. First we define the theory and noise spectra in terms of the auto-covariances:

$$\begin{aligned} C_l^{TE} &= \text{sign}(C_l^{TE}) \sqrt{\text{abs}\left(C_{ll}^{TE \times TE} - \frac{\sqrt{C_{ll}^{TT \times TT} C_{ll}^{EE \times EE}}}{2}\right)} \\ C_l^{TT} + N_l^{TT} &= \sqrt{\frac{C_{ll}^{TT \times TT}}{2}} \\ C_l^{EE} + N_l^{EE} &= \sqrt{\frac{C_{ll}^{EE \times EE}}{2}}. \end{aligned} \quad (5.34)$$

Substituting Equations 5.34 into Equations 5.33, we find that along its diagonal

$$C_{ll}^{TE \times EE} = 2 \text{sign}(C_l^{TE}) \sqrt{\text{abs}\left(C_{ll}^{TE \times TE} - \frac{\sqrt{C_{ll}^{TT \times TT} C_{ll}^{EE \times EE}}}{2}\right)} \sqrt{\frac{C_{ll}^{EE \times EE}}{2}}. \quad (5.35)$$

The off-diagonal shape of the  $TE \times EE$  cross-covariance matrix is of course controlled by its correlation matrix  $\rho^{TE \times EE}$ , which is constructed from the average of the conditioned  $TE$  and  $EE$  correlation matrices. It should be noted that the diagonal of the  $TE \times EE$  correlation matrix can be negative and non-unity since the  $TE$  and  $EE$  spectra are not perfectly (anti)-correlated; the signs of the diagonal follow the signs of the measured  $TE$  bandpowers and are propagated out from the diagonal along  $+45^\circ$  lines according to results from test simulations. By construction, however,  $\rho^{TE \times EE}$  is unity along its diagonal, so it is scaled by the normalized amplitude of the  $TE \times EE$  diagonal along  $+45^\circ$  lines, again according to results from test simulations:

$$\rho^{TE \times EE} = \frac{C_{ll}^{TE \times EE}}{\sqrt{\text{abs}\left(C_{ll}^{TE \times TE}\right) C_{ll}^{EE \times EE}}} \langle \rho^{TE \times TE} + \rho^{EE \times EE} \rangle. \quad (5.36)$$

The final  $TE \times EE$  cross-covariance matrix is computed via

$$C_{ll'}^{TE \times EE} = \rho^{TE \times EE} \sqrt{\text{abs}\left(C_{ll}^{TE \times TE}\right) C_{ll'}^{EE \times EE}} \quad (5.37)$$

In Figure 5.13 we plot a  $TE \times EE$  cross-covariance matrix measured from  $10^5$  simulations of CMB cross-spectra next to the same matrix constructed with the above procedure. Tests indicate that the theoretically expected cross-covariance can be reproduced with high fidelity given sufficient signal-to-noise in the input auto-covariance block matrices. Sufficient signal-to-noise is achieved if there is at least one simulation for every bandpower in the final  $TE$  and  $EE$  spectra.

## 5.5 Jackknives

To look for systematic signals contaminating our maps we design and perform a set of null tests known as jackknives. We define half-season splits designed to enhance a potential systematic signal. For example, if observations made with the Sun above the horizon were contaminated by the Sun, then by subtracting a coadd of “Sun-up” bundles from a coadd of “Sun-down” bundles the true sky signal would difference away and leave the contaminant. We generate cross-spectra from these differenced, or jackknife, bundles using the same procedures as those used to generate pseudo-spectra for the full season of data as described in Section 5.3. We bin these spectra into nine bandpowers of  $\Delta l = 500$  from  $500 < l < 5000$ . Next we calculate the  $\chi^2$  statistic with nine degrees of freedom to quantify the residual power compared to the null hypothesis: that there is no contaminant signal and that the bandpowers should be consistent with zero. We then compute and collect the probabilities to exceed (PTEs) for all jackknife tests performed on the 150 GHz  $TE$  and  $EE$  spectra. A uniform distribution of PTEs is expected between zero and one, and we *a priori* define a PTE less than 0.05 or greater than 0.95 as a jackknife failure and evidence of a systematic contaminant in our maps.

For the 2012 deep field analysis we define four separate jackknife tests. 1) We look for temporally-dependent systematics by differencing coadded bundles of the first half of the season from those of the second half. Potential systematics include drift in detector calibration, non-stationary readout noise, or Sun contamination after it rises at the end of the observing season. 2) We split bundles according to left-going or right-going telescope scans. This test searches for scan-dependent effects such as residual telescope wobble after steps in elevation, which only happen

Table 5.1: PTEs for SPTpol 2012 Deep Field Jackknife Tests

Jackknife	<i>TE</i>	<i>EE</i>
1st Half / 2nd Half	0.43	0.64
Left / Right	0.58	0.06
Ground	0.74	0.44
Moon	0.12	0.58

before right-going scans introducing a decaying modulated atmosphere signal into the maps. 3) Potential contamination from stationary objects or features on the ground is probed by making map coadds in az/el ground coordinates. We measure the RMS noise in these maps as a function of azimuth and rank each CMB field observation from least to most RMS noise based on its azimuth at the time of observation. Differencing the highest-RMS maps from the lowest-RMS maps generates a ground jackknife. 4) We test for potential systematics introduced when the Moon is above the horizon. The jackknife is simply differencing “Moon-up” against “Moon-down” observations.

There are a total of eight jackknife tests for the 2012 deep field analysis: four tests on both the *TE* and *EE* power spectra. The PTEs for each test is summarized in Table 5.1. Based on our *a priori* rubric, we find that our jackknife spectra pass all tests. We therefore conclude that our maps and resulting power spectra are free of significant systematic bias and we proceed to use them to place constraints on cosmological parameters.

## Chapter 6

### Cosmological Parameter Fitting

After data reduction is complete, we are left with three primary data products: a vector of bandpowers, a bandpower covariance matrix, and a set of bandpower window functions that enable one to compare the measured bandpowers to a theoretical spectrum. The task at hand is to take these data products and obtain constraints on cosmological parameters. We will describe in this chapter a fitting technique using a Bayesian likelihood formulation to estimate the goodness of fit of a given model to the data. This technique is easily extended to the process of Fisher Forecasting, a way for estimating the constraining power of an experiment even before data are collected, which we will briefly describe. Finally, we also discuss a Markov Chain Monte Carlo (MCMC) process for intelligently stepping through a many-dimensional parameter space to estimate the probability distribution functions of each model parameter. This discussion includes concerns of chain convergence as well as a description of a new likelihood code written by the author to obtain cosmological constraints from SPTpol data.

#### 6.1 Bayesian Likelihood

We adopt a Bayesian approach to determine the probability distribution functions (PDFs) of cosmological parameters of interest. To begin, Baye's Theorem states that

$$P(\vec{\theta}|\vec{D}) \propto \mathcal{L}(\vec{D}|\vec{\theta})P(\vec{\theta}), \quad (6.1)$$

where  $P(\vec{\theta}|\vec{D})$  is the posterior probability of an  $M$ -length vector of theory parameters  $\vec{\theta}$  given a data vector  $\vec{D}$ ,  $\mathcal{L}(\vec{D}|\vec{\theta})$  is the likelihood of the data given the input theory, and  $P(\vec{\theta})$  is the prior

probability on the theory parameters. Given the data we measure (the CMB polarization power spectra bandpowers), we would like to estimate the PDFs of theoretical cosmological parameters  $\vec{\theta}$ . In other words, we aim to determine the posterior probability of the theory parameters given the measured power spectra.

Estimating  $\vec{\theta}$  equates to maximizing the posterior probability in Equation 6.1. If the prior is uniform then maximizing the likelihood function  $\mathcal{L}(\vec{D}|\vec{\theta})$  also maximizes the posterior probability. What then is the likelihood for the measured bandpowers? Recall that a power spectrum  $C_l$  is the azimuthal average of a 2-D power spectrum, with a constant multipole  $l$  making a circle in Fourier space (Figure 5.8). As  $l$  increases so too does the circumference of the circle and therefore the number of measurements going into the  $C_l$  average. Thus, at even relatively low multipoles, the likelihood of the  $C_l$ 's or the binned bandpowers  $D_b$ 's is well-approximated by an  $N$ -dimensional Gaussian distribution according to the Central Limit Theorem,

$$\mathcal{L}(\vec{D}|\vec{\theta}) \simeq \frac{1}{\sqrt{(2\pi)^N |C_{bb'}(\vec{\theta})|}} \exp \frac{-\left(\vec{D}_b - \vec{D}_b^{\text{th}}(\vec{\theta})\right)^T C_{bb'}^{-1}(\vec{\theta}) \left(\vec{D}_{b'} - \vec{D}_{b'}^{\text{th}}(\vec{\theta})\right)}{2}, \quad (6.2)$$

where  $\vec{D}_b$  is an  $N$ -length vector of measured bandpowers,  $\vec{D}_b^{\text{th}}(\vec{\theta})$  is an  $N$ -length vector of theoretical bandpowers that are functions of the parameters  $\vec{\theta}$ , and  $C_{bb'}(\vec{\theta})$  is the  $N \times N$  bandpower covariance matrix, which is a function of the theory parameters through the sample variance component. Taking the natural log of  $\mathcal{L}(\vec{D}|\vec{\theta})$  and disregarding constants<sup>1</sup> we find

$$-2 \ln \mathcal{L} = \left(\vec{D}_b - \vec{D}_b^{\text{th}}(\vec{\theta})\right)^T C_{bb'}^{-1}(\vec{\theta}) \left(\vec{D}_{b'} - \vec{D}_{b'}^{\text{th}}(\vec{\theta})\right), \quad (6.3)$$

which we note is just a  $\chi^2$  statistic. Thus, maximizing the likelihood to determine best-fit (maximum likelihood) theoretical parameters  $\vec{\theta}_{\text{ML}}$  is simply a  $\chi^2$ -minimization problem.

We have so far assumed the prior  $P(\vec{\theta})$  is uniform, which would only add a constant to the  $\ln \mathcal{L}$ . In the analysis below we will apply a Gaussian prior to some of the parameters. This simply

---

<sup>1</sup> An additional term is also generated,  $\ln |C_{bb'}(\vec{\theta})|/2$ , but since in practice the data covariance matrix is kept constant during the minimization procedure it adds an arbitrary offset that does not effect what values of  $\vec{\theta}$  maximize the likelihood.

adds an additional  $\chi^2$  term to the  $\ln \mathcal{L}$ ,

$$\chi_{prior}^2(\vec{\theta}) = \sum_i \frac{(\theta_i - \hat{\theta}_i)^2}{\sigma_{\theta_i}^2} \quad (6.4)$$

where  $\hat{\theta}_i$  is the expected mean of parameter  $\theta_i$ ,  $\sigma_{\theta_i}^2$  is its variance, and  $i$  indexes all parameters with Gaussian priors. We then minimize the total  $\ln \mathcal{L}$  to find  $\vec{\theta}_{ML}$ .

In summary, by using a Bayesian approach we have reduced the complicated process of cosmological parameter estimation to a simple  $\chi^2$ -minimization operation. The inputs are the measured CMB power spectra bandpowers  $D_b$ , their covariance matrix  $C_{bb'}$ , and the bandpower window functions  $W_l^b/l$  that are used to bin theoretical spectra into bandpowers  $D_b^{\text{th}}(\vec{\theta})$ . By varying  $\vec{\theta}$  we map out the PDFs of the theoretical parameters to determine their maximum likelihood values  $\vec{\theta}_{ML}$  and estimate their variance.

## 6.2 Fisher Forecasting

It is possible to extend the Bayesian treatment above to forecast how well a future experiment will constrain cosmological parameters even before any data are collected. In the following we adapt the treatment of (29) to derive an estimate of new parameter constraints from several CMB power spectra fitted simultaneously with uncertainties quantified by the parameter covariance matrix  $C_{\theta_i \theta_j}$ . We will employ the Fisher information matrix and thus this technique is called Fisher forecasting.

### 6.2.1 Fisher Formalism

We begin by noting that the uncertainty of a given parameter  $\theta_i$  is related to the curvature of the likelihood (85),

$$\mathcal{F} = -\frac{\partial^2 \ln \mathcal{L}}{\partial \theta_i^2}. \quad (6.5)$$

Evaluated at  $\theta_{i,ML}$  where the likelihood is maximized, the curvature tells us how “peaky” the likelihood is. If the curvature is high the likelihood is very peaked at  $\theta_{i,ML}$  and so falls off rapidly as you move away from the parameter’s maximum likelihood value. In this case  $\theta_{i,ML}$  has low

uncertainty. On the other hand, if the curvature is low the likelihood is relatively smooth near  $\theta_{i,\text{ML}}$ . A large region of parameter space has nearly the same value for the  $\ln \mathcal{L}$  and so  $\theta_{i,\text{ML}}$  has a larger uncertainty.

If we take many measurements and average the likelihood curvature we obtain the  $M \times M$  Fisher information matrix,

$$F_{\theta_i \theta_j} = - \left\langle \frac{\partial^2 \ln \mathcal{L}}{\partial \theta_i \partial \theta_j} \right\rangle, \quad (6.6)$$

where we have generalized to multiple variables  $\vec{\theta} = (\theta_i, \theta_j, \dots, \theta_M)$ . In the limit that the  $\ln \mathcal{L}$  is Gaussian the inverse of the Fisher matrix gives us the parameter covariance

$$C_{\theta_i \theta_j} \geq (F^{-1})_{\theta_i \theta_j}. \quad (6.7)$$

We have invoked the Cramer-Rao bound, which states that the true parameter covariance cannot be smaller than that estimated from the inverse Fisher matrix (85).

Given our formulation of the  $\ln \mathcal{L}$  from Equation 6.3, let us now derive the Fisher matrix for cosmological parameter estimation. For ease of derivation we will assume the bandpower covariance matrix is diagonal with elements  $C_{bb}$ . It will later be a trivial matter to generalize to a non-diagonal covariance matrix. We will also work with  $M = 1$  theory parameters to start. First we note that the matrix operation of Equation 6.3 can be rewritten as a summation over the  $N$  bandpowers  $D_b$

$$-\ln \mathcal{L} = \frac{\chi^2}{2} = \sum_{b=1}^N \frac{(D_b - D_b^{\text{th}})^2}{2C_{bb}}. \quad (6.8)$$

We have assumed flat priors on all parameters for simplicity.<sup>2</sup> We must only take the second derivative with respect to a single parameter  $\theta$  to find the curvature matrix:

$$\begin{aligned} \frac{-d \ln \mathcal{L}}{d\theta} &= \sum_b - \left( D_b - D_b^{\text{th}}(\theta) \right) \frac{dD_b^{\text{th}}(\theta)}{d\theta} \\ \mathcal{F} = \frac{-d^2 \ln \mathcal{L}}{d\theta^2} &= \sum_b \frac{1}{C_{bb}} \left[ \left( \frac{dD_b^{\text{th}}(\theta)}{d\theta} \right)^2 + \left( D_b^{\text{th}}(\theta) - D_b \right) \frac{d^2 D_b^{\text{th}}(\theta)}{d\theta^2} \right]. \end{aligned} \quad (6.9)$$

---

<sup>2</sup> In practice the cosmological parameters are quite sensitive to the CMB power spectra bandpowers making the  $\ln \mathcal{L}$  in the vicinity of the best-fit parameters reasonably peaky. Since the data themselves are therefore quite discriminatory, whether the parameter priors are uniform or Gaussian affects the parameter posterior probability very little. We use Gaussian priors only for instrument-specific “nuisance” parameters in our likelihood.

Note that  $D_b$  and  $C_{bb}$  are measured or defined and thus do not vary with  $\theta$ .<sup>3</sup> Averaging over the distribution to obtain the Fisher matrix  $F$  we note that the second term tends to zero since the measured  $D_b$  are sometimes greater and sometimes less than the theoretical  $D_b^{\text{th}}$ . Thus for a single parameter we find that the  $1 \times 1$  Fisher matrix is given by

$$F_{\theta\theta} = \sum_b \frac{1}{C_{bb}} \left( \frac{dD_b^{\text{th}}(\theta)}{d\theta} \right)^2. \quad (6.10)$$

To Fisher forecast the constraining power of a new or on-going CMB experiment we must only have a model or estimate of its bandpower covariance matrix and knowledge of how the theoretical bandpowers vary as functions of our chosen cosmological parameters. The as yet unmeasured bandpowers are conveniently not required, however Equation 6.10 must be evaluated at a specific value of  $\theta$  so the result is model-dependent.

The above discussion assumes a uniform prior on the cosmological parameters. If, on the other hand, we have prior knowledge on the parameters from, say, a past experiment we can forecast the constraints from fitting both experiments' data simultaneously (e.g. 86). If a prior experiment measures a parameter variance  $C_{\theta\theta}^A$  and we calculate a Fisher matrix for a new experiment  $F_{\theta\theta}^B$ , then the combined parameter constraints are just

$$C_{\theta\theta}^{A+B} = \left[ (C_{\theta\theta}^A)^{-1} + F_{\theta\theta}^B \right]^{-1}. \quad (6.11)$$

That is, simply add the Fisher matrices of the two experiments and take the inverse to find the combined parameter constraints.

### 6.2.2 Generalized Fisher Formalism

Equation 6.10 is easily extended to multiple theoretical parameters  $\vec{\theta}$ . The elements of the full Fisher matrix, and in turn the parameter covariance matrix, are then given by

$$(C^{-1})_{\theta_i \theta_j} \leq F_{\theta_i \theta_j} = \sum_b \frac{1}{C_{bb}} \left( \frac{\partial D_b^{\text{th}}(\vec{\theta})}{\partial \theta_i} \right) \left( \frac{\partial D_b^{\text{th}}(\vec{\theta})}{\partial \theta_j} \right). \quad (6.12)$$

---

<sup>3</sup> As noted above,  $C_{bb}$  has a sample variance component and is therefore technically a function of  $\theta$ . However, when forecasting parameter constraints a theoretical model is assumed around which we calculate the curvature of the likelihood. Therefore  $C_{bb}$  remains constant.

This treatment still assumes that the covariance matrix is diagonal, however. Since the CMB power spectra are correlated, resulting in a block-diagonal covariance matrix even in a full-sky treatment where mode-coupling is zero, the theoretical bandpowers are restricted to a single power spectrum;  $TE$  or  $EE$  but not both. If we wish to forecast the constraining power of multiple CMB power spectra fitted simultaneously we must revert to a matrix formalism:

$$F_{\theta\theta'} = \left( \frac{\partial \vec{D}_b^{\text{th}}(\vec{\theta})}{\partial \vec{\theta}} \right)^T (C_{bb'})^{-1} \left( \frac{\partial \vec{D}_{b'}^{\text{th}}(\vec{\theta}')}{\partial \vec{\theta}'} \right). \quad (6.13)$$

$\vec{D}_b^{\text{th}}$  is now an  $N \cdot S$ -length vector and  $C_{bb'}$  is an  $N \cdot S \times N \cdot S$  bandpower covariance matrix for  $S$  power spectra each with  $N$  bandpowers. The bandpower covariance matrix is now inverted, which can be a difficult numerical problem depending on the signal-to-noise of the model covariance matrix. However, no assumptions have been made about its shape so we are free to model off-diagonal effects like mode-coupling if we so choose. Finally, the sum over bandpowers is taken care of automatically by matrix multiplication (outer product) operations.

To evaluate  $F_{\theta\theta'}$  we assume a particular theoretical model  $\vec{\theta}_{\text{ML}}$  about which to calculate the likelihood curvature and determine how the resulting theoretical power spectra vary as functions of the input parameters. This need only be done once for a given model. By using an accurate Boltzmann code called CAMB (Code for Anisotropies in the Microwave Background, (32)) to generate CMB power spectra for given values of cosmological parameters, we numerically evaluate the bandpower partial derivatives

$$\left. \frac{\partial \vec{D}_b^{\text{th}}(\vec{\theta})}{\partial \theta_i} \right|_{\vec{\theta}=\vec{\theta}_{\text{ML}}} \cong \frac{\vec{D}_b^{\text{th}}(\vec{\theta}_{\text{ML}} + \Delta\theta_i) - \vec{D}_b^{\text{th}}(\vec{\theta}_{\text{ML}} - \Delta\theta_i)}{2\Delta\theta_i} \quad (6.14)$$

for a small change in a parameter value  $\Delta\theta_i$ . These are compiled into an  $N \cdot S \times M$  matrix, transposed, and matrix multiplied with the bandpower covariance matrix to obtain the final  $M \times M$  Fisher matrix. Power spectrum partial derivatives as functions of several  $\Lambda$ CDM cosmological parameters are plotted in Figure 6.1. One can immediately glean insight into how parameters affect the CMB power spectra. For example, the spectrum derivatives with respect to  $\Omega_b h^2$  and  $\Omega_c h^2$  oscillate around zero indicating these two parameters affect the location of the acoustic peaks. The scalar amplitude  $A_s$  and the optical depth  $\tau$ , however, mostly affect the amplitude of the spectra.

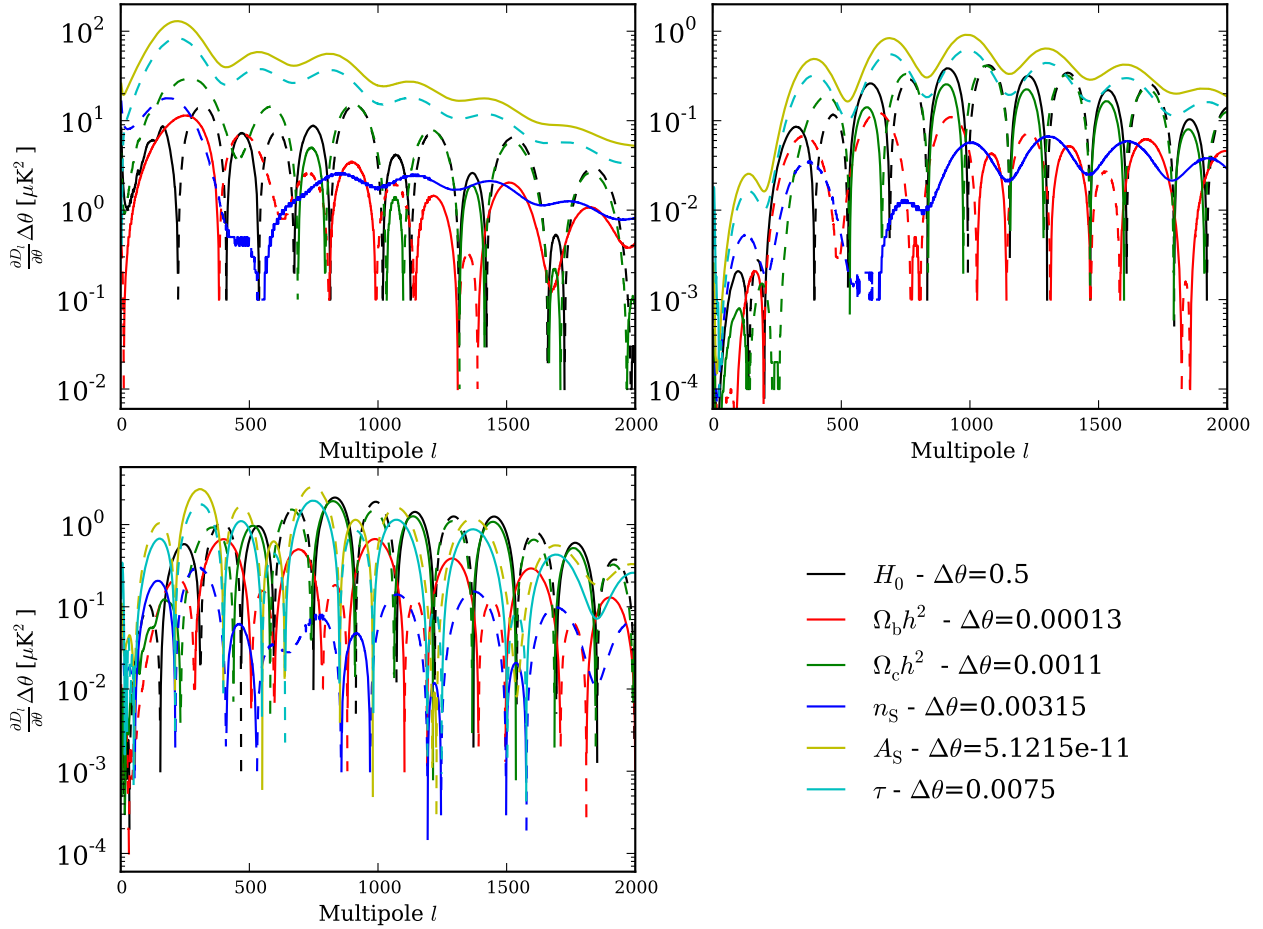


Figure 6.1: Partial derivatives of CMB power spectra with respect to  $\Lambda$ CDM cosmological parameters used to obtain parameter Fisher forecasts. Derivatives are calculated numerically using CAMB and the step sizes printed in the figure legend. (Top Left)  $D_l^{TT}$  derivatives. (Top Right)  $D_l^{EE}$  derivatives. (Bottom Left)  $D_l^{TE}$  derivatives. Dashed lines are negative values.

### 6.2.3 Estimating the Bandpower Covariance Matrix

We must also estimate a future experiment's bandpower covariance matrix in order to carry out the parameter forecast. To do so we again use the theoretical expectations for power spectra covariances from (84) cited in Equations 5.33. We assume the bandpower covariance matrix is block diagonal. While we know this will not be true since no experiment can measure the full sky and therefore mode-coupling will be present, this represents a best-case scenario. Again invoking the Cramer-Rao bound we know that any future parameter constraints after an experiment collects

data must necessarily be no better than those obtained from this treatment assuming we evaluate the Fisher matrix at the true maximum likelihood parameter values  $\vec{\theta}_{\text{ML}}$ . Expanding the noise spectra  $N_l$  we find

$$\begin{aligned} C_{ll}^{TT \times TT} &= \frac{2}{(2l+1)f_{\text{sky}}} \left( C_l^{TT} + w_T^{-1} e^{l^2 \sigma^2} \right) \\ C_{ll}^{EE \times EE} &= \frac{2}{(2l+1)f_{\text{sky}}} \left( C_l^{EE} + w_P^{-1} e^{l^2 \sigma^2} \right) \\ C_{ll}^{TE \times TE} &= \frac{1}{(2l+1)f_{\text{sky}}} \left[ (C_l^{TE})^2 + \left( C_l^{TT} + w_T^{-1} e^{l^2 \sigma^2} \right) \left( C_l^{EE} + w_P^{-1} e^{l^2 \sigma^2} \right) \right], \end{aligned} \quad (6.15)$$

and similarly for the cross-covariance blocks. We will call these “Knox formula errors” after the author who first formulated these theoretical expectations (87). Here we approximate the experiment’s beam as Gaussian with a standard deviation in radians given by

$$\sigma = \frac{\gamma_b}{\sqrt{8 \log 2}} \frac{\pi}{10800}, \quad (6.16)$$

where  $\gamma_b$  is the beam FWHM in arcminutes. In the limit that map noise is white as a function of multipole then the beam function defines the shape of the noise spectrum. The amplitude of the noise term is given by the inverse weight in units of  $\mu\text{K}^2$

$$w_X^{-1} = \left( n_X \frac{\pi}{10800} \right)^2 \quad (6.17)$$

where  $n_X$  is the forecasted survey map depth in  $\mu\text{K}\cdot\text{arcmin}$  and  $X \in \{T, P\}$ .

#### 6.2.4 SPTpol Forecasts

As discussed in Section 5.2, the SPTpol deep field in 2012 achieved a final depth of 7 (10)  $\mu\text{K}\cdot\text{arcmin}$  in  $T$  ( $P$ ) at 150 GHz over  $100 \text{ deg}^2$  and we predict the same depth over  $500 \text{ deg}^2$  after three full years of observing on the full survey field. Using these depths as well as the measured beam FWHM of  $1.18'$  we generate 100 realizations of  $TE$  and  $EE$  bandpowers. To each theoretical bandpower  $D_b^{\text{th}}$  we add a small offset  $\delta D_b$  defined as Knox formula error times Gaussian noise centered at zero with unit standard deviation. An average bandpower over many realizations will be the theoretical expectation, and the standard deviation of a given bandpower will be the Knox

Table 6.1: SPTpol Fisher Forecasts for  $\Lambda$ CDM Parameters

Dataset	Cosmological parameter constraints					
	$\sigma(\Omega_b h^2) \times 10^4$	$\sigma(\Omega_c h^2) \times 10^3$	$\sigma(\log(10^{10} A_s)) \times 10^2$	$\sigma(n_s) \times 10^3$	$\sigma(\Sigma m_\nu)$ [meV]	$\sigma(Y_p) \times 10^2$
PLANCK-2013	2.83	2.67	2.48	7.31	302	2.36
+ SPT-POL-DF	2.77	2.56	2.42	7.06	<b>250</b>	2.33
+ SPT-POL-FF3YR	2.60	<b>2.23</b>	<b>2.21</b>	<b>6.38</b>	<b>177</b>	2.23

**Notes:** Two single-parameter extensions are included; the sum of the masses of neutrino species  $\Sigma m_\nu$ , and the primordial helium abundance  $Y_p$ . SPT-POL-DF is the 100 deg<sup>2</sup> deep field, (500 <  $l$  < 3000), and SPT-POL-FF3YR is the completed 3-year 500 deg<sup>2</sup> full field survey, (50 <  $l$  < 3000). SPT-POL-DF and SPT-POL-FF3YR projections include  $TE$  and  $EE$  150 GHz bandpowers only. Blue (orange) constraints are improvements by at least a factor of 1.10 (1.5) over the PLANCK-2013 temperature-only constraints (31).

error. We plot the average bandpower over 100 realizations  $D_b^{\text{th}}$  with their Knox errors overtop of measured SPTpol deep field  $TE$  and  $EE$  bandpowers in Figure 6.2.

Using the resulting covariance matrix generated from these 100 bandpower realizations we forecasted new  $\Lambda$ CDM parameter constraints including PLANCK-2013 data, which we present in Table 6.1. We consider separately the addition of the 100 deg<sup>2</sup> deep field bandpowers SPT-POL-DF at 500 <  $l$  < 3000 and the bandpowers from the completed three-year 500 deg<sup>2</sup> full survey SPT-POL-FF3YR at 50 <  $l$  < 3000. In both cases we only consider the  $TE$  and  $EE$  bandpowers at 150 GHz but the forecasting process is easily extended to additional power spectra and multiple frequencies (and their cross-spectra). While improvements over  $\Lambda$ CDM parameters are expected to be modest, the SPTpol dataset will begin exploring a large parameter-space of model extensions sensitive to the physics of the power spectra damping tails, of which we only show two: the sum of the neutrino masses  $\Sigma m_\nu$  and the amount of primordial helium  $Y_p$ . Additionally, we note that even without information on  $BB$  spectra, the  $TE + EE$  bandpowers from the completed 500 deg<sup>2</sup> survey will significantly increase our constraints on  $\Sigma m_\nu$  through its effect on the lensing of the CMB power spectra.

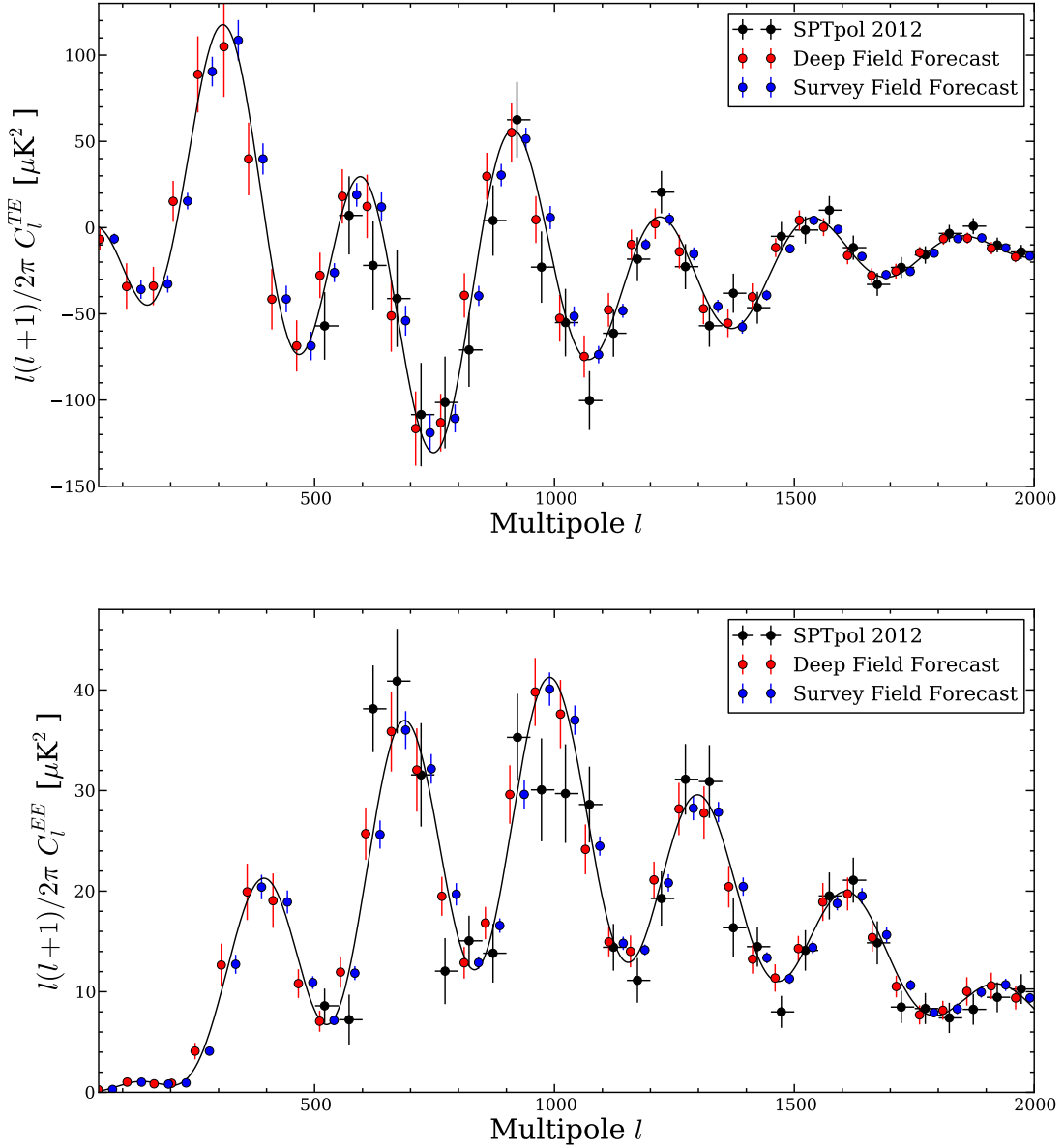


Figure 6.2: The SPTpol 150 GHz 2012 deep field  $TE$  (Top) and  $EE$  (Bottom) power spectra (black) plotted with averaged Fisher forecasted bandpowers for the 2012 deep field and completed full survey (red/blue). Forecasted bandpowers are offset by  $\Delta l \pm 15$  for clarity. The average of 100 random bandpower realizations agrees with the input cosmological theory (solid line). Forecasted error bars for the deep field are everywhere comparable to but better than the measured uncertainties, as expected.

### 6.3 Parameter Fitting Through MCMC

We obtain constraints on cosmological parameters using the CosmoMC package (38). While calculating the likelihood as discussed in Section 6.1 is straightforward, including instrument-specific nuisance parameters we must explore a  $\sim 10$ -D parameter space to search for the global  $\chi^2$  minimum and the curvature of the likelihood about that point. Performing a thorough grid search over this volume is impossible. Instead, we use a Markov Chain Monte Carlo (MCMC) approach to intelligently step through parameter space to find the maximum likelihood values of the cosmological parameters. In this section we will briefly review the basic MCMC algorithm employed by CosmoMC. We will then describe the new likelihood package we have written to handle SPTpol datasets. Finally, we will describe a new  $\Lambda$ CDM extension we have included in CosmoMC to place constraints on energy injected into the CMB via WIMP particle annihilation as explored by (88) to which Fisher forecasts predict SPTpol will be sensitive.

#### 6.3.1 Markov Chain Monte Carlo

In order to intelligently sample a large volume of parameter space one must resort to a method that preferentially finds and samples regions of high probability density. The method employed by CosmoMC is Markov Chain Monte Carlo (MCMC). In this context, a Markov chain is a countable stochastic sequence of parameter states  $\vec{\theta}^n$  with  $n$  steps for which the probability of every state is only dependent on the previous state (e.g. 89),

$$Pr \left( \vec{\theta}^{n+1} | \vec{\theta}^n, \vec{\theta}^{n-1}, \dots, \vec{\theta}^1 \right) = Pr \left( \vec{\theta}^{n+1} | \vec{\theta}^n \right). \quad (6.18)$$

We wish to define an algorithm that chooses steps in parameter space  $\vec{\theta}$  causing a chain to linger in regions of high probability density such that the number of samples in a region is proportional to the probability density. When convergence criteria are met, samples in the chain are drawn from a distribution function  $f(\vec{\theta})$  that approximates the  $N$ -dimensional parameter posterior distribution function  $P(\vec{\theta})$ . As the number of samples  $n$  increases  $f(\vec{\theta}) \rightarrow P(\vec{\theta})$ .

CosmoMC has several stepping algorithm choices and we use the standard Metropolis-Hastings option for the cosmological constraints presented in this work. The algorithm is as follows:

- (1) Choose an initial set of parameter values  $\vec{\theta}^{n=1}$ .
- (2) Step the parameter values to  $\vec{\phi}$  according to a symmetric proposal density  $q(\vec{\phi}|\vec{\theta}^n) = q(\vec{\theta}^n|\vec{\phi})$ .

The proposal density defines the step size one should take in parameter space and is usually taken as Gaussian when no information about the parameters is known. Here it is defined as a parameter-parameter covariance matrix as measured by Planck. It is updated as a chain progresses.

- (3) Calculate an acceptance probability  $\alpha$  to accept the move to  $\vec{\phi}$ ,

$$\alpha(\vec{\phi}|\vec{\theta}^n) = \min \left\{ 1, \frac{P(\vec{\phi})}{P(\vec{\theta}^n)} \right\}. \quad (6.19)$$

The probability density  $P(\vec{\phi})$  is calculated by generating a set of theoretical CMB power spectra given  $\vec{\phi}$  and passing these spectra to the SPTpol likelihood module (see Section 6.3.3) to compare to the measured bandpowers.

- (4) If  $\alpha = 1$  then move to the new position  $\vec{\theta}^{n+1} = \vec{\phi}$ , otherwise move with the probability  $\alpha$ .  
If the move is rejected then set  $\vec{\theta}^{n+1} = \vec{\theta}^n$ .
- (5) Repeat until desired convergence criteria are met (Section 6.3.2). The density of samples in parameter space is then a measurement of the desired probability distribution function  $P(\vec{\theta})$ .

The first point in parameter space  $\vec{\theta}^1$  is not in general near the region of highest probability density. Therefore each chain will have a “burn-in” period. During burn-in the probability distribution  $f(\vec{\theta})$  the chain is sampling does not well-approximate the desired distribution  $P(\vec{\theta})$ . These chain steps must be discarded to keep from biasing our estimate of  $P(\vec{\theta})$ . To quantitatively determine the burn-in period of a chain one can divide the chain into smaller units and study the resulting parameter means and variances. The burn-in portion will yield results discrepant with

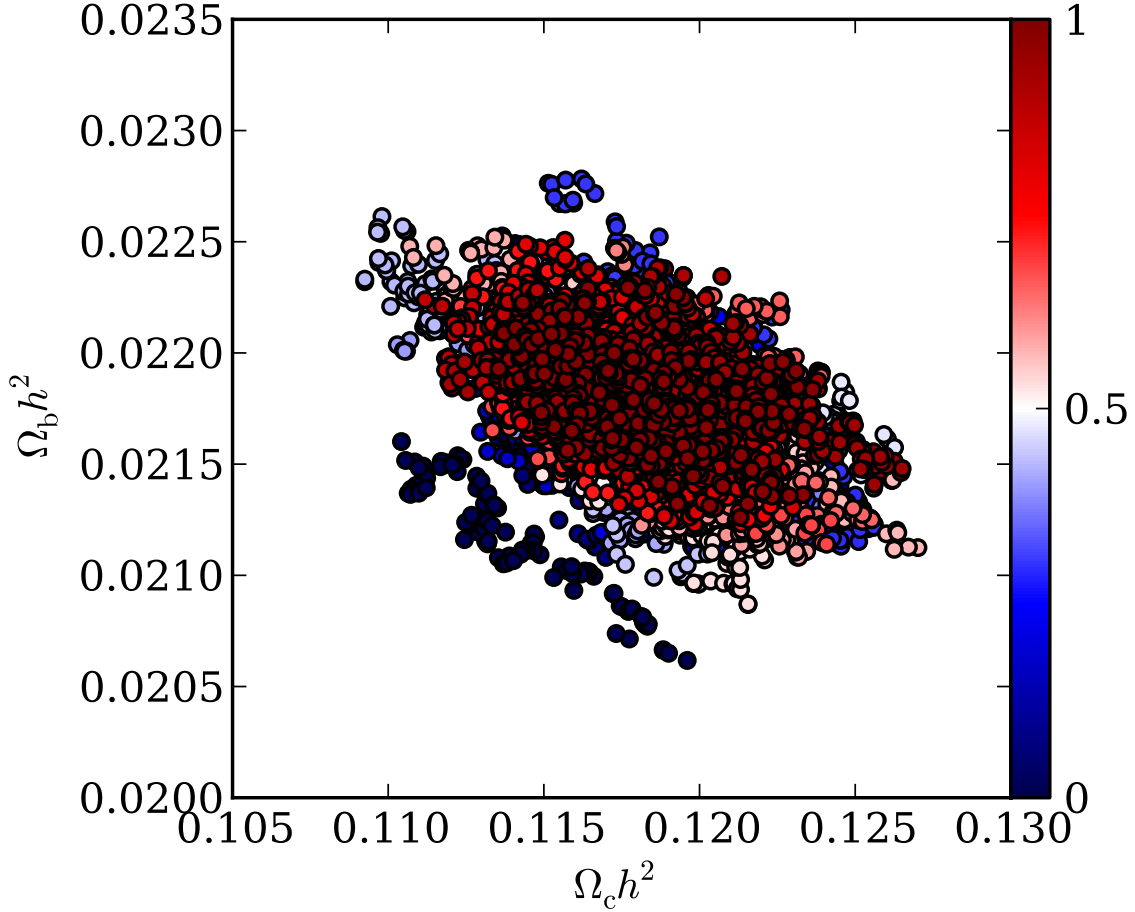


Figure 6.3: Representative 2-D slice in the  $\Omega_{\text{c}}h^2 - \Omega_{\text{b}}h^2$  plane of a Markov chain. The color bar designates at what fractional point in the chain each step takes place. The initial steps of the chain in dark blue are “burn-in.” When the first half of the chain is thrown out, however, the remaining steps are draws from the desired probability distribution function  $P(\vec{\theta})$ .

the distribution of results from the rest of the chain sub-units. Figure 6.3 shows an example of a series of chain steps measuring the probability density of  $\Omega_{\text{c}}h^2$  and  $\Omega_{\text{b}}h^2$ . We conservatively take the burn-in period to be the first 50% of chain steps, which are color-coded blue in the figure. The start of the chain in dark blue clearly measures a distribution that does not well approximate  $P(\vec{\theta})$ . The density of the remaining red chain points, however, directly corresponds to the marginalized probability densities of  $\Omega_{\text{c}}h^2$  and  $\Omega_{\text{b}}h^2$ .

### 6.3.2 Chain Convergence

As discussed above, the distribution function  $f(\vec{\theta})$  a Markov chain draws from only approaches the desired posterior distribution  $P(\vec{\theta})$  as the number of samples  $n \rightarrow \infty$ . We must therefore determine what  $n$  is sufficient to consider  $f(\vec{\theta})$  a reasonable approximation for  $P(\vec{\theta})$ , after which we call the chain “converged.” To test for chain convergence we use a variant of an empirical estimator posed by (90). The test requires running several chains in parallel. In this analysis, we run  $m = 8$  chains for every combination of input data and model of interest. Furthermore, consider chain  $i$  a series of  $n$  steps  $\{\psi_i^1, \psi_i^2, \dots, \psi_i^n\}$  following the nomenclature of (89). Then for each parameter  $\theta$  in a given model we consider the ratio of the variance of the chain means  $B$  over the mean of the chain variances  $W$

$$\begin{aligned}\bar{\psi}_i(\theta) &= \frac{1}{n} \sum_{j=1}^n \psi_i^j(\theta) \\ B(\theta) &= \frac{1}{m-1} \sum_{i=1}^m (\bar{\psi}_i(\theta) - \bar{\psi}(\theta))^2 \\ W(\theta) &= \frac{1}{m(n-1)} \sum_{i=1}^m \sum_{j=1}^n (\psi_i^j(\theta) - \bar{\psi}_i(\theta))^2 \\ R_\theta &= \frac{B(\theta)}{W(\theta)}.\end{aligned}\tag{6.20}$$

Here we have defined  $\bar{\psi}_i(\theta)$  to be the average value for  $\theta$  from chain  $i$  and  $\bar{\psi}(\theta)$  the average value of  $\theta$  from all chains.  $R_\theta$  is always greater than one, but as the number of samples  $n \rightarrow \infty$   $R_\theta \rightarrow 1$ . Typically,  $R_\theta < 1.2$  is taken as evidence for convergence (91); for this analysis we consider  $R_\theta < 1.1$  for all parameters as a necessary condition for chain convergence. A similar statistic is also calculated for each eigenvalue  $\lambda$  of the covariance matrix of the chain means, where there are  $N$  eigenvalues for  $N$  parameters in  $\vec{\theta}$ . For all eigenvalues we require  $R_\lambda < 1.1$  for convergence. We consider  $R_\theta, R_\lambda < 1.1$  for all  $\theta$  and  $\lambda$  as sufficient criteria for chain convergence in this analysis.

### 6.3.3 The SPTpol Likelihood

To calculate the likelihood for the SPTpol bandpowers, we have written a new likelihood module for CosmoMC specific to SPTpol. While only 150 GHz  $TE$  and  $EE$  data are included in

this analysis, with trivial extensions the SPTpol likelihood module will handle all six unique cross- and auto-spectra between  $T$ ,  $E$ , and  $B$  maps, as well as multiple frequencies simultaneously in future analyses.

In addition to the six standard  $\Lambda$ CDM parameters, the SPTpol likelihood introduces four nuisance parameters specific to the SPTpol experiment and analysis. The first two are foreground terms,  $D_{3000}^{\text{PSEE}}$  and  $D_{3000}^{\text{PSTE}}$ , parameterizing the level of residual polarized point source power at  $\ell = 3000$  in the  $EE$  and  $TE$  spectra after point source masking. Point source power between  $T$  and  $E$  maps should not be correlated as there should be no preferred polarization direction for point sources. However, we have found that differential beam ellipticity between two detectors in a polarization-sensitive pair can leak unpolarized Poisson power into our E-mode maps, which shows up as non-zero point source power in our  $TE$  spectrum. Thus we keep the nuisance  $TE$  Poisson term to characterize this systematic power. We give these foreground parameters uniform priors ranging from 0 to  $10 \mu\text{K}^2$ . The third and fourth nuisance parameters are temperature and polarization calibration,  $T_{\text{cal}}$  and  $P_{\text{cal}}$ , respectively. After rescaling the bandpowers and covariance matrix according to the calibration parameters as discussed in Sections 5.2.1 and 5.2.2 we apply a  $\pm 5\sigma$  Gaussian prior to  $T_{\text{cal}}$  centered on unity with a standard deviation of 0.0137. Finally, we keep a uniform prior from 0.5 to 1.5 on  $P_{\text{cal}}$  to obtain an analysis-independent measurement of any residual polarization mis-calibration.

The likelihood module takes as input the three primary SPTpol analysis products: a list of  $TE$  and  $EE$  bandpowers, their  $2 \times 2$  block covariance matrix, and their bandpower window functions. While this analysis includes only 150 GHz data, with keyword flags the likelihood module can accept other auto- and cross-frequency spectra, as well as other CMB power spectra besides  $TE$  and  $EE$ . Therefore future SPTpol analyses will be able to immediately obtain cosmological constraints when considering many more spectra. The module also requires a parameter .INI file to specify the priors to place on the four nuisance parameters. With this parameterization we choose to let CosmoMC find our calibration uncertainties for us by leveraging the prior knowledge we have of the  $\Lambda$ CDM

model<sup>4</sup>. Therefore we do not include calibration covariance in the bandpower covariance matrix.

After initializing data arrays, the likelihood calculates expected “foreground” spectra using  $C_l$  normalization. Both the  $EE$  and  $TE$  foreground spectra contain a WIMP annihilation correction spectrum (see Section 6.3.5). These correction spectra are collectively parameterized by a single amplitude  $e_{\text{WIMP}}$  for  $TT$ ,  $TE$ , and  $EE$  power spectra. The  $EE$  and  $TE$  spectra also include the Poisson terms discussed above to quantify residual polarized point source power after point source masking. These nuisance foreground parameters are converted to  $C_l$  normalization for this calculation. The foreground spectra are then added to the theoretical CMB power spectra calculated by CAMB for a given set of parameter values  $\vec{\theta}$ , which are scaled by the SPTpol calibration parameters:

$$\begin{aligned} C_l^{TE}(\vec{\theta}) &\rightarrow \frac{1}{T_{\text{cal}}^2 P_{\text{cal}}} C_l^{TE}(\vec{\theta}) \\ C_l^{EE}(\vec{\theta}) &\rightarrow \frac{1}{T_{\text{cal}}^2 P_{\text{cal}}^2} C_l^{EE}(\vec{\theta}). \end{aligned} \quad (6.21)$$

The calibration parameters are defined as corrections at the map level so the absolute calibration  $T_{\text{cal}}$  comes in squared while  $P_{\text{cal}}$  comes in as the number of polarization maps used to generate a particular power spectrum. The parameters calibrate the *measured* SPTpol bandpowers, so they are applied to the theoretical spectra in a reciprocal sense.

The combined expected  $TE$  and  $EE$  spectra are converted to  $D_l$  normalization and binned with the SPTpol bandpower window functions to generate theoretical bandpowers  $D_b^{\text{th}}$  according to Equation 5.17. A Gaussian likelihood is then calculated given these theoretical bandpowers, the measured SPTpol bandpowers  $D_b^{\text{SPTpol}}$ , and the SPTpol bandpower covariance matrix  $C_{bb'}$ . Finally, to include the effects of a Gaussian prior on  $T_{\text{cal}}$  we add the negative natural logarithm of a Gaussian centered around the  $T_{\text{cal}}$  expectation  $\mu_T = 1.0$  with a standard deviation of  $\sigma_T = 0.0137$  from Section 5.2.1<sup>5</sup>. The total SPTpol likelihood for a given set of theory and nuisance parameters

---

<sup>4</sup> This could, of course, bias our results if we freeze parameter values to current best-fit values as constrained by other experiments. More accurately, we can fit SPTpol data simultaneously with other data, in particular data from Planck, which for our purposes has effectively zero noise at large angular scales and thus tightly constrains the amplitude of the spectrum.

<sup>5</sup> The absolute calibration factor of 0.8933 is already applied to the SPTpol maps, making the expectation value in the power spectra unity.

$\vec{\theta}$  is thus given by

$$\begin{aligned} -\ln \mathcal{L}_{\text{SPTpol}} &= \left( D_b^{\text{SPTpol}} - D_b^{\text{th}} \right)^T C_{bb'}^{-1} \left( D_{b'}^{\text{SPTpol}} - D_{b'}^{\text{th}} \right) + \frac{|\ln C_{bb'}|}{2} \\ -\ln \mathcal{L}_{\text{Prior}} &= \frac{1}{2} \frac{(T_{\text{cal}} - \mu_T)^2}{\sigma_T^2} + \frac{\ln \sigma_T^2}{2} \\ \ln \mathcal{L}_{\text{Total}} &= \ln \mathcal{L}_{\text{SPTpol}} + \ln \mathcal{L}_{\text{Prior}}. \end{aligned} \quad (6.22)$$

The total likelihood is returned to CosmoMC, which compares it to the current likelihood value and determines whether to take a step in parameter space and how large that step should be. It is clear from Equations 6.22 that  $\vec{\theta} = \vec{\theta}_{\text{ML}}$  when  $\ln \mathcal{L}_{\text{Total}}$  is minimized.

### 6.3.4 Likelihood Validation

To validate the new likelihood module operates as anticipated we ran a test chain in CosmoMC with one of the 204 realizations of simulated bandpowers used to estimate the bandpower sample variance as input. As we do for cosmological constraints from the measured SPTpol deep field bandpowers, 150 GHz *TE* and *EE* bandpowers are included from  $500 < l < 5000$ . We used the complete bandpower covariance matrix as calculated in Section 5.4.5 but left out calibration covariance as discussed above. The final SPTpol 2012 deep field bandpower window functions were also used. If the likelihood module is working as intended, and the covariance matrix properly accounts for correlations between the *TE* and *EE* spectra, the best-fit cosmological parameters should agree with the input parameters used to generate the simulations. In Figure 6.4 we plot the resulting 2D marginalized parameter contours from this test chain. In red we plot the 2D contours from Planck, the best-fit values from which were inputs to the SPTpol simulations. In black are the parameter constraints from the simulated bandpowers binned to  $\Delta l = 50$ . We also plot the bandpowers binned to  $\Delta l = 100$  in blue. The latter is a test that our window functions are calculated properly. So long as the binning is not so coarse that we smooth over relevant features in the power spectra, the cosmological parameter constraints should be independent of multipole binning since the bandpower window functions encode how to translate from bandpowers to single multipoles. All the parameter constraints for both binning cases agree with the input parameters to

Table 6.2: CosmoMC minimizer results for 204 sets of simulated SPTpol bandpowers.

$\theta$	$\theta^{\text{th}}$	$\mu_\theta$	$\sigma_\theta$	$\Delta\theta/\sigma_\theta$
$\Omega_b h^2$	0.0222	0.0221	0.0004	-0.28
$\Omega_c h^2$	0.1185	0.1179	0.0034	-0.17
$n_S$	0.9624	0.9609	0.0077	-0.19
$\ln 10^{10} A_S$	3.0947	3.0987	0.0357	0.11
$100\theta_{\text{MC}}$	1.0415	1.0413	0.0011	-0.12
$H_0$	67.94	68.08	1.37	0.10
$T_{\text{cal}}$	1.00	0.9994	0.0025	-0.24
$P_{\text{cal}}$	1.00	0.9970	0.0218	-0.14

within a fraction of the  $1-\sigma$  uncertainties suggesting that the likelihood and bandpower covariance matrix are working as intended.

The CosmoMC package also has a minimizer routine, which finds the best-fit parameter values but does not thoroughly explore parameter space. By using the minimizer on all 204 sets of simulated bandpowers we can quickly find the best-fit parameters for each realization and compare the resulting parameter distributions to the simulation input parameters. This provides an additional consistency test for the SPTpol likelihood and the bandpower covariance matrix. In Table 6.2 we include the input parameter values  $\theta^{\text{th}}$ , mean parameter values  $\mu_\theta$  from the CosmoMC minimizer, the standard deviation of the minimizer values  $\sigma_\theta$ , and the fractional differences between expected and measured values scaled by the standard deviation from the 204 SPTpol simulated bandpower realizations  $\Delta\theta/\sigma_\theta$ . Only sample variance was included in the bandpower covariance matrix. The optical depth was also frozen at the input value  $\tau = 0.0943$  for this test to avoid a strong degeneracy with the scalar amplitude  $A_S$  as is done when fitting measured SPTpol bandpowers. All parameters are within  $0.3\sigma$  of expected values and often much closer. Combined with the results of the full CosmoMC test chain above, we conclude that the SPTpol likelihood and bandpower covariance matrix function properly.

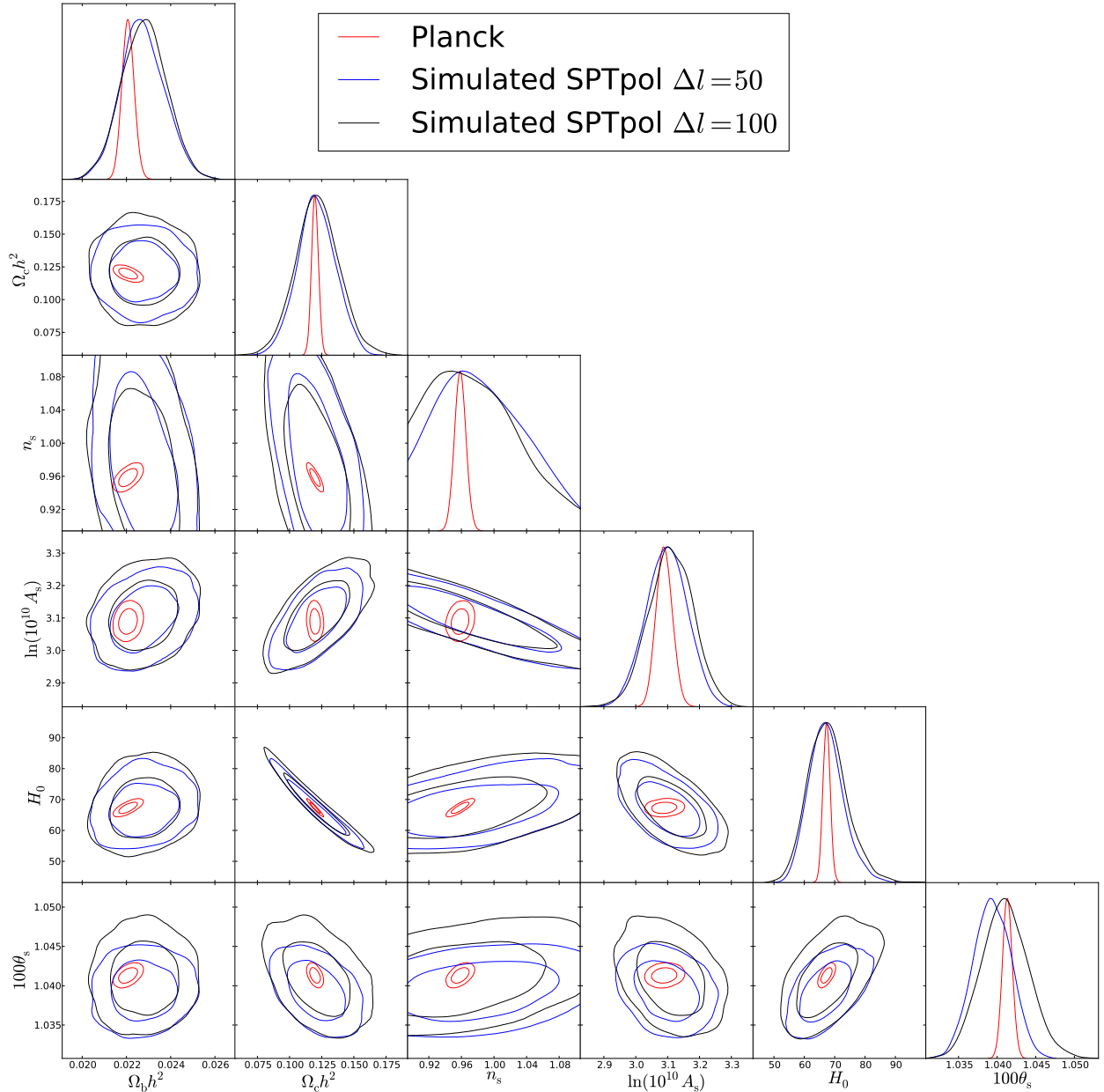


Figure 6.4: 2-D marginalized parameter likelihood contour grid resulting from a test chain using a realization of simulated SPTpol bandpowers. Contours show the 68 and 95% confidence regions. In red are constraints from Planck that define the input cosmology for the sims. In black (blue) are constraints from  $\Delta l = 50$  ( $\Delta l = 100$ ) simulated bandpowers. We also used the actual SPTpol deep field bandpower covariance matrix and window functions for this test. The cosmological constraints all match within a fraction of the  $1-\sigma$  uncertainties on the parameters. This simultaneously validates the likelihood module, bandpower covariance matrix, and the bandpower window functions.

### 6.3.5 Adding WIMP Annihilation

It is possible to constrain the particle properties of dark matter using the CMB power spectra. Potential dark matter particles, e.g. WIMPs, will annihilate and/or decay injecting energy into the radiation background. Different particle models will lead to varying energy injection profiles as a function of redshift  $z$ . As discussed in (88) energy deposition from particle annihilation or decay can be modeled following

$$\begin{aligned} \left( \frac{dE}{dt dV} \right)_{\text{ann}} &= p_{\text{ann}}(z) c^2 \Omega_c \rho_c^2 (1+z)^6 \\ \left( \frac{dE}{dt dV} \right)_{\text{dec}} &= p_{\text{dec}}(z) c^2 \Omega_c \rho_c (1+z)^3, \end{aligned} \quad (6.23)$$

where  $\Omega_c$  is the fraction of the energy density coming from cold dark matter,  $\rho_c$  is the critical density for a flat universe, and  $p_{\text{ann}}(z)$  and  $p_{\text{dec}}(z)$  encode energy deposition as a function of redshift for a given dark matter particle model. Energy injection changes the ionization history of the universe, and using publicly available codes such as CAMB and RECFAST (92) one can calculate resulting perturbations to the CMB power spectra. The perturbations can then be decomposed into orthogonal components. Fitting for the amplitude of these principle components places constraints on the input particle models.

While performing a principle component analysis on energy injection profiles calculated in (93) for a range of WIMP particle mass and Standard Model particle annihilation channels, (88) found that the amplitude of the first principle component captures 99.97% of the relevant information. The effects of a wide range of WIMP particle annihilation models on the CMB power spectra, therefore, can be parameterized by a single variable, namely the amplitude of the first principle component  $e_{\text{WIMP}}(z)$ . This component is normalized such that  $p_{\text{ann}}(z) = \epsilon e_{\text{WIMP}}(z)$ , with  $\epsilon = 2 \times 10^{-27} \text{ cm}^3/\text{s}/\text{GeV}$ .

To constrain WIMP particle annihilation as studied by (88), we added into CosmoMC their corrections  $\delta D_l$  to the CMB power spectra obtained by mapping  $e_{\text{WIMP}}(z)$  to  $D_l$ -space. This introduces a single new parameter  $e_{\text{WIMP}}$ , which parameterizes the amplitude of the principle component. Figure 6.5 contains the perturbations to the  $TE$  and  $EE$  power spectra for  $e_{\text{WIMP}} = 1$ .

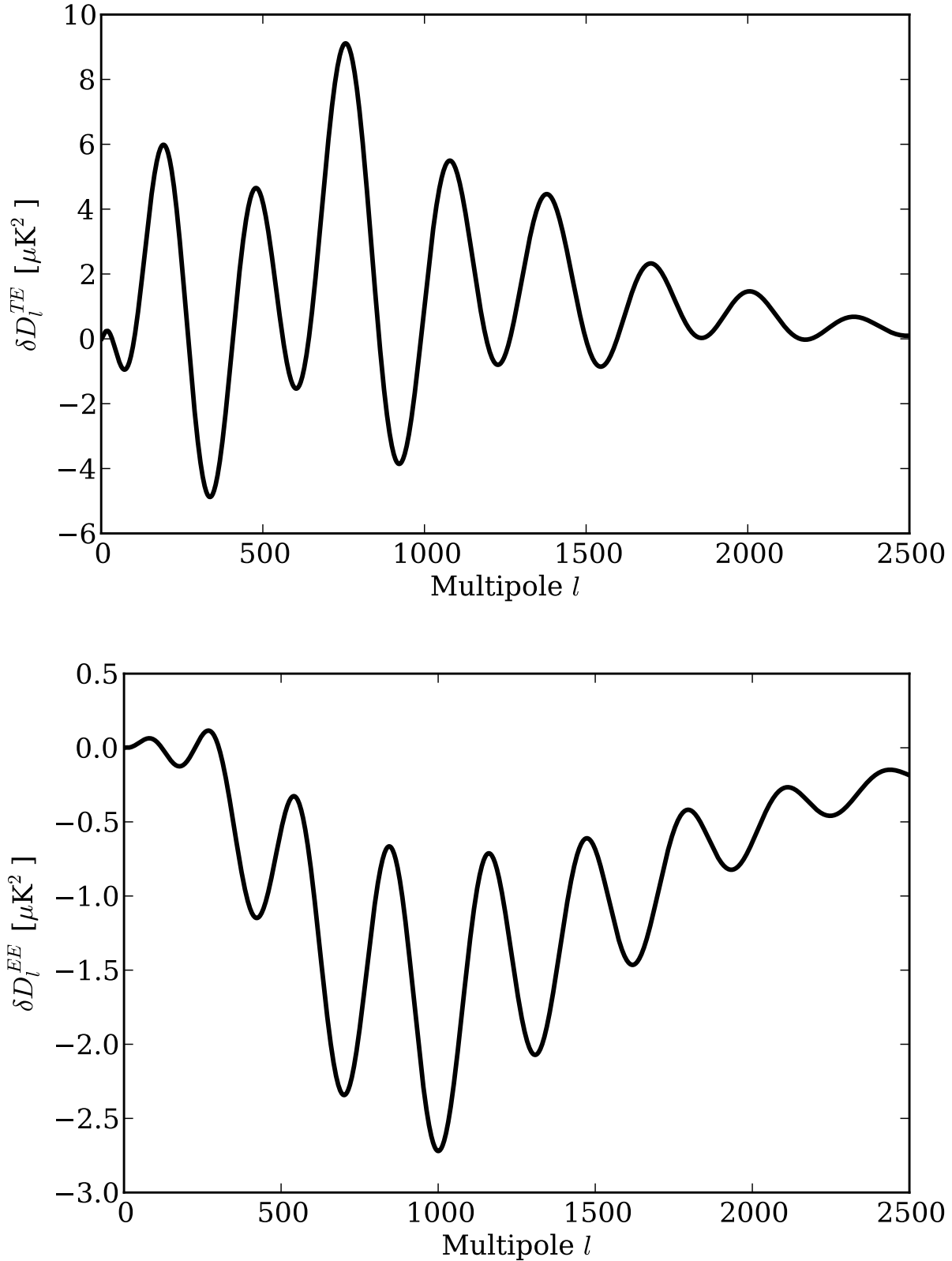


Figure 6.5: Perturbations to the CMB power spectra  $\delta D_l$  from WIMP annihilation scaled to  $e_{\text{WIMP}} = 1$  ( $p_{\text{ann}}(z) = 2 \times 10^{-27} \text{ cm}^3/\text{s}/\text{GeV}$ ). (Top) Corrections to the  $TE$  spectrum. (Bottom) Corrections to the  $EE$  spectrum.

We have included  $eWIMP$  as a fifth nuisance parameter in the SPTpol likelihood with a flat prior range of  $0 - 10$ . Additionally, we have written a modified package of CosmoMC that adds the  $\delta D_l$  to the theoretical expectations from CAMB. This generalized version of CosmoMC allows us to vary the amplitude of the  $\delta D_l$  simultaneously for all experiments that measure the CMB power spectra to obtain a joint-experiment constraint on  $eWIMP$ . Constraints on  $eWIMP$  presented in Chapter 7 use this modified CosmoMC package while all other cosmological constraints use the base CosmoMC package coupled with the SPTpol likelihood module.

## Chapter 7

### Results

In previous chapters we have described the design and operation of the SPTpol experiment, as well as the data analysis tools and techniques required to transform raw detector timestreams into maps, power spectra, and finally constraints on cosmological parameters. We now present the main data products and scientific results from this analysis. These data products are first reported in the form of CMB polarization power spectra bandpowers from the SPTpol 2012 deep field. Efforts taken to validate and cross-check our power spectra measurements are described in some detail. We then present  $\Lambda$ CDM parameter constraints resulting from fitting the SPTpol polarization power spectra. While there is only mild sensitivity in the SPTpol dataset considered here to test for physics beyond  $\Lambda$ CDM, we nevertheless place constraints on three simple single-parameter extensions. The chapter concludes with a brief discussion of the results and their implications.

#### 7.1 Bandpowers

We present bandpowers and uncertainties for the SPTpol 2012 deep field  $TE$  and  $EE$  spectra at 150 GHz in Figure 7.1 as well as in Figure 7.2 plotted with measurements from other experiments. Tables 7.1 and 7.2 quantify the bandpowers and their errors. Errors are the square-root of the diagonal elements of the relevant auto-covariance block and do not include beam or calibration uncertainties. Bandpowers span the range  $501 \leq \ell \leq 5000$ . In this multipole range, the  $TE$  and  $EE$  transfer functions are never less than 0.7 and we have verified that systematic power induced by filtering and analysis choices is sub-dominant to the theoretical input spectrum in our simulations,

Table 7.1: SPTpol 150 GHz  $TE$  Power Spectrum

$\ell$ range	$\ell_{\text{eff}}$	$D_\ell$ [ $\mu\text{K}^2$ ]	$\sigma$ [ $\mu\text{K}^2$ ]	$\ell$ range	$\ell_{\text{eff}}$	$D_\ell$ [ $\mu\text{K}^2$ ]	$\sigma$ [ $\mu\text{K}^2$ ]
501 - 550	521	-57.0	19.6	1501 - 1550	1523	-1.4	7.9
551 - 600	572	7.1	22.6	1551 - 1600	1573	10.1	8.2
601 - 650	622	-21.9	26.1	1601 - 1650	1623	-11.6	7.0
651 - 700	672	-41.1	28.1	1651 - 1700	1673	-32.9	6.7
701 - 750	722	-108.5	30.0	1701 - 1750	1723	-23.1	6.0
751 - 800	772	-101.4	26.6	1751 - 1800	1773	-15.9	5.1
801 - 850	822	-70.9	21.4	1801 - 1850	1823	-3.4	5.0
851 - 900	872	4.1	20.4	1851 - 1900	1873	0.8	4.6
901 - 950	922	62.5	21.9	1901 - 1950	1923	-10.1	4.3
951 - 1000	973	-22.9	20.7	1951 - 2000	1973	-14.1	4.1
1001 - 1050	1023	-55.1	19.6	2001 - 2100	2047	-14.9	2.4
1051 - 1100	1073	-100.3	17.0	2101 - 2200	2147	-2.0	2.0
1101 - 1150	1123	-61.3	13.6	2201 - 2300	2248	-4.1	2.0
1151 - 1200	1173	-18.3	12.7	2301 - 2400	2348	-8.1	1.7
1201 - 1250	1223	20.6	12.3	2401 - 2500	2448	-0.5	1.5
1251 - 1300	1273	-22.6	13.1	2501 - 3000	2745	-2.6	0.5
1301 - 1350	1323	-56.9	12.2	3001 - 3500	3246	-0.1	0.5
1351 - 1400	1373	-38.0	11.4	3501 - 4000	3746	0.5	0.5
1401 - 1450	1423	-46.4	9.2	4001 - 4500	4246	1.8	0.7
1451 - 1500	1473	-5.1	8.4	4501 - 5000	4747	1.0	0.8

**Notes:** We provide the  $\ell$ -band range, weighted multipole value  $\ell_{\text{eff}}$ , bandpower  $D_\ell$ , and associated bandpower uncertainty  $\sigma$ . Errors do not include beam or calibration uncertainties.

Table 7.2: SPTpol 150 GHz  $EE$  Power Spectrum

$\ell$ range	$\ell_{\text{eff}}$	$D_\ell$ [ $\mu\text{K}^2$ ]	$\sigma$ [ $\mu\text{K}^2$ ]	$\ell$ range	$\ell_{\text{eff}}$	$D_\ell$ [ $\mu\text{K}^2$ ]	$\sigma$ [ $\mu\text{K}^2$ ]
501 - 550	521	8.6	1.7	1501 - 1550	1523	14.1	2.0
551 - 600	572	7.2	2.5	1551 - 1600	1573	19.5	2.3
601 - 650	622	38.1	4.3	1601 - 1650	1623	21.1	2.2
651 - 700	672	40.9	5.2	1651 - 1700	1673	14.9	2.1
701 - 750	722	31.6	5.1	1701 - 1750	1723	8.5	1.6
751 - 800	772	12.0	3.3	1751 - 1800	1773	8.3	1.5
801 - 850	822	15.1	2.5	1801 - 1850	1823	7.4	1.5
851 - 900	872	13.8	2.9	1851 - 1900	1873	8.2	1.5
901 - 950	923	35.3	4.3	1901 - 1950	1923	9.5	1.5
951 - 1000	973	30.1	5.1	1951 - 2000	1973	10.3	1.5
1001 - 1050	1023	29.7	4.9	2001 - 2100	2047	6.2	0.9
1051 - 1100	1073	28.6	3.8	2101 - 2200	2147	5.3	0.8
1101 - 1150	1123	14.4	2.3	2201 - 2300	2248	5.9	0.8
1151 - 1200	1173	11.1	2.2	2301 - 2400	2348	4.0	0.9
1201 - 1250	1223	19.3	2.7	2401 - 2500	2448	1.7	0.8
1251 - 1300	1273	31.1	3.5	2501 - 3000	2745	1.7	0.4
1301 - 1350	1323	30.9	3.6	3001 - 3500	3246	0.9	0.5
1351 - 1400	1373	16.4	2.9	3501 - 4000	3746	0.1	0.6
1401 - 1450	1423	14.5	2.0	4001 - 4500	4246	0.0	0.7
1451 - 1500	1473	8.0	1.6	4501 - 5000	4747	1.3	1.0

**Notes:** We provide the  $\ell$ -band range, weighted multipole value  $\ell_{\text{eff}}$ , bandpower  $D_\ell$ , and associated bandpower uncertainty  $\sigma$ . Errors do not include beam or calibration uncertainties.

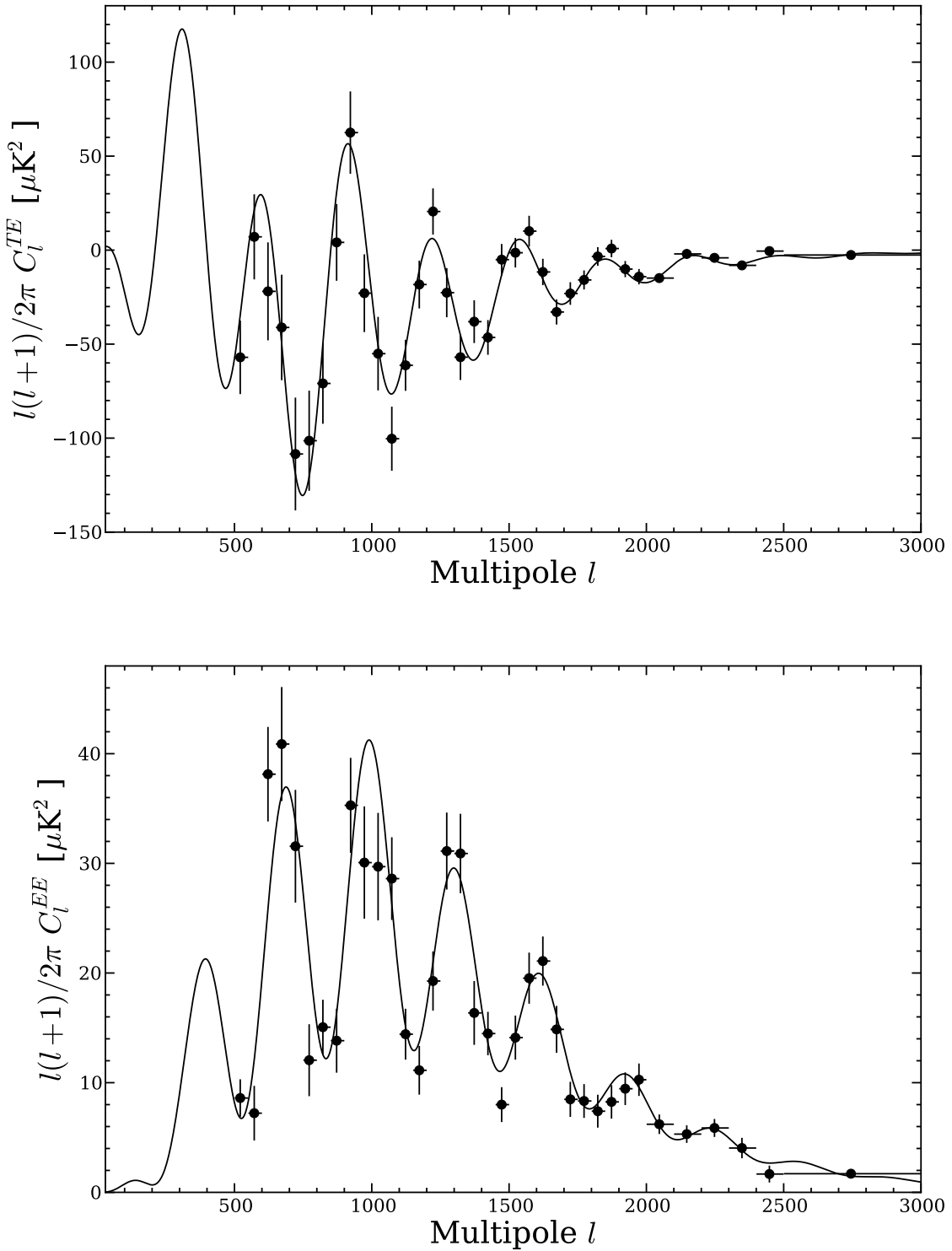


Figure 7.1: The SPTpol 150 GHz 2012 deep field  $TE$  (Top) and  $EE$  (Bottom) power spectra on a linear scale. We measure six acoustic peaks in the  $EE$  spectrum with high significance and achieve the highest signal-to-noise measurements of the  $EE$  damping tail to date. The solid black lines in both plots are the  $\Lambda\text{CDM}$  expectation from Planck (31)  $TT$  measurements and have not been fitted to the SPTpol data.

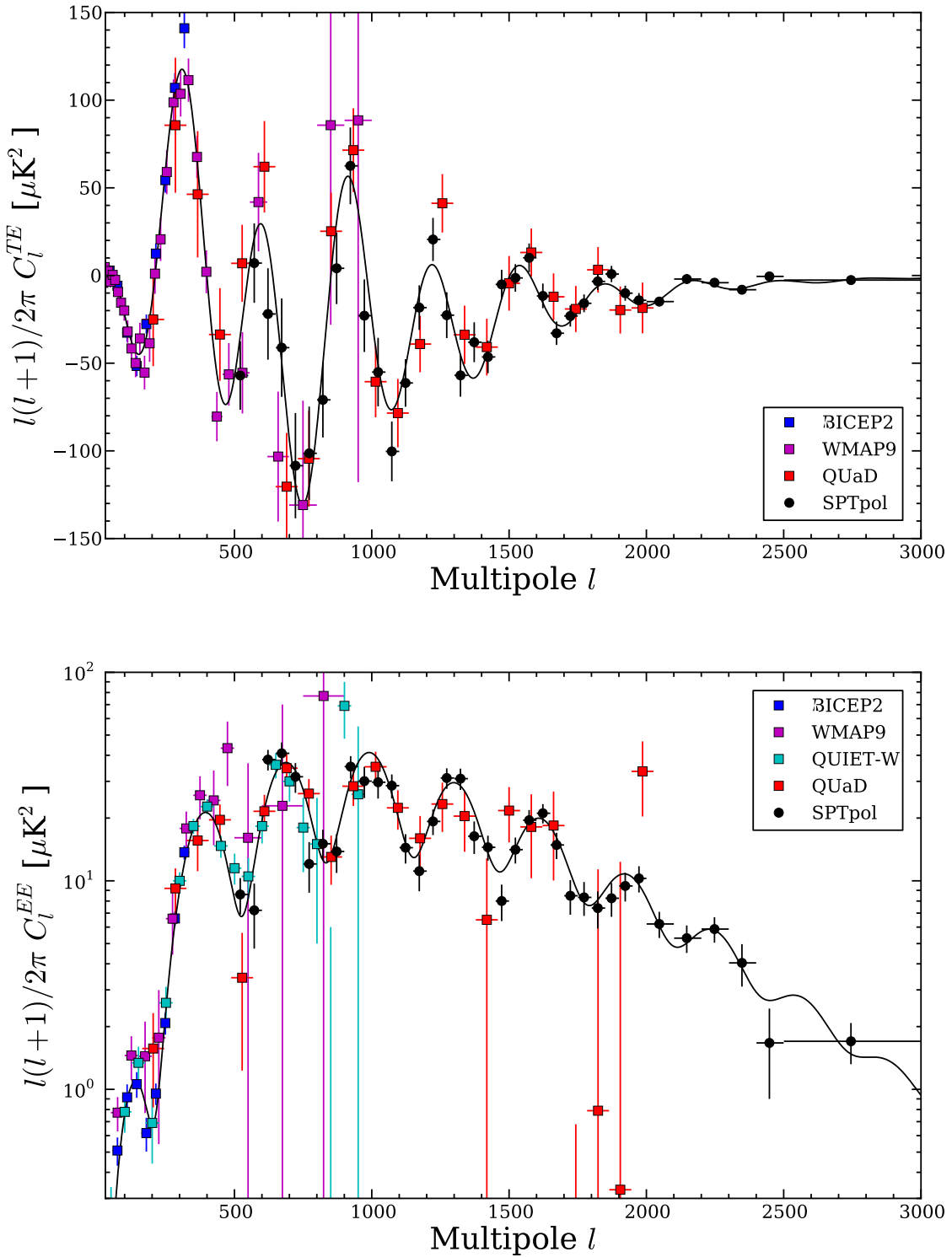


Figure 7.2: The SPTpol 150 GHz 2012 deep field  $TE$  (Top) and  $EE$  (Bottom, log scale) power spectra, plotted with data from BICEP2 (23), WMAP (25), QUIET W-band (14), and QUAID (94). The solid black lines in both plots are the  $\Lambda$ CDM expectation from Planck (31)  $TT$  measurements and have not been fitted to the SPTpol data.

shown as a solid black line in Figures 7.1 and 7.2.

The bandpowers are binned into three widths:  $\delta\ell = 50$  from  $501 \leq \ell \leq 2000$ ,  $\delta\ell = 100$  from  $2001 \leq \ell \leq 2500$ , and  $\delta\ell = 500$  from  $2501 \leq \ell \leq 5000$ . The third through eighth peaks of the  $EE$  power spectrum are apparent with high signal-to-noise. This is the highest signal-to-noise measurement of the  $EE$  damping tail to date, which is less affected by secondary anisotropies like residual point source power and the thermal and kinetic SZ effects than the  $TT$  power spectrum. Many simple extensions to the  $\Lambda$ CDM model, for example the amount of primordial helium  $Y_p$  and the number of relativistic species  $N_{\text{eff}}$ , are sensitive to the damped amplitude of the photon-baryon acoustic oscillations at higher multipoles. A measurement of the  $EE$  damping tail is an important step towards placing tighter constraints on extensions to the  $\Lambda$ CDM model. Indeed, recent forecasts suggest that future measurements of the polarization power spectra will constrain cosmological parameters better than the temperature power spectrum alone given sufficient sky coverage and noise (95).

### 7.1.1 SPTpol Bandpower Validation

Before presenting cosmological constraints from the SPTpol power spectra we note that in addition to cross-checking the SPTpol likelihood, bandpower covariance matrix, and bandpower window functions, we also performed a series of validation tests on the final SPTpol deep field  $TE$  and  $EE$  bandpowers themselves. Three types of cross-checks were performed:

- (1) **Frequency:** While this analysis focuses on the cosmological constraints from the 150 GHz data, we processed 95 GHz data and generated bandpowers using the same pipeline. Timestream and map filtering are slightly different between the 95 and 150 GHz datasets to cater to specific science goals for the different frequency bands, but real CMB features in the deep field should correlate in the power spectra between frequencies. Figure 7.3 overplots both 95 and 150 GHz (pseudo-spectra) bandpowers generated from 2012 deep field observations. Since the bandpowers are generated for the same patch of sky we include

only noise variance in the error bars. The 95 and 150 GHz bandpowers agree within their errors, which is the expected behavior if features in the power spectra are real properties of that particular patch of sky.

- (2) **Alternate Pipeline:** To test for biases due to the bandpower analysis pipeline itself we calculated the bandpowers with an alternate pipeline. The second pipeline varies several key aspects of the bandpower calculation. First, instead of generating cross-spectra for all 122 bundles for the deep field a set of 40 half-season maps are made from combinations of the bundles. These 40 super bundles are then crossed, which varies the effect of noise bias on the bandpowers. Second, we use a harmonic inpainting method discussed in (96) to “paint” over point sources instead of masking them. This greatly reduces the complication of the map apodization window and we therefore assume the resulting mode-coupling matrix is diagonal. Finally, a 2-D transfer function is removed from each super bundle Fourier transform before calculating 2-D power spectra and azimuthally averaging; normally a 1-D transfer function is removed from the azimuthally averaged power spectra in a final “unbiasing” step. The resulting alternate bandpowers for the 150 GHz deep field  $EE$  observations are plotted in Figure 7.4. While there are differences in the bandpowers, they are generally small compared to the calculated errors. Importantly, the  $EE$  peak at  $l \sim 1000$  is low compared to the Planck  $\Lambda$ CDM expectation in both pipelines, suggesting this suppression of  $EE$  power is a feature of the deep field and not of the analysis.
  
- (3) **Sample Variance:** We wished to verify that the low  $EE$  peak at  $l \sim 1000$  as well as the general “peakiness” of the SPTpol bandpowers compared to the Planck  $\Lambda$ CDM expectation were consistent with variations due to sample variance. In parallel to the 2012 deep field cosmological analysis we have been processing full survey observations from the 2013 observing season. The full survey has four contiguous  $100 \text{ deg}^2$  patches the same shape and extent as the 2012 deep field, including the deep field itself, centered at RA22h30m-55, RA23h30m-55, RA0h30m-55, and RA1h30m-55. We generated four sets of 2013

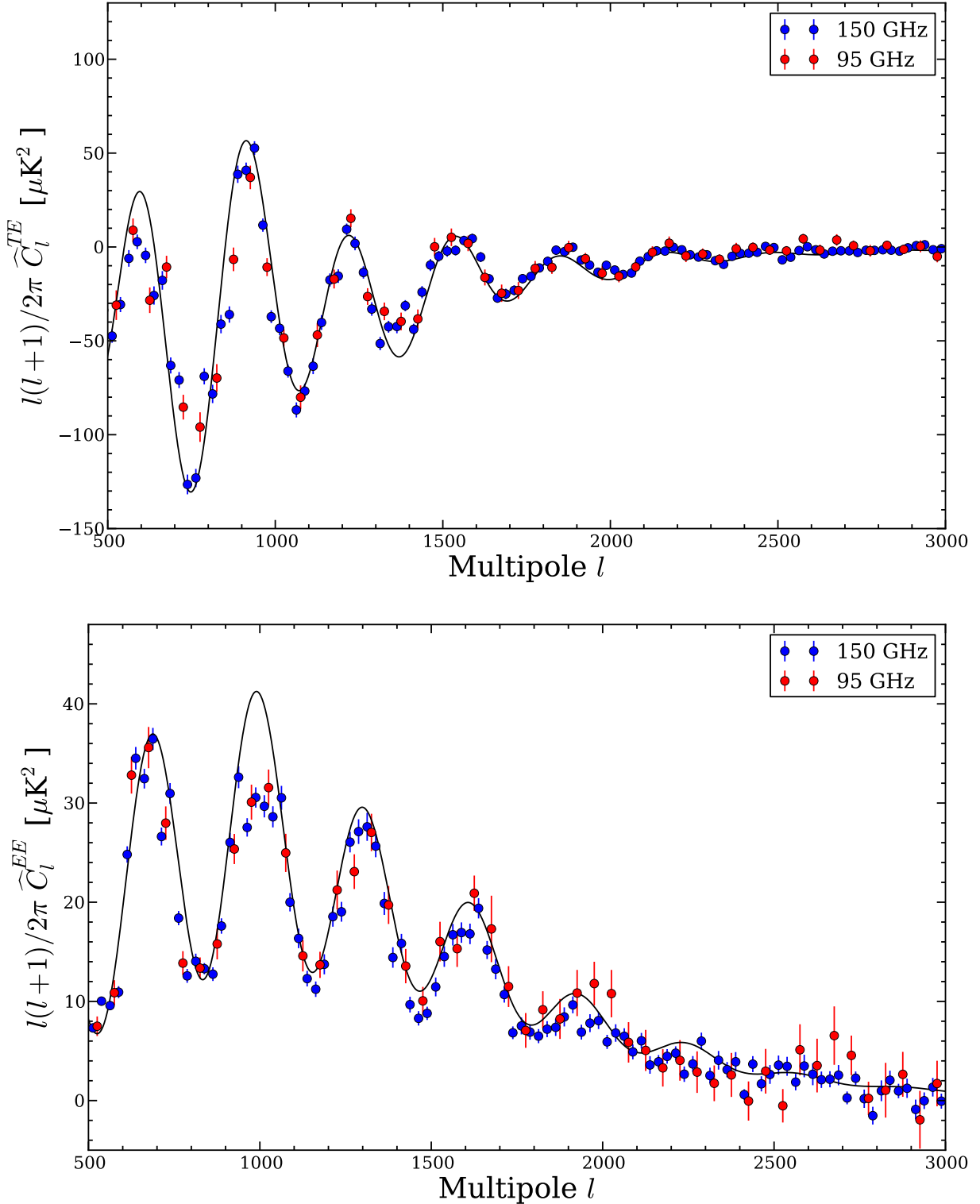


Figure 7.3: *Pseudo-spectra* SPTpol 150 GHz deep field bandpowers (blue) overplotted with 95 GHz bandpowers (red). Error bars include noise variance only. The two sets of bandpowers agree within errors. Since the bandpowers are biased by filtering and analysis systematics, the black theory line is meant only to guide the eye.

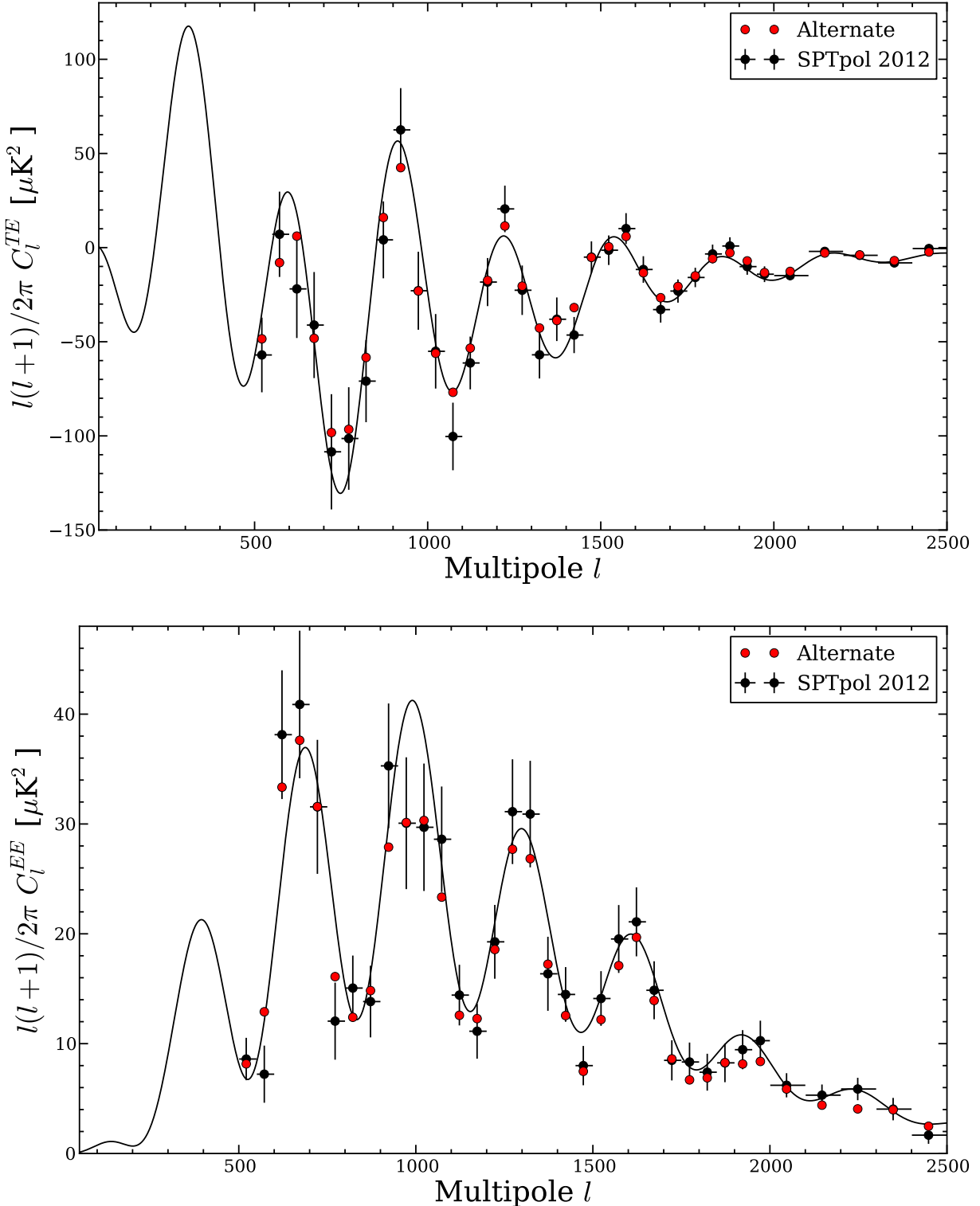


Figure 7.4: SPTpol 2012 deep field bandpowers (black) overplotted with bandpowers calculated with an alternate pipeline (red). The solid black line is the Planck  $\Lambda$ CDM expectation. The two sets of bandpowers agree well indicating no obvious bias introduced by either analysis pipeline.

maps each centered on these sub-fields. The filtering was chosen to be as similar as possible to that used for the 2012 deep field analysis. A notable exception is that a 15th-order polynomial subtraction was applied to the 2013 maps, which closely matches the degrees on the sky per degree of freedom in the fit achieved by the 4th-order polynomial subtraction used on the 2012 deep field timestreams.<sup>1</sup> Additionally, we removed the 10% most non-linear detectors during 2012 deep field map-making while this cut was not made for 2013 observations. We take advantage of the broad similarities in filtering between 2012 and 2013 observations to assume the 2012 transfer function while unbiasing 2013 bandpowers, though we note this is only an approximation. The beam functions were also assumed to be the same between observing years, which again is only approximately true. Since the locations of point sources in each field are different, however, we calculated distinct mode-coupling matrices for each sub-field.

The resulting (approximately) unbiased power spectra bandpowers for the four 2013 sub-fields are plotted in Figure 7.5. Bandpowers have been offset in multipole for clarity. For the 2012 deep field  $EE$  ( $TE$ ) bandpowers, sample variance dominates over noise variance for multipoles  $l < 1700$  ( $l < 2000$ ). In comparison, the sample variance dominated ranges for the 2013  $EE$  ( $TE$ ) bandpowers are  $l < 1150$  ( $l < 1450$ ) due to higher levels of noise in the final maps. However, the bandpowers for the four sub-fields vary by amounts consistent with sample variance. Additionally, we note that the 2012 deep field bandpowers (black) are in good agreement with the 2013 deep field bandpowers (blue).

With these tests we find that the deep field bandpowers are consistent between frequencies, across observation seasons, and when varying the analysis pipeline. Additionally, differences between independent  $100 \text{ deg}^2$  sub-fields of the full survey field are consistent with sample variance between fields. Considering the results of these tests, as well as results from the suite of jackknives performed on the input maps, we conclude that the deep field bandpowers are free from significant bias and

---

<sup>1</sup> Each full survey field observation is  $\sim$  four times wider on the sky, which requires higher-order polynomial filtering to achieve the same effective high-pass filtering on the timestreams. One-to-one timestream filtering is not possible, however.

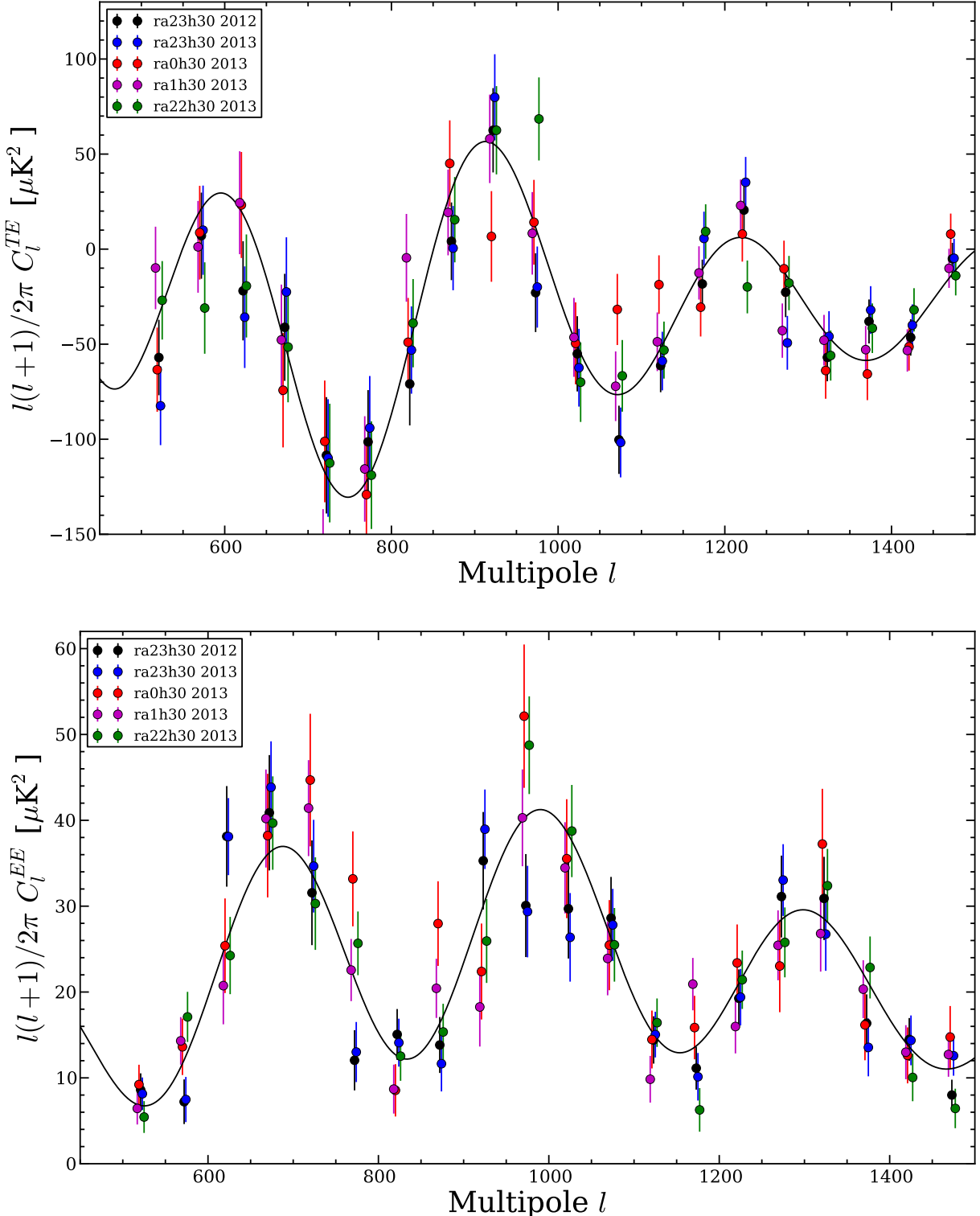


Figure 7.5: SPTpol 2012 deep field bandpowers (black dots) overplotted with bandpowers from four  $100 \text{ deg}^2$  sub-fields from 2013 full survey observations. The solid black line is the Planck  $\Lambda$ CDM expectation. 2013 bandpowers have been offset horizontally for clarity. Differences between the four fields are consistent with sample variance.

we proceed to use them to constrain cosmology.

## 7.2 Cosmological Constraints from SPTpol

The second set of primary results of this analysis consists of cosmological constraints from the SPTpol 2012 deep field 150 GHz *TE* and *EE* bandpowers. We assume a six-parameter  $\Lambda$ CDM model as discussed in Chapter 1 but freeze the optical depth at  $\tau = 0.0927$  and include the four likelihood nuisance parameters discussed above for a total of nine free parameters. We also test several simple one-parameter extensions to the base  $\Lambda$ CDM model. First, we present  $\Lambda$ CDM constraints using SPTpol data, both alone and in combination with other datasets. Second, we explore several  $\Lambda$ CDM extensions, namely the presence of anti-correlated cold dark matter isocurvature perturbations, annihilating WIMP particles injecting energy into the CMB, and a non-zero tensor-to-scalar ratio  $r$ .

### 7.2.1 $\Lambda$ CDM constraints

$\Lambda$ CDM constraints using only SPTpol 150 GHz *TE* and *EE* 2012 deep field bandpowers are presented in the first column of constraints in Table 7.3. 1-D marginalized parameter likelihoods are also plotted in Figure 7.6 in red. We plot the SPTpol bandpowers with the best-fit Planck  $\Lambda$ CDM model from (31) (blue) as well as the best-fit SPTpol  $\Lambda$ CDM model (red) in Figure 7.7. Colored dashed lines are the corresponding bandpower residuals.

Most notably the SPTpol bandpowers prefer a significantly lower fraction of cold dark matter than the recently released Planck *TT* constraints (31). Both the *EE* and *TE* bandpowers are slightly “peakier” than what is expected under the Planck  $\Lambda$ CDM model, which drives  $\Omega_c h^2$  down. This can be better understood when considering the effects of gravitational lensing, which smooths the acoustic peaks by mixing power between nearby Fourier modes. Decreasing the strength of lensing causes the acoustic peaks to become more peaked. However, if you keep the strength of lensing fixed, as is the case in  $\Lambda$ CDM, you can still decrease the net effect of lensing on the CMB by lowering  $\Omega_c h^2$ . This reduces the amount of matter that actually performs the gravitational lensing

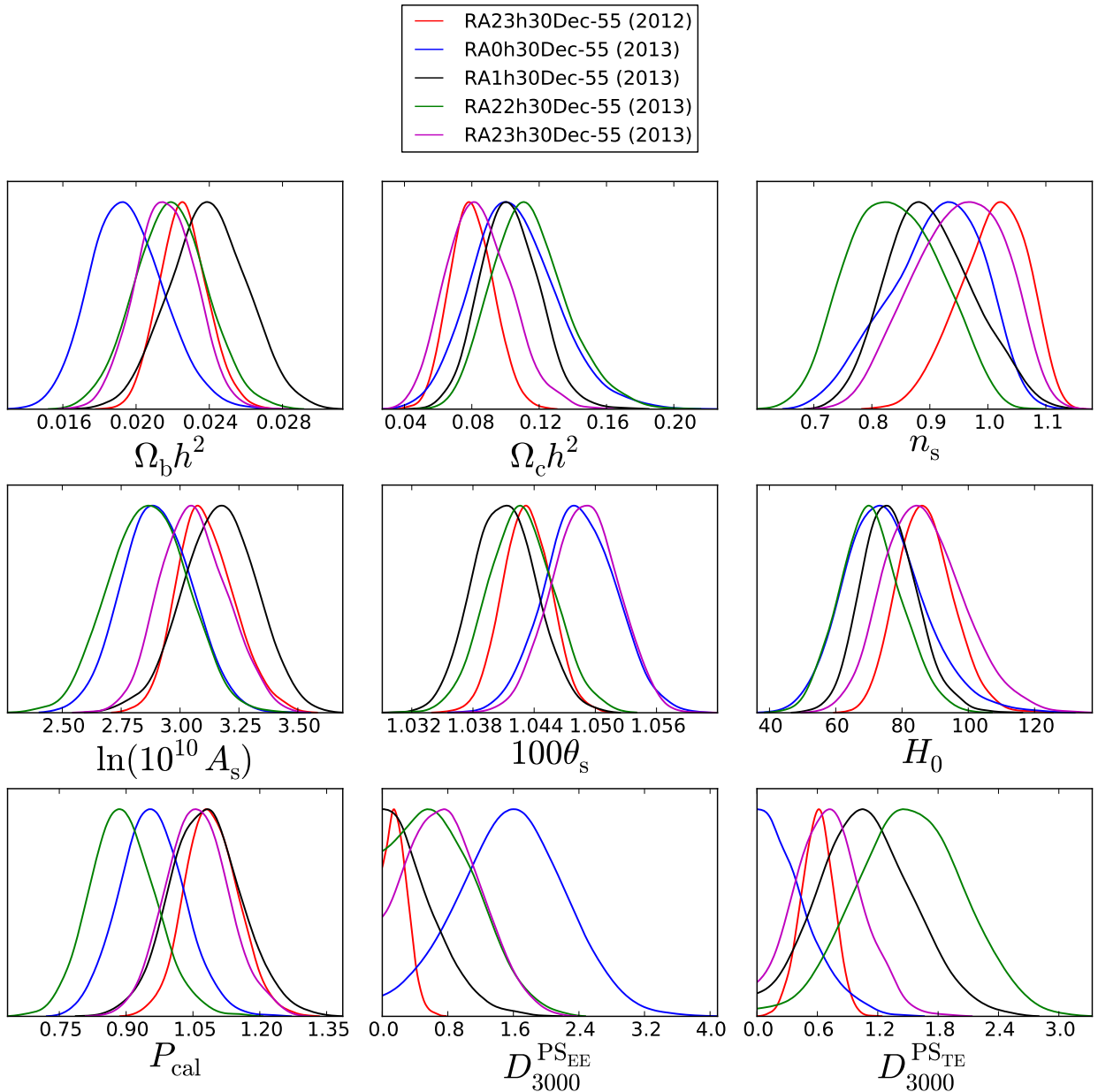


Figure 7.6: 1-D marginalized  $\Lambda$ CDM constraints from 2012 SPTpol data (red). Constraints from the separate 2013 sub-fields are also included.  $H_0$  is a derived quantity, while  $P_{\text{cal}}$ ,  $D_{3000}^{\text{PS}_{\text{EE}}}$ , and  $D_{3000}^{\text{PS}_{\text{TE}}}$  are nuisance parameters in the SPTpol likelihood. The fourth nuisance parameter  $T_{\text{cal}}$  is not shown as it is tightly constrained by its Gaussian prior.

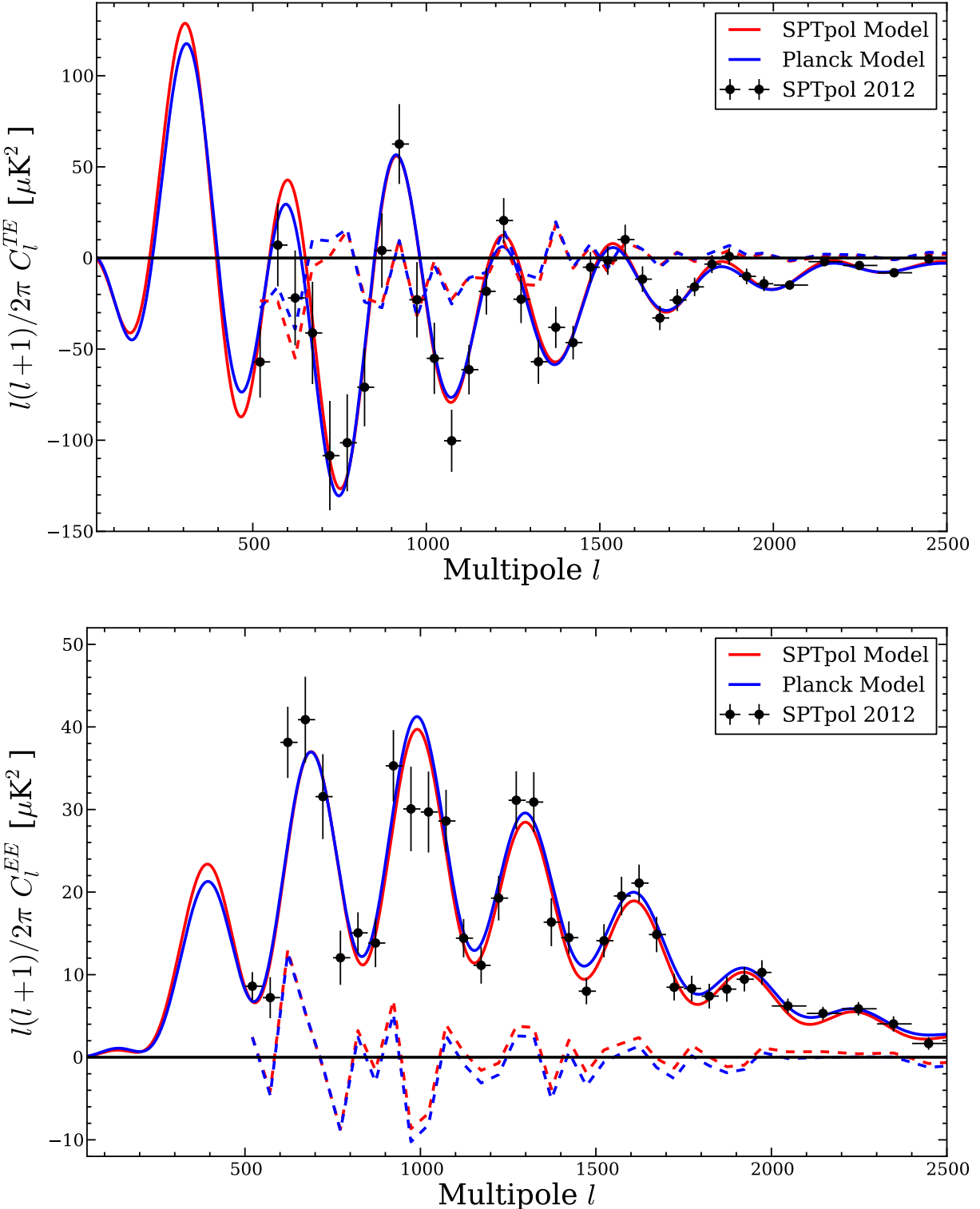


Figure 7.7: SPTpol 2012 deep field bandpowers with two  $\Lambda\text{CDM}$  model curves. The solid blue line is the Planck  $\Lambda\text{CDM}$  expectation while the solid red line is the SPTpol best-fit model. Dashed lines are residuals for the respective models.

and still results in peakier power spectra with all else the same.

To quantify the quality of the fit to the SPTpol bandpowers we calculate  $\chi^2$  statistics by jointly comparing the measured  $EE$  and  $TE$  bandpowers to theoretically expected bandpowers generated from the Planck and SPTpol  $\Lambda$ CDM models and the bandpower window functions. Comparing to the SPTpol model we find  $\chi^2_{\text{SPTpol}} = 75.7$  with 64 degrees of freedom, corresponding to a PTE of 0.15. In comparison, for the Planck model we find  $\chi^2_{\text{Planck}} = 88.5$  with 72 degrees of freedom (PTE=0.09). The Planck PTE corresponds to an effective Gaussian significance of  $1.7\sigma$ . Given the small area of sky obtaining a fit this poor to the Planck  $\Lambda$ CDM model is therefore unlikely, but not significantly so.

We also generated  $\Lambda$ CDM chains for the four 2013 sub-fields, the results of which are also included in Table 7.3. We stress that the cosmological constraints for the four 2013 sub-fields should only be qualitatively compared to the 2012 deep field constraints since the bandpowers have not been rigorously unbiased. Nevertheless, the RA23H30DEC-55 (deep) field constraints from both 2012 and 2013 exhibit the same low values of  $\Omega_c h^2$ . In comparison, the other fields are more consistent with expectations from previously published experiments. This variation in  $\Omega_c h^2$  between sub-fields, together with only a marginally low PTE compared to the Planck model, suggests the low fraction of dark matter density is a chance unlucky feature of the deep field.

It is worth noting that other  $\Lambda$ CDM parameters also vary between the 2013 sub-fields but each are consistent with each other within their errors. Despite good agreement in the DC level of bandpowers between sub-fields, the large variation in scalar spectral amplitude  $A_s$  is due in part to a strong degeneracy between  $A_s$  and the SPTpol polarization calibration  $P_{\text{cal}}$  as can be seen in Figure 7.8. Including other datasets breaks this degeneracy under the assumption that the external data are pre-calibrated. This is evident in Table 7.4 where the errors of both  $A_s$  and  $P_{\text{cal}}$  decrease dramatically when additional datasets are jointly fitted with SPTPol data.

To improve cosmological constraints from SPTpol alone we also consider other datasets simultaneously. In particular, we include measurements of the CMB  $TT$  spectrum from Planck (31) and SPTsz (13), which we label as “S13.” Three nuisance foreground terms accounting for Sun-

Table 7.3:  $\Lambda$ CDM constraints - SPTpol Only

Parameter	SPTpol Field				
	RA23H30 (2012)	RA0H30	RA1H30	RA22H30	RA23H30 (2013)
<b>Free</b>					
$\Omega_b h^2$	$0.023 \pm 0.001$	$0.02 \pm 0.002$	$0.024 \pm 0.002$	$0.022 \pm 0.002$	$0.022 \pm 0.002$
$\Omega_c h^2$	$0.08 \pm 0.013$	$0.106 \pm 0.025$	$0.102 \pm 0.017$	$0.115 \pm 0.022$	$0.085 \pm 0.019$
$100\theta_s$	$1.043 \pm 0.002$	$1.048 \pm 0.004$	$1.041 \pm 0.003$	$1.043 \pm 0.003$	$1.049 \pm 0.003$
$n_s$	$1.004 \pm 0.057$	$0.908 \pm 0.078$	$0.899 \pm 0.074$	$0.84 \pm 0.075$	$0.948 \pm 0.076$
$\ln(10^{10} A_s)$	$3.11 \pm 0.123$	$2.901 \pm 0.147$	$3.165 \pm 0.156$	$2.859 \pm 0.165$	$3.06 \pm 0.14$
$\tau$	(0.0927)	(0.0927)	(0.0927)	(0.0927)	(0.0927)
<b>Derived</b>					
$\Omega_\Lambda$	$0.858 \pm 0.045$	$0.739 \pm 0.142$	$0.769 \pm 0.084$	$0.695 \pm 0.139$	$0.84 \pm 0.075$
$H_0$	$87.36 \pm 8.31$	$74.66 \pm 12.15$	$76.49 \pm 8.5$	$70.49 \pm 9.34$	$86.41 \pm 11.92$
$\sigma_8$	$0.654 \pm 0.08$	$0.693 \pm 0.105$	$0.754 \pm 0.093$	$0.684 \pm 0.08$	$0.654 \pm 0.109$
<b>Nuisance</b>					
$T_{\text{cal}}$	$0.998 \pm 0.013$	$0.999 \pm 0.014$	$0.999 \pm 0.014$	$0.998 \pm 0.014$	$1.0 \pm 0.014$
$P_{\text{cal}}$	$1.091 \pm 0.06$	$0.957 \pm 0.071$	$1.077 \pm 0.081$	$0.891 \pm 0.074$	$1.06 \pm 0.071$
$D_{3000}^{\text{PS}_{\text{EE}}}$	$0.206 \pm 0.128$	$1.566 \pm 0.636$	$0.443 \pm 0.346$	$0.728 \pm 0.458$	$0.783 \pm 0.434$
$D_{3000}^{\text{PS}_{\text{TE}}}$	$0.594 \pm 0.158$	$0.337 \pm 0.264$	$1.095 \pm 0.439$	$1.521 \pm 0.515$	$0.725 \pm 0.328$

**Notes:** We report the mean and standard deviations for each parameter. The primary SPTpol constraints are from the deep field, RA23H30DEC-55 (2012). Constraints from the 2013 sub-fields should be considered qualitative as the bandpowers have not been rigorously unbiased. For all fields the optical depth is frozen at  $\tau = 0.0927$ . We caution the independent use of the scalar amplitude  $\ln(10^{10} A_s)$  due to the degeneracy with  $P_{\text{cal}}$ .

Table 7.4:  $\Lambda$ CDM constraints

Parameter	Dataset			
	SPTPOL	PLANCK+S13	CMB	CMB+BAO+H <sub>0</sub>
<b>Free</b>				
$\Omega_b h^2$	$0.02259 \pm 0.00132$	$0.02208 \pm 0.00026$	$0.02206 \pm 0.00025$	$0.02212 \pm 0.00022$
$\Omega_c h^2$	$0.0799 \pm 0.0127$	$0.11899 \pm 0.00242$	$0.11835 \pm 0.00235$	$0.11784 \pm 0.00131$
$100\theta_s$	$1.04333 \pm 0.00236$	$1.04169 \pm 0.00057$	$1.04165 \pm 0.00054$	$1.04177 \pm 0.00048$
$n_s$	$1.00448 \pm 0.05694$	$0.95992 \pm 0.00668$	$0.96078 \pm 0.00645$	$0.96158 \pm 0.00506$
$\ln(10^{10} A_s)$	$3.10955 \pm 0.12296$	$3.07861 \pm 0.02386$	$3.07188 \pm 0.02355$	$3.07212 \pm 0.02328$
$\tau$	(0.0927)	$0.08509 \pm 0.01247$	$0.0827 \pm 0.01218$	$0.0833 \pm 0.01157$
<b>Derived</b>				
$\Omega_\Lambda$	$0.85805 \pm 0.04452$	$0.69143 \pm 0.01471$	$0.69462 \pm 0.01415$	$0.69822 \pm 0.00761$
$H_0$	$87.36 \pm 8.31$	$67.81 \pm 1.09$	$68.0 \pm 1.05$	$68.27 \pm 0.59$
$\sigma_8$	$0.65449 \pm 0.08043$	$0.82106 \pm 0.01191$	$0.81631 \pm 0.01198$	$0.81477 \pm 0.01066$
<b>Nuisance</b>				
$T_{\text{cal}}$	$0.99831 \pm 0.0134$	—	$0.99656 \pm 0.01292$	$0.99613 \pm 0.01302$
$P_{\text{cal}}$	$1.09053 \pm 0.05994$	—	$1.03804 \pm 0.01695$	$1.03901 \pm 0.01766$
$D_{3000}^{\text{PS}_{\text{EE}}}$	$0.20593 \pm 0.12775$	—	$0.16209 \pm 0.10959$	$0.16807 \pm 0.11561$
$D_{3000}^{\text{PS}_{\text{TE}}}$	$0.59376 \pm 0.1578$	—	$0.61516 \pm 0.15391$	$0.61577 \pm 0.1562$

**Notes:** Here PLANCK refers to Planck  $TT$  bandpowers plus WMAP9 polarization, labeled PLANCK+WP in Table 5 of (31). CMB refers to the combination PLANCK+S13+SPTPOL. Mean fits for SPTpol likelihood nuisance parameters are included for appropriate datasets.

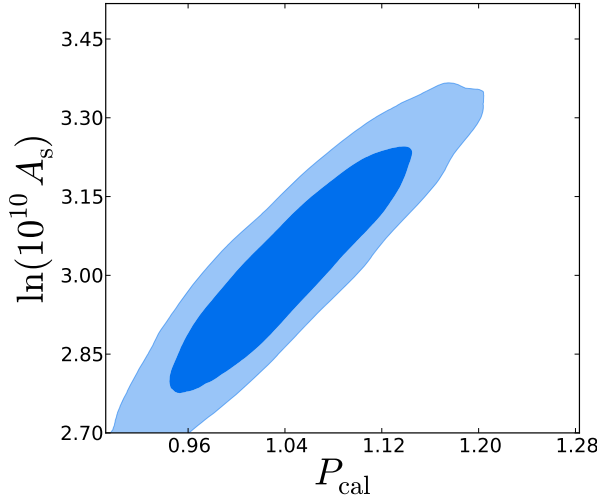


Figure 7.8: 2-D marginalized constraints on the scalar amplitude  $\ln 10^{10} (A_s)$  and  $P_{\text{cal}}$  for the SPTpol 2012 deep field bandpowers. A strong degeneracy between the two parameters is evident.

yaev Zel'dovich and residual poisson power are included with the S13 dataset as outlined in their analysis. We note that the Planck, S13, and SPTpol likelihoods treat foregrounds independently. We also ignore any correlations between experimental results due to, for example, shared sky. We refer to PLANCK+S13+SPTPOL as the “CMB” dataset. Table 7.4 and Figure 7.9 summarize the results of these chains, which are plotted in blue. We also include  $\Lambda$ CDM constraints for CMB-SPTPOL (PLANCK+S13) in red. As anticipated from Fisher forecasts, the inclusion of SPTpol data only marginally improves constraints on  $\Lambda$ CDM parameters. The largest improvement is seen in  $100\theta_s$  where the uncertainty is reduced by a factor of only 1.056. This is not itself surprising as the addition of several new high signal-to-noise acoustic peaks from both the *TE* and *EE* spectra add to our knowledge of the sound horizon at the epoch of recombination. The true power of the completed SPTpol dataset, however, will lie in constraining extensions to the base  $\Lambda$ CDM model, where high signal-to-noise measurements of the power spectra damping tails will be beneficial. The current errors in the damping tail preclude detailed analyses of these effects.

While powerful, CMB-only datasets nevertheless exhibit degeneracies between the rate of expansion  $H_0$ , the sound horizon at the epoch of recombination  $\theta_s$ , and the dark energy content of

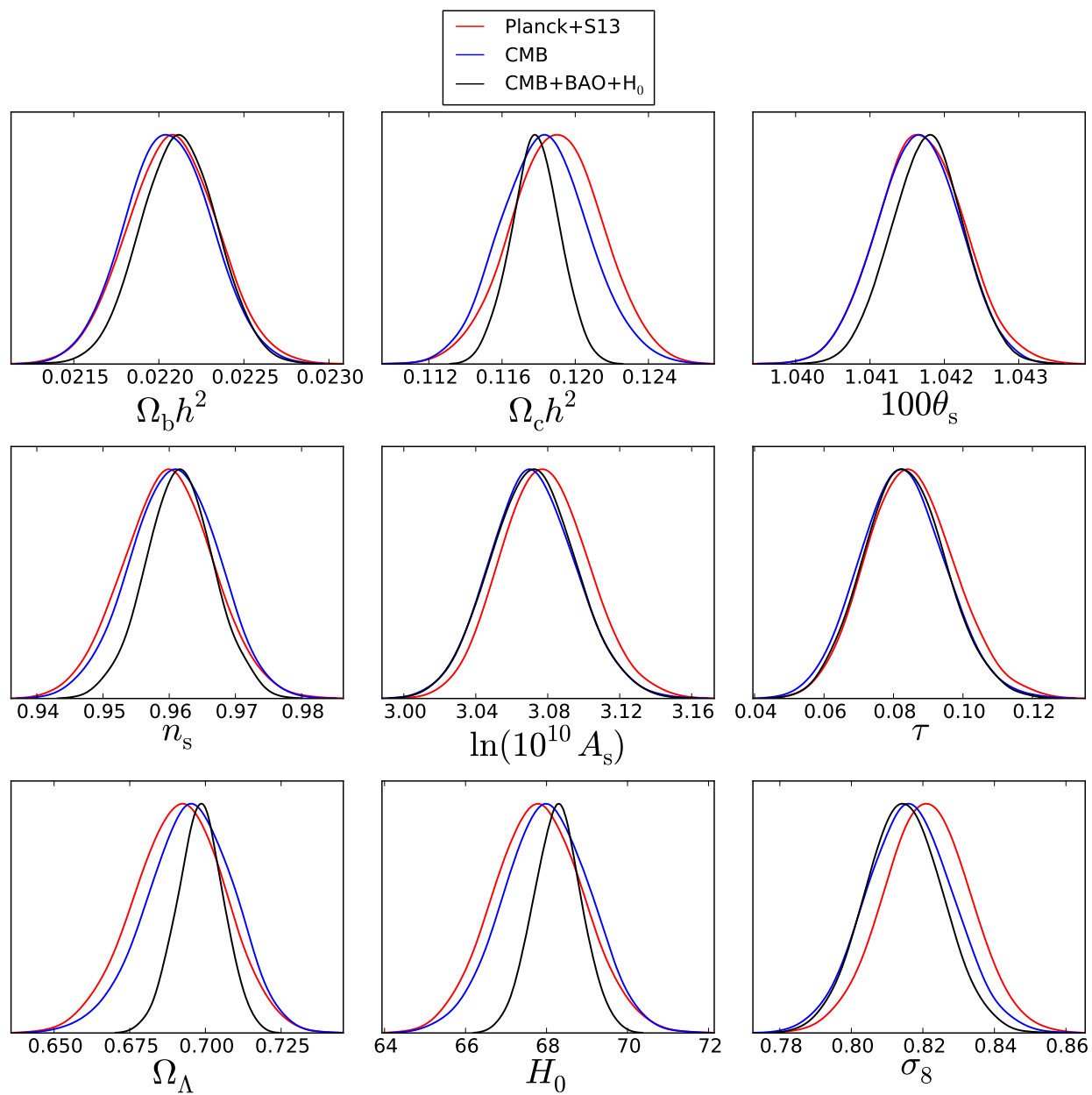


Figure 7.9: 1-D marginalized  $\Lambda$ CDM parameter constraints.

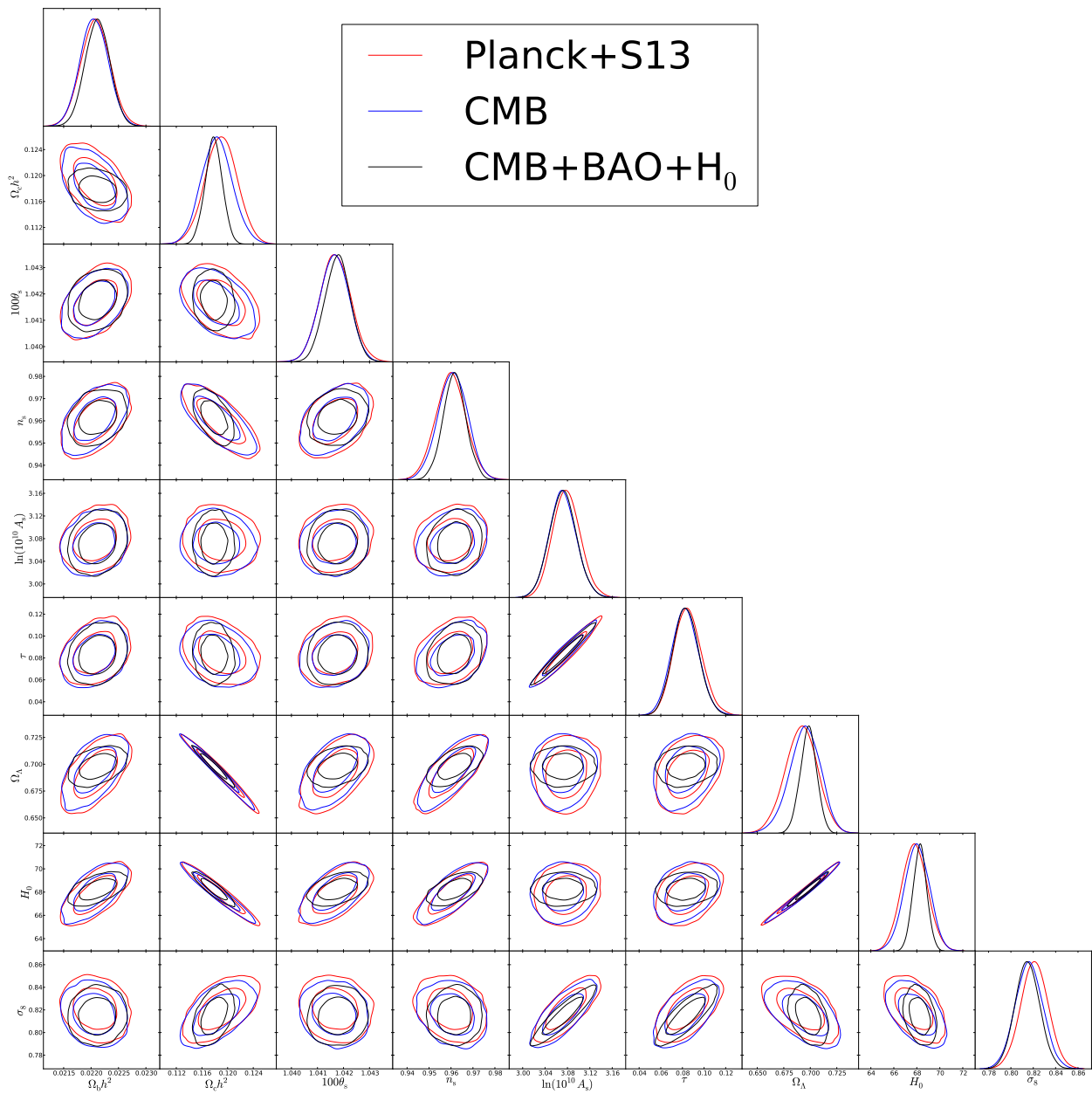


Figure 7.10: 2-D marginalized  $\Lambda$ CDM parameter likelihoods.

the universe  $\Omega_\Lambda$  (or equivalently the curvature  $\Omega_k$ , though it is fixed to zero in the  $\Lambda$ CDM model). Therefore, we also include two non-CMB datasets to partially break these degeneracies: a prior on  $H_0$  from (16) and BAO (baryon acoustic oscillations) measurements from SDSS Data Release 11 (18) which place a prior on  $\theta_s$ . Adding these datasets tightens  $\Lambda$ CDM constraints, as can be seen in Figures 7.9 and 7.10 in black. Given the number of acoustic peaks now measured with high signal-to-noise in multiple CMB datasets the BAO  $\theta_s$  prior contributes relatively little, reducing errors by only a factor of 1.125. An independent measurement of  $H_0$ , however, reduces uncertainties on several parameters through degeneracies with the Hubble constant, the uncertainty on which reduces by 1.78. These degeneracies are obvious as highly elliptical 2-D marginalized parameter likelihood contours like those plotted in Figure 7.10.

### 7.2.2 Extensions to $\Lambda$ CDM

With relatively few parameters the base  $\Lambda$ CDM model does a remarkable job fitting both the temperature and polarization anisotropy power spectra of the CMB. However, as both CMB and external datasets achieve higher signal-to-noise tensions between them are beginning to emerge (13; 47). This tension could possibly point to physics beyond  $\Lambda$ CDM. Indeed, we already know  $\Lambda$ CDM cannot be the full picture. For example, constraints from neutrino oscillation and double beta-decay experiments place limits on the sum of the neutrino masses  $0.06 < \sum m_\nu < 1.8$  eV (97; 98) while  $\Lambda$ CDM assumes  $\sum m_\nu = 0$ .<sup>2</sup> Non-zero neutrino mass has a number of effects on the CMB power spectra including affecting the strength of gravitational lensing and therefore the amplitude of the lensing  $B$ -mode polarization power spectrum, as well as altering  $\Omega_\Lambda$  to keep a constant curvature, which affects large-scale modes through the Integrated Sachs-Wolfe (ISW) effect (47).

While the completed SPTpol survey will be able to place interesting constraints on several well-motivated  $\Lambda$ CDM extensions through their effects on the power spectra damping tails, we instead focus on three extensions that affect larger angular scales better measured by the SPTpol 2012

---

<sup>2</sup> We note, however, that we have fixed  $\sum m_\nu = 0.06$  eV in this analysis to compare directly to results from (31).

deep field power spectra. We explore new constraints on  $\alpha_{-1}$ , the amplitude of an anti-correlated cold dark matter isocurvature perturbation mode in Section 7.2.2.1. We then consider the limits placed on the amplitude  $e_{\text{WIMP}}$  of WIMP particle annihilation energy injection in Section 7.2.2.2. Finally, in light of recent measurements of a non-zero tensor-to-scalar ratio  $r$  by the BICEP2 experiment (23), we explore new limits on  $r$  using solely the SPTpol  $TE$  and  $EE$  polarization power spectra. 2-D marginalized parameter constraints for each extension are plotted in Figures 7.11, 7.12, and 7.13 at the end of the section.

### 7.2.2.1 $\Lambda\text{CDM} + \alpha_{-1}$

Initial perturbations in the density of different components of the content of the universe are of two types, or modes. “Adiabatic” perturbations are such that the relative density of components, such as dark matter, baryons, neutrinos, etc., are in phase. This produces fluctuations in the curvature of the universe. With “isocurvature” modes, on the other hand, the relative densities of components change while maintaining a constant curvature. By changing the relative contributions of adiabatic and isocurvature modes to initial density fluctuations one changes the sound horizon at recombination, which moves the acoustic peaks in CMB power spectra. Current measurements of locations of acoustic peaks in the  $TT$  and  $TE$  spectra are consistent with purely adiabatic initial perturbations (25) but the possibility still exists for isocurvature fluctuations to be present at a small level. The SPTpol dataset provides high signal-to-noise measurements of the acoustic peaks in the  $EE$  spectrum as well, which should tighten constraints on the presence of isocurvature perturbations.

We test for the existence of a cold dark matter isocurvature mode anti-correlated with adiabatic fluctuations, the amplitude of which is parameterized by  $\alpha_{-1}$ . This has been constrained in the past with WMAP data (99; 25) achieving a constraint of  $\alpha_{-1} < 0.0036$  at 95% confidence. New  $\Lambda\text{CDM} + \alpha_{-1}$  constraints including SPTpol data are included at the top of Table 7.5. The SPTpol dataset alone constrains  $\alpha_{-1} < 0.093$  at 95% confidence. The CMB+BAO+ $H_0$  dataset, however, dramatically improves this constraint to just  $\alpha_{-1} < 0.0009$  at 95% confidence, however we stress

that at the time of printing the CMB+BAO+H<sub>0</sub> isocurvature chains had not fully converged, so this result is tentative.

### 7.2.2.2 $\Lambda$ CDM + $e_{\text{WIMP}}$

As discussed above we have added a variable  $e_{\text{WIMP}}$  in CosmoMC that parameterizes energy injection in the CMB from WIMP particle annihilation as explored by (88). The constraint is interpreted as an amplitude of the particle annihilation cross-section, scaled by  $\epsilon = 2 \times 10^{-27}$  cm<sup>3</sup>/s/GeV. Chain results are found in the center of Table 7.5. Perturbations to CMB power spectra from energy injection in (88) are not calculated past  $l = 2500$  so these chains limit bandpowers to below this threshold. Using the dataset PLANCK+SPTPOL+BAO+H<sub>0</sub> we place a limit of  $e_{\text{WIMP}} < 1.23$  at 95% confidence, corresponding to a WIMP particle annihilation cross-section of  $p_{\text{ann}} < 2.46 \times 10^{-27}$  cm<sup>3</sup>/s/GeV at the same confidence level. This is comparable to constraints achieved using WMAP7 data (88). Since the measurement is limited to  $l < 2500$  the addition of more area from the SPTpol survey field should improve these constraints.

### 7.2.2.3 $\Lambda$ CDM + $r$

Recently, the BICEP2 experiment published a detection of presumed inflationary gravitational-wave (IGW)  $B$  modes, which is parameterized by the tensor-to-scalar ratio  $r$  (23). Using data from the 2012 observing season we published the first detection of *lensing B* modes (21), which dominate at intermediate to small angular scales. However, the scan strategy for the first year of observing was not optimized for measuring large angular scale modes to search for IGW  $B$  modes. The SPTpol deep field dataset is therefore not sensitive to  $r$  in the same way as BICEP2. Our ability to constrain  $r$  instead comes from the contribution to scalar modes (temperature and  $E$ -mode polarization) from initial tensor perturbations in the spacetime metric, i.e. inflationary gravitational waves. Allowing a non-zero value of  $r$  therefore adds additional power to our  $EE$  and  $TE$  spectra.

Constraints for  $\Lambda$ CDM +  $r$  chains are included in the bottom of Table 7.5. The previous

best constraint  $r < 0.11$  at 95% confidence<sup>3</sup> comes from a combination of  $TT$  power spectra measurements including Planck, WMAP9 polarization, and SPT and ACT high-multipole bandpowers (31). With only SPTpol data we measure this constraint to be  $r < 0.95$  at 95% confidence. The CMB data, however, improves the constraint to  $r < 0.09$  at 95% confidence. We again stress that the chains for the tensor-to-scalar ratio had not fully converged before printing so this is also a tentative result. While the constraint on  $r$  cited by (31) is near the limit of what is achievable from temperature power spectrum measurements alone (100; 87), future improvements in signal-to-noise of the polarization power spectra will improve limits on  $r$  regardless of the final determination of the source of excess low-multipole  $B$ -mode power detected by BICEP2.

### 7.3 Discussion

We have presented measurements of the 150 GHz CMB  $TE$  and  $EE$  polarization power spectra made from observations with the SPTpol experiment in 2012. The  $EE$  spectrum shows six acoustic peaks with high signal-to-noise, and we have measured the  $EE$  damping tail with the highest significance to date. The measurement is sample variance limited up to  $l = 1700$  (2000) in  $EE$  ( $TE$ ); we must observe more sky to measure these lower multipoles with higher signal-to-noise at the given bandpower width  $\Delta l = 50$ . While there is some tension observed between SPTpol bandpowers and the best-fit Planck  $\Lambda$ CDM model, the tension is not statistically significant and appears to be the result of sample variance. Indeed, the Planck  $\Lambda$ CDM model is a good fit to the bandpowers from a collection of four 100 deg<sup>2</sup> sub-fields of the SPTpol survey field (Figure 7.5) so we anticipate this tension shrinking when expanding the analysis to include the full 500 deg<sup>2</sup> survey field.

The SPTpol full survey is now in its second year of observations and should reach the 2012 deep field map depths across the entire field by the end of 2015. With such a survey, sample variance will be reduced by more than a factor of two compared to the deep field analysis presented

---

<sup>3</sup> Technically, this is a constraint of  $r$  at a spectral pivot point of  $k_0 = 0.002 \text{ Mpc}^{-1}$ , though the fit also assumes the tensor-mode spectral index  $n_T = 0$  making  $r$  insensitive to scale.

Table 7.5:  $\Lambda$ CDM Extensions

Parameter	Dataset			
	SPTPOL	PLANCK+S13	CMB	CMB+BAO+H <sub>0</sub>
$\Lambda$ CDM + $\alpha_{-1}$				
Free				
$\Omega_b h^2$	$0.02262 \pm 0.00127$	$0.02171 \pm 0.00026$	$0.02164 \pm 0.00027$	$0.02194 \pm 0.00022$
$\Omega_c h^2$	$0.07773 \pm 0.01255$	$0.12432 \pm 0.00262$	$0.12273 \pm 0.00226$	$0.11945 \pm 0.00146$
$100\theta_s$	$1.04419 \pm 0.00227$	$1.04105 \pm 0.00065$	$1.04111 \pm 0.00049$	$1.0415 \pm 0.00042$
$n_s$	$1.01122 \pm 0.05744$	$0.94263 \pm 0.00795$	$0.94761 \pm 0.00584$	$0.9521 \pm 0.00475$
$\ln(10^{10} A_s)$	$3.11738 \pm 0.11772$	$3.0607 \pm 0.02062$	$3.06289 \pm 0.02213$	$3.06282 \pm 0.02276$
$\tau$	(0.0927)	$0.06954 \pm 0.01048$	$0.07248 \pm 0.01047$	$0.07663 \pm 0.01162$
$\alpha_{-1}$	$< 0.09294$	$< 0.00075$	$< 0.00081$	$< 0.00091$
Derived				
$\Omega_\Lambda$	$0.86616 \pm 0.04189$	$0.6571 \pm 0.01699$	$0.66625 \pm 0.0147$	$0.68773 \pm 0.00866$
$H_0$	$89.03 \pm 8.46$	$65.45 \pm 1.13$	$65.95 \pm 1.0$	$67.46 \pm 0.62$
$\sigma_8$	$0.65617 \pm 0.08157$	$0.83049 \pm 0.01114$	$0.82844 \pm 0.01271$	$0.81836 \pm 0.01054$
$\Lambda$ CDM + $e_{\text{WIMP}}^{(\text{a})}$				
Free				
$\Omega_b h^2$	$0.02145 \pm 0.00126$	$0.02233 \pm 0.0003$	$0.02216 \pm 0.00027$	$0.02225 \pm 0.00023$
$\Omega_c h^2$	$0.07393 \pm 0.01206$	$0.11777 \pm 0.00273$	$0.11816 \pm 0.00267$	$0.11741 \pm 0.00139$
$100\theta_s$	$1.04362 \pm 0.00221$	$1.04127 \pm 0.0006$	$1.04122 \pm 0.00058$	$1.0413 \pm 0.00054$
$n_s$	$1.05686 \pm 0.06027$	$0.9715 \pm 0.00947$	$0.96721 \pm 0.00862$	$0.96943 \pm 0.00619$
$\ln(10^{10} A_s)$	$3.22366 \pm 0.12469$	$3.12485 \pm 0.03173$	$3.10208 \pm 0.02932$	$3.10663 \pm 0.02773$
$\tau$	(0.0927)	$0.08662 \pm 0.013$	$0.08333 \pm 0.01257$	$0.08516 \pm 0.01194$
$e_{\text{WIMP}}$	$< 3.67642$	$< 1.60479$	$< 1.1956$	$< 1.2268$
Derived				
$\Omega_\Lambda$	$0.87648 \pm 0.03912$	$0.69788 \pm 0.01631$	$0.6948 \pm 0.01604$	$0.69976 \pm 0.00805$
$H_0$	$90.4 \pm 8.64$	$68.31 \pm 1.25$	$68.01 \pm 1.19$	$68.37 \pm 0.63$
$\sigma_8$	$0.67523 \pm 0.08778$	$0.83789 \pm 0.01353$	$0.82918 \pm 0.01317$	$0.82877 \pm 0.01213$
$\Lambda$ CDM + $r$				
Free				
$\Omega_b h^2$	$0.02251 \pm 0.0013$	$0.02208 \pm 0.00027$	$0.02172 \pm 0.00025$	$0.02202 \pm 0.00022$
$\Omega_c h^2$	$0.08035 \pm 0.01303$	$0.11861 \pm 0.00263$	$0.12315 \pm 0.00272$	$0.11911 \pm 0.00205$
$100\theta_s$	$1.04326 \pm 0.00227$	$1.04174 \pm 0.00054$	$1.04108 \pm 0.00057$	$1.04163 \pm 0.00049$
$n_s$	$1.00758 \pm 0.05702$	$0.96217 \pm 0.00762$	$0.94482 \pm 0.00823$	$0.95522 \pm 0.00914$
$\ln(10^{10} A_s)$	$3.10579 \pm 0.12221$	$3.07227 \pm 0.02476$	$3.05919 \pm 0.02076$	$3.06669 \pm 0.02274$
$\tau$	(0.0927)	$0.08271 \pm 0.01273$	$0.07025 \pm 0.01198$	$0.07825 \pm 0.0117$
$r$	$< 0.95497$	$< 0.13149$	$< 0.09135$	$< 0.19434$
Derived				
$\Omega_\Lambda$	$0.85618 \pm 0.04608$	$0.69358 \pm 0.01583$	$0.66404 \pm 0.01781$	$0.69037 \pm 0.01181$
$H_0$	$87.03 \pm 8.42$	$67.96 \pm 1.17$	$65.86 \pm 1.17$	$67.69 \pm 0.85$
$\sigma_8$	$0.65692 \pm 0.08029$	$0.82075 \pm 0.01267$	$0.82581 \pm 0.00927$	$0.8183 \pm 0.01043$

**Notes:** Here PLANCK refers to Planck TT bandpowers plus WMAP9 polarization, labeled PLANCK+WP in Table 5 of (31). CMB refers to the combination PLANCK+S13+SPTPOL. All model extension constraints are 95% confidence level upper limits. As of the time of printing, chains in red have not fully converged.

<sup>(a)</sup> S13 is not included when running the  $e_{\text{WIMP}}$  extension. The maximum multipole is limited to  $l = 2500$  for these chains.

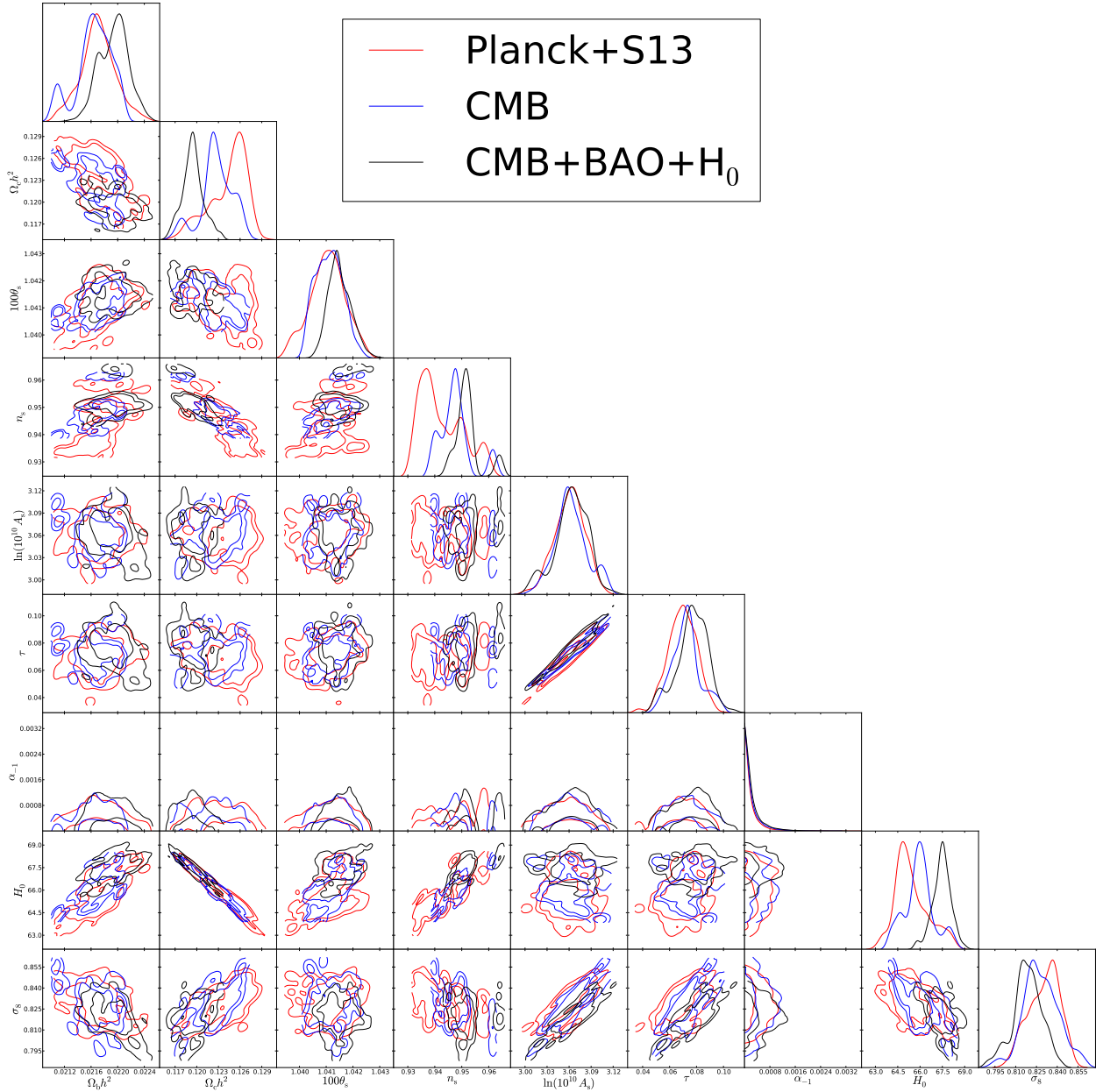


Figure 7.11: 2-D marginalized  $\Lambda$ CDM +  $\alpha_{-1}$  parameter likelihoods. *As of printing these chains had not fully converged.*

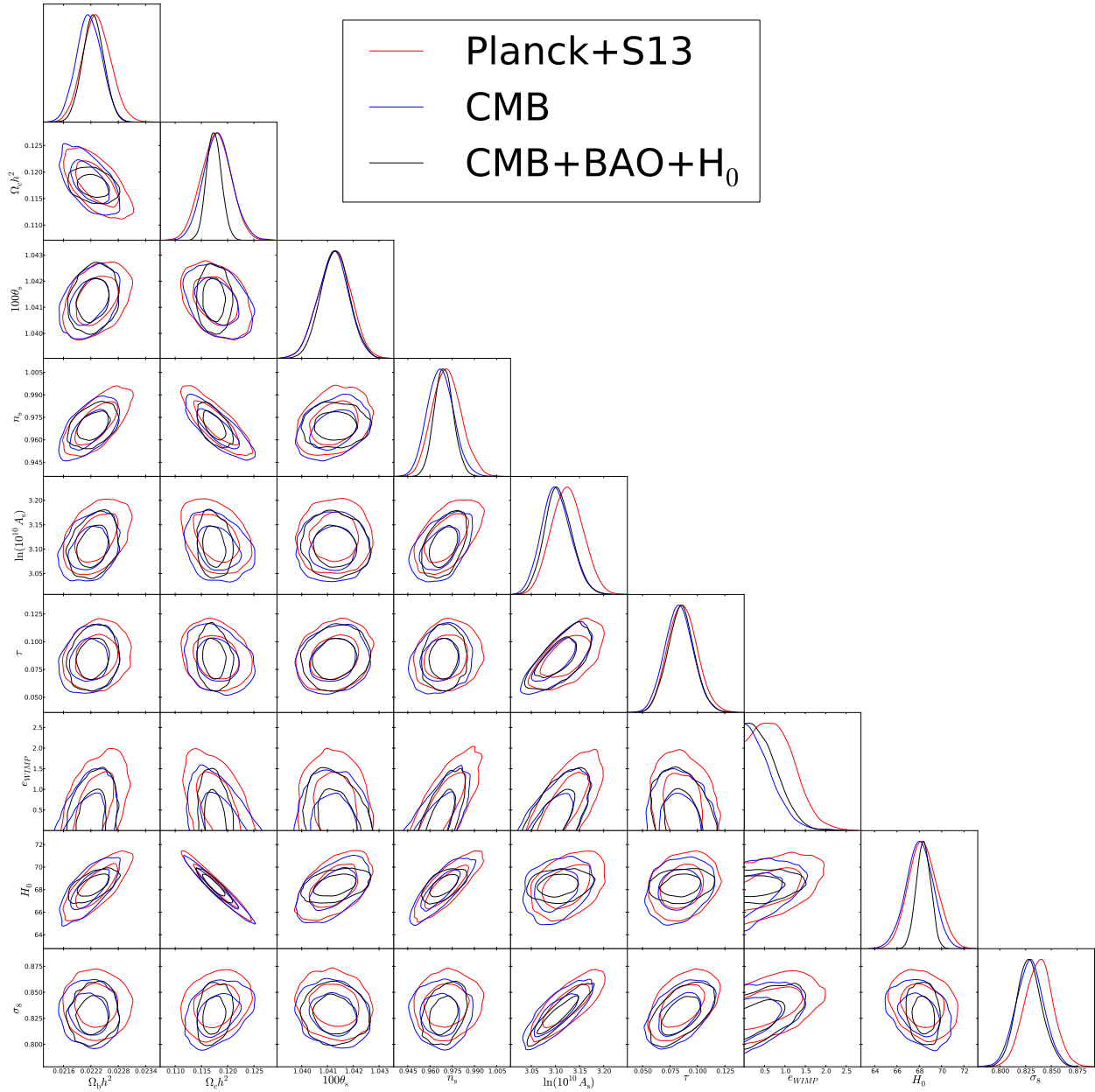


Figure 7.12: 2-D marginalized  $\Lambda$ CDM +  $e_{WIMP}$  parameter likelihoods.

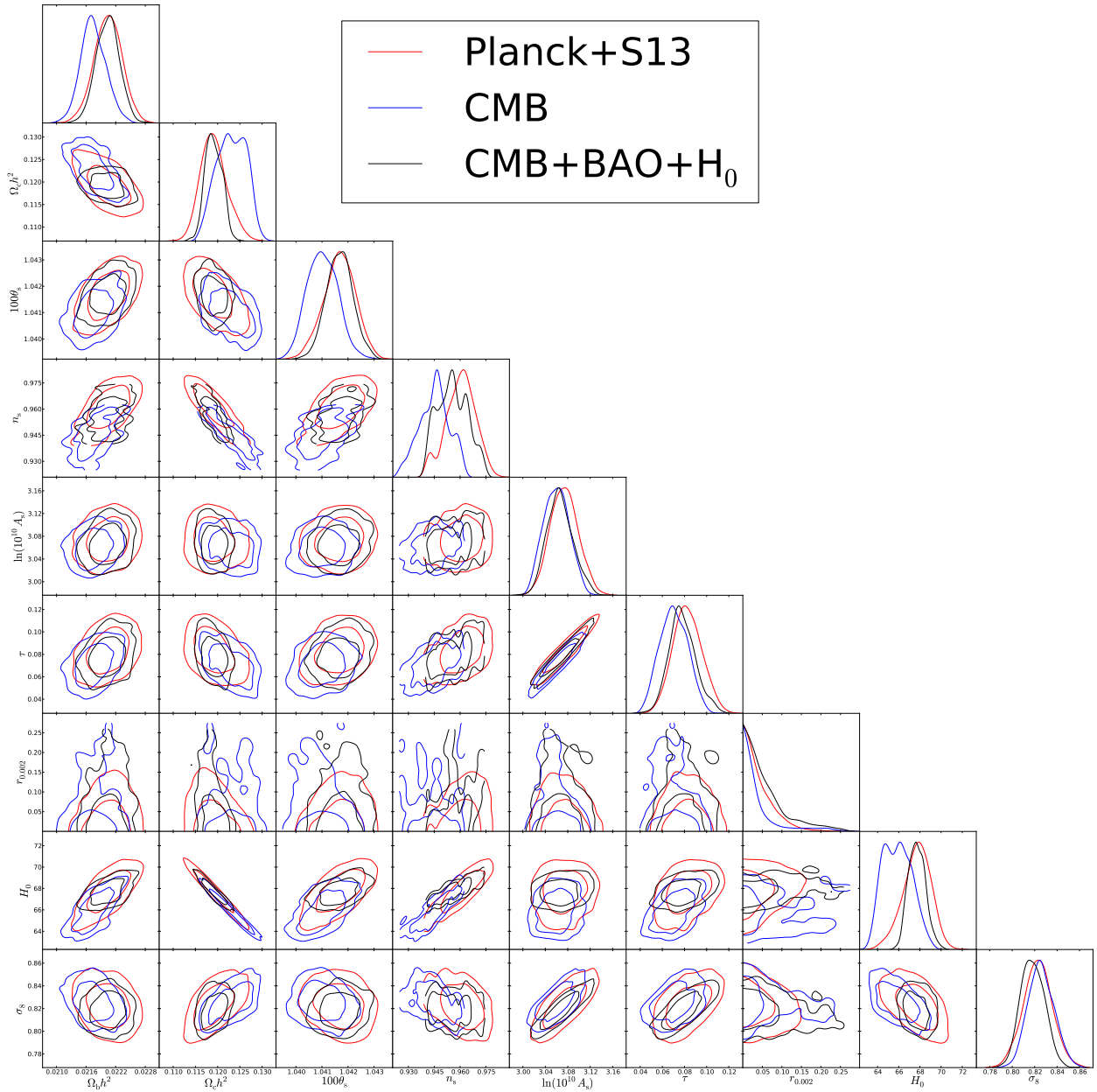


Figure 7.13: 2-D marginalized  $\Lambda$ CDM +  $r$  parameter likelihoods. *As of printing these chains had not fully converged.*

here, and high-fidelity measurements of the damping tail should extend beyond  $l = 3000$ . The final dataset will be rich with cosmological information, allowing us to place tighter constraints on the tensor-to-scalar ratio  $r$  and several other interesting extensions to the  $\Lambda$ CDM model, such as the quantity of primordial helium  $Y_p$ , the sum of neutrino masses  $\Sigma m_\nu$ , and the number of relativistic species  $N_{\text{eff}}$  (see Table 6.1).

With only 100 deg<sup>2</sup> mapped to interesting depths, SPTpol currently contributes little new direct cosmological information. We do see, however, that the addition of the 2012 deep field power spectra improves constraints on  $\Lambda$ CDM parameters at the few percent level. Additionally, we can begin to explore extensions to  $\Lambda$ CDM and we find that the SPTpol deep field bandpowers combined with external datasets can place interesting constraints despite its lack of sensitivity to low multipoles and its high sample variance. Both of these points are in some ways a scientific bonus as the original intent of the 2012 observations was to convincingly detect lensing  $B$  modes; they were not optimized in any way to deliver considerable improvements in cosmological parameter constraints. The fact that improvements can be made with this incomplete dataset speaks to the considerable scientific potential of SPTpol and its forthcoming observations.

Looking towards the future, the search for IGW  $B$  modes has become and will continue to be the primary drive in the CMB community. While recent measurements by BICEP2 are promising (23), more information about polarized foregrounds is needed to *confirm* a discovery of inflationary gravitational waves. Lensing  $B$  modes are also a significant foreground contaminant that not only mask the true amplitude of IGW  $B$  modes but also the shape of their power spectrum, which is vital for distinguishing between different inflationary models. As lensing  $B$ -mode measurements were the primary science goal of the SPTpol experiment, the completed survey will measure the amplitude of the  $B$ -mode spectrum with high significance. With the final SPTpol dataset the primordial  $B$ -mode spectrum can be *delensed*, which increases the significance of a detection and begins to uncover structure in the IGW  $B$ -mode spectrum at multipoles  $l \gtrsim 100$ . SPTpol will therefore play a crucial role in our understanding of the early universe.

## Chapter 8

### Future Work

We have presented a power spectrum analysis of the first year of observations made with the SPTpol experiment. The final coadded deep field map reaches a depth of 7 (10)  $\mu\text{K}\cdot\text{arcmin}$  in temperature (polarization), the deepest ever of the CMB at  $\sim 1$  arcminute resolution. However, the map is relatively small at  $100 \text{ deg}^2$  or just 0.25% of the sky. This means the resulting power spectra are sample variance limited at multipoles below  $\sim 1700$ . It is at these large scales that most sensitivity to  $\Lambda\text{CDM}$  model parameters resides. Additionally, the intriguing gravitational wave  $B$ -mode signal peaks at only  $l \sim 100$ , which is at scales larger than what the SPTpol deep field observations can probe.

To address both of these issues the second season of SPTpol observations was spent mapping the  $500 \text{ deg}^2$  survey field. A power spectrum analysis of these new observations very similar to that discussed in this work is currently underway being led by the author. The larger CMB field and increased scan speed provides sensitivity to much larger scales and the author anticipates no major hurdles to expanding the multipole range of study down to  $l = 100$  or lower. The 2-D  $EE$  spectrum of the 2013 survey field map coadd exhibits six acoustic peaks *before azimuthal averaging*. Figure 8.1 reproduces the 2-D spectrum with  $C_l$  normalization shown in Figure 5.8 and the acoustic peaks are readily apparent by eye. Azimuthally averaged  $EE$  and  $TE$  power spectra from 2013 survey field observations are also plotted in Figure 8.2 with noise variance errors at a resolution of  $\Delta l = 6.25$ , eight times finer than that used for the 2012 deep field analysis discussed in this work. These pseudo-spectra have not yet been fully corrected for filtering and mode-coupling, but

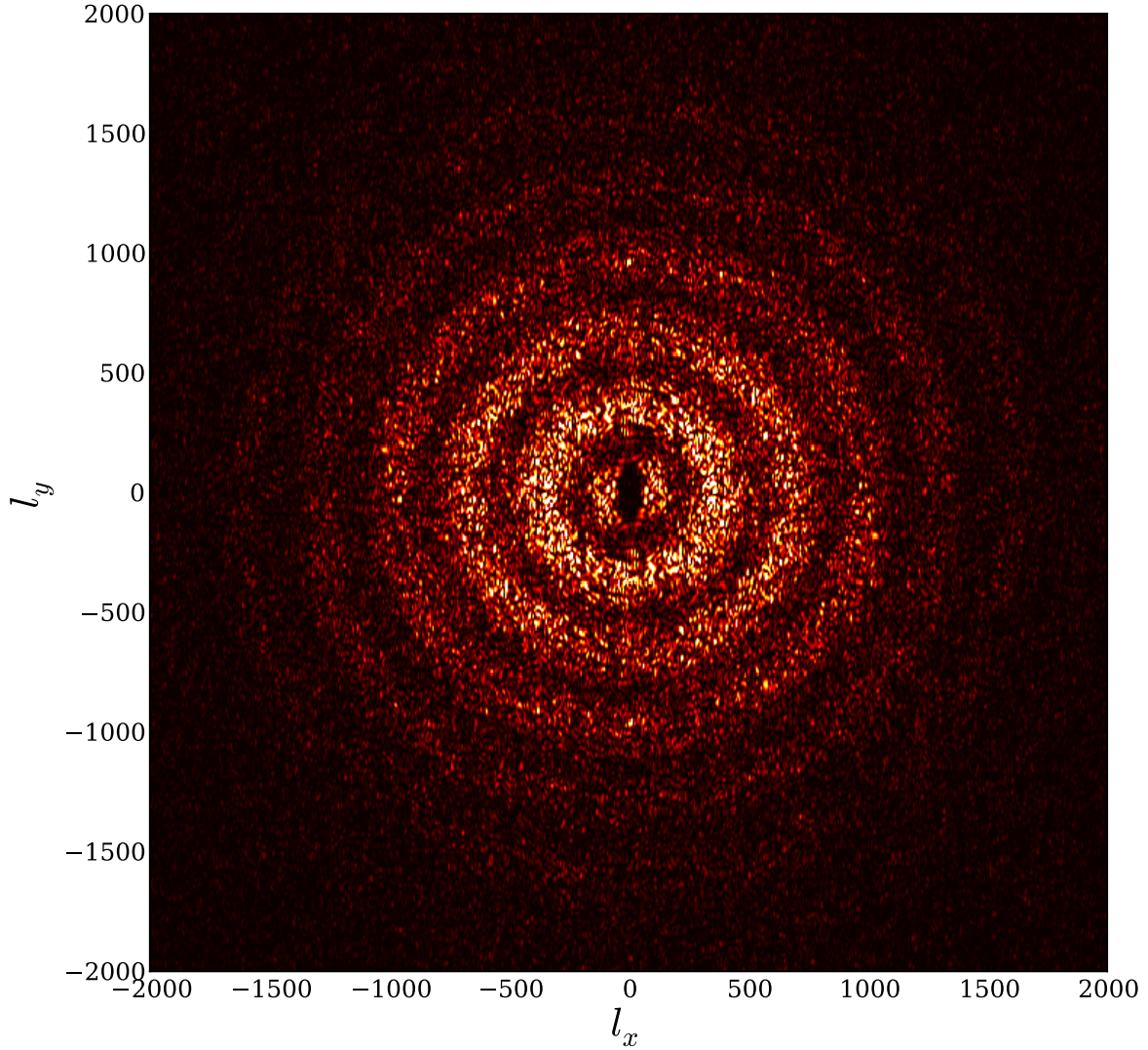


Figure 8.1: SPTpol 2013 survey field 2-D  $EE$  pseudo-power spectrum in  $C_l$  normalization.

the instrument beam and a by-eye calibration factor of 0.85 have been applied. The data show astonishing agreement with the expected Planck  $\Lambda$ CDM model and represent a substantial step forward in signal-to-noise. The strong agreement with  $\Lambda$ CDM at large angular scales is also a demonstration of the ability of SPTpol to actually measure scales at such low multipoles, which is crucial for the search of primordial  $B$ -mode polarization. The power of these new survey field power spectra will manifest as stronger constraints on  $\Lambda$ CDM parameters, particularly the scalar spectra index  $n_s$  that benefits from a long lever arm in angular scales being measured.

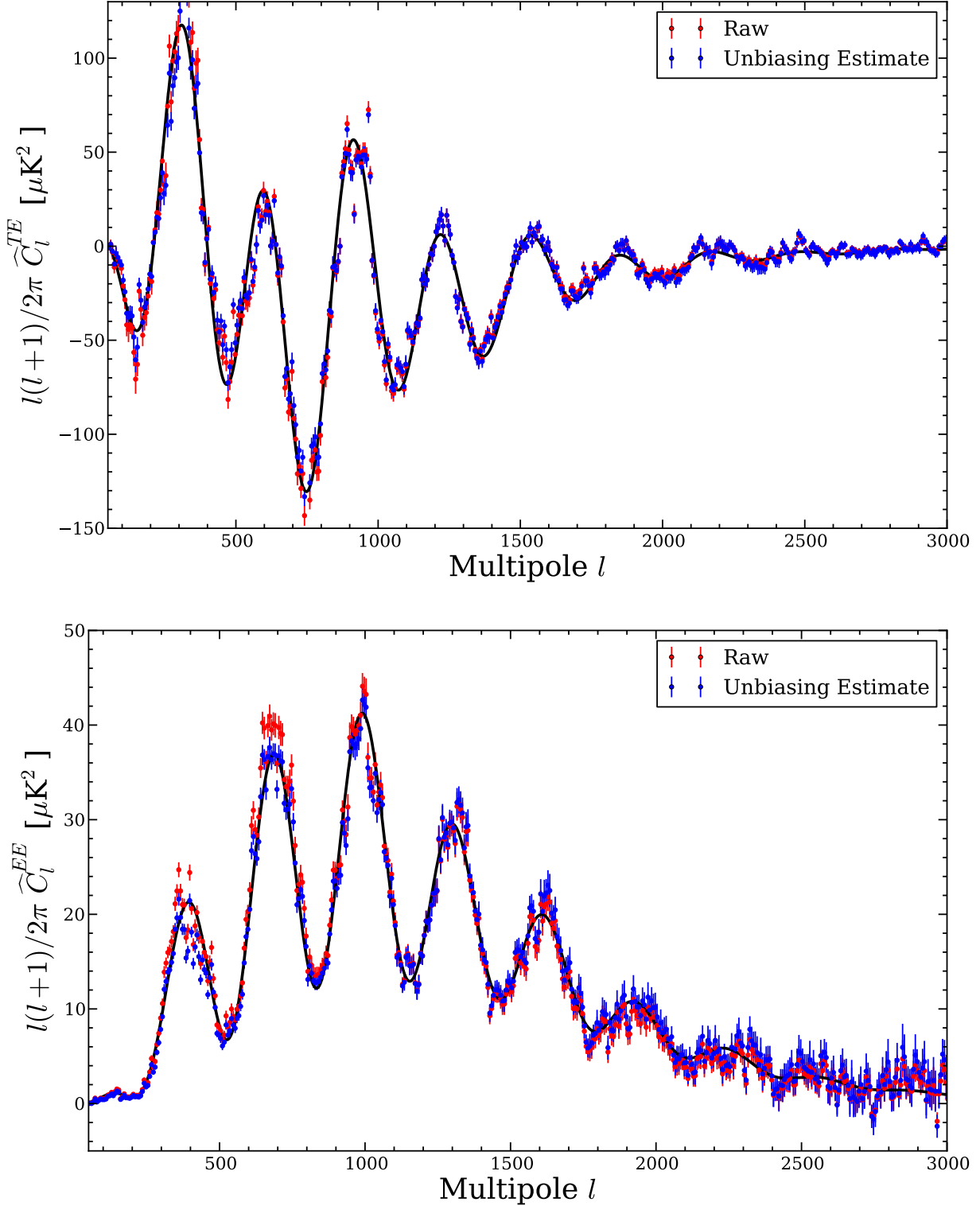


Figure 8.2: Preliminary SPTpol 2013 survey field  $TE$  and  $EE$  power spectra with noise variance error bars. Bandpower resolution is  $\Delta l = 6.25$ . The Planck  $\Lambda$ CDM model is in black. In red we plot the raw pseudo-spectra while in blue we partially unbias the bandpowers by taking into account the instrument beam and a by-eye calibration factor of 0.85. Mode-coupling and the filter transfer function have been ignored.

This new analysis will also include 95 GHz auto-spectra as well as  $95 \times 150$  cross-spectra. The number of CMB power spectra entering into the cosmological parameter constraints therefore increases from two to six, a substantial increase in information. All of these spectra are not independent, of course, and accounting for this greatly complicates the bandpower covariance matrix, which will grow to be a  $6 \times 6$  block of  $\sim 40 \times 40$  matrices (one element per power spectrum band-power). The covariance calculation pipeline is already generalized and able to calculate the various off-diagonal blocks, however. Furthermore, the SPTpol likelihood module has been written to accept any number of CMB power spectra at different auto- and cross-frequency combinations. The addition of 95 GHz data and  $95 \times 150$  power spectra represents a complication in bookkeeping only; the abilities to calculate necessary data products and actually use them to constrain cosmology already exist.

Delensing of low-multipole  $B$  modes will also soon become an important process in searches for primordial  $B$  modes and in constraining various inflationary models. To date the SPTpol dataset contains the deepest maps at the requisite angular scales for delensing and will have significant impact in near-term  $B$ -mode searches such as those conducted by SPTpol, BICEP2, and the Keck experiments. Indeed, based on cross-correlations with tracers of large-scale structure, the 2012 deep field observations can already reduce lensing  $B$ -mode power by a factor of two (21). Since we have observed the same patch of sky, joint-analyses with BICEP2 are also in discussion to both delens their low-multipole  $B$ -mode measurements and cross-correlate the datasets to look for a common cosmological signal. The detection of  $B$  modes at large angular scales must be verified by other experiments, and SPTpol is one such experiment with the capabilities to do so.

As the SPTpol survey field reaches lower map depths its delensing power will only increase. But to significantly increase our delensing capabilities we must map CMB polarization to unprecedented depths, below  $\sim 5 \mu\text{K}\cdot\text{arcmin}$  at multipoles greater than  $l \sim 1000$ . At these depths  $B$  modes will be *imaged* rather than just statistically detected. This will require a more powerful experiment. SPT-3G, the third generation receiver that will be installed on the SPT, is currently in development. It will contain more than 15,000 detectors, and measure CMB polarization at three frequencies,

95, 150, and 220 GHz. Crucially, the multi-frequency data will provide the power to constrain polarized foregrounds like galactic synchrotron and dust, which threaten to overwhelm any true cosmological  $B$ -mode signal. The mapping speed of SPT-3G will also be an order of magnitude greater than that of SPTpol, allowing it to map  $2500 \text{ deg}^2$  down to a depth of  $2.5$  ( $3.5$ )  $\mu\text{K}\cdot\text{arcmin}$  in  $T$  ( $P$ ) at 150 GHz and  $4.2$  ( $6$ )  $\mu\text{K}\cdot\text{arcmin}$  in  $T$  ( $P$ ) at 95 and 220 GHz over a three-year survey. At such un-probed depths, SPT-3G is poised to place tight constraints on the tensor-to-scalar ratio (a standard deviation  $\sigma(r) = 0.01$ ), the sum of neutrino masses ( $\sigma(\Sigma m_\nu) = 74 \text{ meV}$ ), and discover thousands of new galaxy clusters that will inform our understanding of structure formation and dark energy. The SPT-3G dataset will doubtless become a treasure trove of cosmological and astrophysical data with which scientists will be able to tease out more of the intricate workings of nature. The future of CMB observations is bright, and a new era of cosmological discovery is just beginning.

## Bibliography

- [1] L. E. Bleem, *et al.*, *ApJ* **753**, L9 (2012).
- [2] B. D. Sherwin, *et al.*, *Phys. Rev. D* **86**, 083006 (2012).
- [3] G. P. Holder, *et al.*, *ApJ* **771**, L16 (2013).
- [4] Planck Collaboration I, *ArXiv e-prints* (2013).
- [5] R. A. Sunyaev, Y. B. Zeldovich, *Comments on Astrophysics and Space Physics* **2**, 66 (1970).
- [6] R. A. Sunyaev, Y. B. Zeldovich, *Comments on Astrophysics and Space Physics* **4**, 173 (1972).
- [7] J. E. Carlstrom, G. P. Holder, E. D. Reese, *ARA&A* **40**, 643 (2002).
- [8] O. Zahn, *et al.*, *ApJ* **756**, 65 (2012).
- [9] G. F. Smoot, *et al.*, *ApJL* **396**, L1 (1992).
- [10] C. Pryke, *et al.*, *ApJ* **692**, 1247 (2009).
- [11] H. C. Chiang, *et al.*, *ApJ* **711**, 1123 (2010).
- [12] E. Komatsu, *et al.*, *ApJS* **192**, 18 (2011).
- [13] K. T. Story, *et al.*, *ApJ* **779**, 86 (2013).
- [14] QUIET Collaboration, *et al.*, *ApJ* **760**, 145 (2012).
- [15] Planck collaboration XV, *et al.*, *ArXiv e-prints* (2013).
- [16] A. G. Riess, *et al.*, *ApJ* **730**, 119 (2011).
- [17] M. Hicken, *et al.*, *ApJ* **700**, 1097 (2009).
- [18] L. Anderson, *et al.*, *MNRAS* **441**, 24 (2014).
- [19] S. W. Allen, *et al.*, *MNRAS* **383**, 879 (2008).
- [20] B. A. Benson, *et al.*, *ApJ* **763**, 147 (2013).
- [21] D. Hanson, *et al.*, *Phys. Rev. Lett.* **111**, 141301 (2013).
- [22] The POLARBEAR Collaboration, *et al.*, *ArXiv e-prints* (2014).

- [23] BICEP2 Collaboration, *et al.*, *ArXiv e-prints* (2014).
- [24] S. Naess, *et al.*, *ArXiv e-prints* (2014).
- [25] G. Hinshaw, *et al.*, *ApJS* **208**, 19 (2013).
- [26] A. Einstein, *Annalen der Physik* **354**, 769 (1916).
- [27] E. Hubble, *Proceedings of the National Academy of Science* **15**, 168 (1929).
- [28] S. M. Carroll, *Spacetime and geometry. An introduction to general relativity* (2004).
- [29] S. Dodelson, *Modern cosmology* (2003).
- [30] J. A. Peacock, *Cosmological Physics* (1999).
- [31] Planck Collaboration XVI, *et al.*, *ArXiv e-prints* (2013).
- [32] A. Lewis, A. Challinor, A. Lasenby, *ApJ* **538**, 473 (2000).
- [33] A. R. Liddle, *High Energy Physics and Cosmology, 1998 Summer School*, A. Masiero, G. Senjanovic, A. Smirnov, eds. (1999), p. 260.
- [34] A. H. Guth, S.-Y. Pi, *Phys. Rev. Lett.* **49**, 1110 (1982).
- [35] S. W. Hawking, *Physics Letters B* **115**, 295 (1982).
- [36] A. A. Starobinsky, *Physics Letters B* **117**, 175 (1982).
- [37] J. M. Bardeen, P. J. Steinhardt, M. S. Turner, *Phys. Rev. D* **28**, 679 (1983).
- [38] A. Lewis, S. Bridle, *Phys. Rev. D* **66**, 103511 (2002).
- [39] C. L. Reichardt, *et al.*, *ApJ* **755**, 70 (2012).
- [40] J. L. Sievers, *et al.*, *JCAP* **10**, 60 (2013).
- [41] D. J. Eisenstein, *et al.*, *ApJ* **633**, 560 (2005).
- [42] H. C. Chiang, *et al.*, *ApJ* **711**, 1123 (2010).
- [43] V. C. Rubin, W. K. Ford, Jr., *ApJ* **159**, 379 (1970).
- [44] F. Zwicky, *Helvetica Physica Acta* **6**, 110 (1933).
- [45] D. Clowe, *et al.*, *ApJ* **648**, L109 (2006).
- [46] J. Silk, *ApJ* **151**, 459 (1968).
- [47] Z. Hou, *et al.*, *ApJ* **782**, 74 (2014).
- [48] J. D. Jackson, *Classical Electrodynamics, 3rd Edition* (1998).
- [49] W. Hu, M. White, *New Astronomy* **2**, 323 (1997).
- [50] J. Austermann, *et al.*, *Society of Photo-Optical Instrumentation Engineers (SPIE) Conference Series* (2012).

- [51] E. George, *et al.*, *Society of Photo-Optical Instrumentation Engineers (SPIE) Conference Series* (2012).
- [52] A. P. Lane, *Astrophysics From Antarctica*, G. Novak, R. Landsberg, eds. (1998), vol. 141 of *Astronomical Society of the Pacific Conference Series*, pp. 289–295.
- [53] J. Ruhl, *et al.*, *Z-Spec: a broadband millimeter-wave grating spectrometer: design, construction, and first cryogenic measurements*, C. M. Bradford, *et al.*, eds. (2004), vol. 5498 of *Society of Photo-Optical Instrumentation Engineers (SPIE) Conference Series*, pp. 11–29.
- [54] J. W. Henning, *et al.*, *Society of Photo-Optical Instrumentation Engineers (SPIE) Conference Series* (2012), vol. 8452 of *Society of Photo-Optical Instrumentation Engineers (SPIE) Conference Series*.
- [55] T. M. Lanting, Multiplexed readout of superconducting bolometers for cosmological observations, Ph.D. thesis, University of California, Berkeley (2006).
- [56] S. Lee, J. M. Gildemeister, W. Holmes, A. T. Lee, P. L. Richards, *Appl. Opt.* **37**, 3391 (1998).
- [57] P. L. Richards, *Journal of Applied Physics* **76**, 1 (1994).
- [58] J. E. Austermann, *et al.*, *American Institute of Physics Conference Series*, B. Young, B. Cabrera, & A. Miller, ed. (2009), vol. 1185 of *American Institute of Physics Conference Series*, pp. 498–501.
- [59] J. Sayre, *et al.*, *Society of Photo-Optical Instrumentation Engineers (SPIE) Conference Series* (2012).
- [60] K. W. Yoon, *et al.*, *American Institute of Physics Conference Series*, B. Young, B. Cabrera, & A. Miller, ed. (2009), vol. 1185 of *American Institute of Physics Conference Series*, pp. 515–518.
- [61] M. Dobbs, E. Bissonnette, H. Spieler, *IEEE Transactions on Nuclear Science* **55**, 21 (2008).
- [62] P. J. B. Clarricoats, A. D. Olver, *Corrugated horns for microwave antennas / P.J.B. Clarricoats and A.D. Olver* (P. Peregrinus on behalf of the Institution of Electrical Engineers, London, UK :, 1984).
- [63] C. Barnes, *et al.*, *ApJS* **143**, 567 (2002).
- [64] J. M. Kovac, *et al.*, *Nature* **420**, 772 (2002).
- [65] S. Padin, *et al.*, *PASP* **114**, 83 (2002).
- [66] W. C. Jones, R. Bhatia, J. J. Bock, A. E. Lange, *Society of Photo-Optical Instrumentation Engineers (SPIE) Conference Series*, T. G. Phillips, J. Zmuidzinas, eds. (2003), vol. 4855 of *Society of Photo-Optical Instrumentation Engineers (SPIE) Conference Series*, pp. 227–238.
- [67] D. Barkats, *et al.*, *ApJ* **159**, 1 (2005).
- [68] J. J. Bock, J. Gundersen, A. T. Lee, P. L. Richards, E. Wollack, *Journal of Physics Conference Series* **155**, 012005 (2009).

- [69] J. R. Hinderks, *et al.*, *ApJ* **692**, 1221 (2009).
- [70] Y. D. Takahashi, *et al.*, *ApJ* **711**, 1141 (2010).
- [71] J. W. Britton, *et al.*, *Society of Photo-Optical Instrumentation Engineers (SPIE) Conference Series* (2010), vol. 7741 of *Society of Photo-Optical Instrumentation Engineers (SPIE) Conference Series*.
- [72] J. Hubmayr, *et al.*, *Journal of Low Temperature Physics* **167**, 904 (2012).
- [73] L. E. Bleem, *et al.*, *American Institute of Physics Conference Series*, B. Young, B. Cabrera, & A. Miller, ed. (2009), vol. 1185 of *American Institute of Physics Conference Series*, pp. 479–482.
- [74] J. W. Henning, *et al.*, *Society of Photo-Optical Instrumentation Engineers (SPIE) Conference Series* (2010), vol. 7741 of *Society of Photo-Optical Instrumentation Engineers (SPIE) Conference Series*.
- [75] G. Smecher, *et al.*, *IEEE Transactions on Instrumentation and Measurement* (2012), vol. 61.
- [76] Emerson and Cuming Microwave Products, <http://www.eccosorb.com> .
- [77] <http://lartpc-docdb.fnal.gov/0000/000059/001/stycas2850.pdf> .
- [78] M. Lueker, *et al.*, *IEEE Transactions on Applied Superconductivity* **19**, 496 (2009).
- [79] A. A. Stark, *et al.*, *PASP* **113**, 567 (2001).
- [80] J. Snyder, *Map projections—a working manual*, Geological Survey Bulletin Series (U.S. G.P.O., 1987).
- [81] E. Hivon, *et al.*, *ApJ* **567**, 2 (2002).
- [82] NASA JPL Solar System Dynamics Ephemerides Table, <http://ssd.jpl.nasa.gov/horizons.cgi> .
- [83] R. Keisler, *et al.*, *ApJ* **743**, 28 (2011).
- [84] M. Zaldarriaga, U. Seljak, *Phys. Rev. D* **55**, 1830 (1997).
- [85] M. Tegmark, A. N. Taylor, A. F. Heavens, *ApJ* **480**, 22 (1997).
- [86] L. Knox, *ApJ* **480**, 72 (1997).
- [87] L. Knox, *Phys. Rev. D* **52**, 4307 (1995).
- [88] D. P. Finkbeiner, S. Galli, T. Lin, T. R. Slatyer, *Phys. Rev. D* **85**, 043522 (2012).
- [89] D. Gamerman, H. F. Lopes, *Markov Chain Monte Carlo: Stochastic Simulation for Bayesian Inference* (Chapman and Hall/CRC, 2006).
- [90] A. Gelman, D. Rubin, *Statistical Science* **7**, 457 (1992).
- [91] A. Gelman, G. Roberts, W. Gilks, *Bayesian Statistics*, J. M. Bernardo, *et al.*, eds. (OUP, 1996), vol. 5, p. 599.

- [92] S. Seager, D. D. Sasselov, D. Scott, *ApJ* **523**, L1 (1999).
- [93] T. R. Slatyer, N. Padmanabhan, D. P. Finkbeiner, *Phys. Rev. D* **80**, 043526 (2009).
- [94] M. L. Brown, *et al.*, *ApJ* **705**, 978 (2009).
- [95] S. Galli, *et al.*, *ArXiv e-prints* (2014).
- [96] A. van Engelen, *et al.*, *ApJ* **756**, 142 (2012).
- [97] R. G. Hamish Robertson, *Journal of Physics Conference Series* **173**, 012016 (2009).
- [98] A. Gando, *et al.*, *Phys. Rev. C* **85**, 045504 (2012).
- [99] E. Komatsu, *et al.*, *ApJS* **180**, 330 (2009).
- [100] L. Knox, M. S. Turner, *Phys. Rev. Lett.* **73**, 3347 (1994).

## Appendix A

### Determination of Science Band Frequencies in Detector Timestreams

The science band is a function of angular size (or multipole  $l$ ) of relevant features in the CMB as well as the scan speed on the sky. In the flat-sky approximation spherical harmonic transforms are replaced by the more pedestrian Fourier transforms and

$$\vec{l} \cong \vec{k}, \quad (\text{A.1})$$

where  $\vec{k} = (k_x, k_y)$  is the Fourier conjugate to physical dimension  $\vec{x} = (x, y)$  in a flat cartesian grid and multipole  $l$  is just the radial distance from the origin in the Fourier domain,  $l = \sqrt{l_x^2 + l_y^2}$ . If the angular extent  $\theta$  of a feature on the sky is known, one obtains the corresponding multipole using

$$l \cong \frac{180}{\theta}. \quad (\text{A.2})$$

Here  $\theta$  is in degrees on the sky. For example, point sources in SPTpol maps appear at the size of the detector beams,  $\sim 1$  arcminute, which corresponds to  $l \cong 10,800$ . During 2012 deep field observations the telescope azimuthal scan speed was 0.48 deg/s, or 0.27 deg/s on the sky in the field-center at EL = 55° (Dec = -55°). Angular frequency is easily translated to temporal frequency via the simple equation

$$f = \frac{lv_{\text{sky}}}{360}, \quad (\text{A.3})$$

where  $v_{\text{sky}}$  is the scan rate on the sky in degrees/s,  $l$  is the multipole corresponding to a given feature's angular extent, and  $f$  is the resulting temporal frequency at which the feature will present itself in a bolometer's timestream. Thus a multipole range  $100 < l < 5000$  translates to a science

band in the detector timestreams of  $0.075 - 3.75$  Hz. For the 2013 survey field observations, we increased our azimuthal scan speed to  $1.09^\circ/\text{s}$  and the field center was at  $\text{EL} = 57.5^\circ$ . The same multipole range, therefore, is mixed up by the increased scan speed to  $0.16 - 8.13$  Hz. This helps avoid low-frequency detector  $1/f$  noise.